Atomic Coherence Effects: Electromagnetically Induced Transparency and Inversionless Lasing

A thesis presented by
Evangelini Zekou, M.Sc.
to the University of St Andrews in application for the degree of
Doctor of Philosophy

J.F. Allen Physics Research Laboratories
School of Physics and Astronomy
University of St Andrews
North Haugh
St Andrews KY16 9SS
Scotland

Declarations

I, Evangelini Zekou, hereby certify that this thesis, which is approximately 50,000 words in length, has been written by me, that it is the record of work carried out by me and that it has not been submitted in any previous application for a higher degree.

date 5 March 1999 signature of candidate

I was admitted as a research student in October 1995 and as a candidate for the degree of Doctor of Philosophy in November 1998; the higher study for which this is a record was carried out in the University of St. Andrews between 1995 and 1998.

date 5 March 1999 signature of candidate

I hereby certify that the candidate has fulfilled the conditions of the Resolution and Regulations appropriate for the degree of Doctor of Philosophy in the University of St. Andrews and that the candidate is qualified to submit this thesis in application for that degree.

date 5 March 1999 signature of supervisor

In submitting this thesis to the University of St. Andrews I understand that I am giving permission for it to be made available for use in accordance with the regulations of the University Library for the time being in force, subject to any copyright vested in the work not being affected thereby. I also understand that the title and abstract will be published, and that a copy of the work may be made and supplied to any bona fide library or research worker.

date 5 March 1999 signature of candidate .

Abstract

This thesis is concerned with theoretical and experimental studies of atomic coherence effects, such as electromagnetically induced transparency (EIT) and inversionless lasing. Theoretical analysis was carried out using semiclassical density matrix models, while experiments employed continuous-wave Ti:sapphire lasers directly or frequency doubled, to explore energy level schemes within atomic Rb.

A theoretical comparison of systems involving matched and mismatched wavelengths for probe (λ_p) and coupling (λ_c) fields, is presented for the three basic energy level schemes, namely the cascade, the lambda and the V-scheme. The best transparency was predicted for the mismatched case where $\lambda_c<\lambda_p$. This is a direct result of the increased Doppler shifted contribution to the coupling field detuning. In the mismatched regime, $\lambda_c>\lambda_p$, transparency was predicted to occur for coupling field Rabi frequencies less than the Doppler width of the probe transition, but only in the V-scheme. The magnitude of the secondary Autler-Townes components, related to the two-photon process, which overlap with the transparency window is not significant to erode the transparency in this case. Subsequently, inversionless gain was predicted for matched and mismatched ($\lambda_c>\lambda_p$) systems, in a V-scheme. While the inversionless gain expected is higher in the matched scheme, the predicted gain is still significant in the mismatched case.

Transparency was experimentally observed on a probe transition in the blue spectral region (at 422 nm), due to an infrared coupling field, in a V-type scheme in atomic Rb. This was achieved in the absence of optical pumping, but required Rabi frequencies equal to or higher than the Doppler width of the probe transition. The roles of high dephasing rates and coupling field absorption, in delaying the onset of EIT, are explored. The generation of EIT at 422 nm is the first step in the process of creating inversionless gain in this blue spectral region. The effect of further mismatching the wavelengths is explored, and microwave induced transparency is theoretically predicted for both Rb vapour and for an atomic beam. The feasibility of such experiments lies in the power requirements of the microwave field.

Acknowledgements

I would like to thank my supervisor Prof. Malcolm Dunn for his help, encouragement and concern all the way through to the end of this work. He not only introduced me to the quantum coherence world, but he supported me strongly during the period of a serious health problem. I would also like to acknowledge the contribution of Dr. Sara Shepherd and Dr. David Fulton to this work. They were always keen to answer my questions concerning the theory and the lab apparatus. A special thanks must also go to Dr. James Boon for his co-operation and choice of music, while we were trying desperately to operate the Microlase system. I would like to thank David McGloin for his enthusiasm and new spirit in joining our group and carrying out the future work.

I want to thank Dr. Graham Smith who has contributed to the completion of the microwave cavity. I must also thank the technical staff in the workshop for their patience with my drawings. I would like to thank all the secretaries for their support, while I was waiting to meet my supervisor. I like to thank all the postdocs and members of staff who have given solutions with their experience to my questions about lasers.

Thanks especially goes to Graham, Kishan, Johaness, Graham, Neil, Ian and Richard for having lots of fun during the conference in Baltimore. Of course I do not want to forget my portuguese, brazilian, greek, turkish, french, scottish, english, german, italian, iranian and spanish friends for making my time in St.Andrews so joyful and enjoyable. I will really miss them. I wish also to thank Catherine Dunn, Sarah and Ruth for their meals full of colours, drawings and spontaneous music playing. I am grateful to Dr. Suzanne Lyle for her precious help during the year I stayed in Andrew Melville Hall.

I would like to express my thanks to St.Leonard's College and the University of St.Andrews for the award of a studentship, which gave me the chance to complete my studies. I wish also to thank my family who stood by me over the last 3 years.

The life you gave
the smile in your face
the sunshine of your heart
the hand which always holds us
the presence even when you are away
the distance of a hug
the words supporting our dreams
guided me to write an additional sentence
which may fit in this thesis

"To my mother"

Table of contents

Declarations

Abstract

Acknowledgements

Table of contents

Chapter 1: Introduction

Chapter 2: Density matrix analysis for atomic coherence effects

Chapter 3: Atomic system and experimental equipment

Chapter 4: Experimental observation of coherently induced transparency on a blue probe in a Doppler-broadened mismatched V-type system

Chapter 5: Prediction of inversionless gain in a mismatched Doppler-broadened medium

Chapter 6: Comparison of wavelength dependence in Cascade, Lambda and V-type schemes for electromagnetically induced transparency

Chapter 7: The study of microwave induced transparency in Rubidium

Chapter 8: Conclusions and future work

Chapter 1

Introduction

1.1. a What is electromagnetically induced transparency (EIT)?

In the present chapter we will introduce the basic concepts behind EIT, we will then discuss the significance of the present work and we will historically review EIT and the related effects seen in the early years.

Consider a two-level atom to which we apply a weak optical field, indicated as the probe field, resonant on the atomic transition. We then observe a straight forward absorption as depicted in figure 1.1.1.

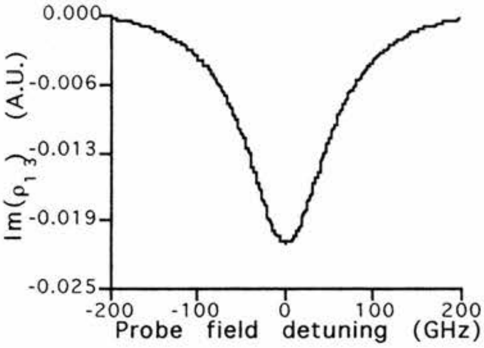

Figure 1.1.1: *Probe field absorption as a function of the probe field detuning. The probe field is on resonance with a two-level atom.*

Electromagnetically induced transparency (EIT) is an effect whereby the allowed transition is rendered transparent, to the resonant probe field, due to the presence of a second strong optical field coupled to one of the probe transition energy levels. The three most common systems studied theoretically and experimentally, are shown schematically in figure 1.1.2.

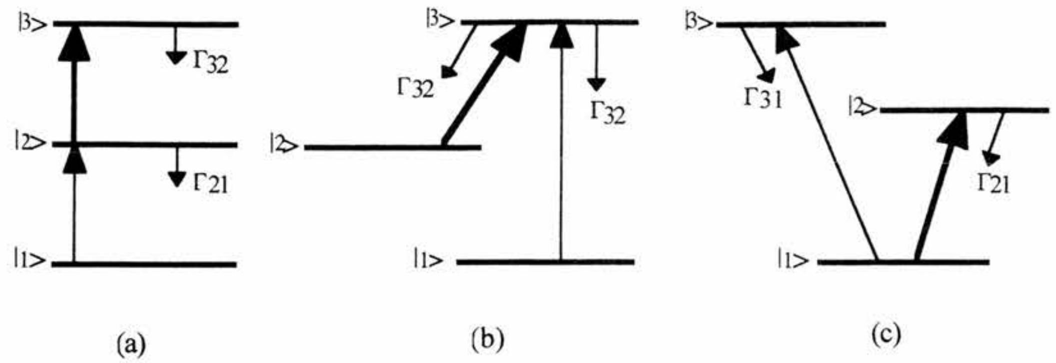

Figure 1.1.2: *Energy level configuration for (a) the Cascade, (b) the Lambda and (c) the V-scheme. Γ_{ij} are the decay rates from the energy level. The thin arrow is the probe field and the thick arrow is the coupling field.*

In the cascade scheme the probe field is on resonance with the ground state of the atom and an excited state. The coupling field is then linked with the common excited state and is coupled to another excited state of higher energy within the atom. This system is also called a ladder scheme. Experiments carried out in this configuration are referred as coherent population trapping, because the probe field is a weak optical field and a big fraction of the population is located in the ground state. The lambda scheme is in a way similar to the cascade scheme. The only difference is that the coupling field is on resonance to the linked energy level and to an excited state of lower energy this time. This energy level does not have a decay rate. In the most experiments the two first levels of the lambda scheme are two hyperfine levels of a ground state. The V-scheme has both the coupling and the probe field resonant to the common ground state. EIT in the V-scheme is the cancellation of absorption on the probe field, due to the presence of the strong coupling field, sharing the common lower state (the ground state). Most of the experiments so far accomplished for the study of EIT and related topics, in a Doppler broadened medium, have used the same probe and coupling field wavelengths. This was for the purpose of obtaining Doppler cancellation. In the present work we will show that this is not a necessary condition for the observation of EIT in a V-scheme, in a Doppler broadened medium.

1.1.b Significance of the present work: Introduction to a mismatched V-type system.

All the previous experiments in which atomic coherence effects were used to obtain electromagnetically induced transparency (EIT) and subsequently inversionless gain, relied on matched wavelengths (the probe field wavelength is comparable to that of the coupling field) to overcome Doppler broadening. However, contrary to conventional wisdom, we have been able to show that the wavelengths of the weak probe laser and that of the strong coupling field need not be matched.

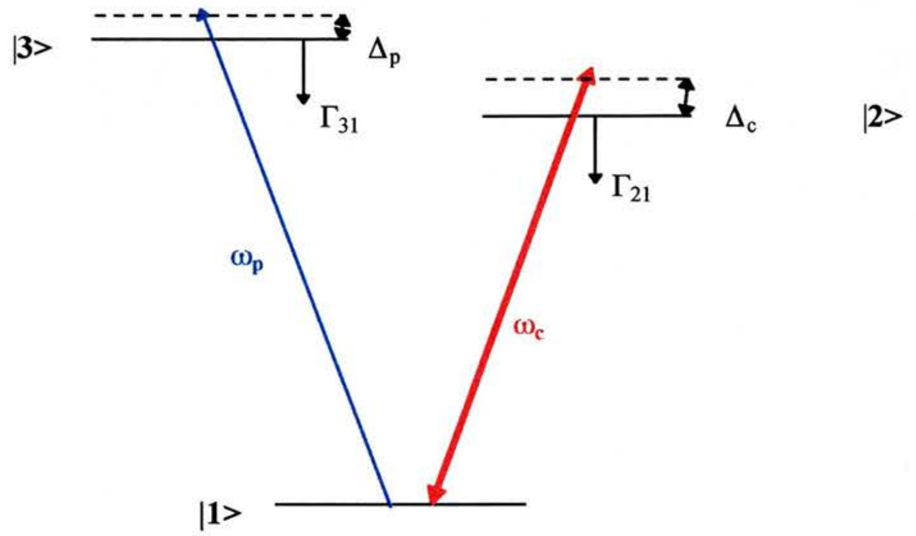

Figure 1.1.3: *V-type energy system within a three level atom. The frequency of the weak field is* ω_p *and of the strong is* ω_c. Γ_{21} *and* Γ_{31} *are the decay rates from levels 2 and 3.* Δ_p *and* Δ_c *are the detunings from resonance of the probe and the coupling fields, respectively.*

Consider a simple three-level atom in a V-configuration, like in figure 1.1.3. The particular system we have employed is atomic rubidium, where transitions are such that the probe field is set to 422 nm and the coupling field to 780 nm. The medium is Doppler broadened, because the atoms move to all directions with a thermal distribution of velocities. For the time being, we neglect the hyperfine structure of the ground state. Coherently induced transparency, the induced dip in the absorption profile, is still possible in such a system, as shown in figure 1.1.4.

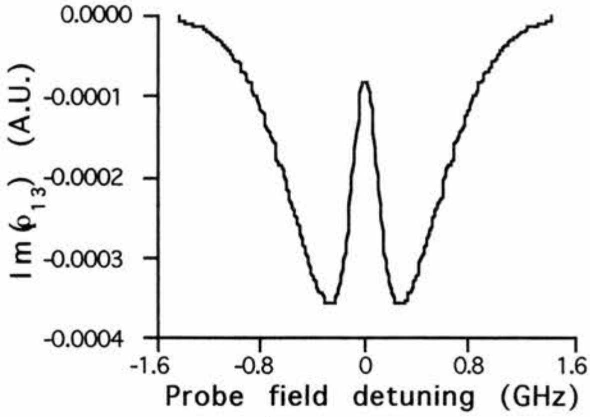

Figure 1.1.4: *The imaginary part of the density matrix element* ρ_{13} *which indicates the probe absorption, as the weak field is detuned from resonance.. The Rabi frequencies were* Ω_c*=160 MHz and* Ω_p*=1 MHz for the coupling and the probe field respectively.*

Under the continued action of a strong resonant coherent field on an atomic medium, the driven population experiences regular sinusoidal oscillations between the two levels |i> and |j>, termed Rabi oscillations, the frequency of which is referred to as the Rabi frequency, defined as:

$$\Omega = \frac{\mu_{ij}E}{\hbar} \tag{1.1.1}$$

where E is the amplitude of the coherent driving electric field, μ_{ij} the associated dipole matrix element and $\hbar$ is related to Planck's constant. For a velocity group centred on v, the Autler-Townes components are detuned from resonance by Δ= kv, where k the wavenumber, giving a generalised Rabi frequency of the coupling field:

$$\tilde{\Omega} = \sqrt{\Omega^2 + \Delta^2} \tag{1.1.2}$$

The amount by which an atomic level is split, $\tilde{\Omega}$, depends upon the induced Rabi frequency and the detuning of the coherent field.

These Autler-Townes components are split as in figure 1.1.5. Initially the optical field is exactly resonant as in figure 1.1.5.a and then detuned by an amount Δ as in figure 1.1.5b. The splitting of the levels is symmetric about the bare state levels when the coherent field is resonant with the transition. Whereas, when the field is detuned from resonance the Autler-Townes splitting becomes asymmetric with respect to the bare states, but symmetric about a position half the detuning away from the bare states.

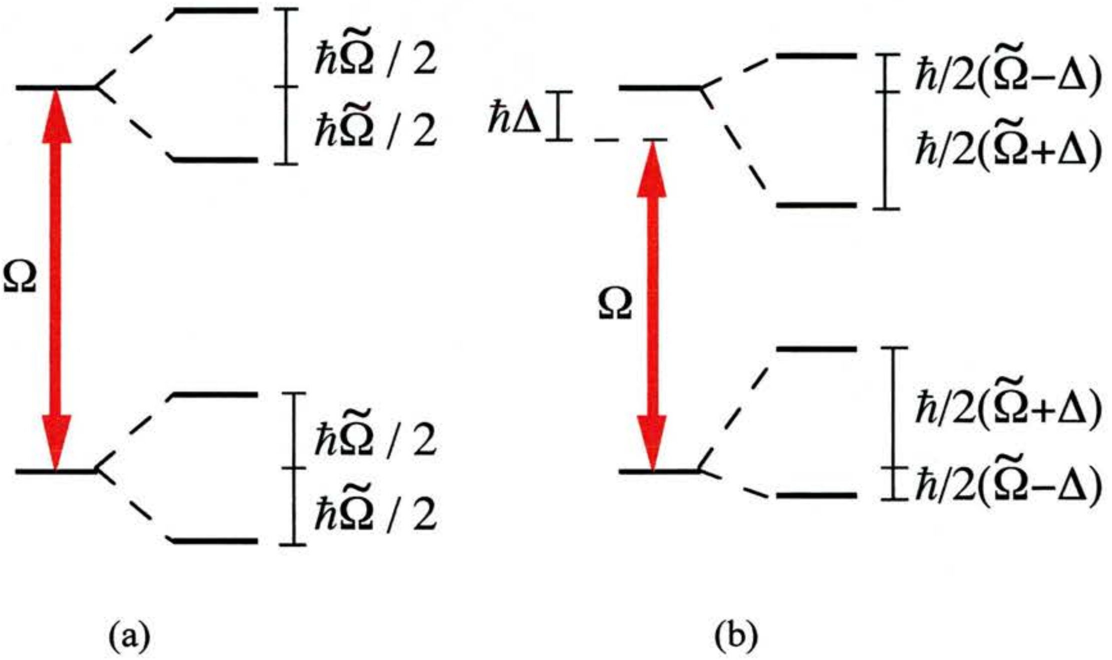

Figure 1.1.5: *Schematic representation of Autler-Townes splitting , $\tilde{\Omega}$, for (a) a resonant driving field of Rabi frequency Ω and (b) the same driving field detuned by Δ from exact resonance.*

Figure 1.1.6 shows a three dimensional plot of the absorption levels of the Autler-Townes components in the V-scheme as a function of the probe detuning for several velocity groups. In this graph it is shown that the transparency window is still significant exactly on resonance despite the overlapping Autler-Townes components.

The magnitude of the components which overlap with the EIT position is small, therefore significant transparency still occurs.

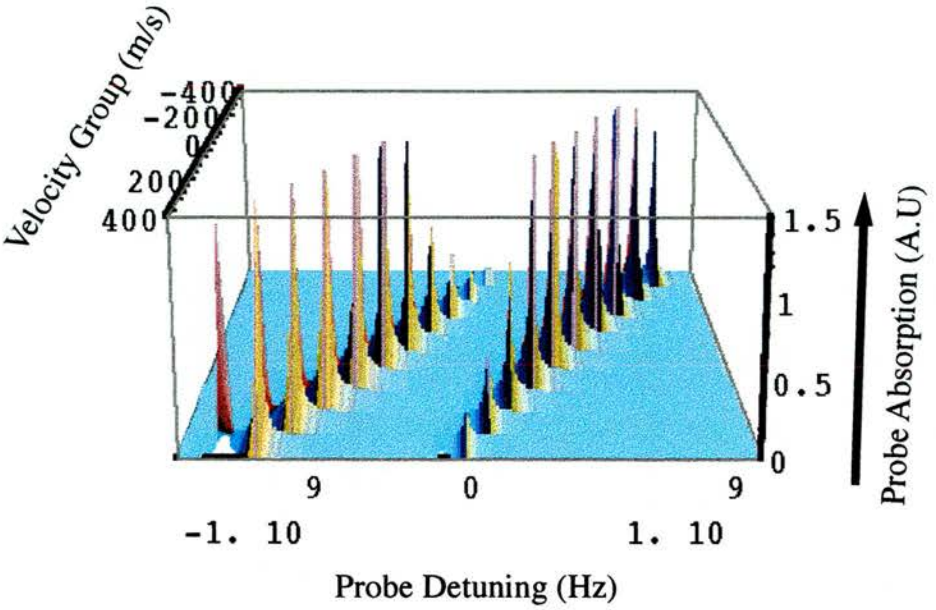

Figure 1.1.6: *Three dimensional plot of Autler-Townes absorptions (vertical axis) vs probe frequency (horizontal axis across the page) and velocity group (horizontal axis into the page), based on V- scheme with 422 nm probe field, Ω_p= 1 MHz and 780 nm coupling field, Ω_c= 1 GHz. This theoretical plot shows that the Autler-Townes components that overlap on resonance are small in magnitude and do not destroy the transparency window.*

1.2 Fano interference and population trapping.

Quantum interference and coherence are responsible for many interesting effects in atomic physics. If two coherent driving fields are set up within the one atomic system then interference between the two routes can arise. One of the initial works on such phenomena was presented by *Fano*. Here, the interference of a discrete autoionised state with a continuum gives rise to characteristically asymmetric peaks in the excitation spectra. In fact a zero in the transition probability was found on one side of the excitation spectra. The concept of a phase relationship between the autoionised state and the continuum was developed which accounts for the observed spectra. This is now considered in more detail below.

Consider an atomic system with one ϕ state belonging to a discrete configuration and a continuum of states $\psi_{E'}$, as a non-degenerate system. The square submatrix of the states ϕ, $\psi_{E'}$ is indicated by:

$$(\phi \mid H \mid \phi) = E_\phi \tag{1.2.1.a}$$

$$(\psi_{E'} \mid H \mid \phi) = V_{E'} \tag{1.2.1.b}$$

$$(\psi_{E''} \mid H \mid \psi_{E'}) = E' \, \delta(E'' - E') \tag{1.2.1.c}$$

The Dirac δ factor implies that the submatrix belonging to the more limited subset of states $\psi_{E'}$ had previously been diagonalised in the zero approximation.

In order to study the resulting variation of the probability of excitation of the stationary state ψ_E, let us take the energy value E within the range of E', to be an eingenvalue of matrix (1.2.1). The corresponding eingenvector has then the form :

$$\psi_E = a\phi + \int dE' \, b_{E'} \psi_{E'} \tag{1.2.2}$$

After a fair amount of calculations it was derived that:

$$a = \frac{\sin\Delta}{\pi V_E} \text{ and } b_{E'} = \frac{V_{E'} \sin\Delta}{\pi V_E (E - E')} - \cos\Delta\,\delta(E - E') \tag{1.2.3}$$

$$\text{where } \Delta = -\arctan\frac{\pi \mid V_E \mid^2}{E - E_\phi - F(E)} \tag{1.2.4}$$

represents the phase shift due to the configuration interaction of ψ_E with state ϕ. In equation (1.2.4), F(E) has the form:

$$F(E) = P\int dE' \frac{\mid V_{E'} \mid^2}{E - E'} \tag{1.2.5}$$

with P indicating "the principal part of".

Whatever is the excitation mechanism, the transition probability may be represented as the squared matrix element of a suitable transition operator T between an initial state i and a state ψ_E . Following substitutions in equation (1.2.2) the matrix element is expressed in terms of the phase parameter Δ by:

$$(\psi_E \mid T \mid i) = \frac{1}{\pi V_E^*}(\Phi \mid T \mid i)\sin\Delta - (\psi_E \mid T \mid i)\cos\Delta \tag{1.2.6}$$

where $$\Phi = \phi + P\int dE' \frac{V_{E'}\psi_{E'}}{E - E'} \tag{1.2.7}$$

indicates that the state ϕ is modified by an admixture of states of the continuum. The sharp variation of Δ as E passes through the resonance at E_ϕ+F causes a sharp variation of $(\psi_E \mid T \mid i)$. More specifically, sinΔ is an even function of E- E_ϕ-F whereas cosΔ is an odd function of this variable. Therefore, the contributions to $(\psi_E \mid T \mid i)$ represented in (1.2.6), by $(\Phi| T \mid i)$ and $(\psi_E \mid T \mid i)$ interfere with opposite phase on the two sides of the resonance.

A physical interpretation of this effect is that the end product, photoionisation, is achieved by two separate routes, that of direct ionisation the other via the autoionisation state. It is the coherent interference between these two routes which causes the observed effects. The asymmetric lineshape of a Fano resonance is the manifestation of quantum interference between two transition pathways leading to the same continuum state: direct photoionisation, on one side and transition to the continuum via the discrete autoionising state, on the other side.

The two-route interference need not necessarily involve the continuum or an autoionised state. Two separate excitation routes to the same end product within a three-level atomic system can produce coherent interference effects and thus population trapping. *Arimondo and Orriolis* in 1976 predicted theoretically that this population trapping could occur. Their system included two ground state levels having an energy separation in the microwave region and an excited level coupled to the lower ones by optical transitions. This system was irradiated by light beams containing two coherent modes, each of which is resonant with one of the coupled transitions. Their density matrix analysis showed that the generation of the coherence between two ground states of sodium could cause the switching off of the absorption from the ground state to an upper state. This interference phenomenon occurs every time the mode separation of the laser matches the ground state frequency splitting.

This theoretical prediction was later confirmed within experiments carried out in sodium vapour, by *Alzett et al*. A multimode dye laser tuned to a D_1 line resonance of sodium was used to coherently pump a sodium cell while an inhomogeneous magnetic field was simultaneously applied . When the splitting of the ground state equalled the mode spacing of the dye laser, black lines have been found in the spectrum of the output fluorescence from the upper level. The population was trapped in the lower states, hence explaining the dark region in the fluorescence signal.

Coherent trapping of atomic population was presented by *Gray et al.* Two CW lasers are tuned so that they couple two different ground state sublevels to a common upper level as in the energy configuration of figure 1.2.1. Two linearly polarised dye laser beams were tuned to two hyperfine components of the Sodium D_1 line. They were brought in together to illuminate an atomic beam at right angles to the atomic velocity vectors. The fluorescence from the excited level was collected and taken as proportional to the population in the excited level. A form of coherent trapping occurred when multiple resonant laser beams are used to couple various ground states to a common upper level. This effect prevents the extraction of the entire population.

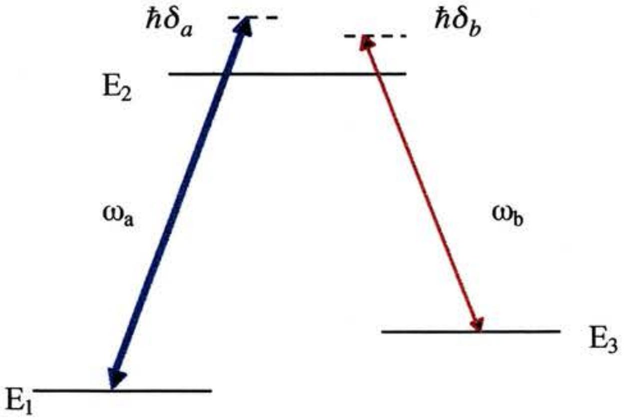

Figure 1.2.1: *Energy level configuration of the system. E_1 and E_3 are non degenerate sublevels of the ground state. E_2 is a common excited state. Two lasers have frequencies ω_a and ω_b respectively, and they are detuned δ_a and δ_b off resonance.*

Whitley and Stroud had previously presented a complete and detailed treatment of three-level atoms, interacting with two near resonant monochromatic fields. A theoretical paper by *Dalton and Knight* discusses the effects of field phase fluctuations on the coherently trapped population. The excitation of a three-level lambda system by two laser field leads to population trapped in two-photon resonant superpositions. They investigated the effects of laser bandwidths on trapping in the lambda system and found that the inclusion of laser bandwidth dephases atomic coherences and leads to the destruction of trapping. However if the driving fields are critically cross-correlated in their fluctuations, two-photon coherences in the system are unaffected and the coherence minimum persists.

A continuation of the work on coherent population trapping was carried out by *Radmore and Knight.* Their analysis was applicable both to two-photon ladder excitation and to lambda configurations strongly driven by two applied fields. Under the condition of two-photon resonance they found that population was trapped and oscillated between the initial and final states. In their paper they were concerned with multiphoton excitation by intense laser fields and they found the expected Rabi oscillatory behaviour and they examined the effect of population trapping.

An important analogy between the interference within atomic systems and that of Fano interference was made by *Coleman and Knight*. They referred to continuum states in photoionisation which may be dressed by laser coupling to bound states. They showed that the photoexcitation of such dressed continuum states can lead to the trapping of part of the population in a coherent superposition state.

Coherent population trapping has been studied by *Akulshin et al.* A narrow high contrast resonance formed due to population trapping, (Lambda resonance) has been observed in ^{87}Rb vapour by using two independent laser diodes. The lambda resonance was used to stabilise the difference of laser frequencies to the hyperfine splitting of the Rb ground state.

In addition, the dispersion was observed in a coherent population trapping experiment by *Schmidt et al.* The index of refraction was measured in the region of a coherent population trapping resonance, in a caesium vapour cell with an interferometric technique. They found very high normal dispersion at low absorption.

1.3 Electomagnetically induced transparency and related topics.

The first explicit reference to EIT was made in 1990 when *Harris et al.* theoretically proposed the employment of EIT to enhance non-linear optical processes. The suggested scheme is depicted in figure 1.3.1.

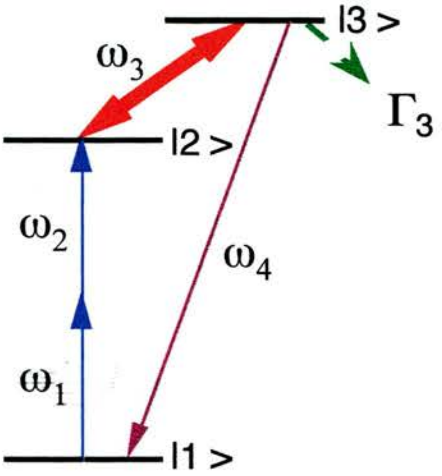

Figure 1.3.1: *Four wave mixing scheme analysed by Harris et al. for the enhancement of non-linear processes by E.I.T.*

They showed that by applying a strong coupling field between a metastable state and the upper state of an allowed transition to the ground state, they could obtain a resonantly enhanced third-order susceptibility while at the same time inducing transparency in the media. It was illustrated that by employing a strong coupling field on the |2>- |3> transition, EIT could be induced on the generated |1> - |3> four-wave mixing transition, hence reducing the reabsorption of the generated field normally experienced.

EIT does not simultaneously reduce the non-linear conversion process and the ratio of the non-linear generation to reabsorption increases dramatically, by up to four orders of magnitude. This transparency occurs because of the destructive interference of the split Autler-Townes components of the |1> - |3> transition. Though one might expect that this interference would also negate the nonlinearity that causes the generation of ω_4 , this is not so; because of a sign change in the dressed eigenvectors, for generation lying between the Autler-Townes components, there is a constructive rather a destructive interference in the non-linear susceptibility.

The first demonstration, by *Boller et al.* , of a technique by which an optically thick medium may be rendered transparent established the term Electromagnetically Induced Transparency (E.I.T). The transparency results from destructive interference of the two dressed states which are created by applying a temporally smooth coupling laser between a bound state of an atom and the upper state of the transition which is to be made transparent. The energy level diagram of the system is shown in figure 1.3.2.

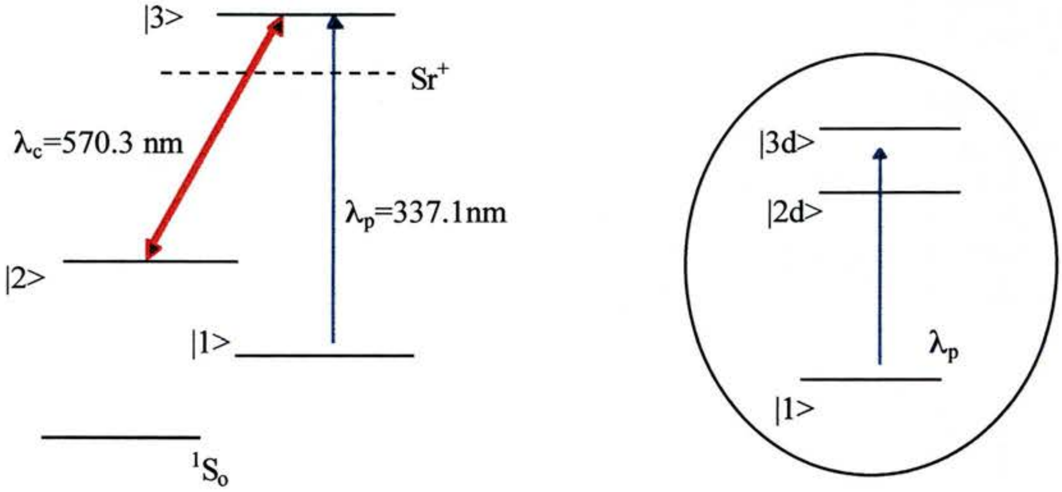

Figure 1.3.2: *Energy level diagram of neutral Sr. In the circle there is a dressed state picture.*

The coupling laser was generated by a single mode pulsed dye laser and the probe by the third harmonic of a pulsed Nd:YAlG laser. The transmittance of the autoionising (U.V.) transition in Sr was changed from exp(-20) without the coupling laser present to exp(-1) in the presence of the strong coupling field. This change in transmittance due to the presence of a coupling field is the effect called EIT. The physical explanation of this phenomenon is that when the probe laser is turned on in the presence of the coupling laser, ground-state atoms evolve to a steady state where a fraction of their population is in state |2>. This coherently phased population produces a dipole moment of equal magnitude and opposite sign to the primary moment at the probe frequency, trapping the population in |2> and leaving |3> empty. Equivalently the transparency may be viewed as the interference in absorption between two ac-Stark split components of |3>. The effect of the coupling field is essentially to create two dressed states, that is, states of the laser-atom system, shown as |2d> and |3d> in the inset of figure 1.3.2. Destructive interference between the ground state transitions to these two levels prevents the absorption of photons whose wavelength lies exactly between the two dressed states.

Furthermore, EIT was observed by *Sander et al.,* in a V-system formed within the ^{87}Rb D1/D2 transitions and a theoretical analysis was followed taking multilevel optical pumping into account. The V configuration with a rapidly decaying uncoupled state is depicted in figure 1.2.3.

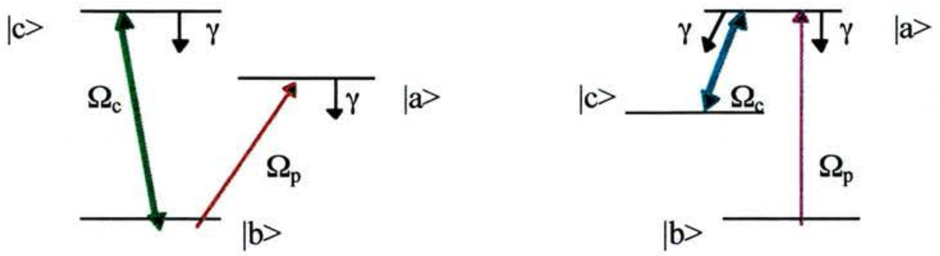

(a) **(b)**

Figure 1.2.3: *(a) V system with rapidly decaying uncoupled state. (b) Λ system. Ω_c, Ω_p are the Rabi frequencies of the coupling and the probe field respectively and γ is the decay rate of the level .*

In such an energy scheme coherent population trapping between long lived states cannot occur. In contrast to the Λ-scheme the population stays between the two coupled states. The physical processes involved in both Λ and V EIT are illuminated by writing the state at time t for an atom initially injected into state |b>. Ignoring decay terms this is given by:

$$\psi^{\Lambda}(t) = -\frac{\Omega_p}{\Omega}\sin\Omega t\,|\,a> + \left(\frac{\Omega_c^2}{\Omega^2} + \frac{\Omega_p^2}{\Omega^2}\cos\Omega t\right)|\,b> - \frac{\Omega_c\Omega_p}{\Omega^2}(1-\cos\Omega t)\,|\,c> \qquad (1.3.1)$$

$$\xrightarrow{\Omega_c \gg \Omega_p} \; |\,b>$$

$$
\begin{aligned}
|\psi^V(t)> &= -\frac{\Omega_p}{\Omega}\sin\Omega t\,|a> + \cos\Omega t\,|b> - i\frac{\Omega_c}{\Omega}\sin\Omega t\,|c> \\
&\xrightarrow{\Omega_c \gg \Omega_p} \cos\Omega t\,|b> - i\sin\Omega t\,|c>
\end{aligned}
\tag{1.3.2}
$$

where Ω_p ,Ω_c are the Rabi frequencies of the weak probe and the strong coupling fields respectively, and $\Omega=(\Omega_p{}^2+\Omega_c{}^2)^{1/2}$.

In the Λ system an atom is effectively trapped in the |b> state. In the V scheme, on the other hand the atom is found in |b> state with probability of $\cos^2\Omega t \rightarrow 1/2$ and in |c> state with a likewise $(\Omega_c/\Omega)^2\sin^2\Omega t$ which also goes to 1/2 when $\Omega_c >> \Omega_p$.

For the experimental verification of EIT in a V-system ^{87}Rb was chosen as an interaction medium using D_1/D_2 transitions, which are accessible with commercial laser diodes (C.W). The probe drove the D_1 (F=2→1) transition and the D_2(F=2→1,2,3) transitions were strongly driven by the coupling laser. For the F=2→1,2 resonances both optical pumping and EIT leads to complete transparency for high coupling laser power and it is difficult to distinguish them. In the case of coupling laser tuned to F=2→3 transition the effects of the EIT and optical pumping are of the opposite sign. This, then together with the different linewidths associated with EIT and optical pumping, gives a high contrast signal even after velocity averaging, which allows the clear distinction of optical pumping.

Observation of EIT on the collisionally broadened resonance line of Pb vapour was reported by *Field et al.* By applying a 1064 nm pulsed laser beam the transmission at 283 nm increased by at least a factor of exp(10) with nearly all the Pb atoms remaining in the ground state. The energy level diagram was a cascade configuration as in figure 1.3.4.

The strong laser dresses the system so as to create the equivalent energy diagram shown in figure 1.3.4. There is now a quantum interference between |1>-|2d> and |1>-|3d> absorption paths. If a collision is fast (impact regime), it establishes a coherence between states |2d> and |3d>. If a perturber interacts dominantly with bare state |3>, this coherence results in a destructive interference and in principle, zero absorption at line centre. If a perturber interacts with bare state |2> then the interference is constructive and the probe laser sees the Lorentzian wings of the dressed states.

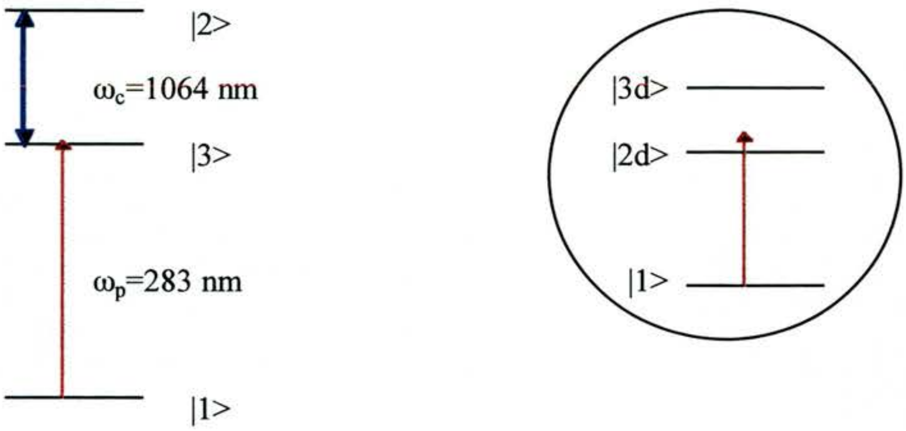

Figure 1.3.4: *Energy configuration (cascade) of neutral Pb. Inset: Dressed state picture.*

A comparison of V, Λ and cascade systems which exhibit CW EIT has been presented by *Fulton et al*. The energy schemes are shown in figure 1.3.5. Optical fields were produced by single frequency CW Ti:Sapphire lasers and the interaction medium was rubidium.

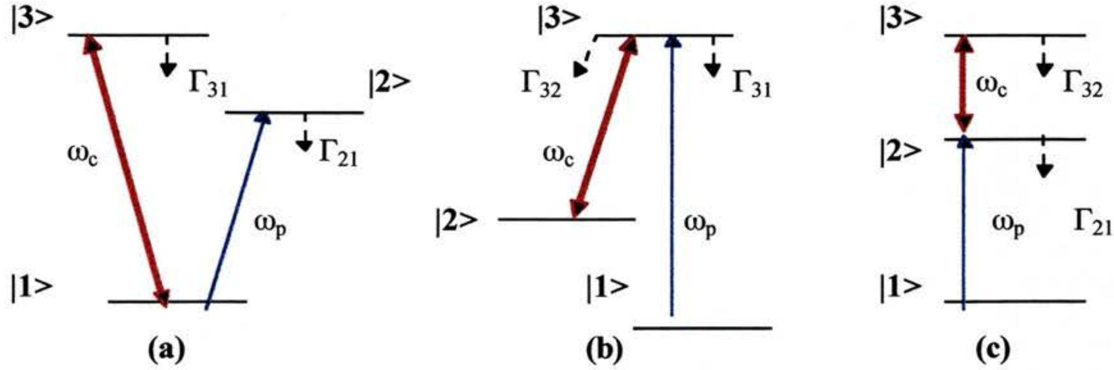

Figure 1.3.5: *Schematic energy level diagrams showing the ideal 3-level atoms, with the relevant population decay values Γ_{ij}, the probe field transitions ω_p and ω_c the coupling field. (a) the V-type system, (b) the Λ-type system and (c) the cascade system.*

In this atomic system, as in figure 1.3.5, the coherence dephasing rates of the dipole-forbidden transitions are:

$\gamma_{23}=(\Gamma_{21}/2)+(\Gamma_{31}/2)$ (V-system) (1.3.3)

$\gamma_{12}=0$ (Λ-system) (1.3.4)

$\gamma_{13}=\Gamma_{31}/2$ (cascade system) (1.3.5)

The strength of the EIT window in a particular case is strongly dependent on the associated dephasing rate. The ideal Λ-type system will produce the best EIT window and the V-system the poorest. However, EIT is not the only source of increased transparency. Within the V configuration EIT cannot be isolated from an increased probe field transmission induced by the coupling field saturating the |1>-|3> transition. Also, the Λ-system is complicated by population being optically pumped into level |2> by the probe field, but the coupling field acts to repump population out of level |2> back into the system.

This paper also discussed a Λ-configuration, where EIT was induced on a two-photon transition. It was also found that systems that have a strong coupling field resonant with the ground state suffer from complicating optical pumping mechanisms that tend to mask EIT window.

Observation of quantum interference between dressed states was reported by *Li and Xiao*. An experimental observation of quantum interference between two dressed states created by a coherent pumping laser, was presented. In a Lambda type three level atomic system in Rb vapour, they reduced the Rabi frequency of the pumping laser in one arm, down below the spontaneous decay rate of the common excited state and still they observed a narrow dip with subnatural linewidth in the absorption curve of a probe beam in another arm. Frequency stabilised diode lasers were used as the probe and the pump field. The size of the effect is currently limited by the laser linewidths of both the pumping and the probe lasers. The Doppler broadening of the atoms in the cell also degrades the interference effect. However, the direct observation of this Fano-type interference effect is very important in proving the existence of a quantum interference effect in EIT experiments.

A similar system was used by *Zhu and Wasserlauf.* They reported the experimental observation of steady state EIT and sub-Doppler linewidth in a Doppler broadened Lambda type Rb atomic system formed on the ^{87} Rb D transitions. The energy level structure of this transition is depicted in figure 1.3.6.

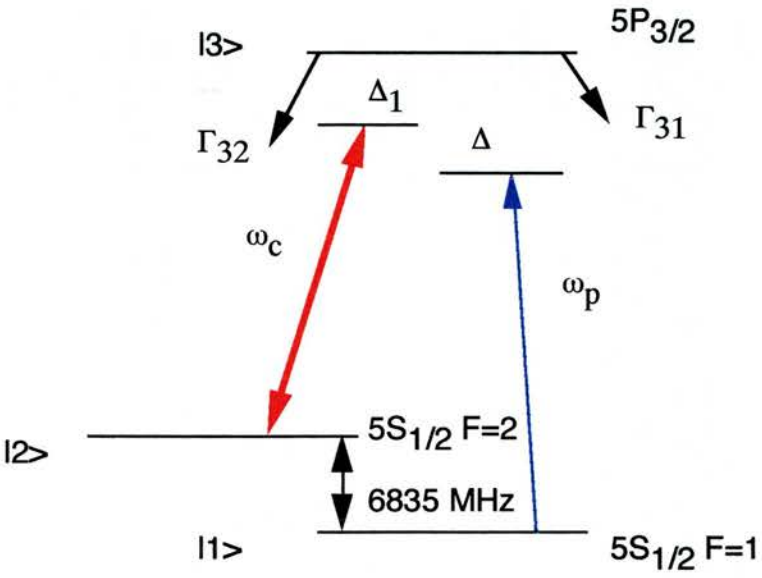

Figure 1.3.6: *The energy level structure of ^{87}Rb D transition and the laser coupling scheme, which forms an effective three level lambda type system.*

The lambda system is coupled on one transition by a strong Ti:Sapphire laser and probed on the other transition by a weak CW external cavity diode laser. The observed sub-Doppler linewidth decreases with the increasing detuning of the strong coupling laser from the atomic transition frequency.

Observation of an electromagnetically induced change of the absorption in multilevel rubidium atoms was presented by *Li et al.* A 64.4 % reduction in absorption at the Rb D_2 line was observed when a pumping field at 775.8 nm was tuned on resonance to the transition between the excited states $5P_{3/2}$ and $5D_{5/2}$. The cascade system is shown in figure 1.3.7. As the pumping field is tuned off resonance, an absorption peak appears at the side of the Doppler broadened D_2 line. This modification in absorption is related to pumping induced atomic coherence in this three level ladder type system. This experiment was done in a Rb cell at room temperature and with CW diode lasers for both pumping and probe beams in a Doppler-free configuration.

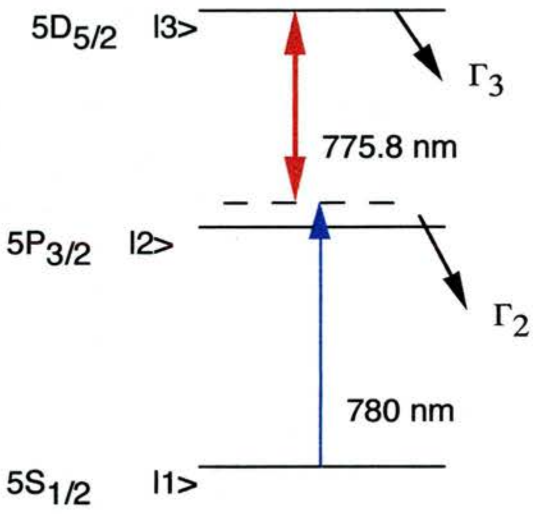

Figure 1.3.7: *Relevant energy levels of the neutral rubidium atom in a cascade scheme.*

EIT in a ladder type inhomogeneously broadened media was also studied by *Gea-Banacloche et al.* They developed a theory of EIT in a three-level cascade Doppler broadened medium, paying special attention to the case where the coupling and probe beams are counterpropagating and have similar frequencies, so as to reduce the total Doppler width of the two-photon process. The theory was compared to the Lambda configuration, where the ideal arrangement involves two copropagating beams. The theory was compared to the results of a recent experiment, using the Rb D_2 line, with generally very good agreement. The maximum absorption reduction observed appears to be mostly limited by the relative large linewidth of the diode lasers used in the experiment.

The transparency described by *Harris* is not a saturation or hole-burning phenomena. He showed that an ensemble of atoms all of which are probed by an electromagnetic field with a time varying envelope, establish transparency through a strong non-linear interaction. This system was a lambda configuration. The essence of this effect is the generation of matching correctly phased frequency components on an alternative transition and therefore of temporally matched envelopes which are decoupled from the atom.

EIT in a V-shaped atomic system was observed by a spectroscopic technique by *Wang et al.* The experimental results showed that the absorption coefficient at maximum coherence was reduced by about 72%. In this experiment sodium vapour was used as an absorptive medium. They found that it was possible to establish atomic coherence between the upper levels of the V-configuration by a coherent standing wave. Under this condition when the stimulated emission was reduced and the population was trapped in the excited states the medium became transparent.

Transparency is not only observed in vapour i.e. Doppler broadened systems. *Hopkins et al.* have observed EIT in laser cooled Rb in magneto-optical trap (MOT). Lambda type configurations as in figure 1.3.8 were studied, as well as a system utilising degenerate Zeeman sublevels of the ground state. The coupling beam and the probe beam used were travelling waves, obtained from laser diodes. The MOT consisted of three mutually orthogonal standing wave laser beams, intersecting at the centre of a weak spherical quadruple magnetic field in a Rb vapour cell. Laser beams at 780 nm were provided by external cavity grating controlled laser diodes. They have demonstrated Doppler free CW EIT signals in the hyperfine levels of laser cooled Rubidium in an MOT with a resolution of about 1MHz , the laser linewidth.

Efficient EIT was also observed in a rare earth doped crystal by *Ham et al.* They have seen up to 100% transmission of a probe field at line centre due to EIT in an optically dense rare earth crystal of Pr^{3+} doped Y_2SiO_5 at 5.5 K. They have chosen Pr:YSO because it has relatively long optical and spin relaxation times and high oscillator strength. These properties make the observation of EIT possible with a commercially available CW dye laser. They have examined both laser field intensity

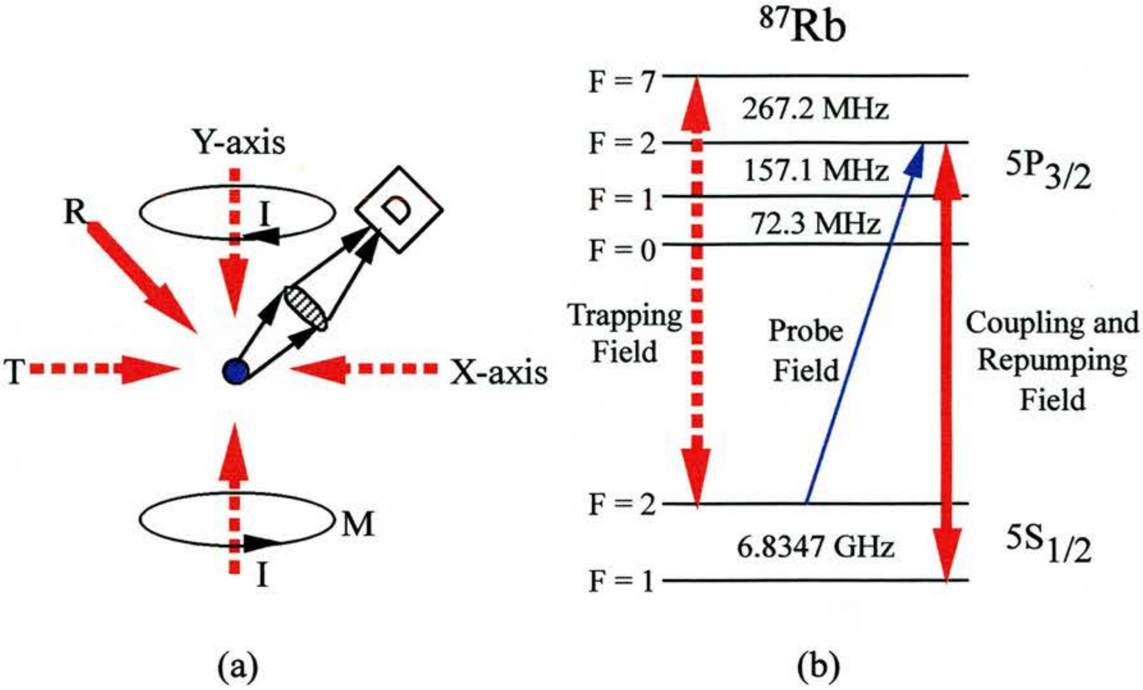

Figure 1.3.8: *(a) Schematic diagram in the x - y plane of the M.O.T. showing trapping fields T and repumping fields R. The trapping field on the z-axis is not shown The magnetic coils M are coaxial with the y-axis and carry currents in an anti-Helmholtz configuration. (b) Energy-level diagram for trapping* ^{87}*Rb, showing also the coupling and probe beams for a lambda system experiment.*

and temperature dependence of EIT. The transparency in this crystal opens up potential applications such as efficient high resolution image processing and optical data storage as well as lasing without population inversion in solids.

EIT or population trapping may have interesting applications such as optical parametric oscillators. *Harris and Jain* proposed an optical parametric oscillator that was pumped by population trapped atoms that are prepared with maximum coherence. A schematic of the suggested technique is shown in figure 1.3.9.

The signal and idler fields were driven by population trapped |1>-|2> transition atoms.

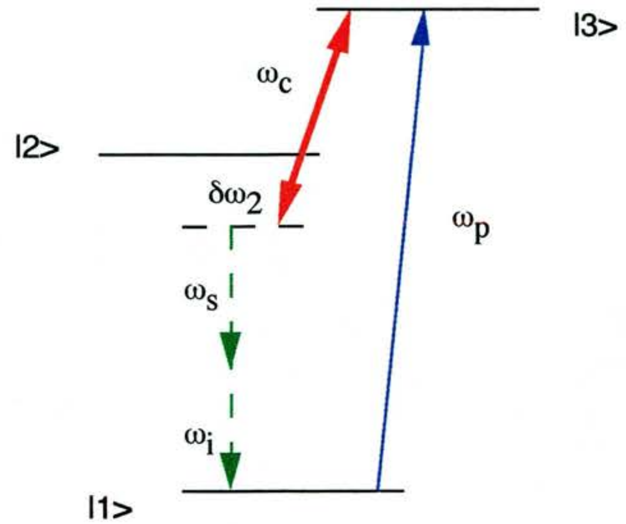

Figure 1.3.9: *Energy schematic for an optical parametric oscillator pumped by population trapped atoms. Electromagnetic fields at frequencies* ω_p *and* ω_c *drive population trapped in |1>-|2> transition atoms. The phase variation of these atoms as a function of z is determined by the detuning of the two-photon resonance* $\delta\omega_2$*. A small detuning of* $\delta\omega_2$*(typically few hundred megahertz) causes phase matching and parametric gain at signal and idler frequencies* $(\omega_s+\omega_i) = (\omega_p-\omega_c)$*.*

This allowed the ground state atoms to evolve smoothly into a population trapped superposition, with approximately equal and oppositely phased probability amplitudes in states |1> and |2> and a probability amplitude of zero in state |3>. Hence $|\rho_{11}| = |\rho_{22}| = -\rho_{12} = 0.5$. To set $\Delta k=0$ at band centre the two-photon detuning $\delta\omega_2$ should be less than 1 GHz. The oscillator was based on the use of an effective non-linear susceptibility that is of the same order as the linear susceptibility. In Pb vapour the calculated gain was maximised at 1.88 μm and has bandwidth of ~ 7500 cm^{-1}.

In recent years a number of potential applications of EIT have been described. In an paper by *Lukin et al.* the effect of an intracavity induced transparency was presented. When a dense ensemble of coherently prepared Lambda atoms was placed inside an optical resonator, the resonator response was drastically modified, resulting in frequency pulling and a substantial narrowing of spectral features. This effect can be used for frequency difference stabilisation of lasers or other two-mode light sources such as broad band parametric oscillators. Intracavity EIT results in locking of the beat note to resonance frequency of a two-photon transition between metastable atomic levels and causes a substantial reduction of quantum and classical noise in the beat signal.

EIT is not only attractive, as a phenomenon by itself, but it includes spatial consequences. Observation of electromagnetically induced focusing (EIF) was first reported by *Moseley et al.* Within an experiment to produce EIT in a cascade configuration the radial intensity profile of the strong coupling laser generated a significant spatial refractive index profile, which was experienced by the weak probe as it was tuned through the transparency window. This lead to focusing and defocusing at separate, but close probe laser detunings. EIF is a novel non-dissipative focusing effect whereby an atomic medium coherently prepared by a coupling field acts as a variable lens to a connected probe transition. A schematic representation of the process is presented in figure 1.3.10. This behaviour was observed by using CW Ti:Sapphire lasers in rubidium vapour. The $5S_{1/2}$-$5P_{3/2}$-$5D_{5/2}$ cascade system was employed as shown in figure 1.3.11.

The mechanism for EIF is the result of the complex combination of the spatially varying absorption and refractive index profiles induced through EIT effects. Regions of focusing and defocusing are caused by these conditions which are varied by many parameters, including relative spot sizes, probe field focal positions, cell temperature and coupling field detuning. As an example figure 1.3.12 shows a three-dimensional plot which is diffraction like rings on the probe field when an initially large probe field waist, relative to the coupling field waist is employed.

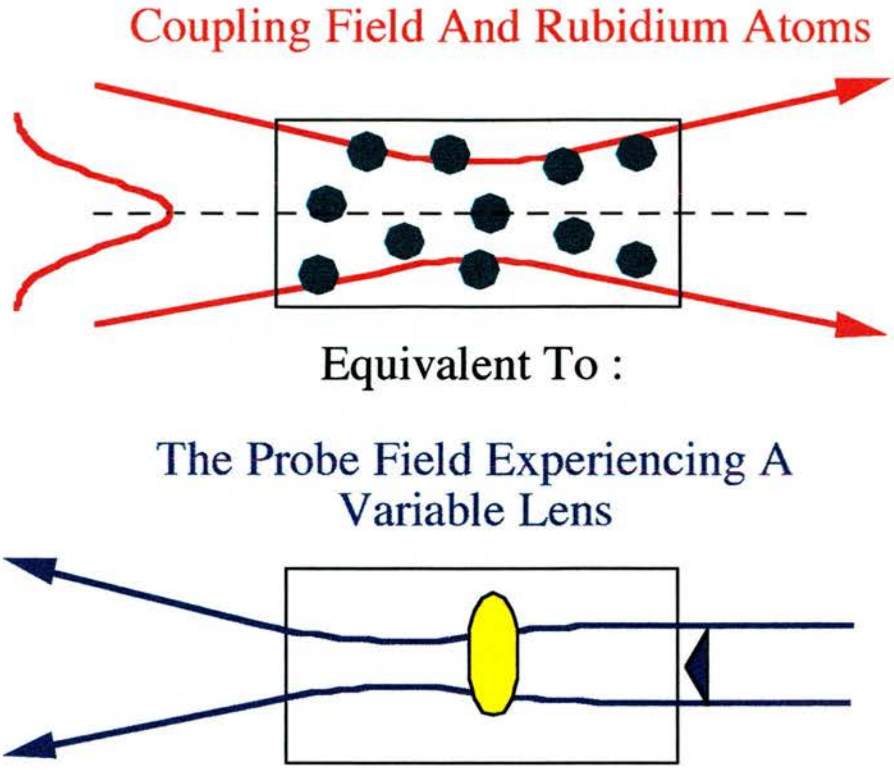

Figure 1.3.10: *Schematic representation of the process involved in producing electromagnetically induced focusing.*

As the probe laser approached in tuning from the low frequency side of the EIT feature, it was initially defocused. As it tuned through the transparency window it was progressively focused and then rapidly defocused, crossing through a point of neutral lensing behaviour at the two-photon resonance. Thereafter, it returned to a focused condition which gradually faded to the high frequency side of the transmission window. There was sufficient radial variation in the refractive index to produce significant focusing. EIF provides a mechanism whereby an optical field can be controlled by the properties of a second field. Thus modulation of the coupling field intensity or frequency will induce a rapidly varying lensing effect upon the probe field.

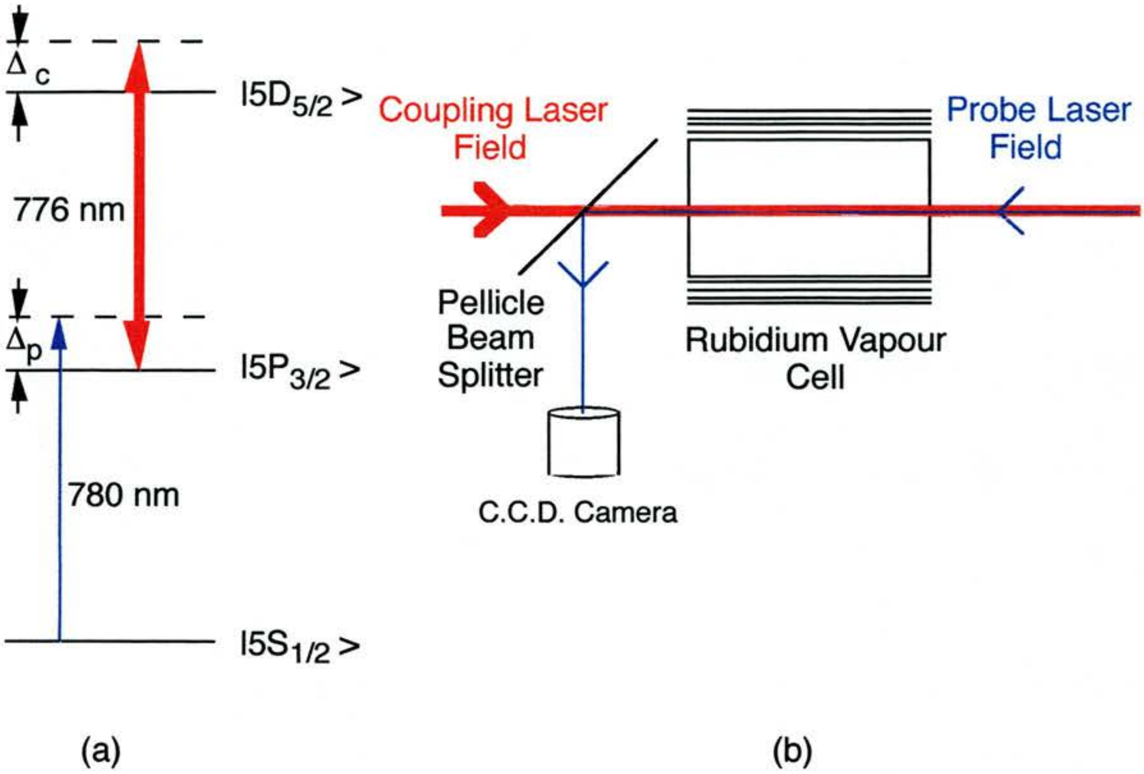

Figure 1.3.11: *A schematic representation of (a) the atomic cascade system employed for this experiment and (b) the experimental set-up, showing the arrangement of the laser beams, vapour cell and C.C.D. camera*

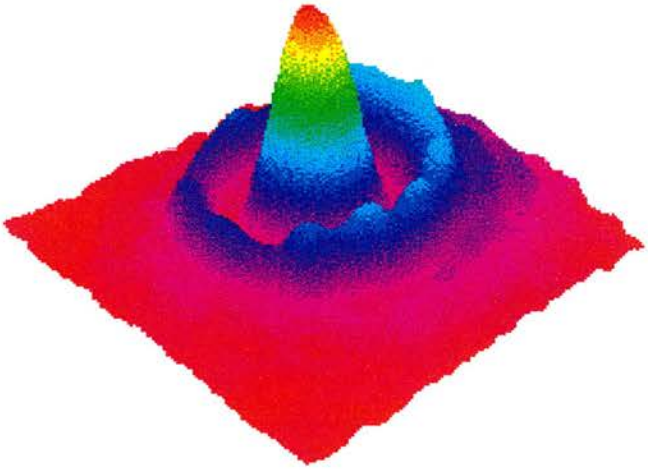

Figure 1.3.12: *A three dimensional-plot of the probe field as it appears on the C.C.D. camera after being transmitted through a much smaller circular transparency. The probe field has a 2 mm waist, the coupling field a 150 μm waist and the cell is at a temperature ~ 50 °C.*

The wavelength dependence of coherently induced transparency in a Doppler-broadened cascade medium was verified by *Shepherd et al.* In addition to the effect of EIT in the probe absorption, the coupling field also induces Autler-Townes (A-T) splitting which are near resonance with the coupling field. The absorption of the probe by any one atom travelling with velocity v, will consequently split into two components separated by the generalised Rabi frequency Ω_c of the coupling field. It is therefore important to ensure that the absorbing A-T components for any velocity group do not overlap with the maximum transparency points of the other velocity groups, as far as possible.

It was shown that this trade-off between absorptions and transparency across the velocity groups results in the best overall transparency occurring for wavelengths such that $\lambda_c < \lambda_p$ in the case where the Rabi frequency Ω_c is less than the Doppler width ν_D and the dephasing term γ_{13} is greater than zero. The optical fields were CW Ti:Sapphire lasers on resonance with rubidium transitions. The amount of transparency for an individual velocity group was set by the dephasing term of the uncoupled transition γ_{13}, but the width was controlled by the A-T splitting. It was possible to increase overall transparency at low coupling powers by altering the coupling laser wavelength.

1.4 Dispersive properties of EIT- Phaseonium.

The dispersive properties of EIT were studied by *Harris, Field and Kasapi.* An atomic transition that has been made transparent by applying an additional electromagnetic field exhibits a rapidly varying refractive index with zero group velocity dispersion at line centre. Because of the absorptive interference the pulsed probe field in a lambda scheme experiences a linear rapidly varying refractive index with very slow group velocity and zero group velocity dispersion.

Measurements of dispersive properties of EIT in Rb atoms were demonstrated by *Xiao et al.* The dispersive properties of the atomic transition in the Rb D line at 780 nm were measured with a Mach-Zehnder interferometer when an additional coupling field at 775.8 nm was applied to an upper transition. This ladder type system was observed to exhibit EIT together with a rapidly changing refractive index with detuning. In addition to the large and rapidly changing index of refraction predicted by the theory, their experiment showed that because of the two-photon nature of the effect, it was possible to observe it in a Doppler broadened medium with much lower laser powers than have been used previously, by making use of the Doppler-free configuration.

The term phaseonium refers to a medium which exhibits high refractivity without absorption via atomic coherence effects and was first outlined by *Scully.* They showed that it is in principle possible to achieve a large enhancement of the index of refraction via quantum interference. This is achieved by operating near an atomic resonance between an excited state |a> and a coherently prepared ground state doublet $|b_1>$ and $b_2>$ in a lambda configuration. In that configuration, in which there is coherence between the lower levels, the dispersion can be large where the absorption vanishes. In such a case the population of the excited state |a> is 0.1 and the populations of both the ground states are equal and their value is 0.495.

A comprehensive study of phaseonium was outlined the following year by *Fleischhauer et al.* An enhancement of the index of refraction accompanied by vanishing absorption was shown to be possible in an ensemble of phase coherent atoms. A survey of various possible schemes, such as lambda and V-type, in which coherence was established by certain coherent or incoherent methods was given and the main results were compared and contrasted. In particular, the influence of processes such as Doppler broadening that degrade the coherence was discussed.

One of the theoretically suggested applications for an index enhanced material is a high sensitivity magnetometer. *Scully and Fleischhauer* showed that the large dispersion of a phase coherent medium, at a point of vanishing absorption, was applied to interferometric measurements of detuning between atomic and radiation frequencies. It was shown that, under certain conditions, the interferometer quantum limited operation was determined by vacuum fluctuation shot noise, while the noise introduced by the interaction of the probe field with the phase coherent atoms can be made negligible. As possible application, an optical magnetometer was analysed whose sensitivity was shown to be potentially superior to the present day devices.

The first experimental demonstration of a phaseonium medium was published by *Zibrov, Lukin and co-workers.* Their experiment can be understood by considering the lambda system in ^{87}Rb outlined in figure 1.4.1.

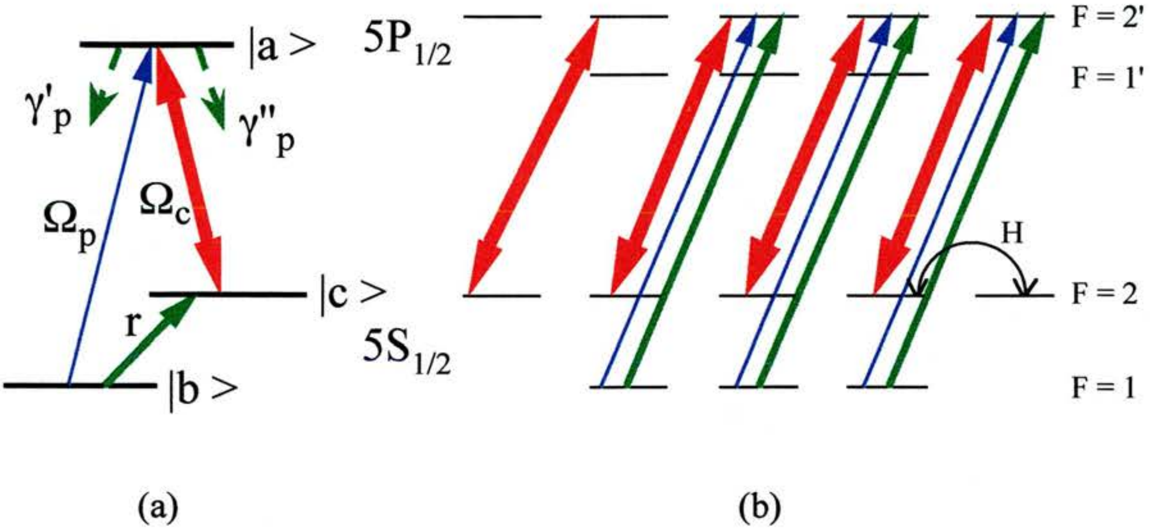

Figure 1.4.1: *(a) Simplified three-level model for index enhancement. (b) The actual atomic level scheme of the D_1 line within ^{87}Rb and the optical fields employed by Zibrov et al. to create a phaseonium medium.*

The coherent driving field with Rabi frequency Ω_c and weak coherent probe, Ω_p, allow the atom to be prepared in a coherent superposition of states $|b>$ and $|c>$. When the detunings of these two fields from their respective transitions are equal, E.I.T. is obtained. The incoherent pumping, r , alters the coherent superposition by pumping some of the population into other states. Depending upon the actual parameters this may result in gain, loss, or complete transparency for the probe field. A detailed theoretical analysis shows that at the point where the medium becomes transparent the resonant index of refraction has a large value and so a phaseonium medium has been created.

The actual atomic system employed by the authors, based on the D_1 line of rubidium, is presented in Figure 1.4.1 (b). Here right circularly polarised coherent driving and probe fields, generated by extended cavity diode lasers at 794 nm, were tuned close to the $|2> - |2'>$ and $|1> - |2'>$ transitions, respectively. To avoid the trapping of population in the state $F = 2$, $M_F = 2$ a weak magnetic field ($H \sim 2 \times 10^{-4}$ T) was employed, which mixed the populations of the magnetic hyperfine levels via Larmor precession. The resonant index of refraction was determined via phase shift measurements using a Mach-Zehnder interferometer.

1.5 Inversionless lasing and related topics.

It has long been believed that a population inversion is an inherent requirement in order to produce laser light. Conventional laser systems operate by the creation of population inversion between an excited state and a lower energy level. A conventional laser transforms incoherent energy into a coherent field at a lower frequency. Why then do we need to exploit atomic coherence effects in order to create light without population inversion, when we already have the technology for lasers with population inversion? The reason becomes obvious if we want to produce coherent X-ray or γ-ray radiation. It is rather difficult to create an inversion of population using incoherent pumping at these frequencies. This is due to the rapid decay rates associated with the highly energetic states. For this reason there has been a considerable interest in phenomena based on atomic coherence and quantum interference, such as inversionless lasing.

The initial ground breaking work in lasers without population inversion was presented by *Harris* in 1989. He showed that if two upper levels of a four-level laser system are purely lifetime broadened and decay to an identical continuum, then there will be an interference in the absorption profile of lower level atoms and that this interference is absent from the stimulated emission profile of the upper level atoms. Laser amplification may then be obtained without population inversion.

A simple model of laser without inversion was proposed by *Narducci et al.* This model was used by *Kleinfield et al.* and it is depicted in figure 1.5.6. Their system has a degenerate or quasi degenerate ground state doublet and two higher excited states. One of these higher levels is coupled to the ground states by a coherent field of variable strength, whose role is to create atomic coherence between the lowest levels; the other is also coupled to the ground state but only when laser action develops. This model includes an incoherent pump mechanism to produce some population in the top lasing state. They found that gain is available over a suitable range of values of the driving field strength and incoherent pump rates.

A theoretical approach of gain without inversion was presented by *Imamoglu et al.* The model system for lasing without inversion was a Λ-scheme as in figure 1.3.5b. This configuration is closed with regard to the atomic basis set and an incoherent pump is induced on the probe field transition R_{13}.

Lets take both the field and the coupling fields to be resonant. The necessary and the sufficient condition for amplification without inversion in an atomic basis set is:

$$\frac{\Gamma_{32}}{\gamma_{12}} > \frac{\Gamma_{31}}{R_{13}} \frac{\Omega_{23}^2 + R_{23}\gamma_{23}}{\Omega_{23}^2} > \frac{\Omega_{23}^2 + (\Gamma_{32} + R_{23})\gamma_{23}}{\Omega_{23}^2} \tag{1.5.1}$$

If the first inequality is satisfied then there is net gain $W_{em}(\rho_{22}+\rho_{33})>W_{abs}\rho_{11}$; if the second is satisfied there is no population inversion $\rho_{11}>\rho_{22}+\rho_{33}$.

For all conditions, observation of gain requires $\Gamma_{32}>\Gamma_{31}$. This is understood by considering a single atom at a time. Atoms which experience a spontaneous decay from state |3> to state |1> exhibit the single atom transient response and produce loss to the probe laser. Atoms which decay to state |2> produce gain. The threshold of this type of laser is determined by the excitation rates into the upper and lower states and not by the population difference.

In order to satisfy equation 1.5.1, it is also necessary that $R_{13}\Gamma_{32}>R_{23}\Gamma_{31}$ or equivalently $n_{13}>n_{23}$, where n is the average number of photons. This inequality states that the modes of the radiation field with higher energy $(\hbar\omega_3 - \hbar\omega_1)$ must have a higher occupancy than the modes with lower energy $(\hbar\omega_3 - \hbar\omega_2)$, if lasing without inversion is to occur. This condition can be thought of as an inversion for the radiation field.

Other interesting proposals advanced by *Kocharovskaya* et al, are based on lasers without inversion (LWI) and coherent trapping. The systems that they investigated were lambda and double lambda configurations interacting with two laser modes. It was shown that in the basis of absorbing and nonabsorbing states resulting from coherent trapping, the atomic preparation involved in LWI may be described as depopulation pumping.

A theoretical paper on inversionless amplification of a monochromatic field by a three level medium was presented by *Mandel and Kocharovskaya.* They consider the P scheme, as shown in figure 1.5.1, for the general nonresonant case where the monochromatic optical field interacts with either one or with both optical transitions, when the two upper sublevels are coupled by either microwave or an external dc field. They showed that amplification without population inversion arises either at line centre or at the sidebands, depending on the sign of the population difference between the upper levels.

The first experimental evidence of inversionless light amplification was reported by *Gao et al.* In the experiment sodium atoms were selected as the active medium. The cell also contained buffer gases. The energy configuration is shown schematically in figure 1.5.2. The weak probe at 589 nm was generated by a ring cavity dye laser and it was amplified by an intense pulsed laser field of wavelength 589.6 nm. Light amplification without population inversion was observed by using a long laser pulse as a driving field.

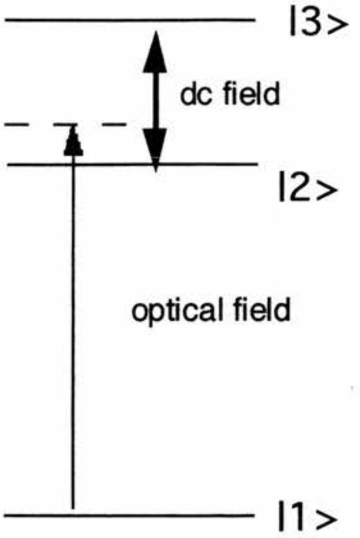

Figure 1.5.1: *The P configuration reported in Mandel and Koncharovskaya paper.*

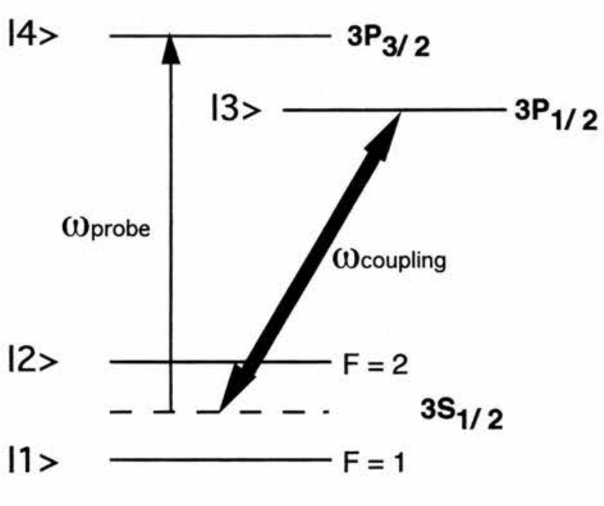

Figure 1.5.2: *Sodium energy levels for amplification without inversion.*

The first evidence of gain was reported by *Nottelmann et. al.* These authors used a scheme based on Zeeman coherence within samarium vapour, as shown in Figure 1.5.3. It is a generalisation of the lambda-scheme, with three lower levels connected to one upper level.

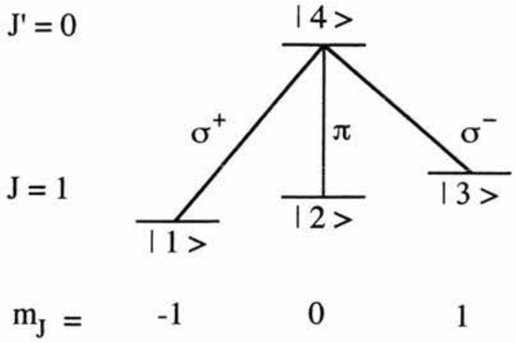

Figure 1.5.3: *Samarium energy level and excitation scheme.*

The atoms are subjected to a static magnetic field which causes the ground state splitting. A low frequency coherence ρ_{13} is created by means of a periodic train of picosecond pulses with r.f. period T_p which excites only the σ^+ and σ^- transitions and therefore provides the source of interference. A test picosecond pulse, similar to those of the train, follows the last pulse of the train after a delay of $T_p / 4$. Depending on the strength of the magnetic field the test pulse can either experience attenuation or gain. Gain when present is related to the upper state population thus a populating picosecond pulse is also sent into the system before the test pulse arrives. The populating pulse has a polarisation orthogonal to the other pulses such that it drives the π transition without affecting the two σ transitions.

Experimental demonstration of light amplification without population inversion was reported by *Van der Veer et al.* A linear superposition of an m=1 and m=-1 magnetic substate is populated coherently. In the experiment cadmium atoms are placed in a magnetic field. A linearly polarised light pulse excites ground state atoms to a coherent superposition of the |m=1> and |m=-1> magnetic sublevels of $^3P_1$ state, see figure 1.5.4. A second pulse excites a part of these atoms to the $^3S_1$ state with perpendicular polarisation. A weak seed beam polarised parallel to the polarisation of the pump stimulates the transition from the $^3S_1$ to the ϕ_- state. When the gain factor is defined as the integral of the amplified pulse divided by the integral of the seed pulse, they observed gain of 4.3 for the seed pulse.

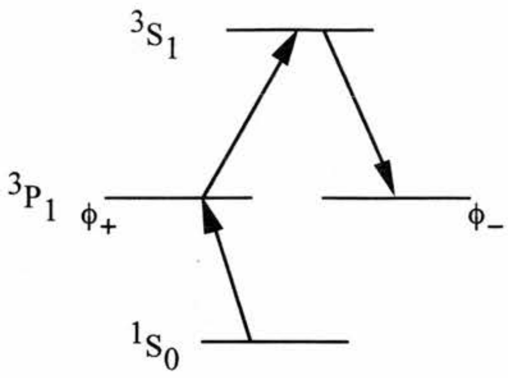

Figure 1.5.4: *The* $^3P_1$ *level is populated by a light pulse with a parallel polarisation, resulting in a* ϕ_+ *state. A second pulse with perpendicular polarisation populates the* $^3S_1$ *level. A probe pulse with parallel polarisation stimulates the transition to the* ϕ_- *state. This arrangement of polarisation yields a maximum amplification at* $B=0$*.*

Inversionless gain was observed by *Fry et. al.*, using the D_1 line of atomic sodium. The structure is quite complicated, as shown in Figure 1.5.5(a). However, the basic principle of the experiment is easy to understand with the help of the generic diagram shown in Figure 1.5.5(b).

Two strong fields are used to drive the $^3S_{1/2}$ (F=2) → $^3P_{1/2}$ (F=2) and the $^3S_{1/2}$ (F=1) → $^3P_{1/2}$ (F=2) transition. The interference process traps the atoms in the lower state only when the two Rabi frequencies Ω_1 and Ω_2 are equal. When a weak populating field is applied to bring atoms into the upper state a, of Figure 1.5.5(b), then amplification without inversion of Ω_1 and Ω_2 occurs, before a redistribution of the atoms among the energy levels decreases the intensity through normal absorption.

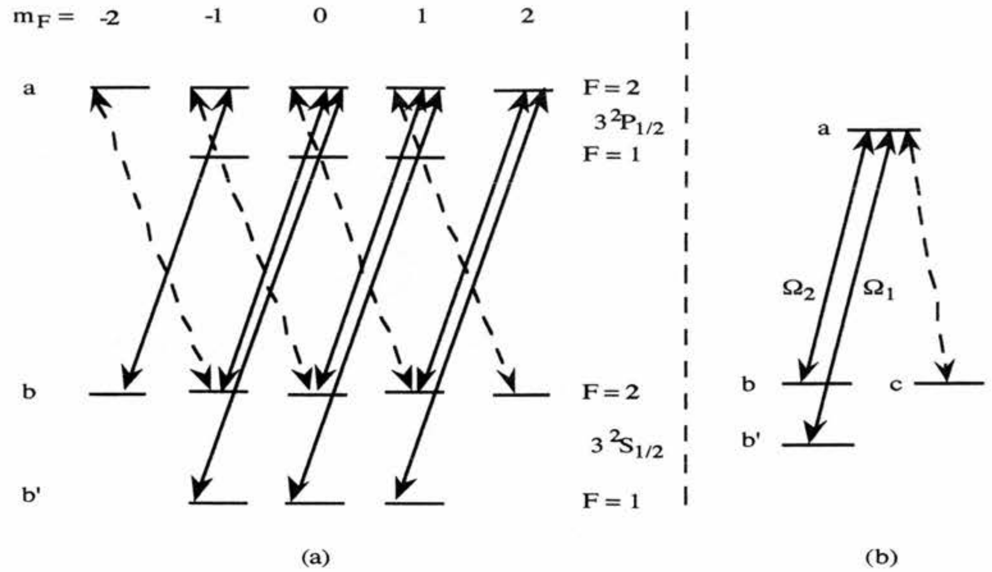

Figure 1.5.5: *Sodium energy level and excitation schemes: (a) complete scheme; and (b) principle of the experiment.*

Steady state gain due to coherence effects in a potassium-helium mixture was reported by *Kleinfeld and Streater*. The strong laser was on resonance near the D_2 line and the probe near the D_1 line. Potassium was chosen as a four-level Raman-driven medium, as in figure 1.5.6. The two ground states were the fine structure 4P(J=3/4) and 4P(J=1/2) levels respectively. The buffer gas was added to achieve the necessary population in level |3> via collisional transfer from level |4>.

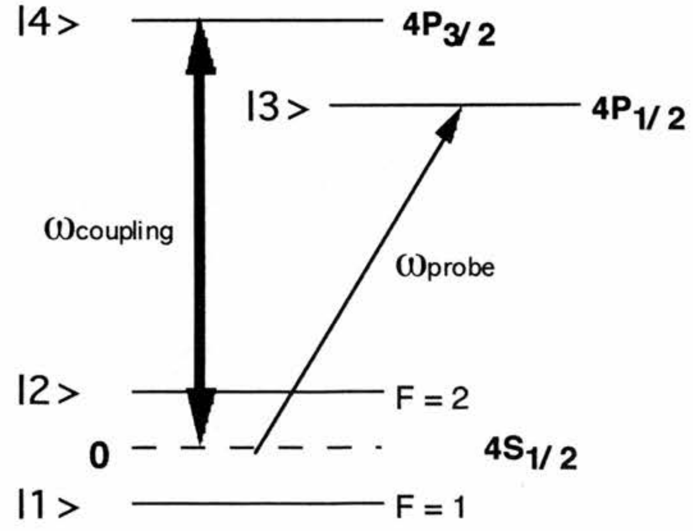

Figure 1.5.6: *Potassium-helium energy level system for cw gain.*

Theoretical analysis of this system used a 4-level optical Bloch equations and the probe beam absorption coefficient is proportional to the sum of the off-diagonal matrix elements $\rho_{13}+\rho_{23}$. The strong driving radiation was provided by a CW single mode dye laser and the probe by a CW Ti:Sapphire laser. The model predicted gain without bare-state population inversion.

Sub-Doppler light amplification in a coherently pumped atomic system was observed by *Zhu and Lin.* The configuration was a Doppler-broadened Λ-type Rb atomic system as in figure 1.5.7. A coupling laser connects the Rb $5S_{1/2}$(F=2 for ^{85}Rb atoms or F=1 for ^{87}Rb atoms)↔$5P_{3/2}$ transition and the probe laser is in near resonance with $5P_{3/2}$↔$5S_{1/2}$(F=3 for ^{85}Rb atoms or F=2 for ^{87}Rb atoms) transition. A resonant incoherent pump laser was applied to the Rb $5S_{1/2}$ (F=3 for ^{85}Rb atoms or F=2 for ^{87}Rb atoms) transition and excites the atoms to the Rb $5P_{3/2}$ state.

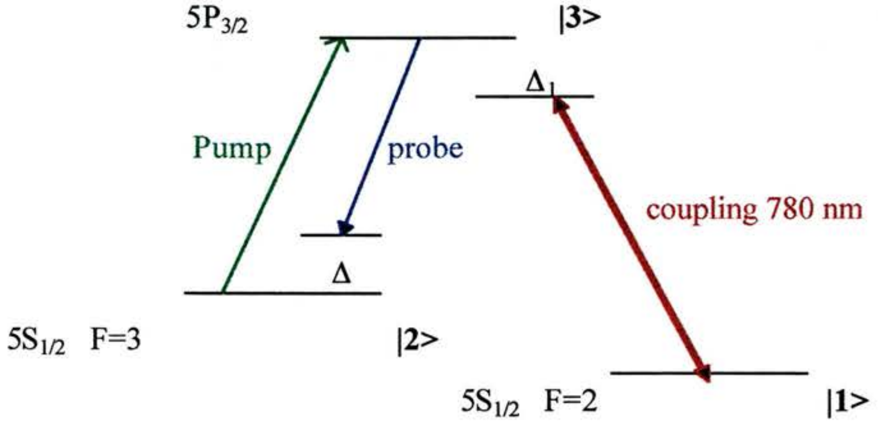

Figure 1.5.7: *Coherently pumped ^{85}Rb three level Λ-system. Δ_1 (Δ) is the coupling (probe) detuning.*

Probe amplification was observed with the Rabi frequency of a coupling field much smaller than the Doppler width. A 10% single-pass amplification of the weak probe was obtained and the measured linewidth of the gain spectral feature approached the Rb natural linewidth.

Experimental demonstration of laser oscillation without population inversion via quantum interference was first reported by *Zibrov et al.* The V-type configuration was applied within D_1 and D_2 lines of Rb vapour, as in figure 1.5.8.

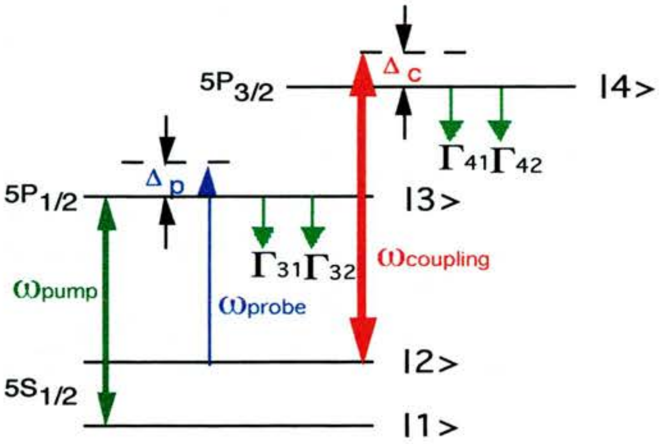

Figure 1.5.8: *Simplified four level V- model for lasing without inversion within* ^{87}Rb.

The strong coherent driving field was an x polarised laser diode and it coupled sublevel |2> of the $S_{1/2}$ state with sublevels of the $P_{3/2}$ and the probe was a z polarised laser diode, on resonance with |2>→|3> transition. Their linewidths were relatively narrow and much less than the atomic radiative decay rates ($\Delta\nu \ll \gamma_a, \gamma_b$). The third beam came from a solitary diode laser that had a broad variable linewidth of 50-200 MHz.

To obtain amplification without inversion, a weak magnetic field in the z direction was required to destroy Zeeman coherences within the F=2 ground state manifold created by the x polarised incoherent pumping field. To prove that the gain was without inversion probe laser linewidths were altered, showing that when the linewidth of the probe exceeded the radiative decay rate the amplification peak disappeared. Self-generated laser oscillation was observed when the gain medium was placed inside the laser cavity that was on resonance with the appropriate transition of the D_1 line.

Laser oscillation without population inversion in a sodium atomic beam was first presented by *Patmabandu et al.* The energy configuration is a Λ-scheme within sodium D_1 line, as shown in figure 1.5.9.

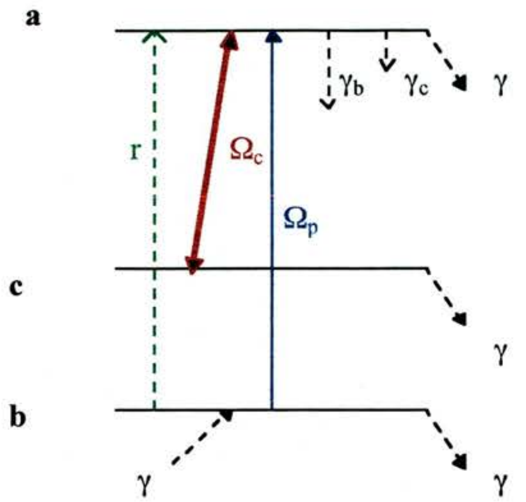

Figure 1.5.9: *The Λ-energy level configuration for lasing without inversion within a sodium atomic beam.* Ω_c *and* Ω_p *are the Rabi frequencies of the strong and the probe fields respectively. The incoherent pump is represented by r.*

The sodium atomic beam was prepared by thermal effusion. The coupling field was provided by a CW ring dye laser and a polarising beam splitter separated a small fraction of it, which passed through an acousto-optic (A.O.) modulator frequency shifter and this was used as a probe beam. The probe light propagated along on the y-axis and was x-polarised. The drive light propagated in the x-y plane at 2° to the y and it was z-polarised. The incoherent pump beam was produced by another dye laser which passed through a noise modulated A.O. in order to destroy its phase coherence.

To achieve inversionless gain the probe and the coupling beams must be precisely aligned in the x-y plane and must have orthogonal linear polarisation. They must copropagate and laser oscillation is only observed around the ring cavity in a direction coinciding with that of the coupling beam in one leg of the ring cavity.

Fort et al. investigated EIT in a V-type system in caesium at room temperature. The strong coupling laser at 852 nm was locked on the D_2 transition while the transmission of a weak probe at 894 nm was recorded as the frequency was scanned through the D_1 transition. The energy level configuration is depicted in figure

1.5.10. The addition of an incoherent pump on the D_1 line has allowed for the observation of inversionless gain. They obtained a maximum gain of 2.5 % on the F=3→F"= 3, D_1 component with the dressing locked on the F=4→F'=4, D_2 component at a temperature of 40° C in a 4 cm long cell.

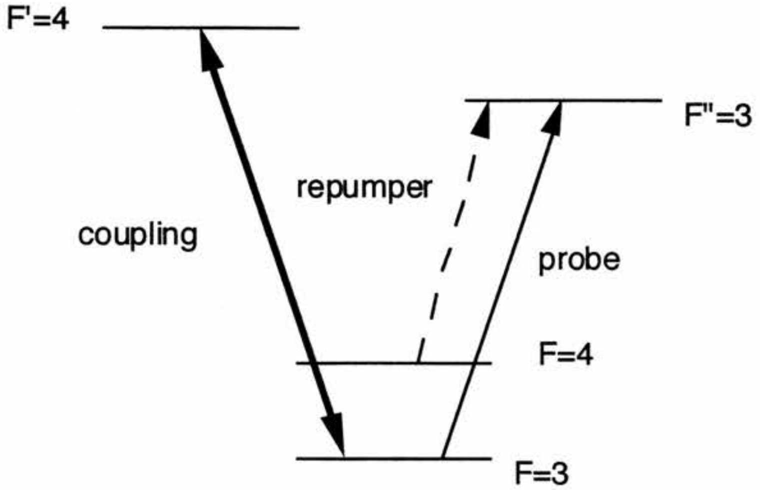

Figure 1.5.10: *Caesium levels involved in the experiment, the lasers are in the configuration that shows maximum gain.*

Jong et al. have performed both amplification and laser oscillation experiments in cadmium vapour. Their system is similar to that used by *Van der Veer et al.* in figure 1.5.4. There is no inversion between any two levels in the system. They consider inversionless amplification and laser action between the $^3S_1$ and the $^3P_1$ state in cadmium, which corresponds to 479 nm. A method based on a local maximum in fluorescence signal was used to calculate the atomic density. Using this density as an input parameter in a model for the gain, they extracted the population fractions of the laser levels involved and verified that there is no inversion in the atomic basis. Inversionless single pass gains were measured. In addition, they obtained synchronously pumped inversionless laser operation.

Koncharovskaya reviews the recent progress in the theory and on experiments on lasing without inversion. The most obvious and appealing potential application of such inversionless schemes would be to get an advantage in the high frequency domain where fast spontaneous relaxation makes the realisation of population inversion difficult. Schemes like the lambda configuration, the double lambda scheme and the P scheme were considered. Another approach developed by *Harris* is centred on the scheme involving no coherent pumping. These schemes contain an upper level doublet , the coherence of which is induced via a decay process to the common level or continuum of states, for instance, via autoionisation or radiative decay. So far most of the studies concentrated on the optical range. The most challenging purpose is certainly, the creation of a gamma ray laser. The new opportunity to realise a grazer without the need for a population inversion on the basis of the coherent and interference effects deserves the most careful study.

The idea of inversionless lasing has several interesting applications. One of these is the free electron lasing without inversion by interference of momentum states, by *Kurizki et al.* It was shown that lasing in free electron devices can be attained without the standard population inversion between the two portions of the electron momentum distribution that contribute to stimulated emission and absorption, respectively. Coherent superpositions of two electronic states in appropriately designed wigglers can strongly suppress stimulated absorption without hampering stimulated emission. The resulting gain curve is symmetric about the emission resonance, and yields a much larger gain than the antisymmetric gain curve of a standard free electron laser with the same parameters.

Inversionless gain was investigated in three or four level systems, using two coherent fields, usually laser sources. It is worth noting a degenerate quantum beat laser with the coupling field in the microwave regime, as predicted by *Scully et al.* Two systems were considered as shown in figure 1.5.11. In the V-quantum beat laser, the lasing medium consists of three-level atoms with the upper two closely spaced, driven by a coherent microwave field. They found that atoms, figure 1.5.11b, in an appropriate superposition of the two upper levels will not decay to the lower one via spontaneous or stimulated emission. On the other hand, they found that the lambda quantum beat laser, figure 1.5.11a, allows gain without population inversion, i.e. can display gain even when only a small fraction of the atoms are in the upper level |a>.

At this point it may be well to mention that Raman lasers also operate without inversion. However, *Scully*'s noninversion laser scheme is very different from a Raman device which parametrically transfers energy from one pump frequency to the Stokes or anti-Stokes line and not from the atoms to the field. In this system the energy of the lasing field comes from the atoms as in a normal laser, and not via parametric conversion from another radiation field.

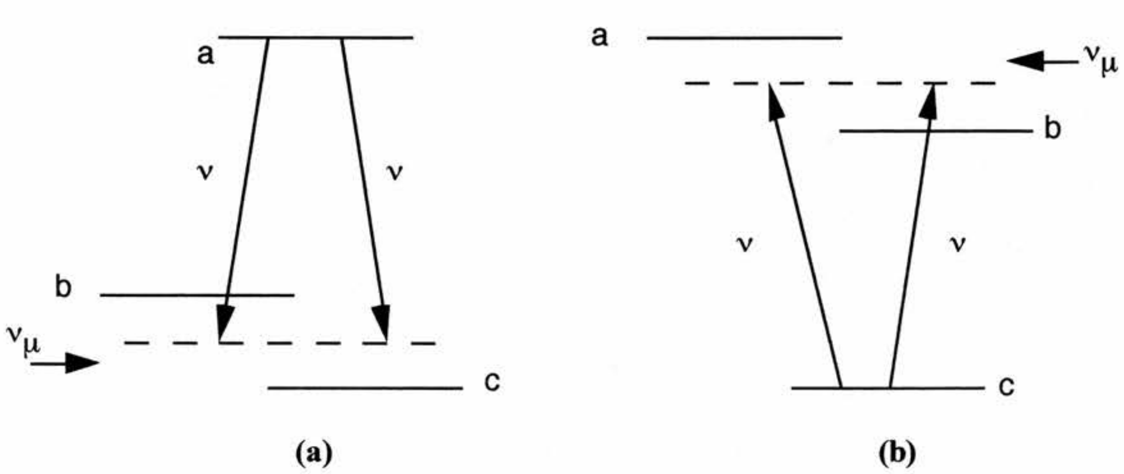

(a) **(b)**

Figure 1.5.11: *Degenerate quantum beat lasers and corresponding atomic level schemes,(a) Lambda type showing lasing without inversion. (b) V-type system showing inversion without lasing.*

Yelin et al. have analysed the specific features of noninversion amplification in the frequency up-conversion regime. In these systems, the frequency of coherence generating (driving) and lasing fields are substantially different. They found that propagation effects and, specifically, rapid absorption of the driving field limit the possible gain in V and lambda systems. They have examined the general conditions of noninversion amplification in a V-type system and have proposed a novel regime for lasing without inversion, in which the driving field is applied on a weakly allowed transition. Additionally, the gain can be made Doppler insensitive if a bichromatic probe field is used. They have considered a hydrogenlike system as a possible realisation of this new regime. Coherent driving can there be accomplished using intense microwave radiation at frequencies close to the hyperfine splitting of the ground state. Lasing without inversion into this ground state from highly excited atomic levels seems feasible.

The Doppler broadening is an effect undesirable in EIT and inversionless gain experiments. Laser cooled samples produced in a magneto-optic trap (MOT) are very attractive for fundamental studies of EIT, because they present virtual absence of Doppler broadening. *Durrant et al.* have demonstrated EIT and gain without inversion produced by coherences among the Zeeman sublevels of the F=1 hyperfine level of laser cooled ^{87}Rb in an MOT in a lambda configuration. The effects of coherent population trapping and optical pumping in the simple F=1 to F'=0 and F=1 to F'=1 systems were studied. These systems show nearly 100 % transparency for relatively low coupling field intensities and for perpendicular as well as near-parallel propagation directions of coupling and probe fields. The importance of light polarisation in controlling the transparency effects of optical pumping was demonstrated. Sub-natural two-photon linewidths were obtained with very small detunings of the coupling field, and gain without population inversion in the bare states was demonstrated in the incoherently pumped F=1 to F'=0 system.

A new class of inversionless laser gives rise to destructive quantum interference for absorption and constructive for emission without atomic population inversion, by the use of band gap engineering. The laser scheme is based on a unipolar double quantum well (DQW) structure, in which the gain occurs at a transition between the conduction band subbands. The prototypical DQW that *Imamoglu et al.* envision is depicted in Figure 1.5.12. The first subband |2> of the narrow well is resonant with the second subband of |3> of the wide well which in turn has a dipole-allowed transition to the lower subband |1>.

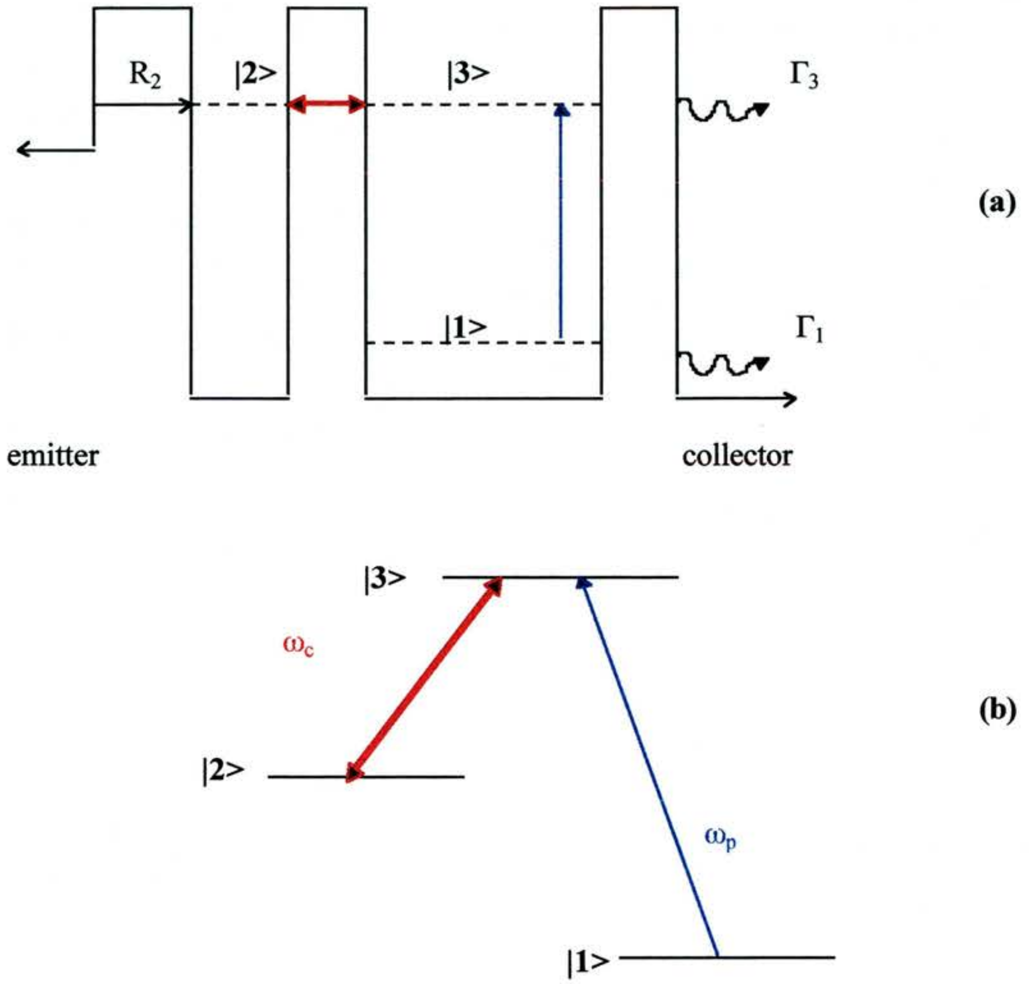

Figure 1.5.12: *Bare state energy level diagrams for (a) a unipolar DQW and (b) the inversionless Λ-atomic scheme which the double well represents.* Γ_1 *and* Γ_3 *are the decay rates of level |1> and |3> and* R_2 *is the incoherent electron pumping rate.*

For steady-state lasing without population inversion three conditions have to be satisfied: 1) The decay rate of state |3>, Γ_3 has to exceed the dephasing rate γ_{21} of the |2>-|1> coherence ρ_{21}, 2) The coupling Rabi frequency Ω_{23} should be greater than $\sqrt{\Gamma_3\gamma_{21}}$ and the inhomogeneous broadening $\Delta\nu$, 3) The incoherent pump into state |2> should not be accompanied by a rate into the pumping reservoir (emitter).

A realistic DQW consists by GaAs/AlGaAs layers. The emitter and collector regions are doped with Si, whereas the quantum wells and barrier regions are undoped. The GaAs subband energy spacing is 0.119 eV, which corresponds to an optical transition wavelength λ_p=10.36 μm.

1.6 Thesis plan.

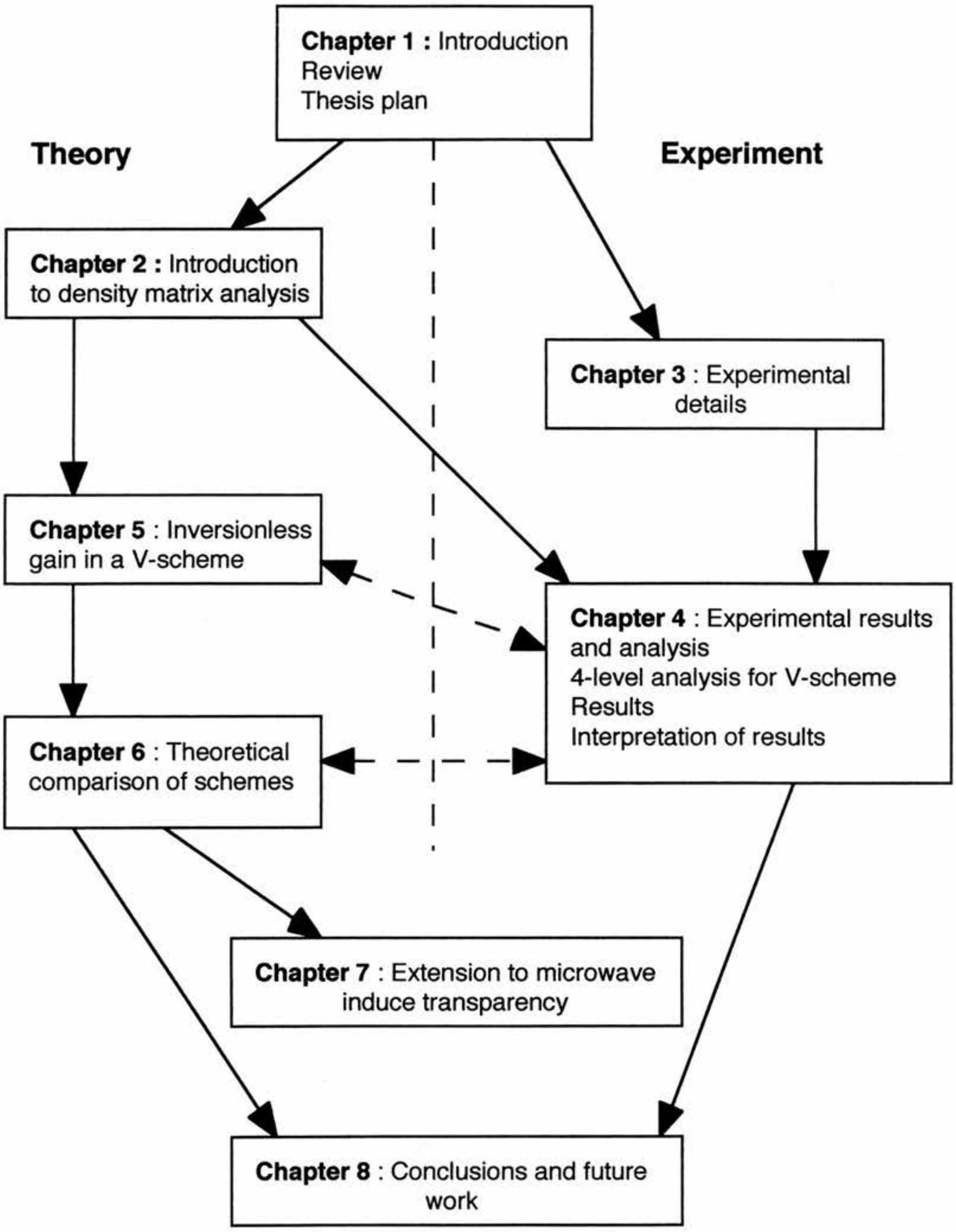

Chapter 1 provides an introduction to the thesis.

Chapters 2, 5, 6 progressively develop the theory from first principles to detailed consideration of blue EIT, inversionless gain and comparison of schemes. Chapter 2 is a necessary introduction for the experimental work.

Chapter 3 includes the experimental details.

Chapter 4 : The main experimental work is described, analysed and discussed, drawing on all previous chapters.

Chapter 7 provides background theory and proposes experimental arrangements for microwave induced transparency.

Chapter 8 : Conclusions and future work.

References

Akulshin A.M., A.A. Celikov and V.L. Velichansky, "Sub-Natural Absorption Resonances On The D_1 Line Of Rubidium Induced By Coherent Population Trapping", Opt. Commun., **84** , p. 139 (1991).

Alzetta G., A. Gozzini, L. Moi and G. Orriols, "An Experimental Method For The Observation Of R.F. Transitions And Laser Beat Resonances In Oriented Na Vapour" Il Nuovo Cimento B, **36B** , p. 5 (1976).

Arimondo E. and G. Orriols, "Nonabsorbing Atomic Coherences By Coherent Two Photon Transitions In A Three-Level Optical Pumping", Nuovo Cimento Lettere, **17** , p. 333 (1976).

Boller K.J., A. Imamoglu and S.E. Harris, "Observation Of Electromagnetically Induced Transparency", Phys Rev Lett, **66** , p. 2593 (1991).

Coleman P.E. and P.L. Knight, "Population Trapping In Photoionisation To Dressed Continuum States", J. Phys. B: At. Mol. Phys., **15** , p. L235 (1982).

Dalton B.J. and P.L. Knight, "Population Trapping And Ultranarrow Raman Lineshapes Induced By Phase-Fluctuating Fields", Opt. Commun., **42** , p.411 (1982).

Durrant A.V, H.X. Chen, S.A. Hopkins and J.A. Vaccaro, " Zeeman coherence induced transparency and gain without inversion in laser cooled Rb", Opt. Commun, **151**, p. 136 (1998).

Fano U., "Effects Of Configuration Interaction On Intensities And Phase Shifts", Phys. Rev., **124** , p. 1866 (1961).

Field J.E., K.H. Hahn, and S.E. Harris, "Observation Of Electromagnetically Induced Transparency In Collisionally Broadened Lead Vapour", Phys. Rev. Lett., **67**, p.3062 (1991).

Fleischhauer M., C.H. Keitel, M.O. Scully, C. Su, B.T. Ulrich and S.Y. Zhu, "Resonantly Enhanced Refractive Index Without Absorption Via Atomic Coherence", Phys. Rev. A, **46** , p.1468 (1992).

Fort C., F.S. Caraliotti, T.N. Hansch, M. Inguscio and M. Prevedelli, " Gain without inversion on the cesium D_1 line", Opt. Commun., **139**, p.31 (1997).

Fry E.S., X. Li, D. Nikonov, G.G. Padmabandu, M.O. Scully, A.V. Smith, F.K. Tittel, C. Wang, S.R. Wilkinson and S.Y. Zhu, "Atomic Coherence Effects Within The Sodium D_1 Line: Lasing Without Inversion Via Population Trapping", Phys. Rev. Lett., **70** , p.3235 (1993).

Fulton D.J., Shepherd S., Moseley R.R, Sinclair B.D. and Dunn M.H., "CW electromagnetically induced transparency: A comparison of V, Lambda and cascade systems", Physical Review A, **52**, p.2302 (1995).

Gao J.Y., H.Z. Zhang, H.F. Cui, X.Z. Guo, Y. Jiang, Q.W. Wang, G.X. Jin and J.S. Li, "Inversionless Light Amplification In Sodium", Opt. Commun., **110** , p.590 (1994).

Gea-Banacloche J., Y. Li, S. Jin and M. Xiao, "Electromagnetically Induced Transparency In Ladder-Type Inhomogeneously Broadened Media: Theory and Experiment", Phys. Rev. A, **51** ,p. 576 (1995).

Gray H.R., R.M. Whitley and C.R. Stroud Jr., "Coherent Trapping Of Atomic Populations", Optics Letters, **3** , p.218 (1978).

Ham B.S., P.R. Hemmer, and M.S. Shahriar, " Efficient EIT in a rare-earth doped crystal", Optics Commun., **144**, p.227 (1997).

Harris S.E., "Lasers Without Inversion: Interference Of Lifetime-Broadened Resonances", Phys. Rev. Lett., **62** , 1033 (1989).

Harris S.E., J.E. Field and A. Kasapi, "Dispersive Properties Of Electromagnetically Induced Transparency", Phys. Rev. A., **46** , p.R29 (1992).

Harris S.E. and M. Jain, "Optical parametric oscillators pumped by population trapped atoms", Optics Letters, **22**, p.636 (1997).

Harris S.E., J.E. Field and A. Imamoglu, "Nonlinear Optical Processes Using Electromagnetically Induced Transparency", Phys. Rev. Lett., **64** ,p. 1107 (1990).

Harris S.E., "Electromagnetically Induced Transparency With Match Pulses", Phys. Rev. Lett., **70** ,p. 552 (1993).

Hopkins S.A., E. Usadi, H.X. Chen and A.V. Durrant, "Electromagnetically Induced Transparency Of Laser-Cooled Rubidium Atoms In Three-Level Lambda Type Systems", Opt. Commun, **138**, p.185 (1997).

Imamoglu A., J.E. Field and S.E. Harris, "Lasers Without Inversion: A Closed Lifetime Broadened System", Phys. Rev. Lett., **66** , p.1154 (1991).

Imamoglu A. and R.J. Ram, "Semiconductor Lasers Without Population Inversion", Optics Letters, **19** , p.1744 (1994).

Jong F.B., A. Mavromanolakis, J.C. Spreeuw and H.B. van Lindenvan den Heuvell, " Synchronously pumped laser without inversion in cadmium", Phys. Rev. A, **57**, p. 4869 (1998).

Kleinfeld J.A. and A.D. Streater, "Observation Of Gain Due To Coherence Effects In A Potassium-Helium Mixture", Phys. Rev. A, **49** ,p. R4301 (1994).

Koncharovskaya O.A., F. Mauri and Arimondo, " Laser without population inversion and coherent trapping", Optics Commun., **84**, p. 393 (1991).

Koncharovskaya O.A, " Lasing without population inversion: problems and prospects", Hyperfine Interactions, **107**, p. 187 (1997).

Kurizki G., Scully M.O. and Keitel C., " Free electron lasing without inversion by interference of momentum states", Physical Review Letters, **70**, p.1433 (1993).

Li Y. and M. Xiao, "Observation Of Quantum Interference Between Dressed States In An Electromagnetically Induced Transparency", Phys. Rev A, **51** ,p. 4959 (1995).

Li Y., S.Z. Jin and M. Xiao, "Observation of an electromagnetically change of absorption in multilevel Rb atoms", Phys. Rev. A, **51**, p. R1754 (1995).

Lukin M. D., M. Fleischhauer , M.O Scully and V.L. Velichansky, " Intracavity EIT", Optics Letters, **23**, p. 295 (1998).

Mandel P. and O. Kocharovskaya, "Inversionless Amplification Of A Monochromatic Field By A Three-Level Medium", Phys. Rev. A, **46** ,p. 2700 (1992).

Moseley R.R., Shepherd S., Fulton D.J., Sinclair B.D. and Dunn M.H., "Spatial consequences of electromagnetically induced transparency: Observation of electromagnetically induced focusing", Physical Review Letters, **74**, p.670 (1995).

Narducci L. M., H.M. Doss, P. Ru, M.O. Scully and Keitel C., " A simple model of a laser without inversion", Optics Commun., **81**, p. 379 (1991).

Nottelmann A., C. Peters and W. Lange, "Inversionless Amplification Of Picosecond Pulses Due To Zeeman Coherences", Phys. Rev. Lett., **70** , p. 1783 (1993).

Padmabandu G.G., G.R. Welch, I.N. Shubin, E.S. Fry, D.E. Nikonov, M.D. Lukin and M.O. Scully, "Laser Oscillation Without Population Inversion In A Sodium Atomic Beam", Phys. Rev. Lett., **76** ,p. 2053 (1996).

Radmore P.M. and P.L. Knight, "Population trapping and dispersion in a three level system", Journal Physics B, **15**, p.561 (1981).

Sander F., Weis A., Kanorsky S.I. and Hansch T.W., private communications.

Schmidt O., R. Wynands, Z. Hussein and D. Meschede, "Steep Dispersion And Group Velocity Below c/3000 In Coherent Population Trapping", Phys. Rev. A, **53** , p. R27 (1996).

Scully M.O., "Enhancement Of The Index Of Refraction Via Quantum Coherence", Phys. Rev. Lett., **67** ,p. 1855 (1991).

Scully M.O. and M. Fleischhauer, "Lasers Without Inversion", Science, **263** ,p. 337 (1994).

Scully M.O., S.H. Zhu and A. Gavrielides, "Degenerate Quantum-Beat Laser: Lasing Without Inversion And Inversion Without Lasing", Phys. Rev. Lett., **62** ,p. 2813 (1989).

Shepherd S., Fulton D.J., and Dunn M.H, " Wavelength dependence of coherently induced transparency in a Doppler-broadened cascade medium", Physical Review A, **54**, p.5394 (1996).

Van der Veer W.E., R.J.J. van Diest, A. Dönszelmann and H.B van Linden van den Heuvell, "Experimental Demonstration Of Light Amplification Without Population Inversion", Phys. Rev. Lett., **70** ,p. 3243 (1993).

Wang Y., G. Xu, C. Ye, J. Zhao, S. Zhou and Y.Liu, "Observation Of Transparency And Population Trapping Due To Atomic Coherence Effects", Phys. Rev. A, **53** , p.1160 (1996).

Whitley R.M. and C.R. Stroud Jr., "Double Optical Resonance", Phys. Rev. A, **14** , p.1498 (1976).

Xiao M., Y. Li, S. Jin and J. Gea-Banacloche, "Measurement Of Dispersive Properties Of Electromagnetically Induced Transparency In Rubidium Atoms", Phys. Rev. Lett., **74** ,p. 666 (1995).

Yelin S.F., M.D. Lukin, M.O Scully and P. Mandel, "Gain without inversion in the frequency up-conversion regime", Phys. Rev. A, **57**, p. 3858 (1998).

Zhu Y. and Lin J., "Sub-Doppler light amplification in a coherently pumped atomic system", Physical Review A, **53**, p.3235 (1993).

Zhu Y. and T.N. Wasserlauf, "Sub-Doppler linewidth with EIT in Rb atoms", Physical Review A, **54**, p. 3653 (1996).

Zibrov A.S., M.D. Lukin, L. Hollberg, D.E. Nikonov, M.O. Scully, H.G. Robinson and V.L. Velichansky, "Experimental Demonstration Of Enhanced Index Of Refraction Via Quantum Coherence In Rb", Phys. Rev. Lett., **76** ,p. 3935 (1996).

Zibrov A.S., M.D. Lukin, D.E. Nikonov, L. Hollberg, M.O. Scully, V.L. Velichansky and H.G. Robinson, "Experimental Demonstration Of Laser Oscillation Without Population Inversion Via Quantum Interference In Rb", Phys. Rev. Lett., **75** , p. 1499 (1995).

Chapter 2

Density matrix analysis for atomic coherence effects

2.1 Density matrix analysis and its physical significance.

Atomic systems which are dominated by coherent excitation and quantum interference phenomena, such as Coherently Induced Transparency (EIT) and inversionless lasing, can no longer be described by a rate equation approach using Einstein coefficients. These effects need to be covered by a comprehensive semiclassical interpretation, where atoms are treated quantum mechanically and electromagnetic fields classically.

One way to present the subject of resonance radiation with atoms is to consider a single atom and describe its evolution by the time dependent Schrödinger equation:

$$\hat{H}\,\Psi = i\hbar\frac{\partial\Psi}{\partial t} \tag{2.1.1}$$

with $\Psi(\mathbf{r},t) = \sum_{n} C_n(t)\,\psi_n(\mathbf{r},t)$ being the wavefunction of the atom and $\hat{H}$ the Hamiltonian of the system. Solving the coupled equations for time-dependent state probability amplitudes one may deduce the oscillating dipole moment per atom and then by averaging over excitation time determine the total effect. However, in this way it is rather difficult to incorporate random decay rates from the levels and coherences.

Alternatively, in order to calculate the average value of atomic observables (say excitation probability or dipole moment), it is only necessary to know the density matrix of atoms. The density matrix is often described by a first order-differential equation called the Liouville equation (*Fulton,PhD thesis*):

$$\begin{aligned}\frac{\partial\rho_{ij}}{\partial t} &= -\frac{i}{h}\left[\hat{H},\rho\right]_{ij} - \Gamma_{ij}\left(\rho_{ij} - \rho^{0}_{ij}\right) \\ &= -\frac{i}{h}\sum_{k=1}^{n}\left(H_{ik}\rho_{kj} - \rho_{ik}H_{kj}\right) - \Gamma_{ij}\left(\rho_{ij} - \rho^{0}_{ij}\right)\end{aligned} \tag{2.1.2}$$

The commutator $\left[\hat{H},\rho\right]$ follows directly from the Schrödinger equation (2.1.1). The Γ_{ij} involve collisional coherence relaxation rates, population transfer rates R_{ij} or ionisation rates, all of which can not be included in the Hamiltonian of the system directly. The $\rho^{0}{}_{ij}$ is the thermal equilibrium value of the density matrix of the atomic system as given by:

$$\rho^{0}_{ij} = \frac{\exp\left(-\frac{H^{0}_{ij}}{kT}\right)}{\mathrm{tr}\left[\exp\left(-\frac{H^{0}}{kT}\right)\right]} \tag{2.1.3}$$

The diagonal density matrix elements are the state populations P_i :

$$\rho_{ii} = P_i \tag{2.1.4}$$

and the off diagonal elements are termed the coherences:

$$\rho_{ij} = \overline{C^{*}_{j}C_{i}} \tag{2.1.5}$$

with the bar in the above equation indicating an ensemble average.

Two of the properties of these statistical elements are the trace normalisation condition:

$$\mathrm{tr}(\rho) \equiv \sum_{i}\rho_{ii} = \sum_{i}C^{*}_{i}C_{i} = 1 \tag{2.1.6}$$

a direct indication of conservation of population and the property of index reversal which ensures that the matrix is Hermitian:

$$\rho_{ij} = \rho^{*}_{ji} \tag{2.1.7}$$

In a simple two-level atom with coherent excitation the Hamiltonian of the system is given by:

$$\hat{H} = \hat{H}_0 + \hat{H}_I = \hat{H}_0 - \hat{\mu}\mathbf{E}(z,t) \tag{2.1.8}$$

with $\hat{H}_0$ being the Hamiltonian of a free atom and $\hat{H}_I$ the Hamiltonian of the electric dipole interaction.

Each individual component of the density matrix has a physical significance. Firstly, the diagonal elements, ρ_{ii} are the average probability of finding an atom in state ψ_i, in other words the population of a particular state in an ensemble. The off-diagonal elements ρ_{ij}, are the coherences and relate to the strength and phase of the interactions between the energy levels. They are directly related to the total polarisation induced in the atomic system as follows (*Moseley, PhD thesis*):

$$P(t) = N\sum_{i\neq j}\mu_{ij}\rho_{ij} = N\sum_{i\neq j}\mu_{ij}(\rho^{r}_{ij} + i\rho^{i}_{ij}) \tag{2.1.9}$$

for an ensemble of N atoms with electric dipole moment μ_{ij}:

$$\mu_{ij} = \int \psi_j^{*}(e\hat{x})\psi_i \, d\tau \text{ , with } \hat{x} \text{ the displacement} \tag{2.1.10}$$

The macroscopic polarisation is given in terms of the medium's susceptibility $\chi(\omega)$ and the electric field $E(z,t)$:

$$P(t) = \varepsilon_0\chi(\omega)\, E(z,t) = \varepsilon_0\,[\chi'(\omega) - i\chi''(\omega)]\, E(z,t) \tag{2.1.11}$$

These two expressions for the polarisation can be related to the density matrix elements, by equating the real parts and subsequently the imaginary parts of (2.1.9) and (2.1.11). The real and the imaginary components of the susceptibility have then the form:

$$\chi'(\omega) = \frac{N\mu_{ij}^2}{\varepsilon_0\hbar}\frac{\rho^{r}{}_{ij}}{\Omega_R} \tag{2.1.12}$$

$$\chi''(\omega) = -\frac{N\mu_{ij}^2}{\varepsilon_o\hbar}\frac{\rho_{ij}{}^{i}}{\Omega_R} \tag{2.1.13}$$

wherein $\Omega_R = {}^{\mu_{ij}\, E(z,t)}\!/_{\hbar}$ is the Rabi frequency induced by the field.

According to Maxwell's wave equation for a plane electromagnetic wave in a dispersive medium the real part of the susceptibility is related to the refractive index variation and the imaginary part to the gain-absorption variation that the atomic system exhibits. That is to say the atomic polarisation alters the phase delay per unit length by:

$$\Delta k = \frac{k\chi'(\omega)}{2n^2} \qquad (2.1.14)$$

and causes the amplitude to vary exponentially with distance as $E = E_0 \exp G = \exp(\alpha_g/2)z$, where G is the gain-absorption and α_g the small gain-absorption coefficient given by:

$$\alpha_g(\omega) = -\frac{k\chi''(\omega)}{n^2} \qquad (2.1.15)$$

Substituting in the above gain-absorption coefficient expression for the susceptibility from (2.1.13) the small signal gain coefficient per unit length is proportional to the density matrix elements as follows:

$$\alpha_g(\omega) = -\frac{N\mu_{ij}^2 k}{\varepsilon_o \hbar n^2}\frac{\rho_{ij}{}^{i}}{\Omega_R} \qquad (2.1.16)$$

The electric dipole moment may be expressed as (*Loudon*):

$$\mu_{ij}^2 = \frac{3A_{ji}\hbar\varepsilon_0\lambda_0^3}{16\pi^2} \qquad (2.1.17)$$

wherein A_{ji} is the Einstein coefficient, $k = 2\pi / \lambda$ is the wavenumber and λ_0 is the wavelength in vacuum. Hence, following the substitution of the electric dipole moment in the small gain coefficient equation 2.1.16, a general expression for the gain of an atomic system has the form:

$$G = -\frac{3NA_{ji}\lambda_0^2\rho_{ij}^i z}{16\pi n^2\Omega_R} \qquad (2.1.18)$$

2.2 Derivation of density matrix equations in three level atoms.

2.2.1 V-scheme (EIT and inversionless gain).

Three-level atomic systems that have been broadly studied are the cascade, V and Λ configurations. In figure 2.2.1 a simple 3 level atom is depicted, with two fields being present on a linked transition in a V-energy scheme. The system is closed with regards to the atomic basis set. The laser field at angular frequency ω_c is the strong coupling field and it is near resonant with the atomic transition ω_{12} and similarly, the weak probe field ω_p is resonant with the ω_{13} transition.

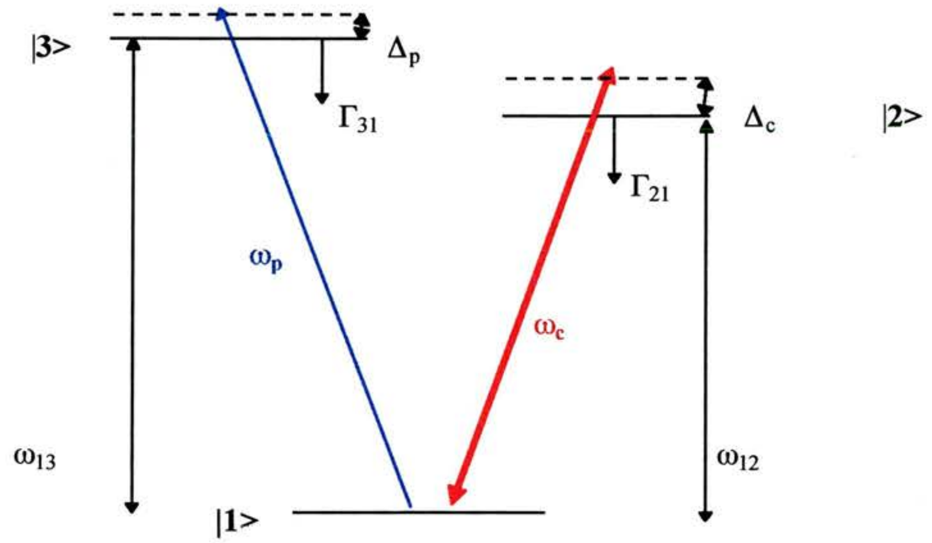

Figure 2.2.1: *V-type energy system within a three level atom. The frequency of the weak field is* ω_p *and of the strong is* ω_c. Γ_{21} *and* Γ_{31} *are the decay rates from levels 2 and 3.* Δ_p *and* Δ_c *are the detunings from resonance of the probe and the coupling fields, respectively.*

In order to discern the evolution of the average probability amplitudes for the above configuration, the interaction Hamiltonian has the form of equation 2.1.8 in which the electric dipole moments may be written as:

$$\mu_{12}=\mu_{21}\neq 0,\ \mu_{13}=\mu_{31}\neq 0,\ \mu_{23}=\mu_{32}=0 \tag{2.2.1}$$

and the two electric fields are defined to be:

$$E_i(z,t)=\frac{E_i^0}{2}\left\{\exp\left[i\left(\omega_i t-k_i z\right)\right]+\text{c.c.}\right\} \quad \text{for i=1,2} \tag{2.2.2}$$

and the half Rabi angular frequencies induced by the fields are given by:

$$\Omega_c=\frac{\mu_{12}E_c^0}{2\hbar} \qquad \text{for the coupling laser} \tag{2.2.3}$$

$$\Omega_p=\frac{\mu_{13}E_p^0}{2\hbar} \qquad \text{for the probe laser} \tag{2.2.4}$$

The optical frequency oscillations of ρ_{ij} are assumed to vary in a V-scheme as follows:

$$\rho_{12}=\bar{\rho}_{12}\exp[i(\omega_c t-k_c z)] \tag{2.2.5}$$

$$\rho_{13}=\bar{\rho}_{13}\exp[i(\omega_p t-k_p z)] \tag{2.2.6}$$

$$\rho_{23}=\bar{\rho}_{23}\exp[i\{(\omega_p-\omega_c)t-(k_p-k_c)z\}] \tag{2.2.7}$$

where the $\bar{\rho}$'s vary only slowly in time and will subsequently be assumed time independent.

The rates of change of the density matrix elements are derived from the Liouville equation (2.1.2) by substituting for the fields and ρ_{ij}. Oscillating terms at twice the optical frequencies or summations of them are removed under the rotation wave approximation, because they will average to zero for an integration time of any time above a few optical cycles. The six equations which express the rate of change of the density matrix elements, for the V-energy configuration of figure 2.2.1 have the form:

$$\dot{\rho}_{11}=i\Omega_c(\bar{\rho}_{21}-\bar{\rho}_{12})+i\Omega_p(\bar{\rho}_{31}-\bar{\rho}_{13})+\Gamma_{21}\rho_{22}+\Gamma_{31}\rho_{33} \tag{2.2.8}$$

$$\dot\rho_{22} = i\Omega_c(\bar\rho_{12} - \bar\rho_{21}) - \Gamma_{21}\rho_{22} \qquad (2.2.9)$$

$$\dot\rho_{33} = i\Omega_p(\bar\rho_{13} - \bar\rho_{31}) - \Gamma_{31}\rho_{33} \qquad (2.2.10)$$

$$\dot{\bar\rho}_{12} = -i\bar\rho_{12}(\Delta_c - i\gamma_{12}) + i\Omega_c(\rho_{22} - \rho_{11}) + i\Omega_p\bar\rho_{23} \qquad (2.2.11)$$

$$\dot{\bar\rho}_{13} = -i\bar\rho_{13}(\Delta_p - i\gamma_{13}) + i\Omega_p(\rho_{33} - \rho_{11}) + i\Omega_c\bar\rho_{23} \qquad (2.2.12)$$

$$\dot{\bar\rho}_{23} = -i\bar\rho_{23}(\Delta_p - \Delta_c - i\gamma_{23}) - i\Omega_p\bar\rho_{12} + i\Omega_c\bar\rho_{13} \qquad (2.2.13)$$

Density matrix elements are complex numbers and can be expressed as:

$$\bar\rho_{ij} = \rho^r_{ij} + i\rho^i_{ij} \text{ and } \bar\rho^*_{ij} = \rho^r_{ij} - i\rho^i_{ij} \qquad (2.2.14)$$

and used to convert the six complex equations into nine real simultaneous equations. Furthermore population conservation implies the trace normalisation :

$$\rho_{11} + \rho_{22} + \rho_{33} = 1 \qquad (2.2.15)$$

and this removes one degree of freedom, leaving only 8 independent variables and 8 simultaneous equations. Finally, in the steady state all the time derivatives may be put equal to zero and the system can be represented in a matrix form **Ax** = **B** as in matrix 2.1.

$$\begin{bmatrix} \Gamma_{21} & 0 & 0 & 0 & 0 & 2\Omega_c & 0 & 0 \\ 0 & \Gamma_{31} & 0 & 0 & 0 & 0 & 2\Omega_p & 0 \\ 0 & 0 & \gamma_{12} & 0 & 0 & -\Delta_c & 0 & -\Omega_p \\ 0 & 0 & 0 & \gamma_{13} & 0 & 0 & -\Delta_p & \Omega_c \\ 0 & 0 & 0 & 0 & \gamma_{23} & \Omega_p & \Omega_c & \Delta_c - \Delta_p \\ -2\Omega_c & -\Omega_c & \Delta_c & 0 & -\Omega_p & \gamma_{12} & 0 & 0 \\ -\Omega_p & -2\Omega_p & 0 & \Delta_p & -\Omega_c & 0 & \gamma_{13} & 0 \\ 0 & 0 & \Omega_p & -\Omega_c & \Delta_p - \Delta_c & 0 & 0 & \gamma_{23} \end{bmatrix} \begin{bmatrix} \rho_{22} \\ \rho_{33} \\ \rho^r_{12} \\ \rho^r_{13} \\ \rho^r_{23} \\ \rho^i_{12} \\ \rho^i_{13} \\ \rho^i_{23} \end{bmatrix} = \begin{bmatrix} 0 \\ 0 \\ 0 \\ 0 \\ 0 \\ -\Omega_c \\ -\Omega_p \\ 0 \end{bmatrix}$$

Matrix 2.1: *The system of a three-level V-energy scheme.*

The dephasing rates are defined as:

$$\gamma_{ij} = \frac{1}{2}\left(\Gamma_{ji}\right) + \gamma_{deph} \tag{2.2.16}$$

wherein γ_{deph} includes macroscopic dephasing rates due to collisions. If an incoherent pump with a pumping rate R_{ij} is resonant with an atomic transition the term may be added in equation (2.2.16) as described in a later discussion (see equation 2.2.22). The detunings from the atomic transitions have the form:

$$\Delta_c = \omega_c - \omega_{12} - k_c V_z \tag{2.2.17}$$

$$\Delta_p = \omega_p - \omega_{13} - k_p V_z \tag{2.2.18}$$

The use of vapours as an atomic interaction medium includes Doppler broadening. In order to derive the absorption or the refractive index, Doppler integration should be considered in the final calculation. The Doppler shift of an atom moving at velocity V_z in the z direction alters the detunings of the fields from exact resonance, by the term $-kV_z$ where k is the wavenumber. Hence the density matrix components are now velocity dependent and are integrated over the Maxwell-Boltzman velocity distribution as:

$$\tilde{\rho}_{ij} = \int_0^\infty f(V_z)\rho_{ij}(V_z)dV_z \tag{2.2.19}$$

where $f(V_z)$ is the velocity distribution of atoms between V_z and V_z+dV_z :

$$f(V_z) = \frac{\exp-\left(\frac{V_z}{u}\right)^2}{\sqrt{\pi}}\frac{dV_z}{u} \quad \text{, with } u \equiv \left(\frac{2k_BT}{M}\right)^{1/2} \tag{2.2.20}$$

Numerical solutions of this atomic system were achieved using the software Mathematica. The main algorithm was composed by *Shepherd S.* and is detailed:

- Define the constants i.e. temperature, wavenumbers (copropagation in our case) etc. and set the variable V_z along with the velocity distribution.
- Set the detunings, the variable detuning for the probe, decay rates, Rabi frequencies as angular frequencies and dephasing terms.
- Define the density matrices of the system $\mathbf{A}x = \mathbf{B}$, $\mathbf{A}$ and $\mathbf{B}$.
- The inverse $\mathbf{A}^{-1}$ is calculated and multiplied by $\mathbf{B}$.

- The density matrix element of interest is then multiplied by the velocity distribution.
- The integration is carried out by Simpson's rule in the velocity range from -500 m/s to 500 m/s in small steps (4000 in our case).
- Set the detuning from -0.95 GHz to 0.95 GHz.

The system was modelled using wavenumbers and decay rates appropriate for a coupling field resonant at the $5S_{1/2}$ to $5P_{3/2}$ transition and the probe set at the $5S_{1/2}$ to $6P_{1/2}$ transition in Rubidium (see table 3.1.4 in chapter 3). The wavelength of the probe is 422 nm and that of the coupling field is 780 nm. The Rabi angular frequencies of the strong and the weak field were $\Omega_c = 160$ MHz and $\Omega_p = 1$ MHz, respectively.

Numerical analysis was carried out. The imaginary part ρ^i_{13} and the real part ρ^r_{13} were plotted against the probe field detuning, when the coupling field is set to zero, in figure 2.2.2a and 2.2.2b, respectively. As it is shown in figure 2.2.2a there is a straight forward absorption of the probe field exactly on resonance. The refractive index displays the expected anomalous dispersion, with a sign change at the point of resonance, as in figure 2.2.2b. Doppler broadening is considered (T=130°C).

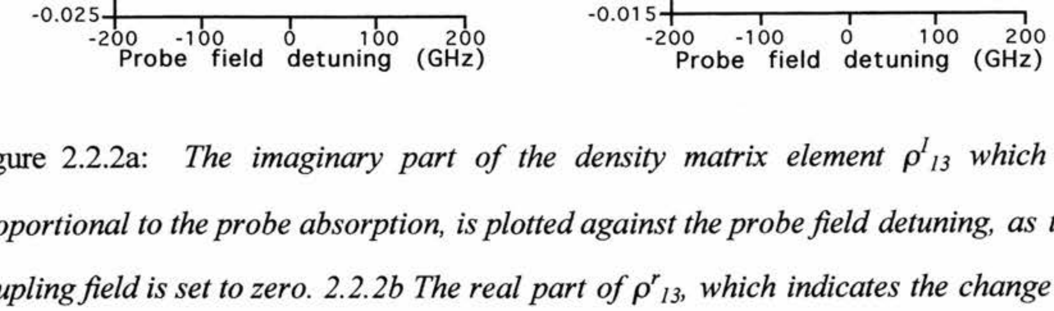
(a) **(b)**

Figure 2.2.2a: *The imaginary part of the density matrix element* ρ^I_{13} *which is proportional to the probe absorption, is plotted against the probe field detuning, as the coupling field is set to zero. 2.2.2b The real part of* ρ^r_{13}, *which indicates the change of the refractive index is plotted against the probe field detuning.*

With both the coupling and probe fields present leading to values of Ω_c and Ω_p of 160 MHz and 1 MHz respectively, the imaginary part ρ^{i}_{13} and the real part ρ^{r}_{13} were plotted against the probe field detuning in figure 2.2.3a and 2.2.3b, respectively. In figure 2.2.3a Coherently Induced Transparency (EIT) is observed exactly on line centre. As shown in the graph, EIT in a V-system is the cancellation of absorption on the weak probe field, by the presence of the strong coupling laser, sharing a common lower state (the ground state). In figure 2.2.3b the real part ρ^{r}_{13} is the refractive index experienced by the probe field and as it is shown it is considerably altered as the probe field frequency approaches resonance.

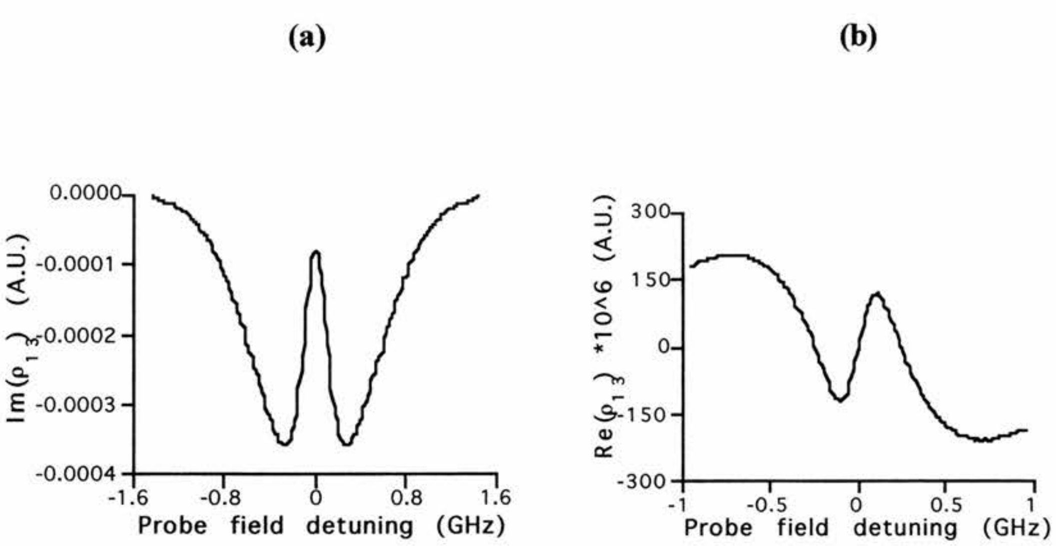

Figure 2.2.3a: *The imaginary part of the density matrix element ρ_{13} which indicates the probe absorption, as the weak field is detuned from resonance. 2.2.3b The real part of the same density matrix element which indicates the change of the refractive index. The Rabi frequencies were Ω_c=160 MHz and Ω_p=1 MHz for the coupling and the probe field respectively. The temperature is 130° C.*

Subsequently, incoherent pumps such as discharges or flashlamps can also be incorporated into the density matrix model by adding phenomenological terms into the Liouville equation. These terms are mainly present when inversionless lasing systems are being considered since it is required that a small amount of population is put into the upper lasing level. Incoherent pump sources are more useful than coherent ones, because they do not destroy the coherence already present in the system.

Incoherent pump terms can be added to the Liouville equation in two different forms. The first form considers the effect of excitation by collisions induced in a discharge. These are accounted for by the addition of terms which describe both the removal of population from the lower level of an excitation and the addition of it to the upper level in a non-reversible manner. Consider the incoherent excitation of population from level |1> to level |2>. The related Liouville equation must be altered such that:

$$\frac{\partial \rho_{11}}{\delta t} = -\frac{i}{\hbar}\left[\hat{H},\rho\right]_{11} - \Pi_{12}\rho_{11} \tag{2.2.21}$$

$$\frac{\partial \rho_{22}}{\delta t} = -\frac{i}{\hbar}\left[\hat{H},\rho\right]_{22} + \Pi_{12}\rho_{11} \tag{2.2.22}$$

where Π_{12} is the incoherent pump rate. For excitation via thermal incoherent radiation, with radiative processes dominating, transitions can be stimulated in both directions and so the terms become:

$$\frac{\partial \rho_{11}}{\delta t} = -\frac{i}{\hbar}\left[\hat{H},\rho\right]_{11} + R_{12}\left(\rho_{22} - \rho_{11}\right) \tag{2.2.23}$$

$$\frac{\partial \rho_{22}}{\delta t} = -\frac{i}{\hbar}\left[\hat{H},\rho\right]_{22} - R_{12}\left(\rho_{22} - \rho_{11}\right) \tag{2.2.24}$$

where R_{12} is related to the incoherent radiation intensity. It should be noted that the dephasing between the levels is raised by the introduction of incoherent pumps. To account for this an additional term must be added to the coherence dephasing rates each time either component of the incoherent pump rate's index appears in the index of the coherence dephasing rate as follows for non-degenerate system (*Imamoglu*):

- The pump rate is R_{ij} added into the rate of change of the populations ρ_{ii} in a similar way as the decay rates (see Appendix of *Moseley PhD thesis*)
- The pump rate is added into the dephasing terms γ_{ij} as follows:

R_{ij} in the term γ_{ij}

$R_{ij} / 2$ in the term γ_{im}, where $m \neq j$

$R_{ij} / 2$ in the term γ_{nj}, where $n \neq i$

0 in the term γ_{nm}, where $n \neq i$ and $m \neq j$

- $R_{ij} = R_{ji}$

The addition of an incoherent pump R_{13} = 10 MHz as in figure 2.2.4 allows the system to exhibit gain. The incoherent pump which is resonant with the atomic transition, is included in the density matrix system of Matrix 2.2.

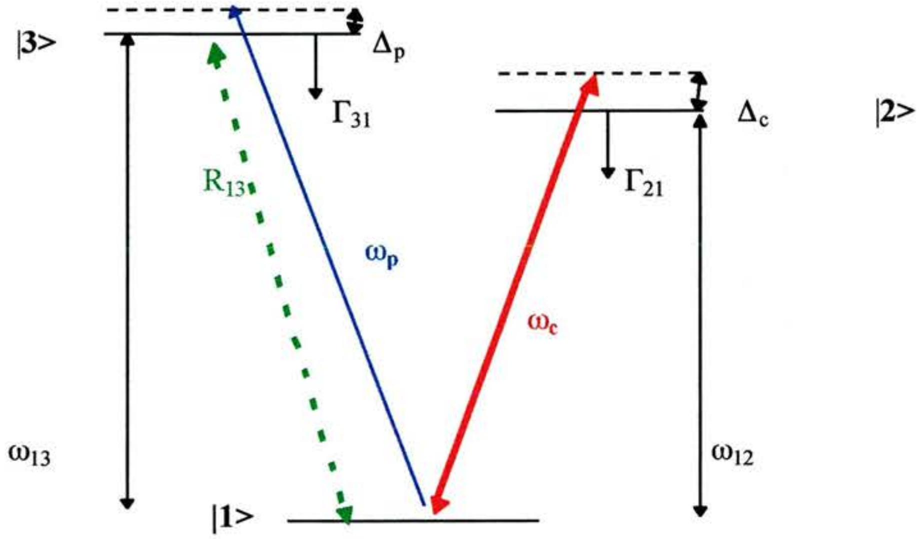

Figure 2.2.4: *Schematic of a closed V-scheme with the addition of an incoherent pump R_{13}.*

$$\begin{bmatrix} \Gamma_{21} & 0 & 0 & 0 & 0 & 2\Omega_c & 0 & 0 \\ R_{13} & \Gamma_{31}+2R_{13} & 0 & 0 & 0 & 0 & 2\Omega_p & 0 \\ 0 & 0 & \gamma_{12} & 0 & 0 & -\Delta_c & 0 & -\Omega_p \\ 0 & 0 & 0 & \gamma_{13} & 0 & 0 & -\Delta_p & \Omega_c \\ 0 & 0 & 0 & 0 & \gamma_{23} & \Omega_p & \Omega_c & \Delta_c-\Delta_p \\ -2\Omega_c & -\Omega_c & \Delta_c & 0 & -\Omega_p & \gamma_{12} & 0 & 0 \\ -\Omega_p & -2\Omega_p & 0 & \Delta_p & -\Omega_c & 0 & \gamma_{13} & 0 \\ 0 & 0 & \Omega_p & -\Omega_c & \Delta_p-\Delta_c & 0 & 0 & \gamma_{23} \end{bmatrix} \begin{bmatrix} \rho_{22} \\ \rho_{33} \\ \rho_{12}^r \\ \rho_{13}^r \\ \rho_{23}^r \\ \rho_{12}^i \\ \rho_{13}^i \\ \rho_{23}^i \end{bmatrix} = \begin{bmatrix} 0 \\ R_{13} \\ 0 \\ 0 \\ 0 \\ -\Omega_c \\ -\Omega_p \\ 0 \end{bmatrix}$$

Matrix 2.2: *The system of a three-level V-energy scheme with the addition of an incoherent pump with a pumping rate R_{13}.*

Gain exactly on resonance in the V-scheme is shown in figure 2.2.5a. The pump transfers sufficient population for gain which is achieved without population inversion. The origin of this gain is quantum coherence. Contrary to conventional wisdom of population inversion, gain could be achieved with most of the population retained in the ground state. Initially an atomic coherence is established, leading to EIT. Then when the pump moves a small fraction of the population to the upper level, overall inversionless gain results. It is obvious in figure 2.2.5b that the population in level |1> is greater than that in level |3>, which are the lower and the upper levels respectively of the lasing transition. Inversionless gain is the goal of quantum coherence and it is possible in this 3-level V-energy configuration.

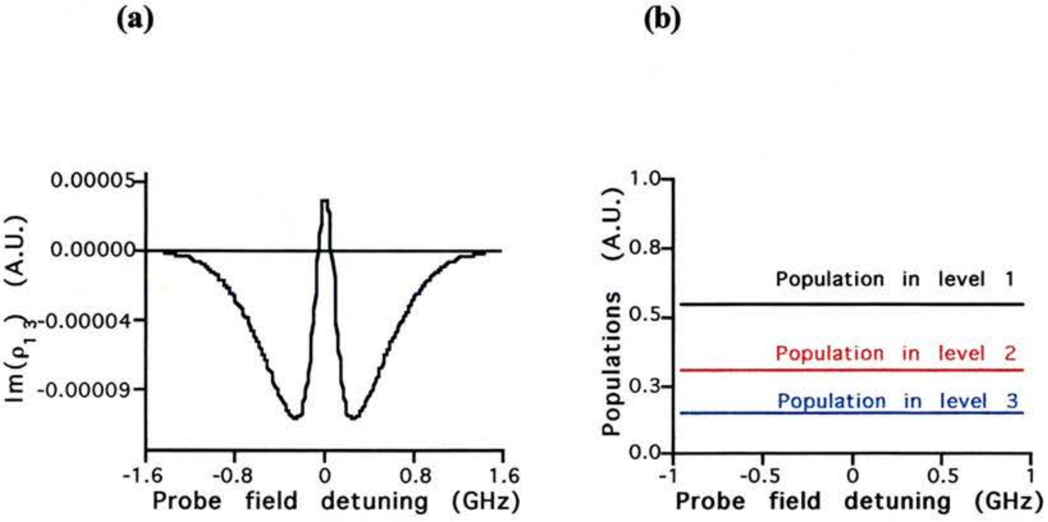

Figure 2.2.5a: *The imaginary part of ρ_{13} is plotted against the probe field detuning, when the incoherent pumping rate is R_{13}=10 MHz. 2.2.5b The populations are plotted for the closed V- system.*

2.2.2 Cascade-scheme (EIT) .

Another system within a three-level atom is the cascade configuration as in figure 2.2.6. The system is again closed with regards to the atomic basis set. The laser field at angular frequency ω_c is the strong coupling field and it is near resonant with the atomic transition ω_{23} and similarly, the weak probe field ω_p is resonant with the ω_{12} transition.

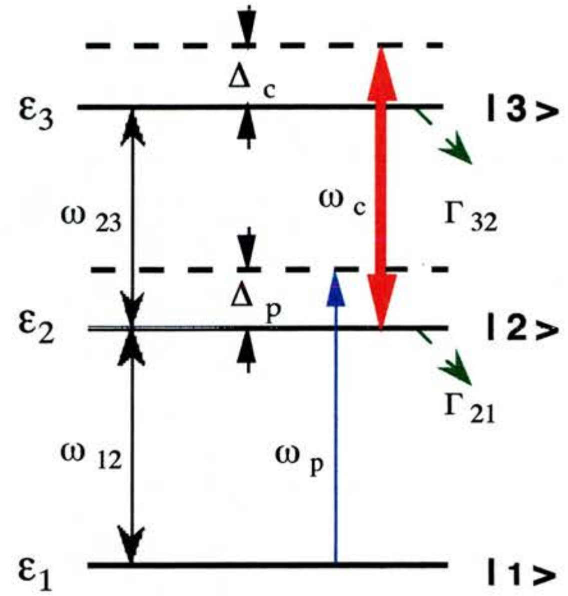

Figure 2.2.6: *Cascade-energy system within a three level closed atom. The frequency of the weak field is ω_p and of the strong is ω_c. Γ_{21} and Γ_{32} are the decay rates from levels 2 and 3. Δ_p and Δ_c are the detunings from resonance of the probe and the coupling fields, respectively.*

The interaction Hamiltonian of such system has the form of equation 2.1.8, in which the electric dipole moments are:

$$\mu_{12}=\mu_{21}\neq 0,\ \mu_{13}=\mu_{31}=0,\ \mu_{23}=\mu_{32}\neq 0 \qquad (2.2.25)$$

The two electric fields are defined as in equation 2.2.2 and the Rabi angular frequencies as in equation 2.2.3 for the coupling laser and 2.2.4 for the probe field.

The ρ_{ij} elements vary at optical frequencies in a cascade scheme as follows:

$$\rho_{12} = \bar{\rho}_{12}\exp[i(\omega_p t - k_p z)] \qquad (2.2.26)$$

$$\rho_{13} = \bar{\rho}_{13}\exp\{i[(\omega_p + \omega_c)t - (k_p + k_c)z]\} \qquad (2.2.27)$$

$$\rho_{23} = \bar{\rho}_{23}\exp[i(\omega_c t - k_c)z] \qquad (2.2.28)$$

where the barred elements vary only slowly with time, or are assumed time independent.

The rates of change of the density matrix elements are derived from Liouville equation in the same way as for the calculations in the V-scheme. The six equations which describe the rate of change of the density matrix elements, for the cascade-energy configuration of figure 2.2.5 have the form:

$$\dot{\rho}_{11} = i\Omega_p(\bar{\rho}_{21} - \bar{\rho}_{12}) + \Gamma_{21}\rho_{22} \tag{2.2.29}$$

$$\dot{\rho}_{22} = i\Omega_p(\bar{\rho}_{12} - \bar{\rho}_{21}) + i\Omega_c(\bar{\rho}_{32} - \bar{\rho}_{23}) - \Gamma_{21}\rho_{22} + \Gamma_{32}\rho_{33} \tag{2.2.30}$$

$$\dot{\rho}_{33} = i\Omega_c(\bar{\rho}_{23} - \bar{\rho}_{32}) - \Gamma_{32}\rho_{33} \tag{2.2.31}$$

$$\dot{\bar{\rho}}_{12} = -i\bar{\rho}_{12}(\Delta_p - i\gamma_{12}) + i\Omega_p(\rho_{22} - \rho_{11}) - i\Omega_c\bar{\rho}_{13} \tag{2.2.32}$$

$$\dot{\bar{\rho}}_{13} = -i\bar{\rho}_{13}(\Delta_p + \Delta_c - i\gamma_{13}) + i\Omega_p\bar{\rho}_{23} - i\Omega_c\bar{\rho}_{12} \tag{2.2.33}$$

$$\dot{\bar{\rho}}_{23} = -i\bar{\rho}_{23}(\Delta_c - i\gamma_{23}) + i\Omega_c(\rho_{33} - \rho_{22}) + i\Omega_p\bar{\rho}_{13} \tag{2.2.34}$$

The same density matrix derivation is employed for the cascade scheme as was previously used for the V-configuration, resulting in the matrix system represented by Matrix 2.3.

$$\begin{bmatrix} -\Gamma_{21} & \Gamma_{32} & 0 & 0 & 0 & -2\Omega_p & 0 & 2\Omega_c \\ 0 & -\Gamma_{32} & 0 & 0 & 0 & 0 & 0 & -2\Omega_c \\ 0 & 0 & \gamma_{12} & 0 & 0 & -\Delta_p & -\Omega_c & 0 \\ 0 & 0 & 0 & \gamma_{13} & 0 & -\Omega_c & -(\Delta_p + \Delta_c) & \Omega_p \\ 0 & 0 & 0 & 0 & \gamma_{23} & 0 & \Omega_p & -\Delta_p \\ -2\Omega_p & -\Omega_p & \Delta_p & \Omega_c & 0 & \gamma_{12} & 0 & 0 \\ 0 & 0 & \Omega_c & \Delta_p + \Delta_c & -\Omega_p & 0 & \gamma_{13} & 0 \\ \Omega_c & -\Omega_c & 0 & -\Omega_p & \Delta_c & 0 & 0 & \gamma_{23} \end{bmatrix} \begin{bmatrix} \rho_{22} \\ \rho_{33} \\ \rho_{12}^r \\ \rho_{13}^r \\ \rho_{23}^r \\ \rho_{12}^i \\ \rho_{13}^i \\ \rho_{23}^i \end{bmatrix} = \begin{bmatrix} 0 \\ 0 \\ 0 \\ 0 \\ 0 \\ -\Omega_p \\ 0 \\ 0 \end{bmatrix}$$

Matrix 2.3: *The system of a three-level cascade-energy scheme.*

The detunings from the atomic transitions have the form:

$$\Delta_c = \omega_c - \omega_{23} - k_c V_z \tag{2.2.35}$$

$$\Delta_p = \omega_p - \omega_{12} - k_p V_z \tag{2.2.36}$$

The dephasing rates are defined in equation 2.2.16.

The system is Doppler broadened and has been analysed using the Mathematica implementation on Power Macintosh, as before. It was modelled using wavenumbers and decay rates appropriate for a coupling field resonant at the $5P_{3/2}$ to $5D_{5/2}$ transition and the probe set at the $5S_{1/2}$ to $5P_{3/2}$ transition in rubidium. The wavelength of the probe field is 780 nm and this of the coupling field is 776 nm. The Rabi angular frequencies of the strong and the weak fields were $\Omega_c = 160$ MHz and $\Omega_p = 1$ MHz, respectively.

Figure 2.2.7 shows the imaginary and the real components of ρ_{12} for coupling field strength 160 MHz, as a function of the probe field detuning. These components correspond to the relative probe absorption and the refractive index variation of the probe field, as in the V-scheme. Coherently induced transparency is clearly seen in figure 2.2.7a and the fast change of the refractive index is shown in figure 2.2.7b, as the probe field is detuned from resonance.

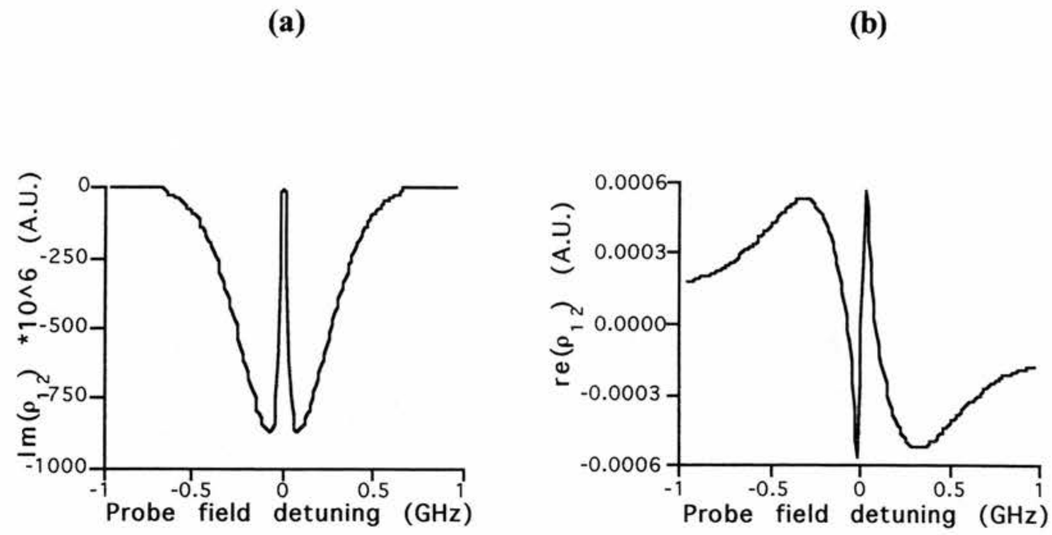

Figure 2.2.7a: *The imaginary part of the coherence* ρ_{12} *which is proportional to the probe field absorption is plotted for a cascade closed system, incorporating the effects of Doppler broadening (T=50° C), with* $\Omega_c = 160$ *MHz and* $\Omega_p = 1$ *MHz. 2.2.7b The real part of* ρ_{12} *which is proportional to the refractive index is plotted.*

The addition of an incoherent source in a cascade system does not show any gain. Modelling of such a system with an incoherent pumping rate R_{12} was followed and no inversionless gain was present. Hence, such systems are only sufficient for the study of coherent phenomena such as EIT.

2.2.3 The lambda scheme (EIT and inversionless gain).

Consider the three-level scheme shown in figure 2.2.8, which is the lambda configuration because of its geometry. The system is again closed with regards to the atomic basis set. The laser field at angular frequency ω_c is the strong coupling field and it is near resonant with the atomic transition ω_{23} and similarly, the weak probe field ω_p is resonant with the ω_{13} transition. The atomic selection rules are such that the dipole allowed transitions are now |1>-|3> and |2>-|3>.

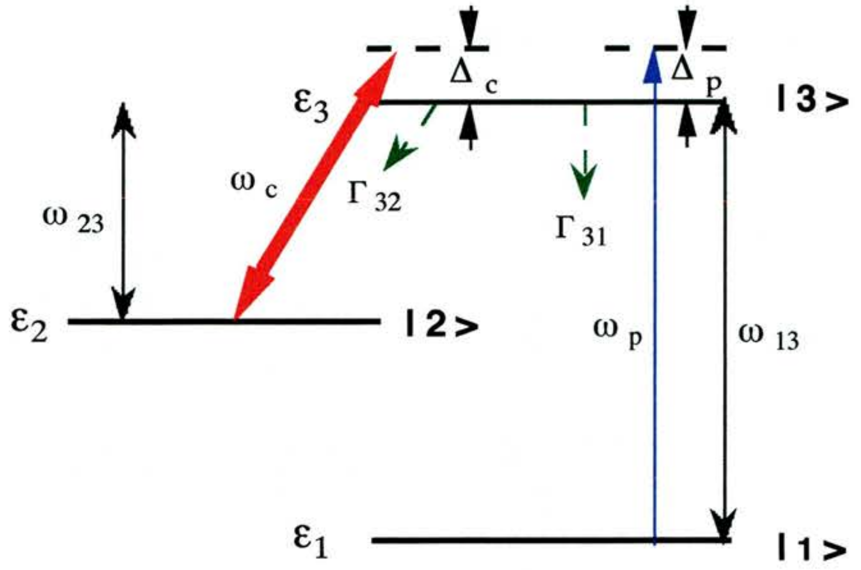

Figure 2.2.8: *Lambda-energy system within a three-level closed atom. The frequency of the weak field is ω_p and of the strong is ω_c. Γ_{31} and Γ_{32} are the decay rates from level 3. Δ_p and Δ_c are the detunings from resonance of the probe and the coupling fields, respectively.*

The interaction Hamiltonian of such system has the form of equation 2.1.8, in which the electric dipole moments take the following values:

$$\mu_{12}=\mu_{21}=0,\ \mu_{13}=\mu_{31}\neq 0,\ \mu_{23}=\mu_{32}\neq 0 \qquad (2.2.37)$$

The two electric fields are again defined as in equation 2.2.2 and the Rabi angular frequencies as in equation 2.2.3 for the coupling laser and 2.2.4 for the probe field.

The optical frequency oscillations of ρ_{ij} elements are varied in a lambda scheme as follows:

$$\rho_{12} = \bar{\rho}_{12}\exp\{i[(\omega_p-\omega_c)t-(k_p-k_c)z]\} \qquad (2.2.38)$$

$$\rho_{13} = \bar{\rho}_{13}\exp[i(\omega_p t-k_p z)] \qquad (2.2.39)$$

$$\rho_{23} = \bar{\rho}_{23}\exp[i(\omega_c t-k_c z)] \qquad (2.2.40)$$

The rates of change of the density matrix elements are derived from the Liouville equation in the same way as with all the calculations of the V and the cascade scheme . The six equations which describe the rate of change of the density matrix elements, for the lambda- energy configuration of figure 2.2.8 have the form:

$$\dot{\rho}_{11} = i\Omega_p(\bar{\rho}_{31}-\bar{\rho}_{13})+\Gamma_{31}\rho_{33} \tag{2.2.41}$$

$$\dot{\rho}_{22} = i\Omega_c(\bar{\rho}_{32}-\bar{\rho}_{23})+\Gamma_{32}\rho_{33} \tag{2.2.42}$$

$$\dot{\rho}_{33} = i\Omega_p(\bar{\rho}_{13}-\bar{\rho}_{31})+i\Omega_c(\bar{\rho}_{23}-\bar{\rho}_{32})-\Gamma_{31}\rho_{33}-\Gamma_{32}\rho_{33} \tag{2.2.43}$$

$$\dot{\bar{\rho}}_{12} = -i\bar{\rho}_{12}(\Delta_p-\Delta_c-i\gamma_{12})+i\Omega_p\bar{\rho}_{32}-i\Omega_c\bar{\rho}_{13} \tag{2.2.44}$$

$$\dot{\bar{\rho}}_{13} = -i\bar{\rho}_{13}(\Delta_p-i\gamma_{13})+i\Omega_p(\rho_{33}-\rho_{11})-i\Omega_c\bar{\rho}_{12} \tag{2.2.45}$$

$$\dot{\bar{\rho}}_{23} = -i\bar{\rho}_{23}(\Delta_c-i\gamma_{23})+i\Omega_c(\rho_{33}-\rho_{22})-i\Omega_c\bar{\rho}_{21} \tag{2.2.46}$$

The same density matrix derivation is employed for the lambda scheme as was previously used for the V and the cascade configuration, resulting in the matrix system represented by Matrix 2.4.

$$\begin{bmatrix} 0 & -\Gamma_{32} & 0 & 0 & 0 & 0 & 0 & -2\Omega_c \\ 0 & (\Gamma_{32}+\Gamma_{31}) & 0 & 0 & 0 & 0 & 2\Omega_p & 2\Omega_c \\ 0 & 0 & \gamma_{12} & 0 & 0 & \Delta_c-\Delta_p & -\Omega_c & -\Omega_p \\ 0 & 0 & 0 & \gamma_{13} & 0 & -\Omega_c & -\Delta_p & 0 \\ 0 & 0 & 0 & 0 & \gamma_{23} & \Omega_p & 0 & -\Delta_c \\ 0 & 0 & \Delta_p-\Delta_c & \Omega_c & -\Omega_p & \gamma_{12} & 0 & 0 \\ -\Omega_p & -2\Omega_p & \Omega_c & \Delta_p & 0 & 0 & \gamma_{13} & 0 \\ \Omega_c & -\Omega_c & \Omega_p & 0 & \Delta_c & 0 & 0 & \gamma_{23} \end{bmatrix} \begin{bmatrix} \rho_{22} \\ \rho_{33} \\ \rho_{12}^{r} \\ \rho_{13}^{r} \\ \rho_{23}^{r} \\ \rho_{12}^{i} \\ \rho_{13}^{i} \\ \rho_{23}^{i} \end{bmatrix} = \begin{bmatrix} 0 \\ 0 \\ 0 \\ 0 \\ 0 \\ 0 \\ -\Omega_p \\ 0 \end{bmatrix}$$

Matrix 2.4: *The system of a three-level lambda-energy scheme.*

The detunings from the atomic transitions have the form:

$$\Delta_c = \omega_c-\omega_{23}-k_c V_z \tag{2.2.47}$$

$$\Delta_p = \omega_p - \omega_{13} - k_p V_z \qquad (2.2.48)$$

The dephasing rates are defined in equation 2.2.16.

The Doppler broadened system is analysed using the Mathematica software. It was modelled using wavenumbers and decay rates appropriate for a coupling field resonant at the $5S_{1/2}$ (F=3) to $5P_{3/2}$ transition and the probe set at the $5S_{1/2}$ (F=2) to $5P_{3/2}$ transition in ^{85}Rb. The wavelength of the probe field and the coupling field is the same 780 nm. The Rabi frequencies (linear) of the strong and the weak fields were $\Omega_c = 160$ MHz and $\Omega_p = 1$ MHz, respectively.

Figure 2.2.9 shows the imaginary and the real components of ρ_{13} for coupling field strength 160 MHz, as a function of the probe field detuning. These components correspond to the relative probe absorption and the refractive index variation of the probe field, as in the V and the cascade-scheme. Coherently induced transparency is clearly seen in figure 2.2.9a and the fast change of the refractive index is shown in figure 2.2.9b, as the probe field is detuned from resonance.

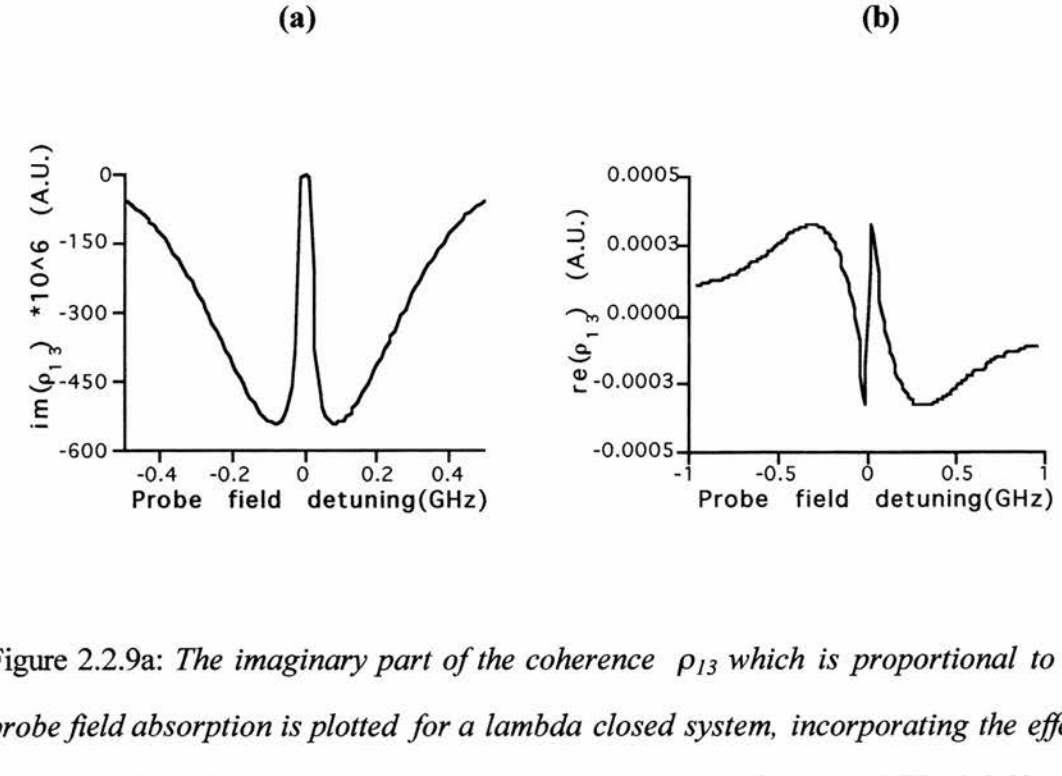

Figure 2.2.9a: *The imaginary part of the coherence* ρ_{13} *which is proportional to the probe field absorption is plotted for a lambda closed system, incorporating the effects of Doppler broadening (T=50° C) with* $\Omega_c = 160$ *MHz and* $\Omega_p = 1$ *MHz.* 2.2.9b: *The real part of* ρ_{13} *which is proportional to the refractive index is plotted.*

Subsequently, the addition of an incoherent pump R_{13} = 30 MHz as in figure 2.2.10 allows the system to exhibit inversionless gain. This system has attracted a lot of interest with regard to atomic coherence effects, since it has an ideal form, where level |2> is assumed metastable and the dephasing rate γ_{12} is approximately equal to zero. The incoherent pump which is resonant with the atomic transition, is included in the density matrix system of Matrix 2.5.

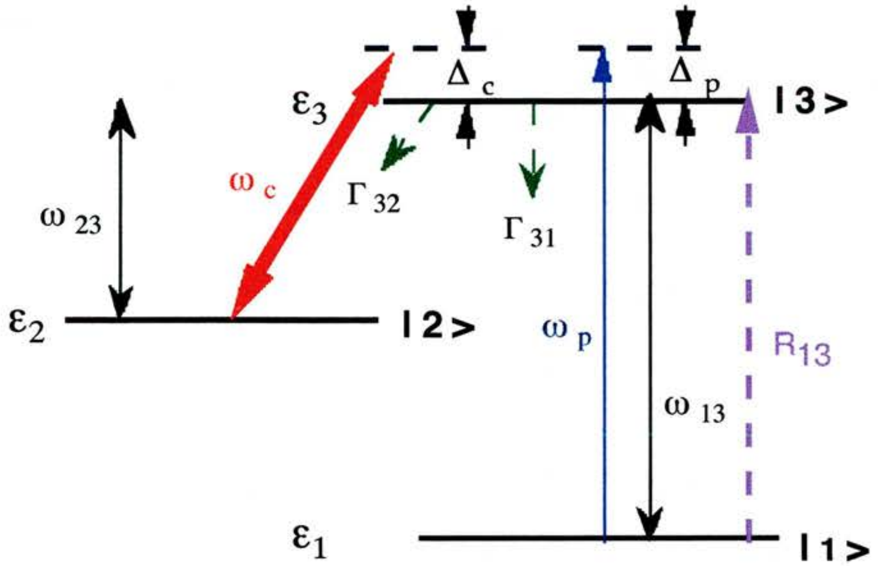

Figure 2.2.10: *Schematic of a closed Lambda-scheme with the addition of an incoherent pump R_{13}.*

$$\begin{bmatrix} 0 & -\Gamma_{32} & 0 & 0 & 0 & 0 & 0 & -2\Omega_c \\ R_{13} & (\Gamma_{32}+\Gamma_{31}+2R_{13}) & 0 & 0 & 0 & 0 & 2\Omega_p & 2\Omega_c \\ 0 & 0 & \gamma_{12} & 0 & 0 & \Delta_c-\Delta_p & -\Omega_c & -\Omega_p \\ 0 & 0 & 0 & \gamma_{13} & 0 & -\Omega_c & -\Delta_p & 0 \\ 0 & 0 & 0 & 0 & \gamma_{23} & \Omega_p & 0 & -\Delta_c \\ 0 & 0 & \Delta_p-\Delta_c & \Omega_c & -\Omega_p & \gamma_{12} & 0 & 0 \\ -\Omega_p & -2\Omega_p & \Omega_c & \Delta_p & 0 & 0 & \gamma_{13} & 0 \\ \Omega_c & -\Omega_c & \Omega_p & 0 & \Delta_c & 0 & 0 & \gamma_{23} \end{bmatrix} \begin{bmatrix} \rho_{22} \\ \rho_{33} \\ \rho_{12}^r \\ \rho_{13}^r \\ \rho_{23}^r \\ \rho_{12}^i \\ \rho_{13}^i \\ \rho_{23}^i \end{bmatrix} = \begin{bmatrix} 0 \\ R_{13} \\ 0 \\ 0 \\ 0 \\ 0 \\ -\Omega_p \\ 0 \end{bmatrix}$$

Matrix 2.5: *The system of a three-level Lambda-energy scheme with the addition of an incoherent pump with a pumping rate* R_{13}.

Gain exactly on resonance in the Lambda-scheme is depicted in figure 2.2.11a. The pump transfers sufficient population for gain which is achieved without population inversion. Most of the population is trapped in level |1>. It is obvious in figure 2.2.11b that population in level |1> is greater than that in level |3>, which is the lasing transition. CW inversionless gain is possible in this 3-level Lambda-energy configuration.

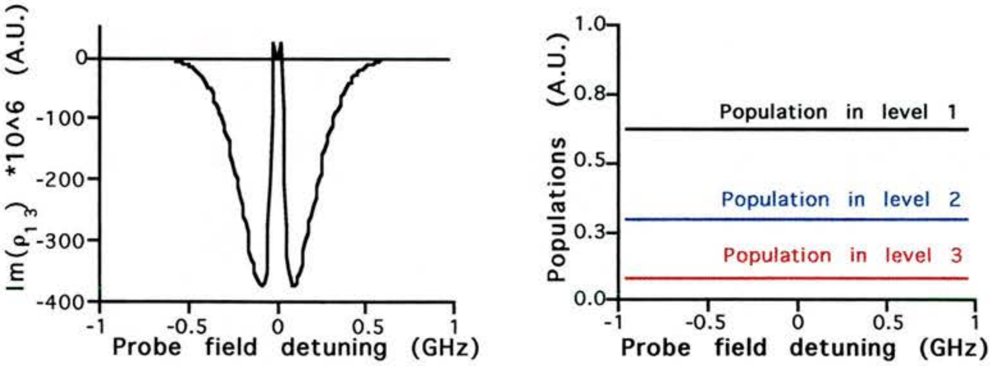

Figure 2.2.11a: *The imaginary part of* ρ_{13} *is plotted against the probe field detuning, when the incoherent pumping rate is* R_{13}= *30 MHz.* 2.2.11b: *The populations are plotted for the Lambda closed system.*

2.3 Derivation of density matrix equations in four level atoms.

The ground state of rubidium atoms has hyperfine structure due to the electronic magnetic field and the magnetic moment associated with the nuclear spin I. Alkalis exhibit fairly strong coupling and the Rb ground state has structure of the order of few GHz. Optical pumping is then unavoidable if we employ a V-scheme within rubidium.

A four-level energy scheme is considered in order to study the optical pumping mechanism, see figure 2.3.1. The coupling field is set near resonant with the $5S_{1/2}$(F=2) to $5P_{3/2}$ in ^{85}Rb. The weak probe is tuned to the transition from $5S_{1/2}$(F=2) to $6P_{3/2}$.

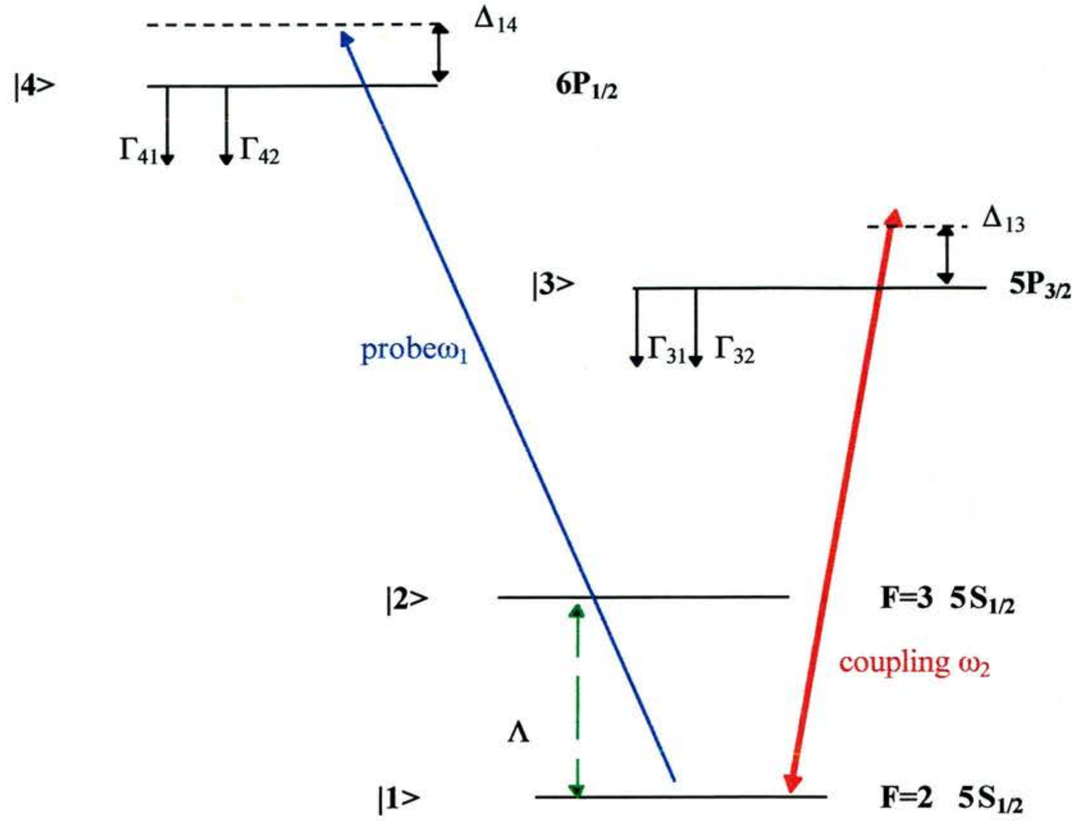

Figure 2.3.1: *Four-level V-scheme in ^{85}Rb with the ground state collisional mixing rate Λ.*

The relaxation rate of the ground state or else the collisional mixing rate is included as an incoherent pump rate Λ between levels |1> and |2>. An estimate for the value of the hyperfine mixing rate was made according to its variation with the average thermal velocity and the atoms density. The ground state collisional mixing rate is defined:

$$\Lambda = \sigma v N \tag{2.3.1}$$

where σ is the cross section of Rb-Rb collisions, v the average thermal velocity and N the atoms density.

The rate may be calculated as follows:

According to *Cohen-Tannoudji and Kastler* the Rb-Rb exchange collisions is determined to be $\sigma = 6\times10^{-17}$ m^2. The average thermal velocity may be expressed as:

$$v = \sqrt{\frac{2k_B T}{m}} \qquad (2.3.2)$$

and operation at temperature T provides a value of the thermal velocity of v. Vapour densities have the form of the empirical relation as it was used in *Mosley's thesis*:

$$N(\mathrm{atoms/m^3}) = \frac{9.66084 \times 10^{24}}{T(K)} \exp[-\frac{9140.07}{T(K)} + 16.0628] \qquad (2.3.3)$$

For the same temperature T the density of atoms is N atoms/m^3. Substituting the above values in equation 2.3.1 the ground state collisional mixing rate Λ can be evaluated for specific circumstances. To illustrate the effectiveness of this mixing process, the situation where Λ=200 MHz is now considered.

For ^{85}Rb the ground states have populations in the ratio ρ_{22}=7/5 ρ_{11} due to the magnetic hyperfine sublevels and this was incorporated into the rate equations. Thus the rate of change of the population in the two ground state levels have incoherent pump terms such that in the absence of any fields:

$d\rho_{11}/dt = -\Lambda(\rho_{11} - 5/7\rho_{22})$ (2.3.4)

$d\rho_{22}/dt = \Lambda(\rho_{11} - 5/7\rho_{22})$ (2.3.5)

The 15×15 density matrix system of the above energy configuration is derived by using Moseley 's rules (see *Moseley PhD thesis*) in matrix 2.1 of the Appendix. The Rabi angular frequencies were set Ω_p=1MHz , Ω_c=1.4 GHz and for the probe field, the coupling fields, respectively. The dephasing and decay rates were considered for ^{85}Rb and the detunings included in Doppler broadening, with the probe and the coupling fields co-propagating.

The real and the imaginary part of ρ_{14} was plotted against the probe detuning in figure 2.3.2. The imaginary component represents the probe field absorption at 422 nm. In figure 2.3.2a transparency is coherently induced on a blue laser field using an infrared coupling source at the other end of the spectrum. This way will let us one day to proceed to a shorter wavelength regime. The fast change in the refractive index, as the absorption changes to EIT, is presented in figure 2.3.2b.

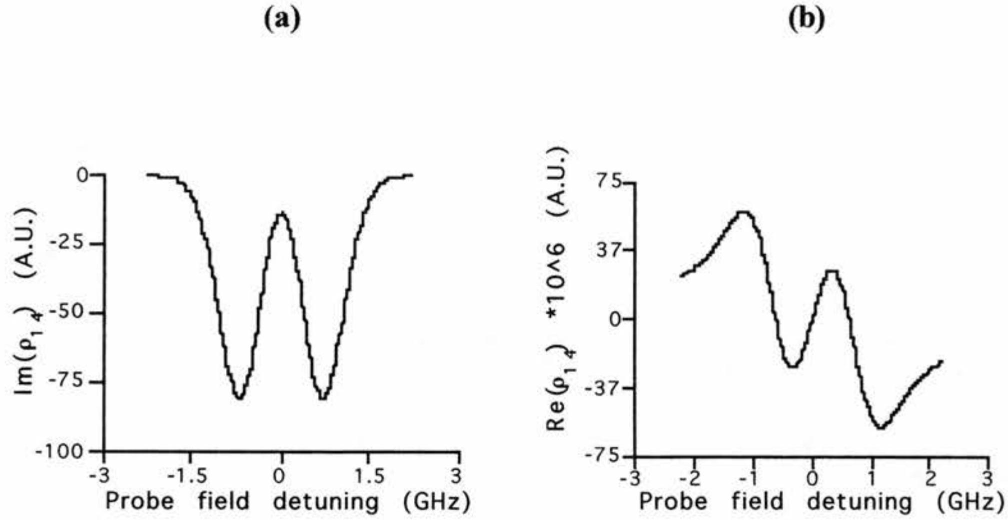

Figure 2.3.2a: *The imaginary part of the coherence* ρ_{14} *while the probe is detuned of resonance is plotted.* 2.3.2b: *The real part of the coherence* ρ_{14} *is plotted against the probe field detuning. The Rabi angular frequencies were* $\Omega_p=1$ *MHz ,* $\Omega_c=1.4$ *GHz for the probe field and the coupling fields, respectively.*

This four-level system exhibits a well-defined EIT feature exactly on resonance, as it is expected with a three-level V-configuration. It is distinguishable from optical pumping and an evidence of this argument is the graph of the populations in figure 2.3.3. There is not any population transfer from one level of the ground state to the other, due to the presence of the strong coupling field. This happens because of the existence of the collisional mixing rate. This rate has a value which redistributes the population in the ground state, setting in this way another equilibrium condition in the system.

The populations of all four levels are then plotted in figure 2.3.3 and the ground state collisional mixing rate can be seen to destroy the optical pumping induced by the strong coupling field. As we can see from the graph, there is no population transfer in level |2>. The population is redistributed between levels |2> and |1> in the ground state, due to the temperature dependent collisional mixing rate of the ground state. The possible role played by the collisional mixing process under real experimental conditions will be further considered in chapter 4.

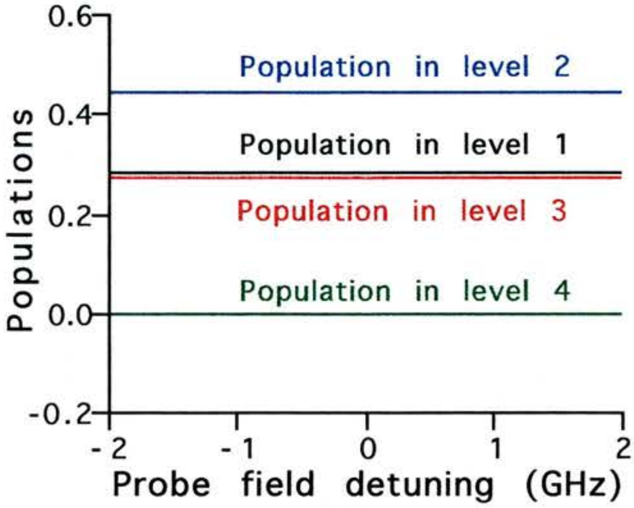

Figure 2.3.3: *The population of the four levels against the probe detuning.*

Subsequently, the addition of an incoherent pump R_{34} = 60 MHz, as in figure 2.3.4 allows the system to exhibit gain. The incoherent pump which is resonant with the atomic transition and it is spectrally broad, is included in the density matrix system of Matrix 2.2 in the Appendix.

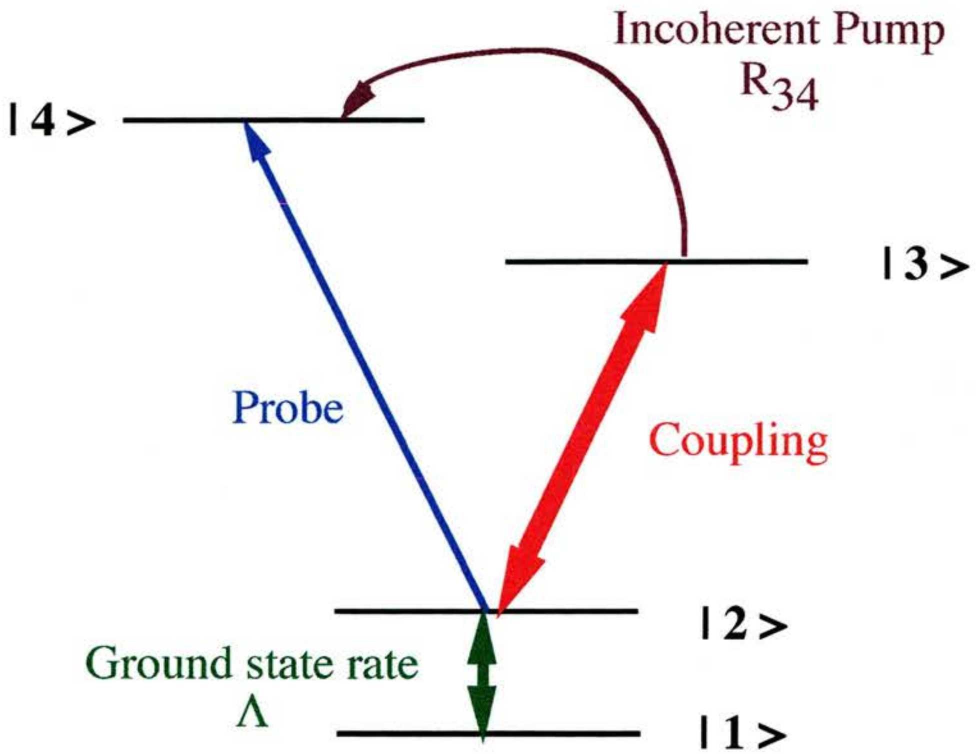

Figure 2.3.4: *Schematic of a closed four-level V -scheme with the addition of an incoherent pump R_{34}.*

The model was run with the same parameters as before, but with the thermal incoherent pumping rate being R_{34} = 60 MHz. Gain exactly on resonance in the V-scheme is shown in figure 2.3.5a. The pump transfers sufficient population for gain which is achieved without population inversion. This system permits the existence of a pump transferring population from another level and not only that of the ground state, saving in this way the population in level |1>. It is shown in figure 2.3.5b that population in level |1> is greater than that in level |4>, which is the lasing transition. The probe transition of 422 nm may be amplified while the population of |1> is sustained greater than that of the upper energy levels |2>, |3> and |4>.

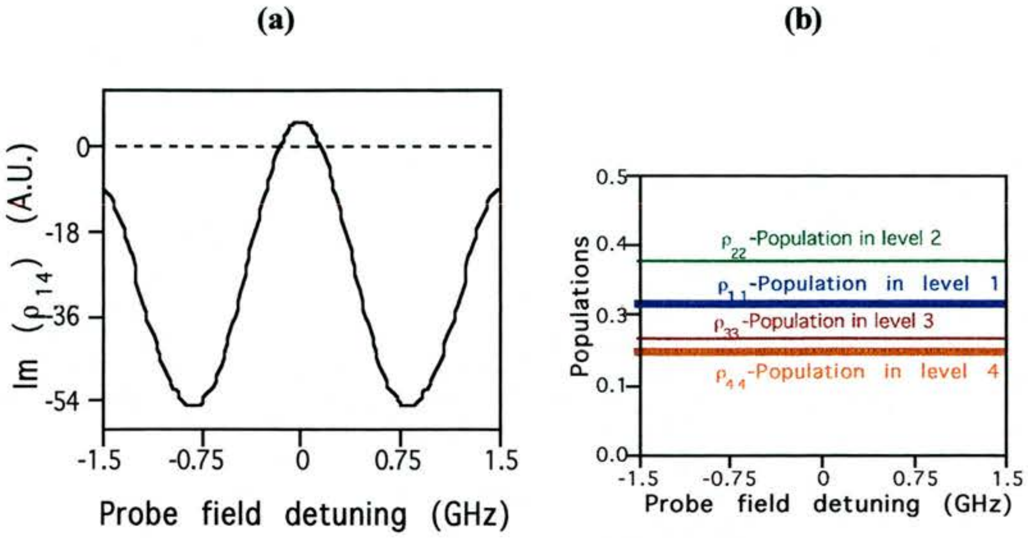

Figure 2.3.5a: *The imaginary part of ρ_{14} is plotted against the probe field detuning, when the incoherent pumping rate is R_{34}=60 MHz.* 2.3.5b: *The populations are plotted for the V closed system.*

2.4 What is coherently induced transparency (or EIT)?

The origin of EIT may be understood in terms of the state amplitude model which describes the evolution of state amplitudes for the case of a single three-level atom. Let's consider an isolated atom which preferentially has three-energy levels and two coherent laser sources are chosen as perturbers at its time independent evolution, as shown in figure 2.4.1 (*Dunn, SUSSP 1996*). It is the simplest cascade configuration where the decay rates (damping) are neglected at the moment. The three levels have energies E_1, E_2 and E_3, and associated eigenfunctions u_1, u_2 and u_3 respectively. The Rabi strength of the radiation fields between the two pair of states are Ω_p for the probe field (between state |1> and |2>) and Ω_c for the coupling field (between state |2> and |3>).

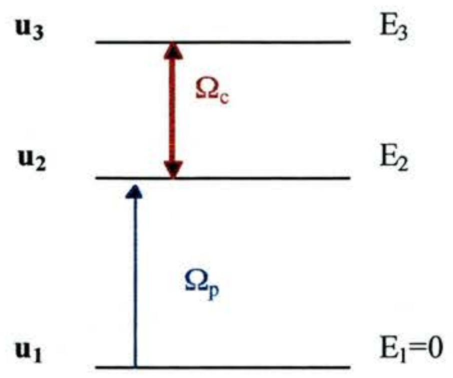

Figure 2.4.1: *A simple three-level isolated atom.*

To anticipate transitions induced the overall wavefunction of the atom is assumed to be:

$$\Psi = a_1(t)u_1 + a_2(t)u_2 \exp(-i\omega_{21}t) + a_3(t)u_3 \exp(-i\omega_{31}t) \tag{2.4.1}$$

where ω_{21} and ω_{31} are the angular frequencies of the resonant transitions and importantly a_1, a_2 and a_3 are allowed to be functions of time. The above wavefunction is tried as the solution of the time-dependent Schrödinger equation:

$$\hat{H}\Psi = i\hbar\frac{\partial\Psi}{\partial t} \tag{2.4.2}$$

where the total Hamiltonian of the system is expressed as :

$$\hat{H} = \hat{H}_0 + exE_p\cos(\omega_p t) + exE_c\cos(\omega_c t) \tag{2.4.3}$$

where ω_p and ω_c are the angular frequencies, E_p and E_c the electric field amplitudes of the probe radiation field and the coupling radiation field, respectively, e is the electronic charge and x the generalised position of the electron in the atom. The Hamiltonian consists of two components, namely that associated with the isolated atom and that describing the additional energy of the atom as a result of the interaction with the two time-varying radiation fields.

The time evolution of the state amplitudes of this model can be found by employing the above procedures:

- The expressions for the Hamiltonian, H, given by equation 2.4.3 and the wavefunction, $\Psi(r,t)$, given by equation 2.4.1, are substituted into the time dependent Schrödinger equation 2.4.2.
- Employing the orthonormality properties of the basis set i.e.

$$\int u_1 u_1^* d\tau = 1, \int u_1 u_2^* d\tau = 0$$

allows the three coupled time-dependent equations for $a_1(t)$, $a_2(t)$ and $a_3(t)$ to be recovered by multiplying the resultant equation by u_1^*, u_2^* and u_3^* respectively and integrating over space.

- For this model *Dunn* invokes the rotating wave approximation which allows the effects of high frequency terms to be neglected. A further assumption is that the two radiation fields are on exact resonance with their associated transitions, i.e. $\omega_p=\omega_{21}$ and $\omega_c= \omega_{32}$. These assumptions provide a simplified form of the equations obtained for $a_1(t)$, $a_2(t)$ and $a_3(t)$ but are adequate for the purpose of examining the fundamental nature or E.I.T.

Hence the three coupled equations obtained by the method outlined above, describing the rate of change of the state amplitudes are given by:

$$\dot{a}_1 = -i\Omega_p a_2 \tag{2.4.4a}$$

$$\dot{a}_2 = -i\Omega_p a_1 - i\Omega_c a_3 \tag{2.4.4b}$$

$$\dot{a}_3 = -i\Omega_c a_2 \tag{2.4.4c}$$

where Ω_p and Ω_c are the probe and the coupling field Rabi frequencies respectively:

$$\Omega_p = \frac{E_p \mu_{21}}{2\hbar} \text{ and } \Omega_c = \frac{E_c \mu_{23}}{2\hbar} \tag{2.4.5}$$

with the dipole matrix elements being real numbers such as:

$$\begin{aligned} \mu_{21} &= \int u_2^*(ex) u_1 d\tau \\ \mu_{23} &= \int u_2^*(ex) u_3 d\tau \end{aligned} \tag{2.4.6}$$

If equation 2.4.4b is differentiated and the rate of changes are substituted from 1.4a and 1.4c, it has then the form :

$$\ddot{a}_2 = -(\Omega_p^2 + \Omega_c^2)a_2 = -\Omega^2 a_2 \qquad (2.4.7)$$

where Ω is the generalised Rabi frequency. Hence, the state amplitude of level 2, a_2 oscillates with angular frequency Ω.

Let's take the general solution $a_2 = A\exp(i\Omega t) + A^* \exp(-i\Omega t)$

If $a_2(t = 0) = A+A^* = 0$,

$$\dot{a}_2(t = 0) = i\Omega(A + A^*) = -i\Omega_p a_1(t = 0) - i\Omega_c a_3(t = 0) \qquad (2.4.8)$$

If $a_1(t=0) = p / \Omega_p$ and $a_3(t=0) = -p / \Omega_c$, then $\dot{a}_2 = 0, A = 0, A^* = 0$.

Hence $a_2 = 0$ for all t, thus no population ever transfers to state E_2 and population is trapped in levels E_1 and E_3. Consequently in such conditions there is a coherent superposition of states E_1 and E_3 or else there is a destructive interference between routes E_1 to E_2 and E_3 to E_2.

Summarising the above, the state amplitudes i.e. a_i, may be written as $a_i= |a_i|\exp(i\phi_i)$, with ϕ_i being the initial phase of the state. If coherent fields with amplitudes in inverse ratio to the state amplitudes (probabilities) are applied, then the evolution of the system is determined by the phase of each state amplitude. Coherently induced transparency is located at the point, where the phase difference of state amplitudes a_1 and a_3 is π, (i.e. they are out of phase). This position ensures that the rate of change of a_2 is zero from equations 2.4.4 and the atom exists in a superposition of states E_1 and E_3. In our system the laser probing the |1> to |2> transition is a weak field and therefore only a small amount of atoms will populate level |2>. This is the reason that this coherent superposition of states is called coherent population trapping.

The present chapter which includes the density matrix analysis and the physical explanation of atomic coherence, is the theoretical basis for all chapters that follow. This analysis is widely used in all schemes applied in both the experiment and in the theoretical comparison for matched and mismatched wavelength configurations.

References

Cohen-Tannoudji M. and Kastler D., Optical pumping, Progress in Optics, Vol V, p.3-81, 1982.

Dunn M.H., Electromagnetically Induced Transparency,47 Scottish University Summer School in Physics, Laser sources and applications, IoP publication, p.411-446, 1996.

Fulton D.J, Quantum Interference Effects: EIT and focusing, Ph.D. thesis, University of St. Andrews, 1996.

Imamoglu A., Field J.E. and Harris S.E., "Lasers without inversion: A closed lifetime broadened system", Physical Review Letters, **66**, p1154 (1994)

Loudon R., The quantum theory of light, Clarendon Press-Oxford, 1st edition, 1973.

Moseley R.R., Sum frequency mixing and quantum interference in 3-level atoms, Ph.D. thesis, University of St.Andrews, 1994.

Chapter 3

Atomic system and experimental equipment

3.1 Atomic system.

3.1.1 Rubidium.

Rubidium is an alkali metal having one unpaired electron in the outermost orbit and therefore can be studied extensively with the theoretical models of the previous chapter. Rubidium ignites spontaneously in air and reacts violently with water, hence its applications are limited. However, it is chosen as a interaction medium because all the wavelengths involved in the most basic configurations of cascade, V and Λ-schemes are in the near-infrared and blue and easily covered by titanium:sapphire laser sources or diode laser technology.

Rubidium has an atomic number 37 and atomic weight 85.4678 a.m.u. Its melting point is 38.89 °C and its boiling point is 686 °C. It has a density at 20 °C of 1.532 g cm^{-3} . Some of the more relevant properties of rubidium are listed in Table 3.1.1, according to *Fulton PhD thesis*.

Rubidium consists of two stable isotopes: ^{85}Rb and ^{87}Rb. The relative abundances are 72.17 % for ^{85}Rb and 27.83 % for ^{87}Rb, with nuclear spins I=5/2 and I=3/2 respectively. The difference in the nuclear spin between the two isotopes leads to different hyperfine constants, and hence to a relatively complex sublevel structure.

Atomic Property	Value
Atomic Number	37
Atomic Weight	85.4678 a.m.u.
Crystal Structure	Body Centred Cubic
Physical Property	Value
Melting Point	38.89 ° C
Boiling Point	686 ° C
Density @ 20 ° C	1.532 g cm^{-3}
Natural Isotope Mass No.	%
85	72.17
87	27.83

Table 3.1.1: *Atomic properties of rubidium*

3.1.2 Spin-Orbit coupling: Fine structure.

Spin-orbit interaction is the largest relativistic effect and is responsible for fine structure. The interaction energy is of the form, *Woodgate* :

$$V = -\mu B_{el} \tag{3.1.1}$$

where B_{el} is the internal magnetic field at an electron whose intrinsic magnetic momentum is μ.

The two angular momenta, orbital **L** and spin **S** are coupled to produce states labelled by **J** and m_j where **J=L+S**. Since spin orbit coupling effects are inversely proportional to the average radial distance of the electron from the nucleus, its effects produce significant fine structure on the P and D states of Rubidium, but become less significant for higher orbital angular momentum. In one electron systems the J=L+S and J=L−S states are separated by ΔE_F , where ΔE_F is related to the fine structure constant A_F , (*Moseley PhD thesis*), by:

$$\Delta E_F = \frac{A_F}{2}(2L+1) \tag{3.1.2}$$

Some of the more relevant fine structure constants for rubidium , *Fulton PhD thesis*, are presented below in Table 3.1.2 along with the corresponding fine level energy separations. Negative values indicate an inversion of the fine states such that the lower valued J = L - S state actually occurs at a higher energy than the J = L + S state.

Level	A_F / GHz	ΔE_F / GHz
5P	4748.8	7123.2
4D	-5.3	-13.2
6P	1549.0	2323.5
5D	35.5	88.7
7P	701.3	1052.0
6D	27.1	67.8
5F	-0.09	-0.3
8P	376.9	565.4
7D	18.1	45.3

Table 3.1.2: *Fine level structure constants for rubidium along with corresponding energy separations.*

The new wavefuctions can be related to the original L, S and m_L ,m_S basis by means of Clebsch-Gordon coefficients or the 3-j symbols which describe the coupling of two angular momenta.

3.1.3 Hyperfine structure.

The interaction of the nuclear magnetic moment with the magnetic field produced by the electrons gives rise to the smallest interaction so far to be considered. This is called hyperfine structure. In general the splittings are very small, especially for levels whose wavefunction has minimal overlap with the nucleus. The ground state exhibits fairly strong coupling.

The coupling **J** to the nuclear spin **I**, leads to a basis described by **F** and m_F , where **F=J+I**. For the S states L=0 and J=1/2, the hyperfine structure can be said to directly replace the fine structure by the substitution of J→F, L→J and S→I.

For J=1/2 states the two hyperfine structure states F=I+1/2 and F=I-1/2 are displaced by ΔE_{HF} which is related to the hyperfine dipole constant A_{HF} by :

$$\Delta E_{HF}(F) = \frac{A_{HF}}{2}[F(F+1) - I(I+1) - J(J+1)] \tag{3.1.3}$$

The J=3/2 states structure depends also on the quadruple hyperfine constant B_{HF} and is described by:

$$\Delta E_{HF}(F) = \frac{A_{HF}}{2}\kappa + \frac{B_{HF}}{2}\,\frac{[\frac{3}{2}\kappa(\kappa+1) - 2I(I+1)J(J+1)]}{I(2I-1)2J(J-1)]} \tag{3.1.4}$$

with κ=F(F+1)–I(I+1)–J(J+1). The hyperfine structures of rubidium 5S and 5P lines for each isotope have been calculated previously by others (see *Moseley thesis*) and those of 6P have been calculated here. Both are tabulated in figure 3.1.1.

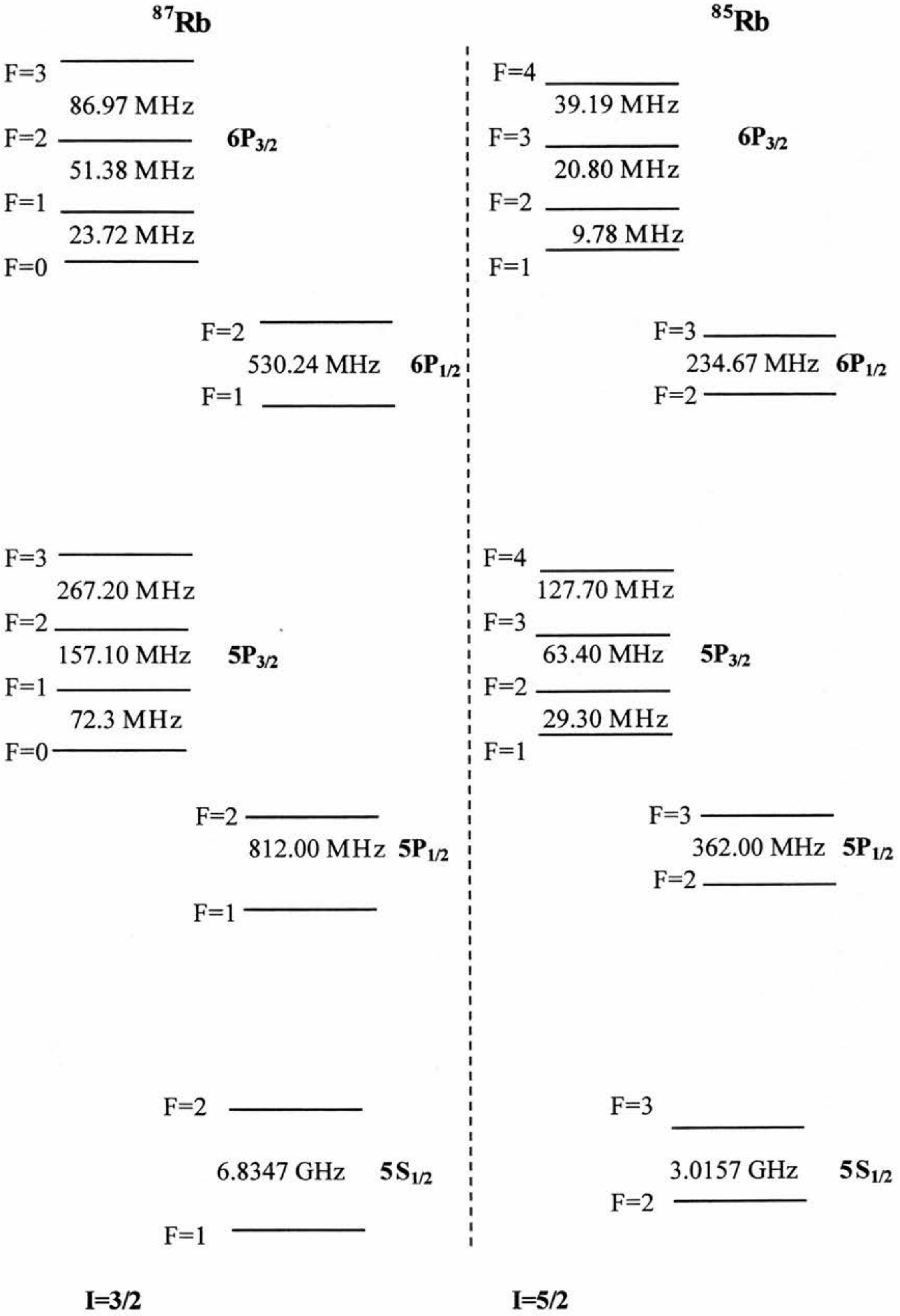

Figure 3.1.1: *The small scale splitting of rubidium atomic levels.*

A review of the measurements of the hyperfine structure of free, naturally occurring, alkali atoms has been carried out by *Arimondo et al.*, in *Fulton thesis*. Some of these values for rubidium have been tabulated below in Table 3.1.3. Negative values of A_{HF} indicate an inversion of the F states such that lower valued F states occur at higher energies than those of the higher valued F states.

Isotope	^{85}Rb		^{87}Rb	
Level	A_{HF} / MHz	B_{HF} / MHz	A_{HF} / MHz	B_{HF} / MHz
$5S_{1/2}$	1011.9		3417.3	
$5P_{1/2}$	120.7		406.2	
$5P_{3/2}$	25.0	25.9	84.8	12.5
$5D_{3/2}$	4.18	<5	14.4	3.5
$5D_{5/2}$	-2.12	No value	-7.4	<5
$6S_{1/2}$	239.3		809.1	
$6P_{1/2}$	39.1		132.6	
$6P_{3/2}$	8.2	8.2	27.7	4.0

Table 3.1.3: *Some hyperfine structure constants for rubidium*

In Figure 3.1.2 a schematic energy level diagram is presented which shows the fine structure of rubidium from the $5S_{1/2}$ ground state up to the $7D_{5/2}$ excited state. The fact that rubidium has an intrinsic nuclear spin results in complex sub-level structure. Since two separate isotopes exist naturally, each having its own values for I, A_{HF} and B_{HF} , the splitting of the sub-level structure differs significantly. Figure 3.1.3 presents a second schematic energy level diagram of rubidium which again shows the $5S_{1/2}$ ground state and the first two excited states, $5P_{1/2}$ and $5P_{3/2}$, but the hyperfine and magnetic hyperfine levels are now included. It is obvious from this second diagram that when the effects of nuclear spin are taken into account the structure of rubidium rapidly becomes much more complex. Likewise, the mathematics to fully describe the atom requires the inclusion of 3j and 6j-symbols.

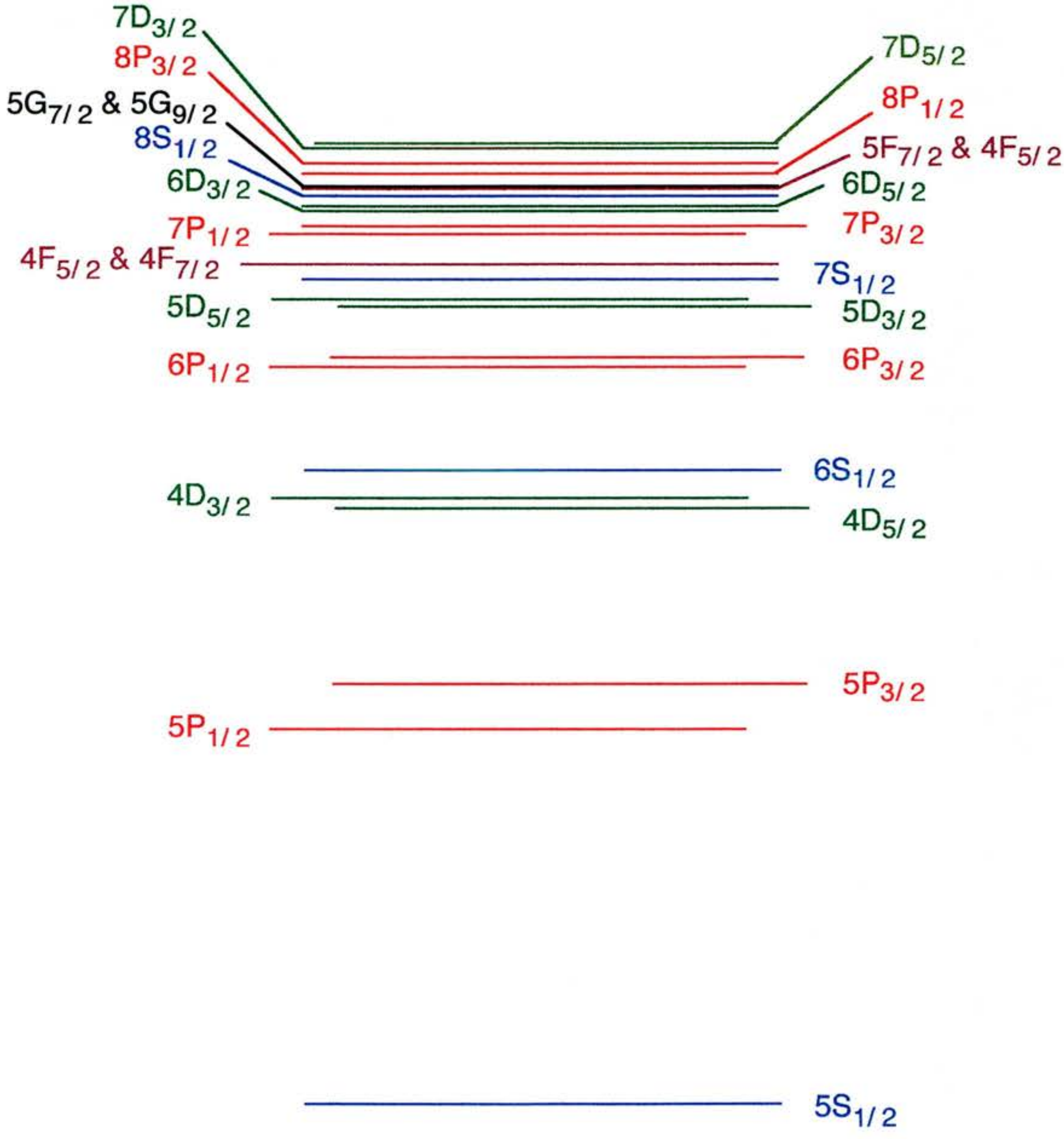

Figure 3.1.2: *Schematic energy level diagram of the fine states within rubidium from the $5S_{1/2}$ ground state to the $7D_{5/2}$ excited state.*

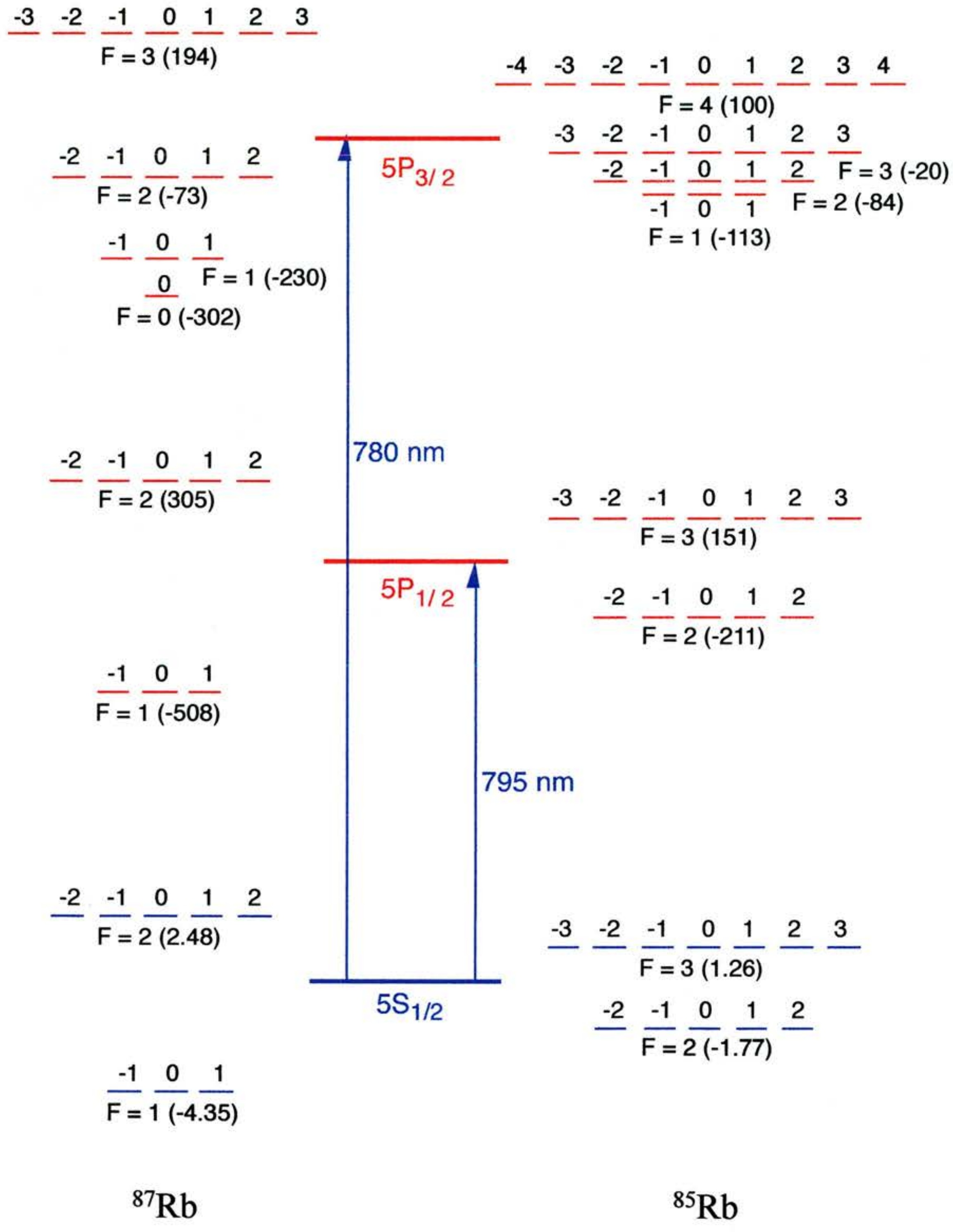

Figure 3.1.3: *Schematic energy level diagram of the hyperfine and magnetic hyperfine states within the* $5S_{1/2}$ *ground state and the first two excited states,* $5P_{1/2}$ *and* $5P_{3/2}$ *, of rubidium. The relevant splittings of the levels from the fine state energy level are also indicated. It should be noted that the unit of splitting in the ground state is GHz whereas it is MHz in the excited states.*

The most common transitions incorporate wavelengths and decay rates are classified in table 3.1.4 (*Lindgard and Nilsen*, with correction for the RI from CRC).

Transition	λ (nm in air)	A_{coeff} (10^8/sec)	ϖ=(2J+1)	Γ_{ij} (MHz)
$5P_{3/2}$-$5S_{1/2}$	780.0262	3.773 x 10(-1)	2	40.0
$5P_{3/2}$-$6S_{1/2}$	1366.2996	1.943 x 10(-1)	2	19.0
$5P_{3/2}$-$7S_{1/2}$	740.8170	6.008 x 10(-2)	2	10.0
$5P_{3/2}$-$8S_{1/2}$	615.9622	2.841 x 10(-2)	2	5.6
$5P_{3/2}$-$9S_{1/2}$	565.3743	1.586 x 10(-2)	2	3.3
$5P_{3/2}$-$10S_{1/2}$	539.0561	9.767 x 10(-3)	2	2.1
$5P_{3/2}$-$4D_{5/2}$	1528.9956	1.176 x 10(-1)	6	11.2
$5P_{3/2}$-$5D_{5/2}$	775.7650	2.288 x 10(-2)	6	3.7
$5P_{3/2}$-$6D_{5/2}$	629.8327	2.546 x 10(-2)	6	3.3
$5P_{3/2}$-$7D_{5/2}$	572.4110	1.816 x 10(-2)	6	2.6
$5P_{3/2}$-$8D_{5/2}$	543.1528	1.237 x 10(-2)	6	1.9
$6P_{3/2}$-$5S_{1/2}$	420.1792	3.346 x 10(-2)	2	8.0

Transition	λ (nm in air)	A_{coeff} (10^8/sec)	ϖ (2J+1)	Γ_{ij} (MHz)
$5P_{1/2}$-$5S_{1/2}$	794.7598	3.773 x 10(-1)	2	40.0
$5P_{1/2}$-$6S_{1/2}$	1323.3273	1.943 x 10(-1)	2	19.0
$5P_{1/2}$-$7S_{1/2}$	727.9993	6.008 x 10(-2)	2	10.0
$5P_{1/2}$-$8S_{1/2}$	607.0750	2.841 x 10(-2)	2	5.6
$5P_{1/2}$-$9S_{1/2}$	557.8780	1.586 x 10(-2)	2	3.3
$5P_{1/2}$-$10S_{1/2}$	532.2373	9.767 x 10(-3)	2	2.1
$5P_{1/2}$-$4D_{3/2}$	1475.2861	1.176 x 10(-1)	4	11.2
$5P_{1/2}$-$5D_{3/2}$	761.8927	2.288 x 10(-2)	4	3.7
$5P_{1/2}$-$6D_{3/2}$	620.6309	2.546 x 10(-2)	4	3.3
$5P_{1/2}$-$7D_{3/2}$	564.7764	1.816 x 10(-2)	4	2.6
$5P_{1/2}$-$8D_{3/2}$	536.2596	1.237 x 10(-2)	4	1.9
$5P_{1/2}$-$5S_{1/2}$	421.5523	3.346 x 10(-2)	2	8.0

Table 3.1.4: *Most of the transitions within rubidium, λ is the wavelength in air, A_{coeff} the Einstein coefficient, ϖ the degeneracy and Γ_{ij} the decay rate of the population.*

3.1.4 Optical pumping.

Rubidium has hyperfine structure in its ground state. In a V-energy scheme experiment the probe and the coupling fields co-propagate and are resonant with the ground state. The existence of the strong optical fields leads to optical pumping and all the population will eventually decay to the second level. The optical pumping mechanism is shown in figure 3.1.4.

Atomic selection rules for allowed electric dipole transitions are that $\Delta F=0,\pm1$ for both excitation and decay (*Fulton , Shepherd et al.*). Thus, with an initial ground state level with hyperfine quantum number F, optical pumping into the F-1 ground state occurs if level |3> has hyperfine quantum number F or F-1, as in figure 3.1.4. The contribution of this mechanism acts to increase the transmission of the probe field and as a result E.I.T. is indistinguishable from the optical pumping.

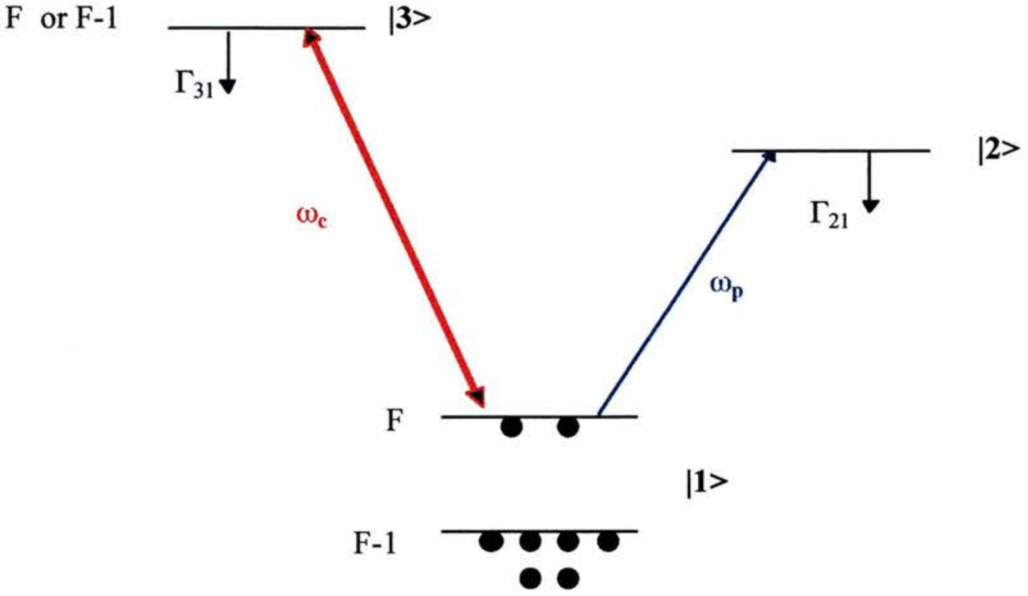

Figure 3.1.4: *The optical pumping mechanism which occurs in the ground state populates one of the fine levels increasing the transmission of the probe field.*

3.2 Laser sources.

The optical fields mainly used for the electric dipole transitions within rubidium are coherent tuneable laser sources in the visible and the near-infrared. Steady state solutions require operation in the continuous wave mode.

3.2.1 Pump Lasers.

The primary source of power for the lasers in this work were continuous-wave, mainframe argon-ion lasers. The first, a Spectra-Physics 2030 laser, was employed to pump either a Spectra-Physics 380D dye laser or a Schwartz Ti:sapphire laser. The 2030 argon-ion laser can produce up to 20 W of power, when operating on all lines, or 8.5 W on single line operation at 514.5 nm. It was usual to run the laser multiline, so producing 10 W of TEM $_{00}$ output power, for pumping either of the above mentioned lasers. The second pump laser source was a Spectra-Physics 2080 argon-ion laser with BeamLok^{TM}, which was used to pump a Microlase MBR-110 Ti:Sapphire laser. This laser can also produce up to 20 W of power, when operating on all lines, or 9 W on single line operation at 514.5 nm. Usually it was run multiline, with 7 W of TEM $_{00}$ output power produced for pumping the Microlase Ti:Sapphire. It was found that it was important to ensure that the mode of the pump lasers were as close to TEM $_{00}$ as possible, to allow optimum mode matching between the pump and the circulating laser beams.

3.2.2 Schwartz Ti:Sapphire laser (700-1000 nm).

The strong coupling laser is a tuneable Ti:Sapphire laser. It is applied in atomic coherence experiments in the wavelength range of 700-1000 nm. The ring cavity Schwartz Electro Optic Titan-CW is depicted in figure 3.2.1 and it is described in detail in the *Shepherd thesis.*

A Spectra Physics 2030 argon ion laser which produces power up to 20 W is employed as a pump for this Ti:Sapphire . Usually, it is run at 10 W and it provides a TEM_{oo} vertically polarised pump beam. The vertically polarised light is rotated by a half-waveplate to give the optimum horizontal polarisation required to pump the crystal. The pump beam is focused by a lens onto the rod which is cut in the horizontal plane at Brewster's angle.

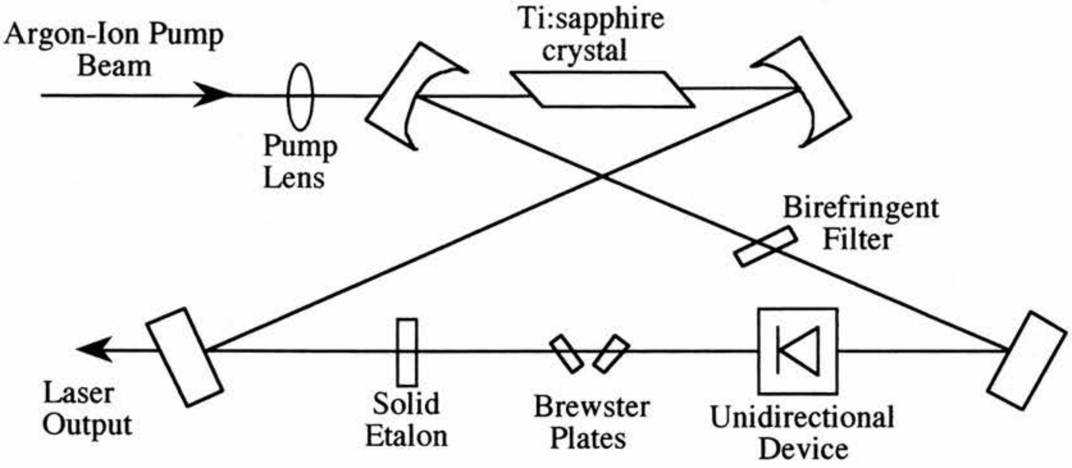

Figure 3.2.1: *Schematic of the modified Schwartz Ti:sapphire laser.*

The two curved mirrors with 100 mm radius of curvature, the flat reflector and the flat output coupler are in three sets. They are coated for three operational frequency ranges of 700-800 nm, 800-900 nm and 900-1000 nm.

The main tuning element in the cavity is the birefringent filter and it narrows the spectral output to just a few cavity modes. The linewidth is then further reduced by the insertion of a thin etalon (1 mm) with a FSR=115 GHz which is coated with a finesse 1.76. This allows the laser to hold in a single longitudinal mode. The free running linewidth was measured to be<5MHz (*Moseley*) over short periods as long as the laser was insulated from acoustic noise.

The direction of lasing is set by the optical diode (unidirectional device). This consists of a waveplate and a Faraday rotator. The two tuning plates are able to scan the laser frequency over a range of few tens of GHz while keeping the output as a single stabilised longitudinal mode. When it is pumped with 10 W power by argon-ion laser, the Schwartz Ti:sapphire supplies up to 1 W output power in a fairly stable single longitudinal TEM_{00} in the near-infrared. The laser is not stabilised and it sometimes mode hopes when its power is not high enough.

3.2.3 Microlase Ti:Sapphire laser (~780 nm).

A Microlase MBR-110 Ti:Sapphire is utilised to provide the weak probe beam. This laser is pumped by a Spectra Physics 2080 with a BeamLok™ argon-ion laser. The argon-ion laser can also produce power up to 20 W, but it is run multiline with 7W power of TEM_{00} at 514.5 nm for the present purpose.

The bow tie configuration is employed for the Ti:sapphire laser cavity, as shown schematically in figure 3.2.2. The Microlase laser uses a stabilised, single mode scanning system which scans up to 40 GHz . It incorporates frequency stabilisation via side of fringe locking on an external temperature-controlled confocal etalon. With this locking active, linewidths of ≤200kHz are specified. Furthermore, microprocessor controlled scans of the laser may be initiated by the control unit and mode-hop free operation is attained by the servo-lock of the single solid etalon in the cavity.

When the Ti:Sapphire laser is pumped with 7W of power it produces output powers of approximately 500 mW. When it is desirable to lock on a single frequency and scan over 10 GHz the optimum power is then < 300 mW.

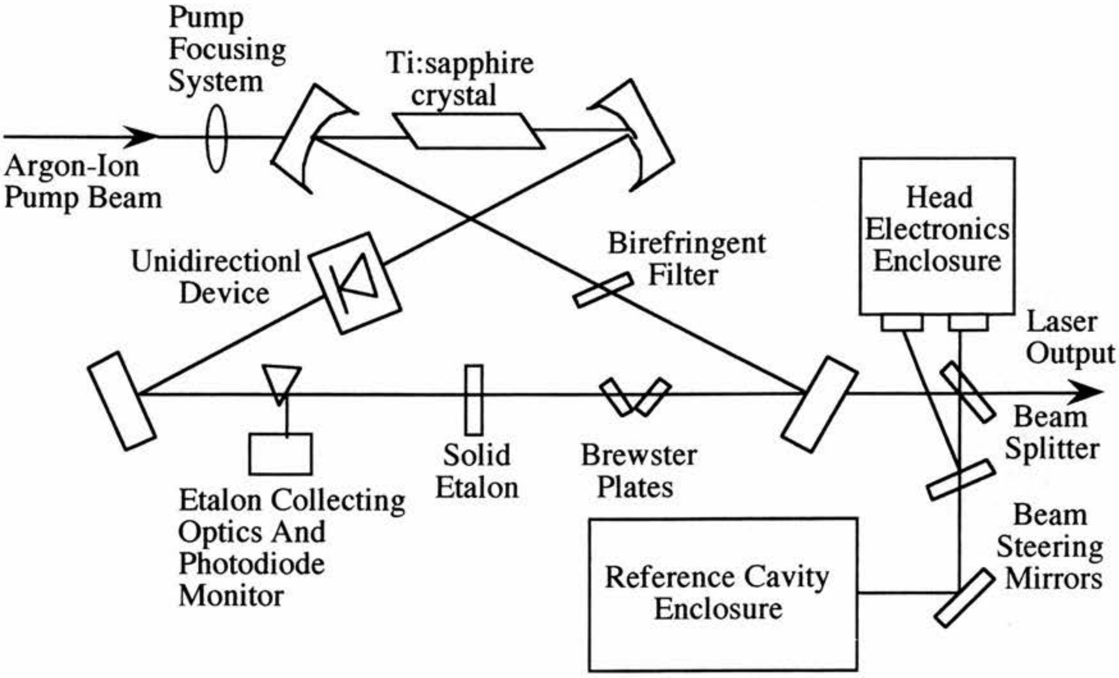

Figure 3.2.2: *Schematic of the Microlase Ti:sapphire laser.*

3.2.4 Ring Dye laser (~589 nm).

The Schwartz Ti:Sapphire was replaced occasionally by a Spectra Physics 380 D dye laser with a wavelength range in the visible spectral region, dependent on the dye which was used. The cavity design was also a bowtie configuration, with a unidirectional device and an air-spaced etalon to ensure single frequency operation, as illustrated in figure 3.2.3.

The laser is a CW, frequency stabilised single mode scanning system with a linewidth of approximately 1 MHz and could scan up to 30 GHz. Rhodamine 6G was dissolved in ethylene glycol to provide the lasing medium and typically had an operating lifetime around 6 weeks. With a 7 W all lines argon-ion laser as the pump source the dye laser produced up to 250 mW at 589 nm and constituted a reliable source.

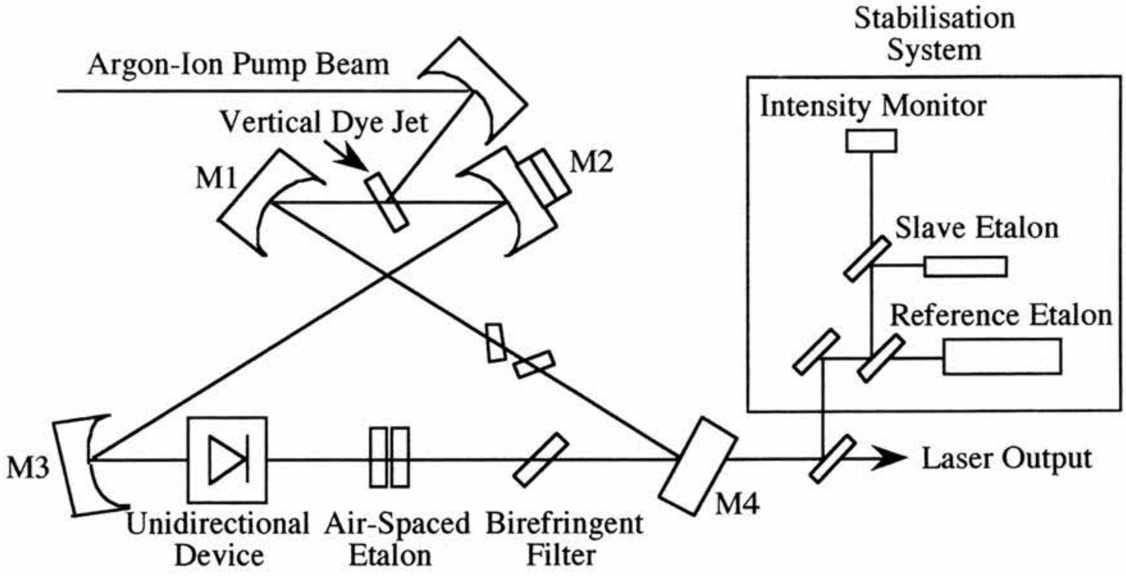

Figure 3.2.3: *Schematic of the dye laser.*

3.2.5 Spectra Physics 3900 Ti:Sapphire laser (700-1000 nm).

Another tuneable source over a broad range of near infrared wavelengths is provided by a Ti:sapphire laser with a standing-wave cavity. The Z-shaped linear cavity is shown in figure 3.2.4. Some of the key features of this system are the 4-mirror folded cavity, astigmatic pumping design, birefringent filter, dual optics set and argon-ion pumping requirements (Instruction Manual Model 3900). Two sets of mirrors allow the laser to be operated over wavelengths from 700 to 850 nm or 850 to 1000 nm.

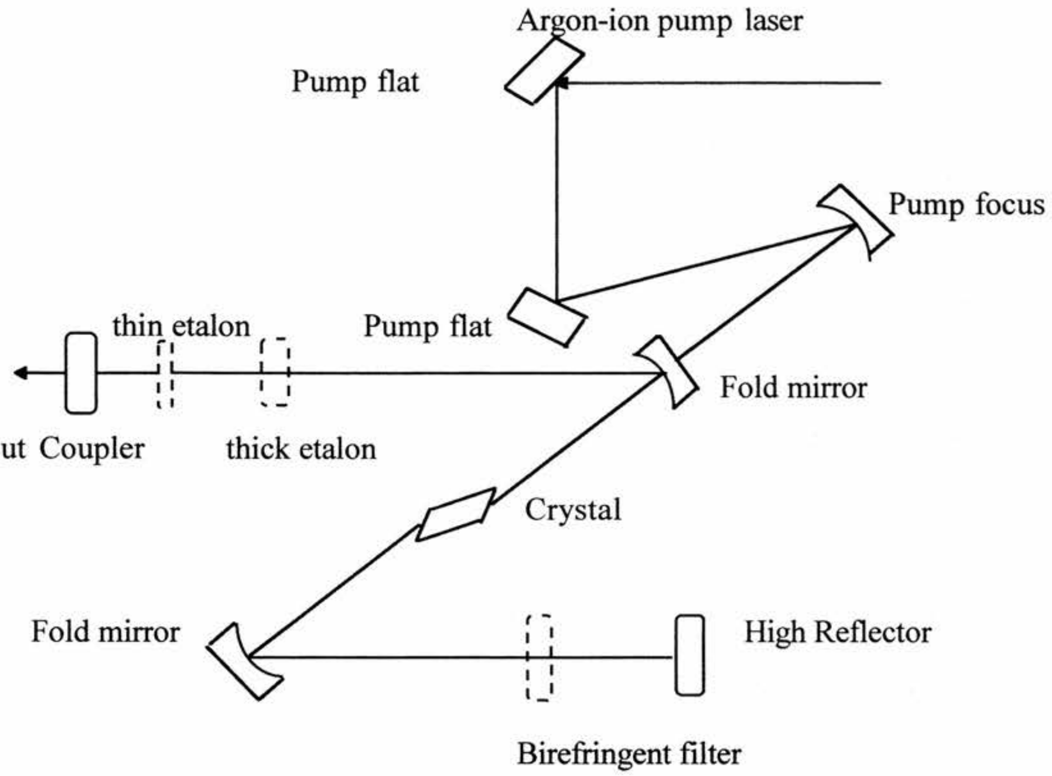

Figure 3.2.4: *Schematic of the modified Spectra Physics 3900 Ti:sapphire laser.*

A 50% beam splitter was used to direct the beam of the Spectra 2030 argon-ion laser into both the Microlase and the 3900 Ti:Sapphire lasers. The pump argon-ion laser power was usually set at 14 W (horizontally polarised) in order to provide 7W of power to each Ti:Sapphire.

The 3900 model incorporated a polarisation rotator, but this was replaced by a plane mirror (pump flat), because the argon-ion laser beam was already horizontally polarised. The use of a concave pump focusing mirror at an angle away from normal incidence allows astigmatism to be induced in the pump beam that most efficiently matches the astigmatism of the cavity mode. The Z-shaped linear cavity is asymmetric.

The crystal is cut at Brewster's angle and placed in the middle of the two fold concave mirrors with radius of curvature of 100 mm. The birefringent filter consists of three crystalline plates, placed within the laser cavity at Brewster's angle. It has a

FSR greater than 150 nm, and thus resulted in a linewidth of 30 GHz across this tuning range.

The linewidth could be typically reduced to 1.5 GHz by the insertion of a combination of thin and thick solid etalons. The thin etalon has a free spectral range FSR=115 GHz and it is uncoated with a reflectivity of R=0.04. Its finesse is given by: $F = \frac{\pi\sqrt{R}}{1-R}$ (*Yariv*) and its value is F=0.655. The thick etalon is 10 mm thick and its free spectral range is hence FSR=15 GHz. Its finesse is unknown. This combination resulted in three modes operating within 1.5 GHz, equal in amplitude and spaced by the FSR of the laser which is 265 GHz.

3.3 Second Harmonic Generation. The production of blue light.

The blue probe field for one of our experiments was obtained by the use of non-linear optics, *Boon* thesis. A non-linear crystal, potassium niobate is employed to double the frequency of a Ti:Sapphire laser. Potassium niobate was chosen for this purpose, because of its favourable non-linear coefficient and temperature-tuned phase matching. It has a low optical damage threshold but this is not an important requirement, since probe laser power requirements are low.

Potassium niobate can be temperature tuned which allows a single crystal to be manipulated to access a range of wavelengths. The transition we wished to probe in rubidium is $5S_{1/2}$ - $6P_{1/2}$ and has a wavelength of 421.5550 nm. This requires a fundamental wavelength of approximately 823 nm, which is outside the room temperature range of potassium niobate. We must therefore rely on temperature tuning to provide the required phase matching. The appropriate temperature that is required for the above wavelength is approximately -15° C and this was achieved with a thermoelectric cooler (TEC) mounted in a specially designed oven.

A TEC is advantageous in this application since it provides localised cooling, precision temperature control and comes in a small package. Our system uses a Marlow DT12-4 TEC. Figure 3.3.1 shows the cooling mount to stabilise the crystal at

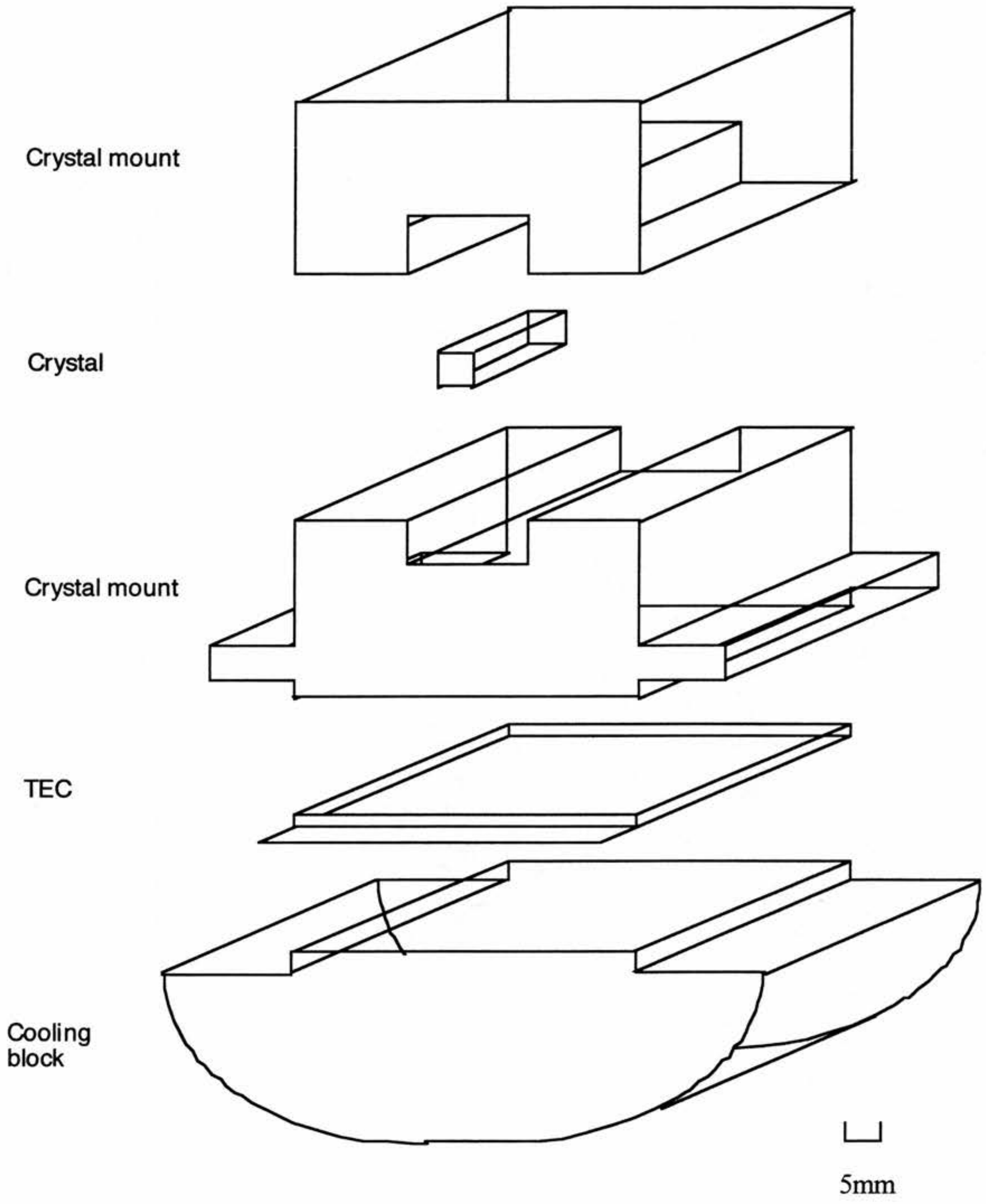

Figure 3.3.1.: *Cooling mount designed to stabilise potassium niobate crystal at approximately -15 ° C.*

approximately -15° C. The method chosen to remove heat from the hot side of the TEC was water cooling. The drive current for the TEC is controlled by a Newport Model 325 Temperature Controller, which allows the temperature to be stabilised at a specified value to an accuracy of 0.01° C.

With the potassium niobate crystal cooled to -15° C condensation will form on the crystal and the mount. It was therefore decided to seal the crystal inside a perspex box. The box has pipes for water cooling passing through one wall via rubber grommets and the integrity of these seals was improved with the liberal application of vacuum grease. The same approach was employed to pass electrical connections into the box. The lid of the box is securely fastened against a rubber seal (also greased) and can be removed to allow angular and rotational adjustments of the crystal at room temperature.

A pipe connected to a bottle of oxygen-free nitrogen was also fed into the box with an adjustable escape valve placed in the opposite wall. The box was designed so that the crystal would be at the correct height for the light from the Ti:sapphire laser to pass through it. Quartz windows allowed the light to pass in and out of the box. These windows were sealed in with rubber o-rings for a good seal and it was found in practice that the seal in the box was not sufficient to prevent condensation without the addition of nitrogen to the system. The nitrogen fills the box, maintaining a steady flow and therefore a slight positive pressure that prevents air and hence water vapour from re-entering the box.

3.4 Other experimental apparatus.

3.4.1 Laser diagnostics.

Single frequency operation of the lasers was monitored using separate piezo-tuned confocal Fabry-Perot interferometers of FSR=1.5 GHz. A low finesse etalon of FSR=300 MHz was used to monitor the scanning of the Microlase Ti:Sapphire, as a marker for the EIT scans.

In order to measure and set the absolute frequency of the lasers a Kowalski-style travelling wavemeter was employed, capable of 1 part in 10^6 accuracy. The accuracy was sufficient to set the lasers to within an etalon mode of the relevant atomic transition, typically within a few GHz. This wavemeter incorporated a double Michelson interferometer arrangement with a scanning arm. Fringe counting compared the wavelength of the incident light with that of the light from a temperature stabilised

He-Ne laser, operating on the 633 nm transition. (The wavelength of the He-Ne laser is used as a standard since it is known to better than 1 part in 10^6). The operating wavelength range was very wide due to the use of aluminium coated optics. A full description is given by *Kane*.

The rubidium vapour was contained in quartz cells, obtained from Opthos Instruments, with lengths 10 cm, 4 cm and 2 cm, and a diameter of 2.5 cm. The cell was evacuated to 10^{-6} torr, filled with Rb vapour and sealed. Care is taken due to the explosive nature of rubidium in air. The cell was heated by passing a current from the mains supply via a Variac transformer, through heating tape woven into a glass jacket that is secured around the length of the cell. The temperature of the cell controls the particle density of the vapour. Calculations of vapour particle density are based on the empirical relation of Miles and Harris, valid for vapour pressures around 1 torr.

$$\mathrm{N} = \frac{9.66084 \times 10^{24}}{\mathrm{T}} \exp\left[-\frac{a}{\mathrm{T}} + d\right] \tag{3.4.1}$$

where N is in units of atoms/m^3 and the constants a and d are the vapour pressure constants for rubidium, 9140.07 and 16.0628 respectively.

3.4.2 Signal detection and collection.

A schematic representation which shows the basic configuration for an EIT V-scheme experiment is depicted in figure 3.4.1. Modifications to the direction of propagation of the optical fields were applied by changing the position of the beam steering mirrors, to suit the different energy schemes investigated within Rb.

The probe absorption was recorded on a 486 PC (Elonex PC-433), usually via phase sensitive detection methods. A filtered photodiode was used to detect the selected weak probe absorption, whereas a filtered photomultiplier was used for fluorescence detection. A few hundred Hz frequency chopper and a phase sensitive detector improved considerably the signal to noise ratio of the signals. Neutral density

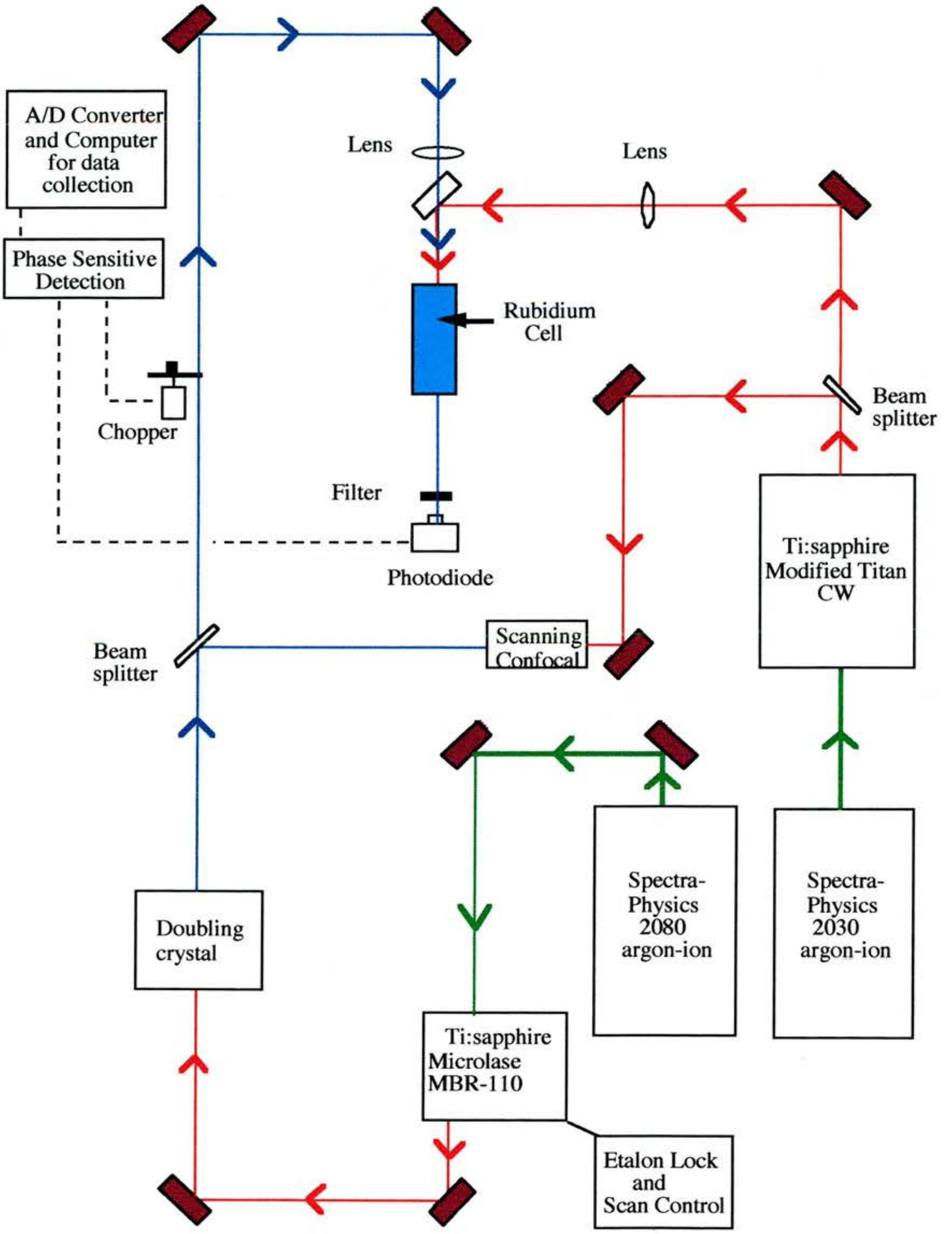

Figure 3.4.1: *Schematic of apparatus for a V- type atomic coherent experiment.*

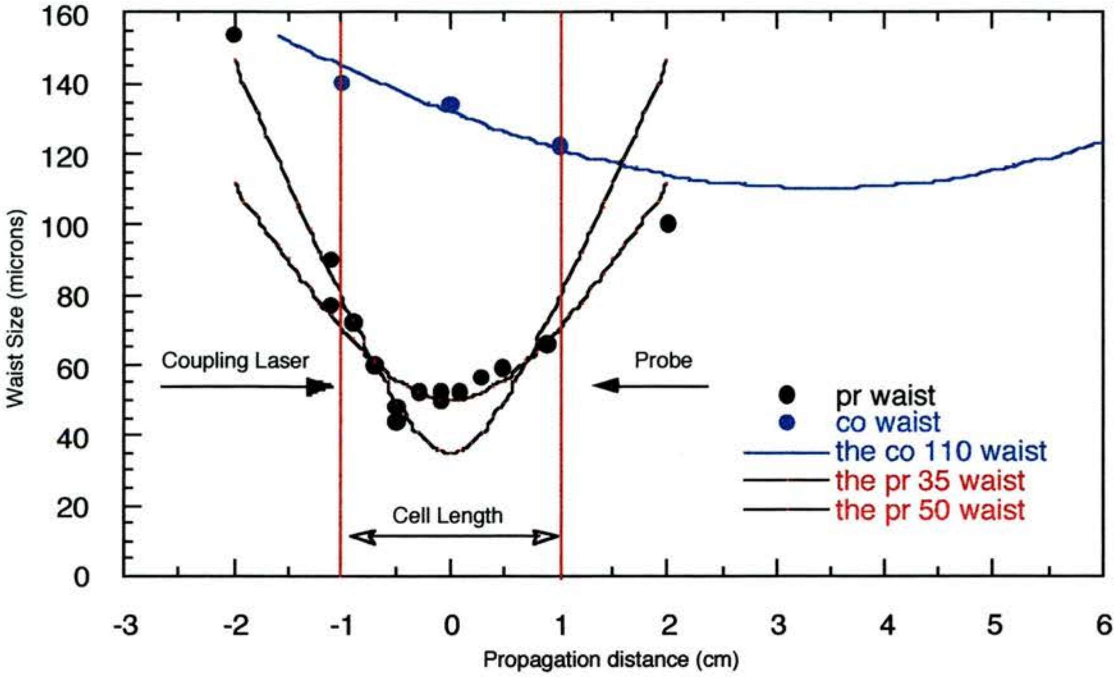

Figure 3.4.2: *Waist sizes of the probe and the coupling fields inside the cell.*

filters or graduated wheels allowed control of the input optical fields powers, in order to avoid signal saturation.

Data collection was achieved via a 12-bit 16-channel A to D board (Amplicon Linelive PC30AT) fitted to the computer. This board provided the required analogue to digital conversion required for the data. A multichannel connection box was constructed to feed the individual channels to standard BNC connectors. Amplicon Dash-300 software allowed the storage of the data.

In experiments in which more than one laser beam propagates through the cell simultaneously it is important to utilise the appropriate focusing optics. Lenses are chosen as to the requirements of the experiment. Figure 3.4.2 shows beam waist measurements of the probe and coupling laser in a standard EIT type experiment. The measurements were taken with a beam profiler. The important aspect in this example is that the probe laser beam lies within the width of the coupling laser beam, as the beams propagate through the 2 cm long vapour region in the cell. This set up was achieved using a 20 cm lens to focus the probe and a 40 cm lens to focus the coupling beam. In figure 3.4.2 it is seen that the probe beam was slightly astigmatic, the waist measured being 35 μm in one dimension and 50 μm in the orthogonal dimension. The coupling field waist was 110 μm, with no discernible astigmatism.

3.4.3 Incoherent pump source.

In certain studies, an incoherent pump was required to transfer a small fractional population to the upper state, without affecting the coherence of the system. It was generated by passing the output of the Ti:sapphire laser through an acousto-optic (AO) modulator, which was driven by a noise generator.

The light angular frequency (ω_i) is diffracted (Bragg diffraction) by acoustic waves with angular frequency (ω_{ac}) at frequency $\omega_i+\omega_{ac}$ or $\omega_i-\omega_{ac}$, depending on the direction of the Doppler shift, as in figure 3.4.3. The material of the AO deflector is tellurium dioxide (TeO_2), with a spectral range 633 nm-850 nm. It may be operated in the range of 70 MHz-110 MHz. The acoustic velocity in the material is 0.617 mm/μs and its refractive index is 2.35.

For several materials the transferred power in a distance l into the diffracted beam is given by:

$$\frac{I_{\text{diffracted}}}{I_{\text{incident}}} = \sin^2\left(1.4\frac{0.6328}{\lambda(\mu\text{m})}l\sqrt{M_\omega I_{\text{acoustic}}}\right)$$

where $M_\omega = M_{\text{material}} / M_{H_2O}$ is the diffraction figure of merit of the material ($M_{TeO_2} = 5$) .

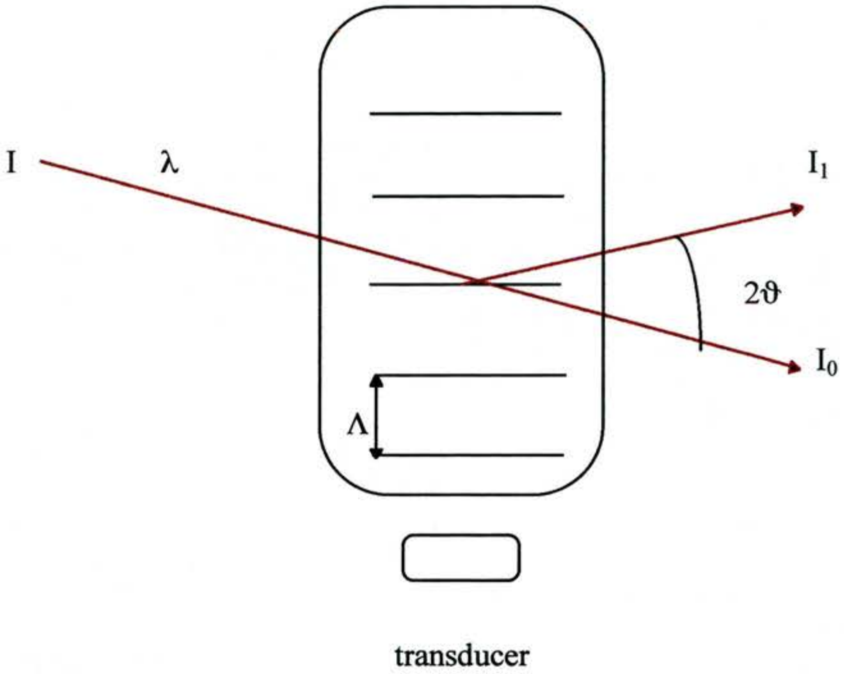

$$2\vartheta = \frac{\lambda}{\Lambda}$$

Figure 3.4.3: *Bragg diffraction using an acousto-optic modulator. Here λ and Λ are the wavelength of the incident radiation and the acoustic wave, respectively. The Bragg angle is denoted by ϑ.*

The transducer attached to the AO is driven by a voltage controlled oscillator (VCO) and an RF amplifier. The VCO has frequency and power modulation. The FM input of the device may be connected to a noise generator and hence broadens the linewidth of the acoustic wave by up to 40 MHz. The noise generator is a Schottky diode which provides noise in the range 0.1-500 MHz. Filters, either passband or a combination of low-band-pass and high-band-pass are useful for the selection of the 40 MHz bandwidth of noise.

3.5 The derivation of the Rabi frequency and the incoherent pump rate.

In a degenerate two-level system as in figure 3.5.1 each pair of the sublevels (with quantum numbers M_a for the lower level and M_b for the upper level), are linked with selection rules. They have a distinct Rabi frequency. Thus, there is no single Rabi frequency appropriate to a two-level transition. It is sometimes useful to define a root-mean-square (r.m.s.) Rabi frequency $\tilde{\Omega}_{ab}$ (*Shore*) for such a degenerate transition by the rule:

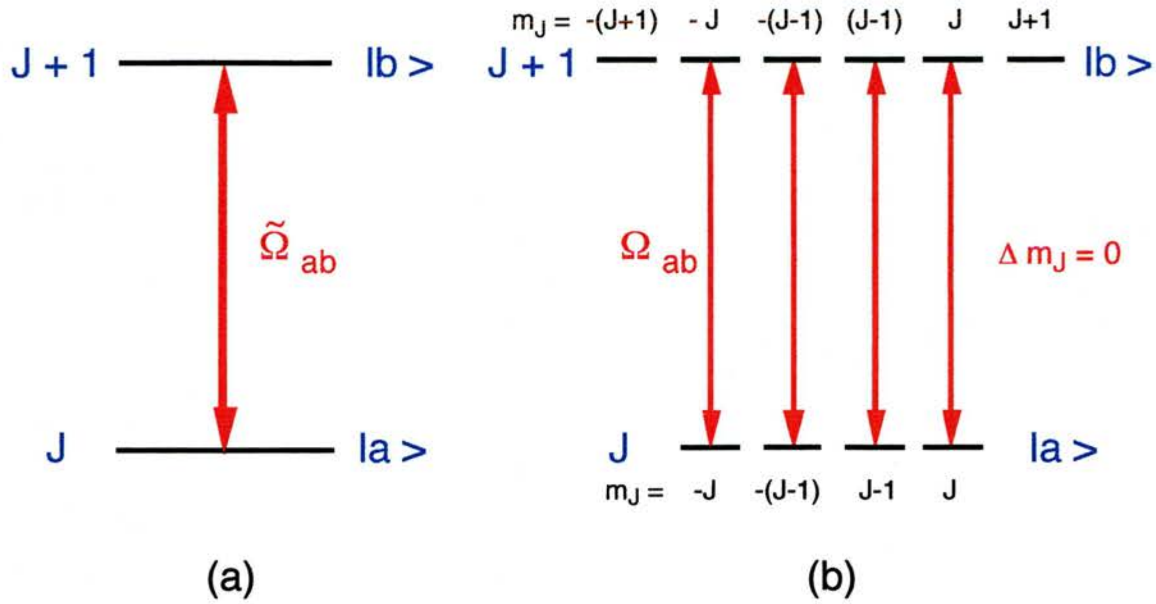

Figure 3.5.1: *(a) A schematic two level atom, with total angular momentum J for the lower state |a> and J+1 for the upper state |b> interacting with a linearly polarised optical field. (b) The same system as (a) but with the degeneracy m_J of the system taken into consideration.*

$$\left(\tilde{\Omega}_{\mathrm{ab}}\right)^2 = \sum_{\mathrm{M_a\,M_b}} (\Omega_{\mathrm{ab}})^2 \tag{3.5.1}$$

The subscript on Ω_{ab} imply specification of magnetic quantum numbers, whereas the average $\tilde{\Omega}_{\mathrm{ab}}$ has no dependence upon magnetic quantum numbers.

Employing the summation properties of 3j-symbols and by defining the optical field phase as ϕ, *Shore* uses the r.m.s. value to express the specific Rabi frequency as:

$$\Omega_{ab} = \tilde{\Omega}_{ab} \frac{\sqrt{3}}{2\pi} e^{i\phi} (-1)^{J_{>} - M_a} \sum_q (-1)^q \varepsilon_{-q} \begin{pmatrix} J_a & 1 & J_b \\ -M_a & q & M_b \end{pmatrix} \tag{3.5.2}$$

where the 2π term in the denominator is present to give the angular Rabi frequency as a pure frequency value, $J_>$ is the larger value of J_a or J_b and ε_{-q} refers to the polarisation state of the optical field. One way of expressing the r.m.s. Rabi frequency that provides connections with other parameters, like the intensity of the radiation is obtained by:

$$\left|\tilde{\Omega}_{ab}\right|^2 = \frac{(\lambda_{ab})^3}{4\pi^2\hbar c} I\, \varpi_b\, A_{ba} \tag{3.5.3}$$

where λ_{ab} is the wavelength of the transition |a> - |b> (m), I is the intensity of the optical field ($\mathrm{Wm^{-2}}$), ϖ_b is the degeneracy of |b>, A_{ba} is the Einstein A coefficient (Hz), $\hbar$ is Planck's constant divided by 2π (Js)and c is the speed of light in vacuum (m/s).

The intensity of the field with waist size w_f, is calculated by considering the following expression for the total power in a Gaussian field, P_T:

$$P_T = I_{max}\int_0^{2\pi}\int_0^{\infty} \exp\left(\frac{-2r^2}{w_f^2}\right) r\, dr\, d\vartheta \tag{3.5.4}$$

Employing the substitution $u = r^2$ provides the following expression for the total power, P_T:

$$P_T = \frac{I_{max}\, \pi\, w_f^2}{2} \tag{3.5.6}$$

In a simple three-level scheme the normalised intensities of the coupling and the probe field overlap as in figure 3.5.1.

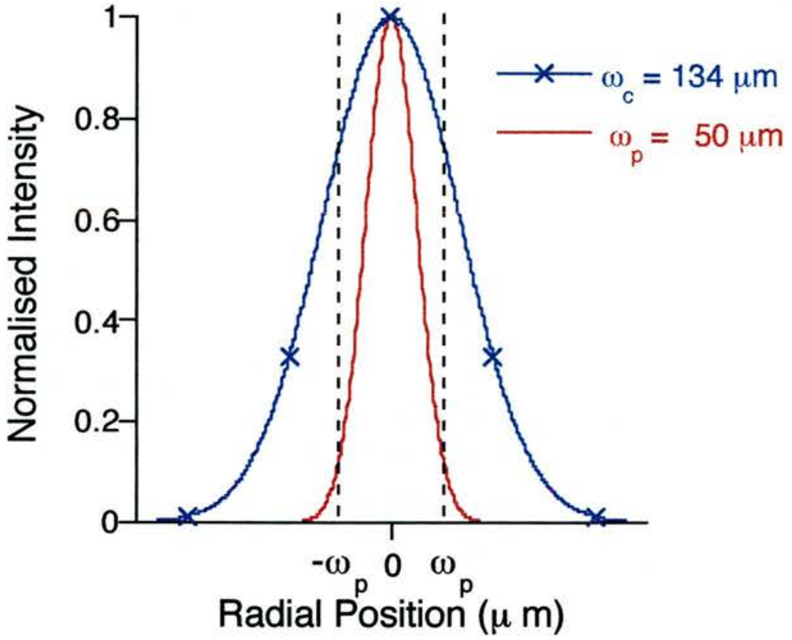

Figure 3.5.1: *The overlap region between the probe and the coupling field intensities.*

The overlap between the probe and the coupling field intensity is such that the probe is contained spatially within the coupling field distribution. The intensity of this system may be derived as follows. If the power and waist of the coupling field are known then using equation (3.5.6) a value for I_{max} can be calculated.

The corresponding coupling field power within the probe field area, P_p, is then found by solving the expression :

$$P_p = I_{max}\int_0^{2\pi}\int_0^{w_p} \exp\left(\frac{-2\left(r^2\right)}{w_c^2}\right) r\,dr\,d\vartheta \tag{3.5.7}$$

where I_{max} is as given in equation (3.5.6). Thus, by dividing this value by the cross-sectional area of the probe field ($\pi\ w_p^2$) a more accurate value for the coupling field intensity is obtained, which is the value for I then used in equation 3.5.3:

$$I = \frac{P_c}{\pi w_p^2}\left[1 - \exp\left(-\frac{2w_p^2}{w_c^2}\right)\right] \tag{3.5.8}$$

The estimation of the Rabi frequency is important not only as an experimental value used in the density matrix analysis, but also in the calculation of an incoherent pump rate. According to *Zibrov et al.*, the incoherent pumping rate is expressed in terms of Rabi frequency and a linewidth of a pumping laser as:

$$R = \frac{2\,|\,\Omega_{pump}\,|^2}{(\Delta\nu + \frac{\gamma_a}{2})\gamma_a} \tag{3.5.9}$$

where Ω_{pump} is the angular Rabi frequency of the equivalent coherent source, $\Delta\nu$ is the linewidth of the incoherent pump and γ_a is the decay rate of the upper level.

References

Arimondo E, Inguscio M and Violino P. "Experimental determination of the Hyperfine Structure in the Alkali atoms.", Rev.Mod.Phys., **49**, p.31 (1977).

Boon J.R., "Electromagnetically induced transparency and Inversionless gain in Doppler broadened systems", Ph.D. thesis, University of St. Andrews, 1998.

Fulton D.J, Quantum Interference Effects: EIT and focusing, Ph.D. thesis, University of St. Andrews, 1996.

Fulton D.J., Shepherd S., Moseley R.R, Sinclair B.D. and Dunn M.H., "Continuous wave EIT: A comparison of V, Λ and cascade systems." Physical Review A, **52**, p.2302 (1995).

Kane D.M. , Atomic spectroscopy in the UV and visible, Ph.D.thesis, University of St.Andrews 1983.

Lindgard A. and Nielsen S.E., Atomic data and nuclear data tables, transition probabilities for alkali, **19,** No 6, Academic Press (1977).

Miles R.B and Harris S.E., " Optical third harmonic generation in alkali metal vapours", IEEE J. Quantum Electron.QE-9, p.470 (1973).

Moseley R.R., Sum frequency mixing and quantum interference in 3-level atoms, Ph.D. thesis, University of St.Andrews, 1994.

Shepherd S., Use and development of a CW Titanium Sapphire laser for non-linear optics, Ph.D. thesis, University of St.Andrews, 1993.

Shore B.W., The theory of coherent atomic excitation, Wiley Interscience publication, 1990.

Woodgate G.K., Elementary atomic structure, Oxford Science publication, 2nd edition, 1992.

Yariv A., Optical Electronics, Saunders College publishing, 4th edition, 1991.

Zibrov A.S., Lukin M.D., Nikonov D., Hollberg L., Scully M.O, Velichansky V.L. and Robinson H.G., "Experimental demonstration of laser oscillation without population inversion via quantum interference in Rb", Physical Review Letters, **75**, p.1499 (1995).

Chapter 4

Experimental observation of coherently induced transparency on a blue probe in a Doppler-broadened mismatched V-type system

---

4.1.a Introduction.

This chapter introduces some of the fundamental concepts in coherently induced transparency or as is traditionally known electromagnetically induced transparency (EIT) in a novel mismatched V-type system, and presents experimental observation of EIT on a blue probe field using an infrared coupling source. EIT is theoretically possible in mismatched schemes even in the presence of Doppler broadening. This chapter concludes with a discussion of the role of the Autler - Townes splitting and EIT in a V-scheme in order to create inversionless gain in mismatched Doppler broadened systems.

Prior to the present work, the wavelengths involved in the configurations of most of these rubidium cascade, lambda and V-type systems are in the near infrared, and therefore easily covered by both diode and Ti: sapphire laser sources. Since the wavelengths of the probe and coupling fields in these configurations are similar, the proper choice of co or counter-propagating beams can reduce the Doppler broadened vapour to a virtually Doppler-free medium. To date, all schemes in rubidium, including that of the first cw inversionless laser by *Zibrov et al*, have taken advantage of these Doppler-free schemes. It had been thought that the use of a Doppler free medium was a necessary requirement for the observation of coherent transparency since it was believed that these reduced the power requirements on the coupling field laser. In this chapter it will be shown, both theoretically and experimentally, that this is in fact not the case. When the wavelength mismatch is such that the coupling field has a larger wavelength than that of the probe field there is still no significant reduction in the depth of an induced transparency feature.

Wavelength dependence of Coherently Induced Transparency was first experimentally demonstrated in a cascade scheme in *Fulton PhD thesis*. The work involved the examination of the effect of changing the coupling laser transition and hence the wavelength, on the Coherently Induced Transparency experienced by a probe beam in a Doppler broadened medium. The transparency of the vapour is shown to be an effect not just of quantum coherence, but of the velocity group dependent Autler-Townes splitting within the vapour. Consequently, the best overall transparency for Rabi splittings less than the Doppler width is not at the position of matched coupling and probe wavelengths, but for coupling field wavelengths less than that of the probe. The most important in the present work is to move the mismatch in the other direction, so as to get to the shorter probe wavelength regime. This is possible in a V-configuration.

This chapter shows that transparency is produced on a blue, 422 nm, probe field by the application of an infrared, 780 nm, coupling laser in a V-type Doppler broadened system. Although blue wavelengths are not "outwith" the capabilities of current laser technology this experiment represents a significant step towards extending EIT and inversionless lasing to shorter wavelength regimes, by rendering atomic rubidium vapour virtually transparent to a probe field that is nearly half the wavelength of the employed coupling field. This system represents the initial work towards achieving mismatched inversionless gain in a Doppler broadened medium.

4.1.b Theoretical ideal four-level system.

The relevant energy level structure of atomic rubidium in a closed form is shown in figure 4.1.1. Theoretical modelling was carried out utilising standard density matrix analysis for a three level V-scheme *Fulton, Shepherd et al,* with appropriate modifications to take into account the hyperfine splitting of the ground state. The equations for the slowly varying density matrix components, in a closed system, are (for a discussion on the general principles involved in deriving such equations, see *Moseley, thesis)*:

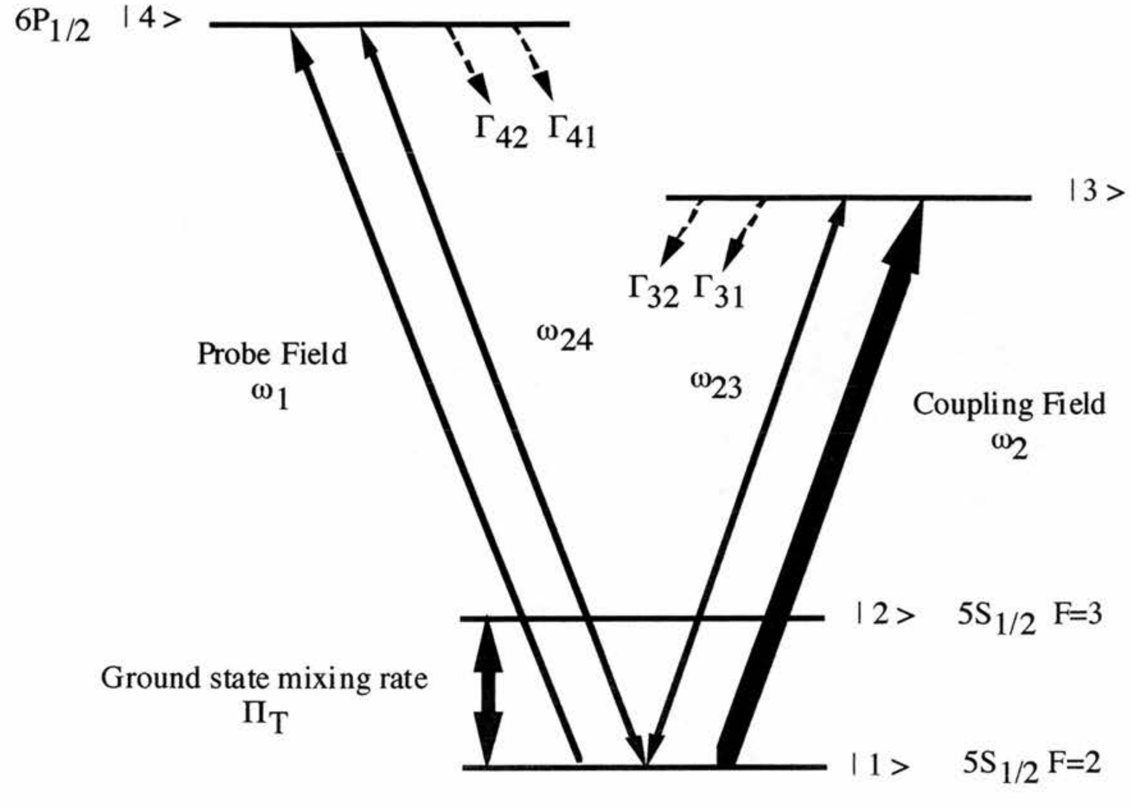

Figure 4.1.1: *Energy level picture of the V- scheme employed in rubidium vapour, including hyperfine splitting of the* $5S_{1/2}$ *ground state. The probe is applied to the* $5S_{1/2}$ *-* $6P_{1/2}$ *transition and the coupling field is applied to the* $5S_{1/2}$ *-* $5P_{3/2}$ *transition, where* ω_{13} *and* ω_{14} *are the frequencies of the transitions,* ω_2 *and* ω_1 *are the coupling and probe frequencies respectively and* Π_T *is the ground state collisional mixing rate.*

$$\dot{\rho}_{11} = i\Omega_c(\tilde{\rho}_{31} - \tilde{\rho}_{13}) + i\Omega_p(\tilde{\rho}_{41} - \tilde{\rho}_{14}) + \Gamma_{41}\rho_{44} + \Gamma_{31}\rho_{33} + \frac{5}{12}\Pi_T\rho_{22} - \frac{7}{12}\Pi_T\rho_{11} \tag{4.1.a}$$

$$\dot{\rho}_{22} = \Gamma_{42}\rho_{44} + \Gamma_{32}\rho_{33} + \frac{7}{12}\Pi_T\rho_{11} - \frac{5}{12}\Pi_T\rho_{22} \tag{4.1b}$$

$$\dot{\rho}_{33} = i\Omega_c(\tilde{\rho}_{13} - \tilde{\rho}_{31}) - \Gamma_{31}\rho_{33} - \Gamma_{32}\rho_{33} \tag{4.1c}$$

$$\dot{\rho}_{44} = i\Omega_p(\tilde{\rho}_{14} - \tilde{\rho}_{41}) - \Gamma_{41}\rho_{44} - \Gamma_{42}\rho_{44} \tag{4.1d}$$

$$\dot{\tilde{\rho}}_{12} = i(\Delta_{12} + i\gamma_{12})\tilde{\rho}_{12} + i\Omega_c\tilde{\rho}_{32} + i\Omega_p\tilde{\rho}_{42} \tag{4.1e}$$

$$\dot{\tilde{\rho}}_{13} = -i(\Delta_{13} - i\gamma_{13})\tilde{\rho}_{13} + i\Omega_c(\rho_{33} - \rho_{11}) + i\Omega_p\tilde{\rho}_{43} \tag{4.1f}$$

$$\dot{\tilde{\rho}}_{14} = -i(\Delta_{14} - i\gamma_{14})\tilde{\rho}_{14} + i\Omega_p(\rho_{44} - \rho_{11}) + i\Omega_c\tilde{\rho}_{34} \tag{4.1g}$$

$$\dot{\tilde{\rho}}_{23} = -i(\Delta_{13} + \Delta_{12} - i\gamma_{23})\rho_{23} - i\Omega_c\rho_{21} \tag{4.1h}$$

$$\dot{\tilde{\rho}}_{24} = -i(\Delta_{14} + \Delta_{12} - i\gamma_{24})\rho_{24} - i\Omega_p\rho_{21} \tag{4.1i}$$

$$\dot{\tilde{\rho}}_{34} = -i(\Delta_{14} + \Delta_{13} - i\gamma_{34})\tilde{\rho}_{34} + i\Omega_c\tilde{\rho}_{14} - i\Omega_p\tilde{\rho}_{31} \tag{4.1j}$$

where subscripts refer to the four levels numbered from the lowest to the highest energy state. The mixing term Π_T is the collisional mixing rate and was included to allow for thermalisation of the hyperfine split ground state (i.e. thermalisation between states 1 and 2). The detunings are defined as

$$\Delta_{14} = \omega_1 - \omega_{14} - k_1 V_Z \tag{4.2a}$$

$$\Delta_{13} = \omega_2 - \omega_{13} - k_2 V_Z \tag{4.2b}$$

$$\Delta_{12} = -3\mathrm{GHz}(\times 2\pi) \tag{4.2c}$$

where ω_1 and ω_2 denote the frequencies of the applied optical fields, V_Z is the atomic velocity along the cell length, k_1 and k_2 are the wave numbers of the applied optical fields and ω_{14} and ω_{13} are the energy separations of the appropriate levels. The Rabi frequencies are defined as:

$$\Omega_p = \frac{\mu_{14}E_1}{2\hbar} \tag{4.3a}$$

$$\Omega_c = \frac{\mu_{13}E_2}{2\hbar} \tag{4.3b}$$

where E_1 and E_2 are the electric-field strengths of the applied probe and coupling fields respectively, and μ_{14} and μ_{13} are the dipole matrix elements for the transitions. The population decay rates (Γ_{ij}) were set to Γ_{41}= 4 MHz, Γ_{42}= 4 MHz, Γ_{31}= 20 MHz and Γ_{32}= 20 MHz, and the coherence decay rates (γ_{ij}) according to:

$$\gamma_{12} = \frac{\Pi_T}{2} \tag{4.4a}$$

$$\gamma_{13} = \frac{\Gamma_{32}}{2} + \frac{\Gamma_{31}}{2} + \left(\frac{7}{12} \times \frac{\Pi_T}{2}\right) \tag{4.4b}$$

$$\gamma_{14} = \frac{\Gamma_{41}}{2} + \frac{\Gamma_{42}}{2} + \left(\frac{7}{12} \times \frac{\Pi_T}{2}\right) \tag{4.4c}$$

$$\gamma_{34} = \frac{\Gamma_{41}}{2} + \frac{\Gamma_{42}}{2} + \frac{\Gamma_{31}}{2} + \frac{\Gamma_{32}}{2} \tag{4.4d}$$

$$\gamma_{23} = \frac{\Gamma_{32}}{2} + \frac{\Gamma_{31}}{2} + \left(\frac{5}{12} \times \frac{\Pi_T}{2}\right) \tag{4.4e}$$

$$\gamma_{24} = \frac{\Gamma_{41}}{2} + \frac{\Gamma_{42}}{2} + \left(\frac{5}{12} \times \frac{\Pi_T}{2}\right) \tag{4.4f}$$

Density matrix elements are complex numbers and can be expressed as:

$\tilde{\rho}_{ij} = \rho^{r}_{ij} + i\rho^{i}_{ij}$ and $\tilde{\rho}^{*}_{ij} = \rho^{r}_{ij} - i\rho^{i}_{ij}$

The equations are solved by invoking steady-state conditions (appropriate because of the employment of single-frequency cw lasers in the experiment) and thus setting all time derivatives to zero. Equations (4.1a)-(4.1j) can then be split into sixteen real simultaneous equations, using properties of the density matrix, and solved, using normal linear algebra routines. Further more population conservation implies the trace normalisation and the 15×15 system can represented in a matrix form **A** x = **B** as in matrix 2.1 of the appendix.

The solutions yield values for the real and imaginary parts of the coherence on each transition, which can be related to the refractive index and the absorption/gain respectively, and the proportion of the atomic population in each of the energy levels. Doppler-broadening is then taken into account by integrating over the velocity distribution (i.e. over V_z), so providing a comprehensive modelling of the system.

4.2 Wavelength Dependence.

Before applying the above analysis to the particular experimental situation under consideration here, it is useful to extend the earlier work of *Shepherd et al.* to the case of the V- scheme. In this earlier work it was shown both theoretically and experimentally that for cascade configurations, if the wavelength of the coupling laser is less than that of the probe, there is no disadvantage in using mismatched wavelengths.

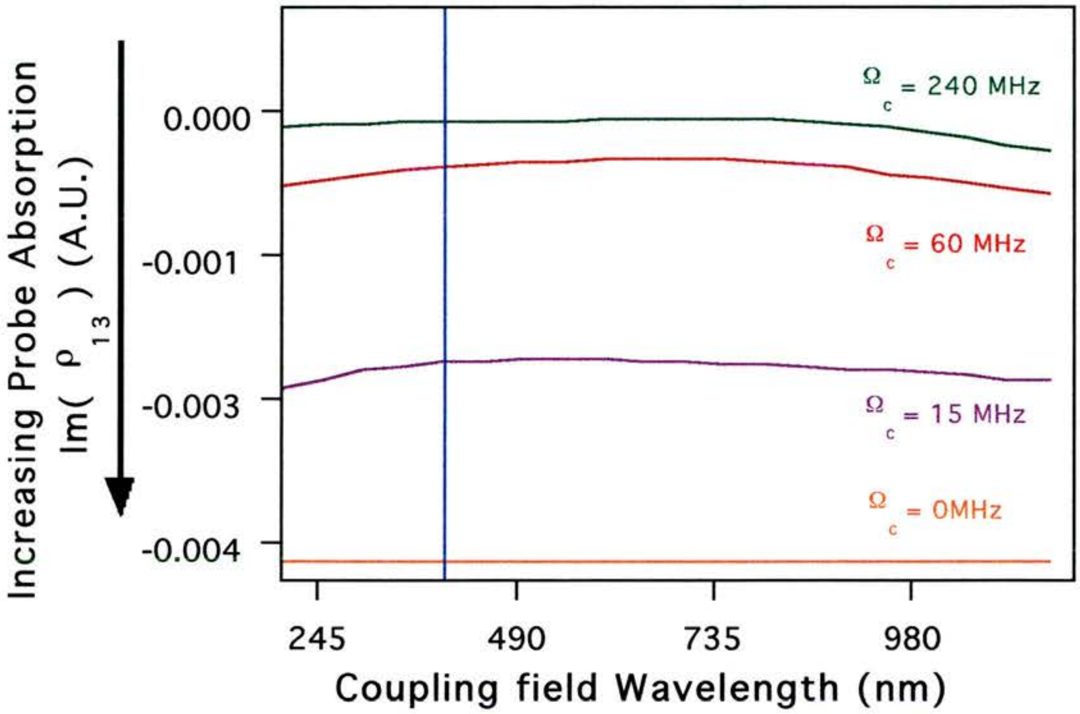

Figure 4.2.1: *For a probe field wavelength* λ_p *=422 nm and a Rabi frequency* Ω_p*= 1 MHz , the transparency does not vary on changing the coupling field wavelength.*

Figure 4.2.1 depicts a theoretical curve representing the level of induced transparency in relation to the degree of wavelength mismatch in a V-type system. These results indicate that the V-type system, unlike the Cascade scheme and a Lambda scheme as in figure 4.2.2, is insensitive to the relative direction of wavelength mismatch. The probe absorption does not alter if we change the coupling field wavelength for a specific probe at 422 nm and for different Rabi angular frequencies. This attribute of the V-scheme enables the use of a probe laser that has a lower wavelength than the coupling field. This will lead us to the shorter wavelength regime, which is of the most interest for future inversionless lasing schemes.

It has previously been shown by *Shepherd et al*, for the case in which the coupling wavelength is greater than that of the probe, that the secondary Autler-

Townes components of the high and low velocity groups overlap with the EIT window of the zero velocity group on resonance, thus eroding the induced transparency. This result holds for the Cascade, Lambda and V- schemes, but the amplitude of the secondary Autler-Townes components is significantly smaller in a V-scheme. This occurs because there is no two-photon contribution to the absorption for the high velocity groups for which the coupling field is effectively widely detuned.

For high velocity atoms the coupling laser is detuned by the Doppler shift, -$k_c v_z$ and the two-photon process becomes negligible. This occurs because the two-photon process |3>-|1>-|4> in a V-scheme starts in the upper level of the coupling transition. This level is only populated when the coupling field is on or close to resonance with the particular velocity group. The result in a V-scheme is that for a detuned coupling laser field the population available for two-photon absorption will reduce dramatically. In the cascade and lambda schemes on the other hand, the two-photon process will actually increase when the coupling laser is detuned. Consequently, the two-photon contribution of the high velocity groups may be disregarded and the residual secondary Autler-Townes components which overlap with the EIT point are of smaller magnitude. Hence the V-scheme is the best scheme to create a mismatched system, for the production of EIT in a Doppler broadened medium.

We can then show how the single-photon and the two-photon resonances change with respect to the applied probe detuning. Figure 4.2.3 shows a closed three-level V-scheme with the associated detunings of the probe and the coupling fields. The total detuning is defined for the probe field:

$$\Delta_1 = \Delta_p - k_1 v_z \tag{4.2.1}$$

where $k_1 = 2\pi/\lambda_p$ the wavevector of the probe field, v_z the single velocity group and Δ_p the manual detuning of the probe field.

The single-photon resonance condition is given when :

$$\Delta_1 = 0, \; \Delta_p = k_1 v_z \tag{4.2.2}$$

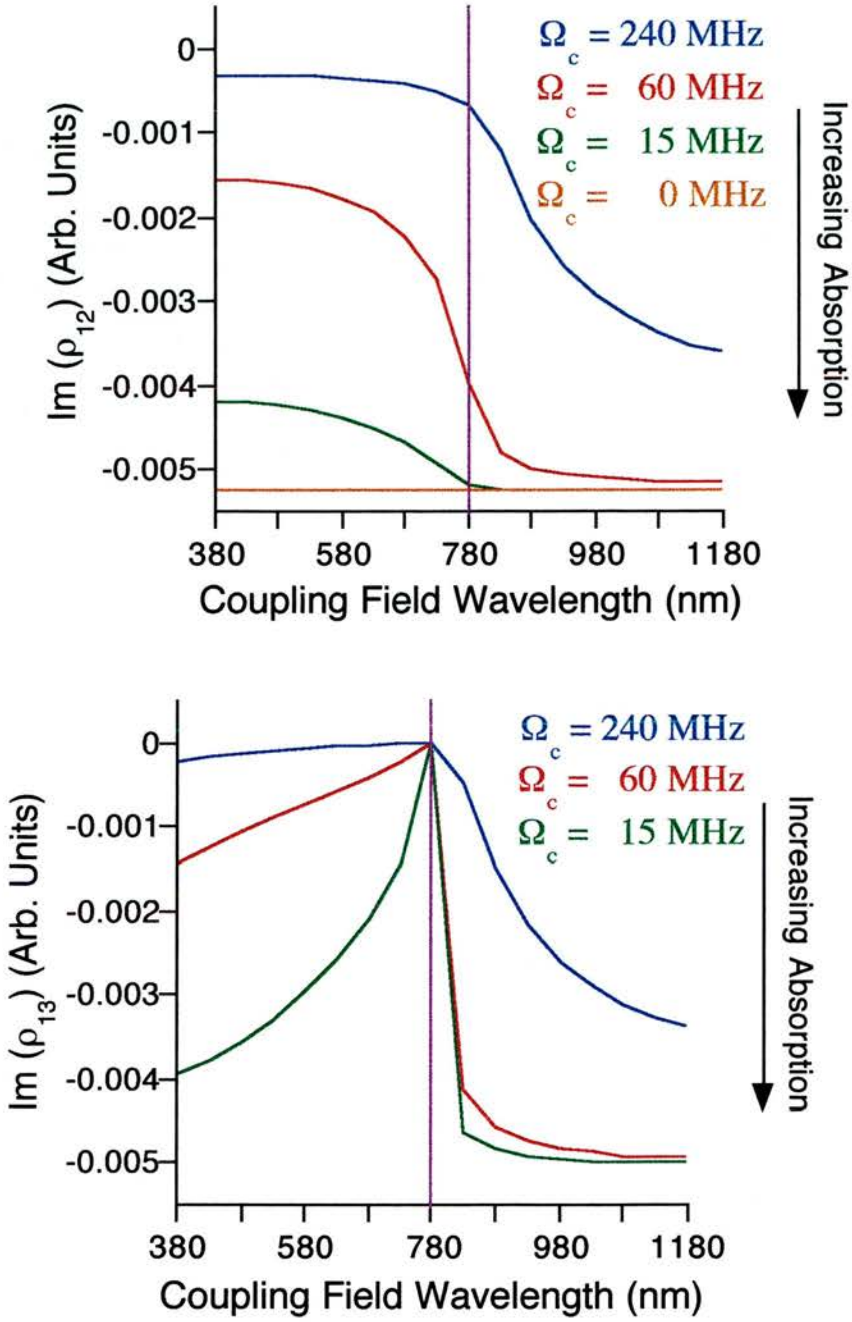

Figure 4.2.2 : (a) *Probe absorption within a cascade system versus coupling field wavelength as a function of coupling field power* (b) *Probe absorption within a lambda system versus coupling field wavelength as a function of coupling field power Ω_c = 240 MHz (blue curve), Ω_c = 60 MHz (red curve) and Ω_c = 15 MHz (green curve)*

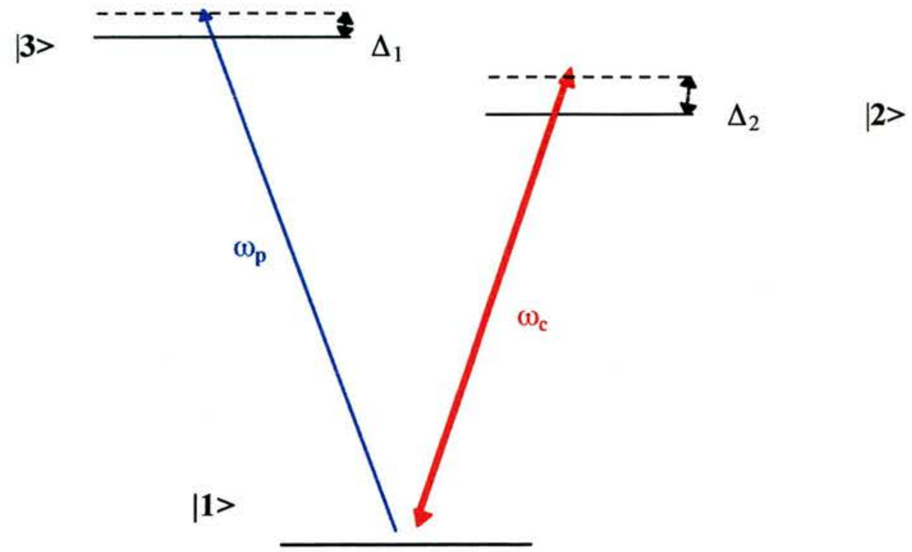

Figure 4.2.3: *A closed V-scheme with the detunings Δ_1 for the probe field and Δ_2 for the coupling field.*

The two-photon absorption process involves both fields hence the resonance condition will include both Doppler shifts and detunings. For a V-scheme the two-photon resonance occurs when:

$$\Delta_1 = \Delta_2 \tag{4.2.3}$$

but the detunings include Doppler broadening for copropagating beams as in the following equations:

$$\Delta_1 = \Delta_p - k_1 v_z \tag{4.2.4}$$

$$\Delta_2 = \Delta_c - k_2 v_z \tag{4.2.5}$$

where $k_2 = 2\pi/\lambda_c$ the wavevector of the coupling field, v_z the single velocity group and Δ_c the manual detuning of the coupling field. By substituting equations 4.2.4 and 4.2.5 in 4.2.3 we then have the two-photon resonance condition for a V-scheme:

$$\Delta_p = k_1 v_z - k_2 v_z + \Delta_c \tag{4.2.6}$$

If we assume zero-detuning of the coupling field this becomes:

$$\Delta_p = k_1 v_z - k_2 v_z \tag{4.2.7}$$

As is obvious from equations 4.2.2 and 4.2.7 the two-photon process is distributed between the Autler - Townes components differently from the single-photon absorption, because the resonance for each process occurs at a different probe detuning for a single velocity group. The distribution of absorption for the two processes will always be different for a given velocity group in a mismatched scheme.

In figure 4.2.4a the single-photon resonance as a function of the applied probe detuning is depicted. Figure 4.2.4b shows the two-photon absorption resonance with respect to the applied probe field detuning. These resonances define the distribution of the overall absorption between the two Autler-Townes components. It is therefore important to ensure that the absorbing Autler-Townes components for any one velocity group do not overlap with the maximum transparency points of the other velocity groups , as far as possible, in the presence of Doppler broadening.

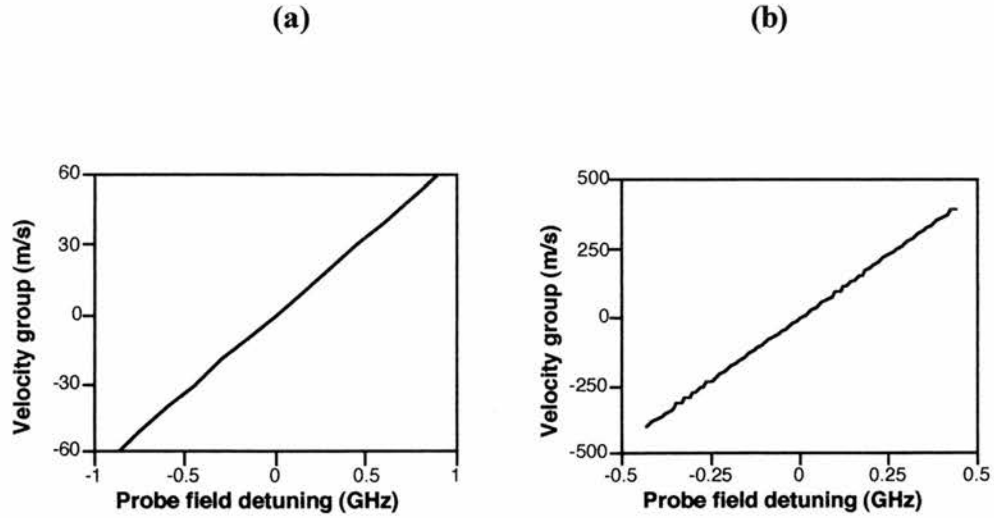

Figure 4.2.4: *(a) The single-photon resonance is plotted as a function of the applied probe detuning. (b)The two-photon absorption resonance is plotted with respect to the applied probe field detuning.*

Figure 4.2.5 shows a three-dimensional plot of the absorption levels of the Autler-Townes components in the V- scheme as a function of probe field detuning and atomic velocity group, from which we can see that the transparency window is still significant, on resonance, despite the overlapping secondary Autler-Townes components. The magnitude of these components is not big enough to erode the transparency window. EIT is maintained in the V-mismatched scheme in a Doppler broadened medium.

4.3 Transparency and coupling field saturation.

Integrating over the velocity groups gives us the 'net' absorption and a significant transparency window is predicted on resonance. The magnitude of the transparency is too great to be explained solely by coupling field saturation, which at most will reduce the population in level 1 to half its initial value. The transparency is thus a consequence of the quantum coherent effect that occurs in the presence of the coupling field. Coupling field saturation is one mechanism induced by the coupling field, that can alter the transmission of the probe field. Experimental results are presented in figure 4.7.2.

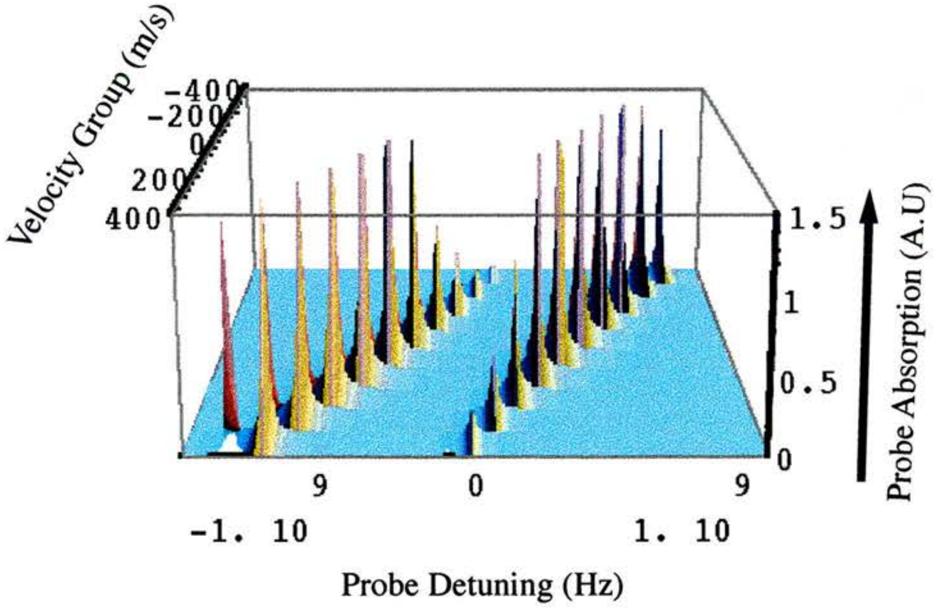

Figure 4.2.5: *Three-dimensional plot of Autler-Townes absorptions (vertical axis) vs probe frequency (horizontal axis across the page) and velocity group (horizontal axis into the page), based on V- scheme with 422 nm probe field, Ω_p= 1 MHz and 780 nm coupling field, Ω_c= 1 GHz. This theoretical plot shows that the secondary Autler-Townes components that overlap on resonance are small in magnitude and do not destroy the transparency window.*

4.4 Optical Pumping.

Under normal conditions optical pumping effects would be expected to occur as a result of the strong coupling field depopulating one of the hyperfine ground state levels. However, experimental investigation demonstrated that optical pumping effects were in fact absent. Reasons for this will be considered shortly in the context of the theoretical model.

The ground state collisional mixing rate is calculated using the formula, $\Pi_T=\sigma v N$ as in chapter 2, where σ is the collision cross-section, v is the average atom velocity (dependent on temperature) and N is the atomic number density (also dependent on temperature).

A comparison of a mixing rate of $\Pi_T = 1$ MHz with that of $\Pi_T = 200$ MHz is presented in figure 4.4.1. In the first case when the collisional mixing rate equals $\Pi_T =$ 1 MHz, it is obvious from the graph of the populations in figure 4.4.1b, that all the population is optically pumped in level 2. Thus optical pumping is indistinguishable from EIT. When the mixing rate has the value of 200 MHz, figure 4.4.1d , the populations are now redistributed in the ground state and equilibrium is obtained. The relative populations in the hyperfine ground state levels are hence returned to close to their thermal-equilibrium relative values ($\rho_{11}:\rho_{22}=5:7$).

In our experiment there is substantial evidence that there is no optical pumping, see §4.7. However, the collisional mixing rate calculated using available data under the conditions of our experiment (T=428 K, N=Rb particle density=1.135×10^{20} atoms/m^3, σ=the Rb-Rb exchange collision cross-section=6×10^{-18} m^2, according to *Cohen-Tannoudgi and Kastler*, v=the average velocity=289 m/s), is only 50 kHz. Hence, it is inadequate to explain the absence of optical pumping. This is considered more fully, after the experimental observations have been discussed.

It is appropriate at this point to explore how the populations of the ground state vary as a function of velocity group, see figure 4.4.2. Figure 4.4.2a shows a graph of the populations in level 1 and level 2 of figure 4.1.1, against the velocity groups in the case where the coupling field Rabi frequency is Ω_c = 10 MHz and the collisional mixing rate is 100 kHz. The value of the collisional mixing rate is close to that of the experiment. The population of level 1 shows a deep depletion exactly on resonance and the population in level 2 presents an expected increase on line centre. This velocity selected feature corresponds to optical pumping of the population from level 1 to level 2. In this case optical pumping has an identical outcome with that of EIT and we can not distinguish the quantum coherence effect from optical pumping.

If we now increase the coupling field Rabi frequency to 1 GHz and the collisional mixing rate to 200 MHz we do not observe the velocity selected effect. Instead the changes in both the populations extend over the velocity groups as shown in figure 4.4.2b. With such values of Rabi frequency and collisional mixing rate EIT is observable, because optical pumping is not present, see figure 4.4.1c.

In general, mixing rates contribute to dephasing of coherences involving the levels being mixed, in the same way as a standard population decay. Fortuitously, the ground state mixing rate is not directly linked to the coherence, ρ_{34}, that drives EIT, and therefore does not directly dephase it. Consequently, the level of transparency is not significantly affected.

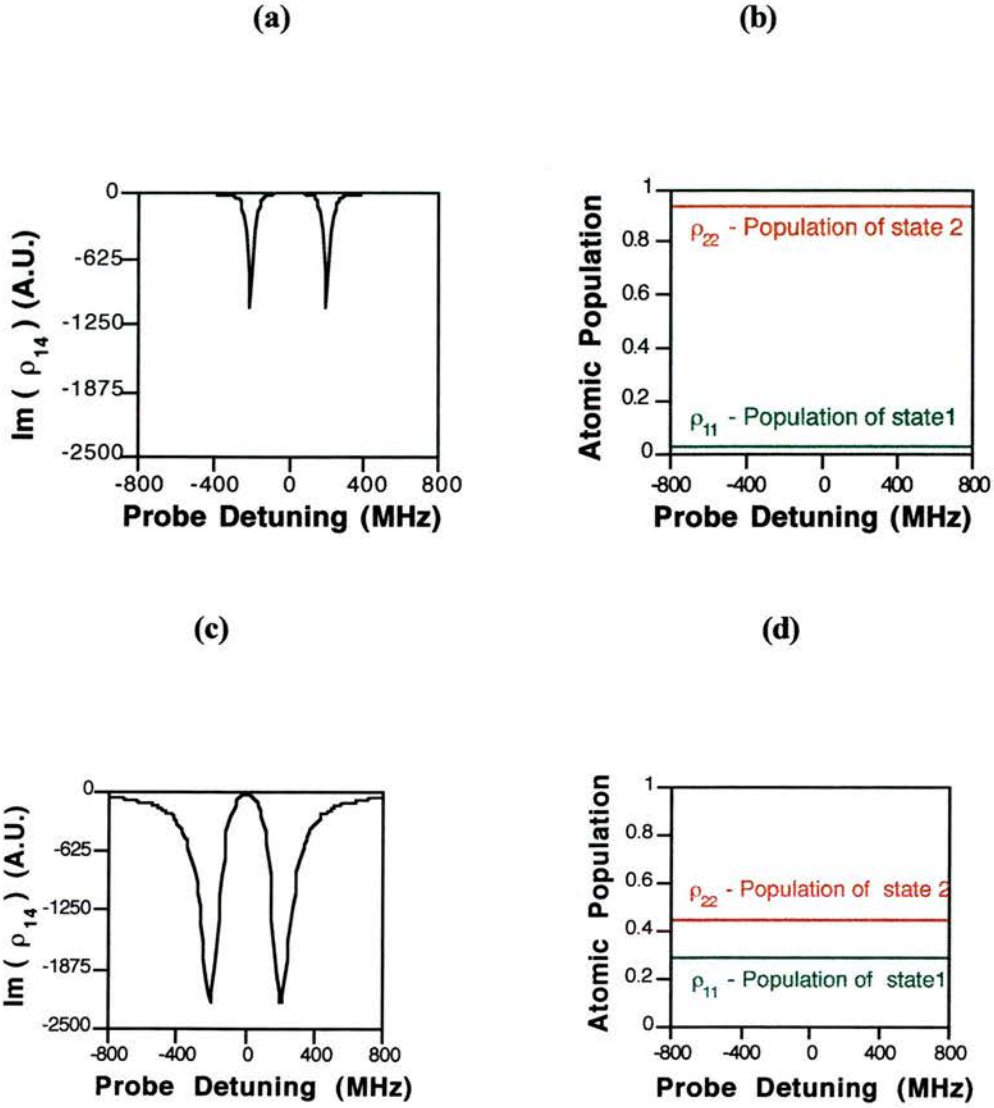

Figure 4.4.1: *(a) The probe absorption is plotted against the probe detuning when the mixing rate is* $\Pi_T = 1$ *MHz. The Rabi frequency of the coupling field is* $\Omega_c = 800$ *MHz. EIT is indistinguishable from optical pumping as it is shown from the populations in levels |1> and |2> (b) All the population is optically pumped in level |2> when the mixing rate is* $\Pi_T = 1$ *MHz.(c) The probe absorption is plotted against the probe detuning when the mixing rate is* $\Pi_T = 200$ *MHz. We can see clearly EIT.(d)The populations are redistributed between the two ground state levels when the mixing rate is* $\Pi_T = 200$*MHz.*

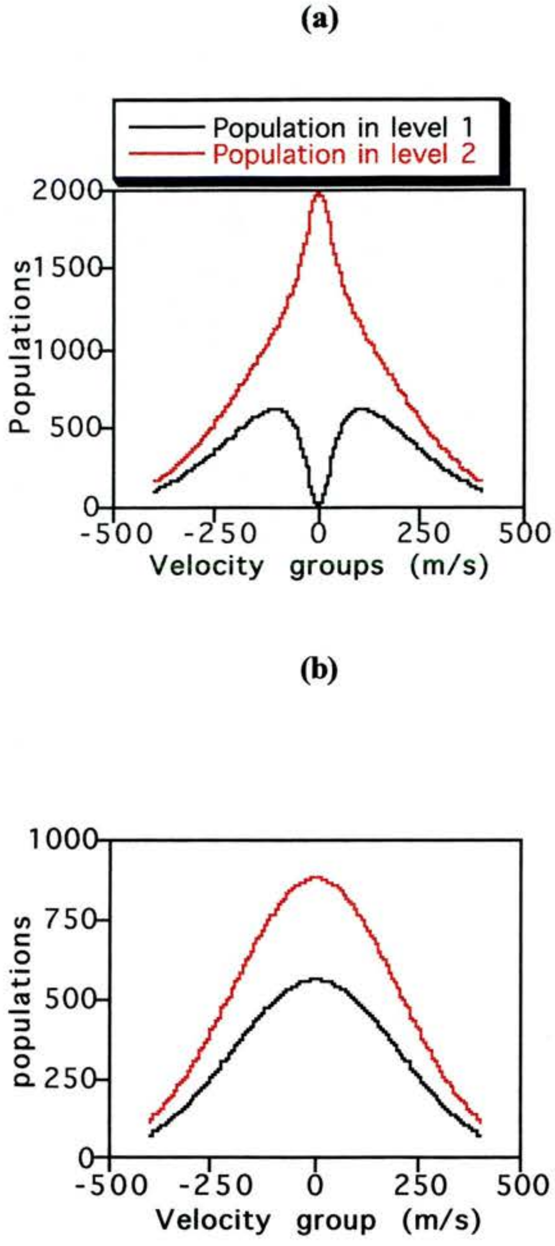

Figure 4.4.2: *(a) The populations of the ground state levels are plotted as function of the velocity groups, when the coupling field Rabi frequency is 10 MHz and the collisional mixing rate is 100 kHz. (b) The populations of the ground state are plotted against the velocity groups, while the Rabi frequency is set 1 GHz and the collisional mixing rate is set 200 MHz.*

4.5 The Role of Coherence.

Theoretical modelling has also been carried out to investigate the role of coherence in this system. Previous work concerned with the wavelength dependence of coherently induced transparency raised the issue that the nature of the observed transparency window was dictated by the interplay of EIT and Autler-Townes splitting, *Shepherd et al.* It was shown that the overlap of Autler-Townes components from different velocity groups controlled the width of the transparency, while the depth of the window was set by the level of EIT and the related quantum coherence.

The coherently induced transparency is driven by the coherence, ρ_{34}, on the unlinked transition, $6P_{1/2}$ - $5P_{3/2}$, which has both real and imaginary components. An ideal coherence exists which creates maximum transparency. The concept of an ideal coherence may be most easily explained in relation to a cascade scheme, and this is what we now consider. Figure 4.5.1 shows a cascade scheme with the state amplitudes a_1, a_2 and a_3 and the coupling and probe field Rabi frequencies.

The ideal coherence is such that the rate at which amplitude is added to state 2 by a transition from state 3 is of equal magnitude, but opposite phase (π phase difference), to that rate at which amplitude is added to state 2 from state 1. In this case there is no net change in the amplitude of state 2, as a result of destructive interference between the transitions. In particular, no absorption occurs from state 1 to state 2. Since the rate of amplitude transfer is given by the product of state amplitude with Rabi frequency, then the phase difference of amplitudes a_1 and a_3 is π and it is:

$$|a_3|\Omega_c = |a_1|\Omega_p \tag{4.5.1}$$

or else

$$|a_3| = |a_1|\frac{\Omega_p}{\Omega_c} \tag{4.5.2}$$

The off-diagonal density matrix element for the ideal coherence is defined as:

$$\rho_{13} = \overline{a_1 a_3^*} \qquad (4.5.3)$$

where

$$\begin{aligned} a_1 &= | a_1 | \exp(i\phi_1) \\ a_3 &= | a_3 | \exp(i\phi_3) \end{aligned} \qquad (4.5.4)$$

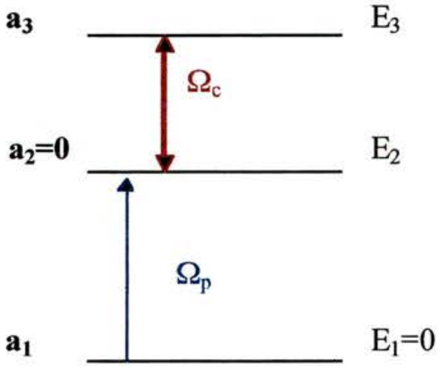

Figure 4.5.1: *An ideal cascade scheme with no decay rates, with the state amplitudes a_1, a_2 and a_3 and the coupling and probe field Rabi frequencies.*

Hence $\rho_{13} = | a_1 || a_3 | \exp[i(\phi_1 - \phi_3)]$ and substituting for $|a_3|$ from equation 4.5.2 it becomes:

$$\rho_{13} = | a_1 |^2 \frac{\Omega_p}{\Omega_c} \exp(i\pi) \qquad (4.5.5)$$

Therefore the equation for the ideal coherence for EIT , in a Cascade scheme may be defined as:

$$[\rho_{13}]_{ideal} = -\rho_{11} \frac{\Omega_p}{\Omega_c} \qquad (4.5.6)$$

The only difference between a V and a Cascade scheme is that the two levels of the unlinked transition have a relative phase of 2π in this case. We can now define the ideal coherence of the V-scheme in figure 4.1.1 as:

$$[\rho_{34}]_{ideal} = \rho_{11} \frac{\Omega_p}{\Omega_c} \qquad (4.5.7)$$

An analytical expression for the ideal coherence in a V-scheme can also be derived by setting the dephasing and decay terms to zero in the density matrix. From equation (4.1g) we have:

$$\dot{\rho}_{14} = i\Omega_p(\rho_{44} - \rho_{11}) + i\Omega_c \tilde{\rho}_{34} \tag{4.5.8}$$

Under steady-state conditions, we rearrange the equation 4.5.8 to solve for ρ_{34}. By making the additional assumption that the population in the upper level of the probe transition is zero, in a weak probe approximation, then the ideal coherence is given by

$$[\rho_{34}]_{\text{ideal}} = \rho_{11}\frac{\Omega_p}{\Omega_c} \tag{4.5.9}$$

This corresponds exactly to the situation in the Cascade system, in which the ideal coherence is intuitively seen to occur when the state amplitudes feeding into the upper level of the probe transition are equal in magnitude and π out of phase, for the coupling and probe fields respectively. The principal difference, however, is that in a V- scheme the two atomic levels of the unlinked transition have a relative phase of 2π. The normalised coherence is defined by

$$\frac{[\rho_{34}]}{[\rho_{34}]_{\text{ideal}}} = 1 \tag{4.5.10}$$

It is necessary to define the coherence in this way because, there is a specific, ideal coherence for which maximum transparency is produced and any departure from this value, will cause a reduction in the observed transparency. In order to assess the role of quantum coherence in a V-scheme the normalised coherence was plotted as a function of dephasing on resonance. Figure 4.5.2 shows the real part of the normalised coherence falling away from the 'ideal' value as dephasing is increased and an exactly corresponding increase in the absorption and hence a reduction in the transparency level. [The imaginary part of the normalised coherence is fixed at zero while the probe field is on resonance, consequently it is the real part of the driving coherence that dictates the normalised coherence in this case.] The decrease in the normalised coherence is more pronounced for low Rabi frequencies.

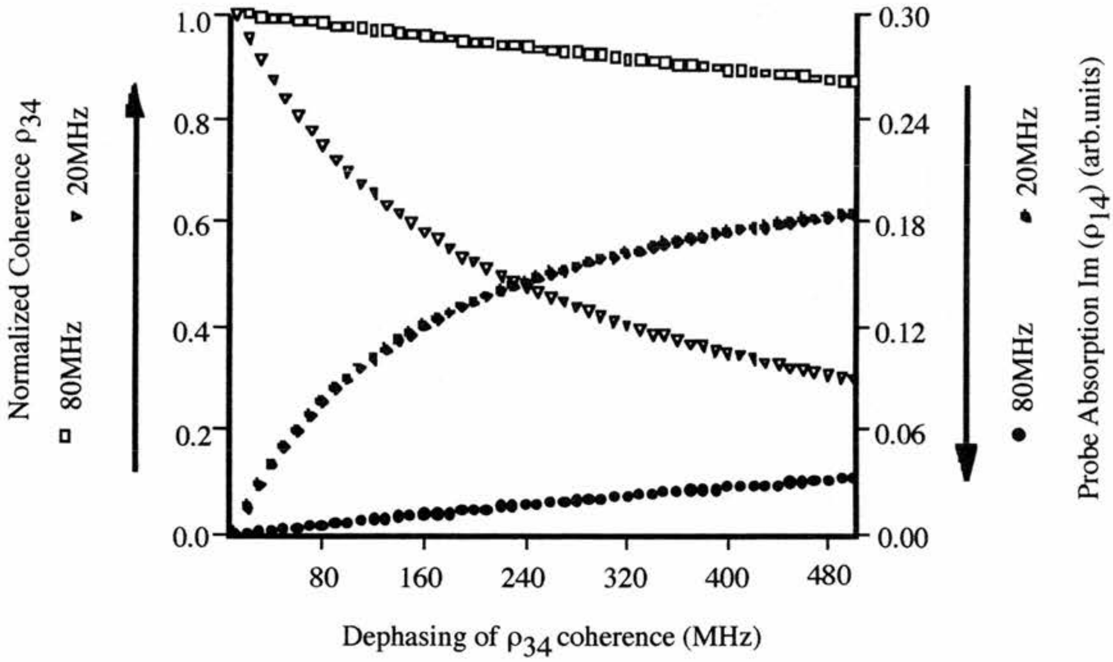

Figure 4.5.2: *The real component of the normalised coherence (left vertical axis) and Im (ρ_{14}) (proportional to probe field absorption, right vertical axis) are plotted with respect to the dephasing of the driving coherence, ρ_{34}, in the V- scheme, for coupling field Rabi frequencies Ω_c=20MHz and Ω_c=80MHz. As the normalised coherence falls away from its ideal value, there is a corresponding reduction in the level of the induced transparency.*

Importantly, the model shows that the driving coherence is the only factor controlling the level of induced transparency, irrespective of the Rabi frequency on the coupling field transition. This result is deduced from the linear relationship predicted between the normalised coherence and the induced transparency, for the range of coupling field powers depicted in figure 4.5.3. As is shown in this graph there is a strong correlation between the normalised coherence and the level of transparency.

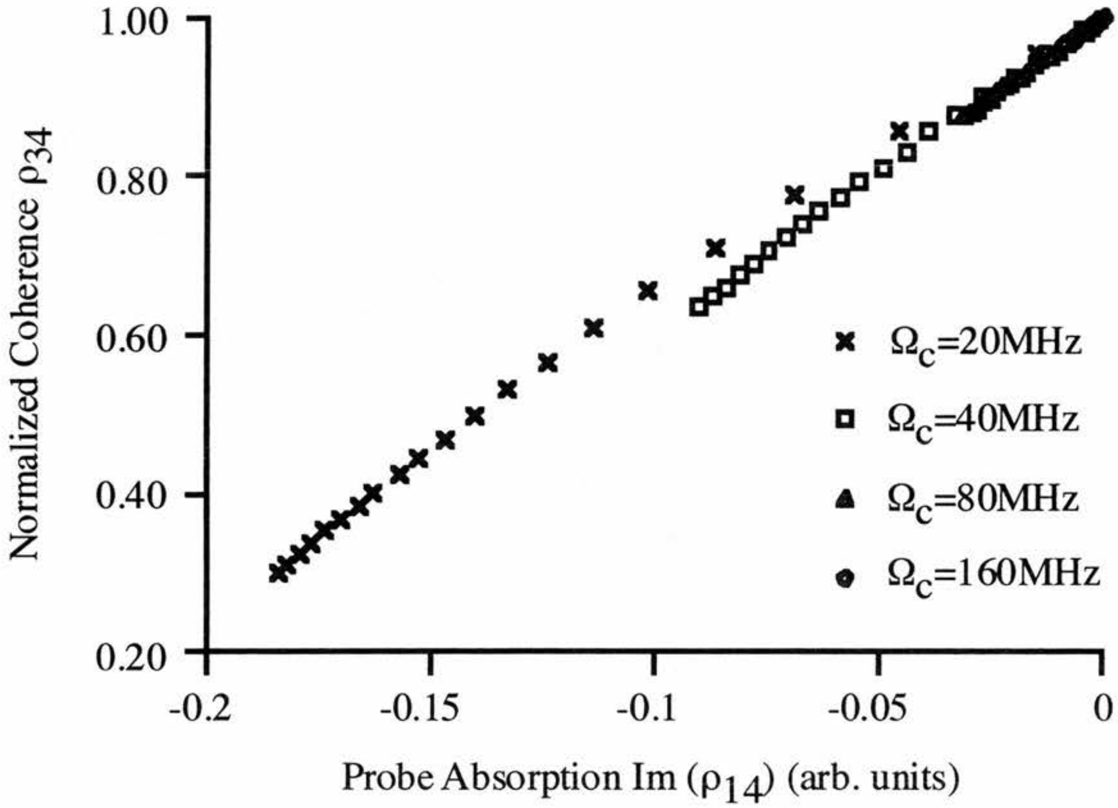

Figure 4.5.3: *The real part of the normalised coherence vs Im (ρ_{14}) (proportional to the probe field absorption), for various coupling field Rabi frequencies in the V-scheme, Ω_c=20MHz, Ω_c=40MHz, Ω_c=80MHz, and Ω_c=160MHz. A linear relationship is demonstrated.*

At high coupling field intensities, the Rabi frequency induced on the transition can be relatively large, and it follows that the Autler-Townes splitting of the $5S_{1/2}$ and $5P_{3/2}$ states will also be high. Referring again to figure 4.5.2, the normalised coherence stays closer to its ideal value, as dephasing is increased, for higher values of Rabi frequency. This happens because the overlapping Autler-Townes components are split further away from resonance and they do not overlap with the transparency window. From the theory presented, the normalised quantum coherence is still the principal determining factor for the level of transparency, regardless of the magnitude of the associated Autler-Townes splitting, because there is a strong correlation between the normalised coherence and the level of transparency.

4.6. Experimental apparatus.

The experiments conducted on this mismatched transparency scheme were carried out by utilising a 2 cm length cell of rubidium vapour (Opthos Instruments). The cell was heated to around 125 °C to give an appreciable level of absorption (>80%) of the focused probe beam. This relatively high temperature *Moseley et al* was necessary due to the low dipole matrix element on the probe transition. The laser radiation was supplied by two single-frequency cw Ti:sapphire lasers. The fundamental source for the blue probe beam was a scanning Microlase MBR-110 laser tuned around 844 nm; the radiation being subsequently frequency doubled by a temperature tuned potassium niobate crystal. The resulting second harmonic output was tuned to the $5S_{1/2}$ - $6P_{1/2}$ transition at 422 nm. The coupling field was supplied by a modified Schwartz Electro-Optic Titan cw laser tuned to the $5S_{1/2}$ - $5P_{3/2}$ transition at 780 nm. The laser beams were copropagated in the vapour cell to minimise the residual Doppler width and optimise the overlap of the transparency windows and Autler-Townes components of the various velocity groups, *Fulton thesis.* The output of the Microlase Ti:Sapphire laser, approximately 450 mW, produced around 300μW of second harmonic at 422 nm. The resulting probe beam was chopped, to allow subsequent phase sensitive detection of the light transmitted through the vapour cell. The probe beam was focused into the cell with a 20 cm lens to produce a spot size of approximately 40μm and the coupling laser was focused by a 40 cm lens, producing a spot size of around 100μm, thereby ensuring that the probe beam remained within the coupling beam over the region of the cell. The schematic of the experimental apparatus is shown in figure 3.4.1 of chapter 3.

4.7 Experimental results.

The measured absorption exhibits the hyperfine structure of the two rubidium isotopes, ^{85}Rb and ^{87}Rb. Figure 4.7.1 shows an experimental trace which is a scan across all four resulting absorption peaks in the absence and presence of the coupling laser. The coupling laser is on resonance with peak 3 (^{85}Rb, F=2) at a power of 800 mW. This experimental trace demonstrates the magnitude of the induced transparency which removes more than 70% of the absorption. The Doppler-width is measured to

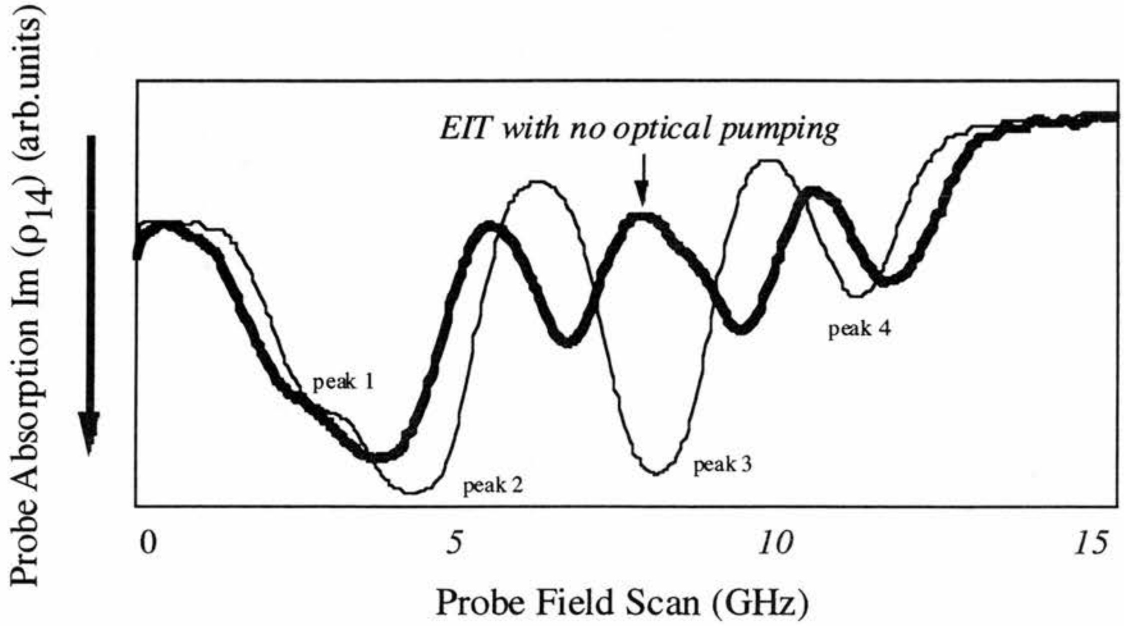

Figure 4.7.1: *Experimental trace of Im (ρ_{14}) (proportional to probe field absorption) vs probe field detuning in the presence (bold line) and absence (faint line) of the coupling laser. The coupling field power equals 800 mW. The four absorption peaks, from left to right, correspond to peak 1 (^{87}Rb,F=2), peak 2 (^{85}Rb,F=3), peak 3 (^{85}Rb,F=2), peak 4 (^{87}Rb,F=1) for the probe field transition $5S_{1/2}$ - $6P_{1/2}$. Maximum absorption on peak 3 is 82%. Induced transparency removes 73% of absorption, in the absence of optical pumping.*

be approximately 1.3 GHz. As it is shown in the experimental trace, there is no optical pumping present. This is deduced because we do not observe a corresponding increase in the absorption of peak 2 (^{85}Rb, F=3), which would accompany the observed reduction in absorption if it was due to optical pumping.

Figure 4.7.2 depicts experimental results of EIT at various coupling field powers. There is correlation in terms of the relationship between coupling field power and the level of transparency. As the coupling field power is reduced the amount of EIT is significantly reduced as well and the EIT window is getting smaller for low coupling field power. The results show that when the coupling field is 800 mW the magnitude of transparency is the highest observed. When the coupling field is 200 mW there is obviously a transparency window roughly half of its initial magnitude at 800 mW. Coherently induced transparency has almost disappeared for coupling field power of 50 mW. Throughout all these observations there is a noticeable absence of optical pumping, the evidence, as before, being no observable increase in peak 2.

The effects of detuning the coupling laser are demonstrated in figure 4.7.3 and figure 4.7.4. These experimental traces were obtained using a coupling field power of 800 mW and 200 mW respectively. In both figures the top trace was obtained with the coupling laser on resonance with peak 3 (^{85}Rb, F=2). As the detuning of the coupling laser is increased the transparency window shifts away from resonance. This movement can be mapped by observing the changing positions in figure 4.7.3 and magnitudes of the two Autler-Townes peaks associated with the transparency. These are marked with solid vertical lines, obtained by calculation. These lines can be seen to diverge as the observed Rabi frequency increases because of the increased detuning from peak 3 (^{85}Rb, F=2), see equation 4.7.1. It is also evident that as the frequency of the coupling laser is moved away from resonance towards one of the split Autler-Townes absorptions, that component closest to the unsplit level (the higher frequency component in this case), is enhanced while the other component is simultaneously reduced in magnitude. Previous results in Cascade and Λ schemes have shown a velocity selected feature , *Moseley et al.* which is not observed in this case due to the reduction of any two-photon process with detuning in a V-type scheme.

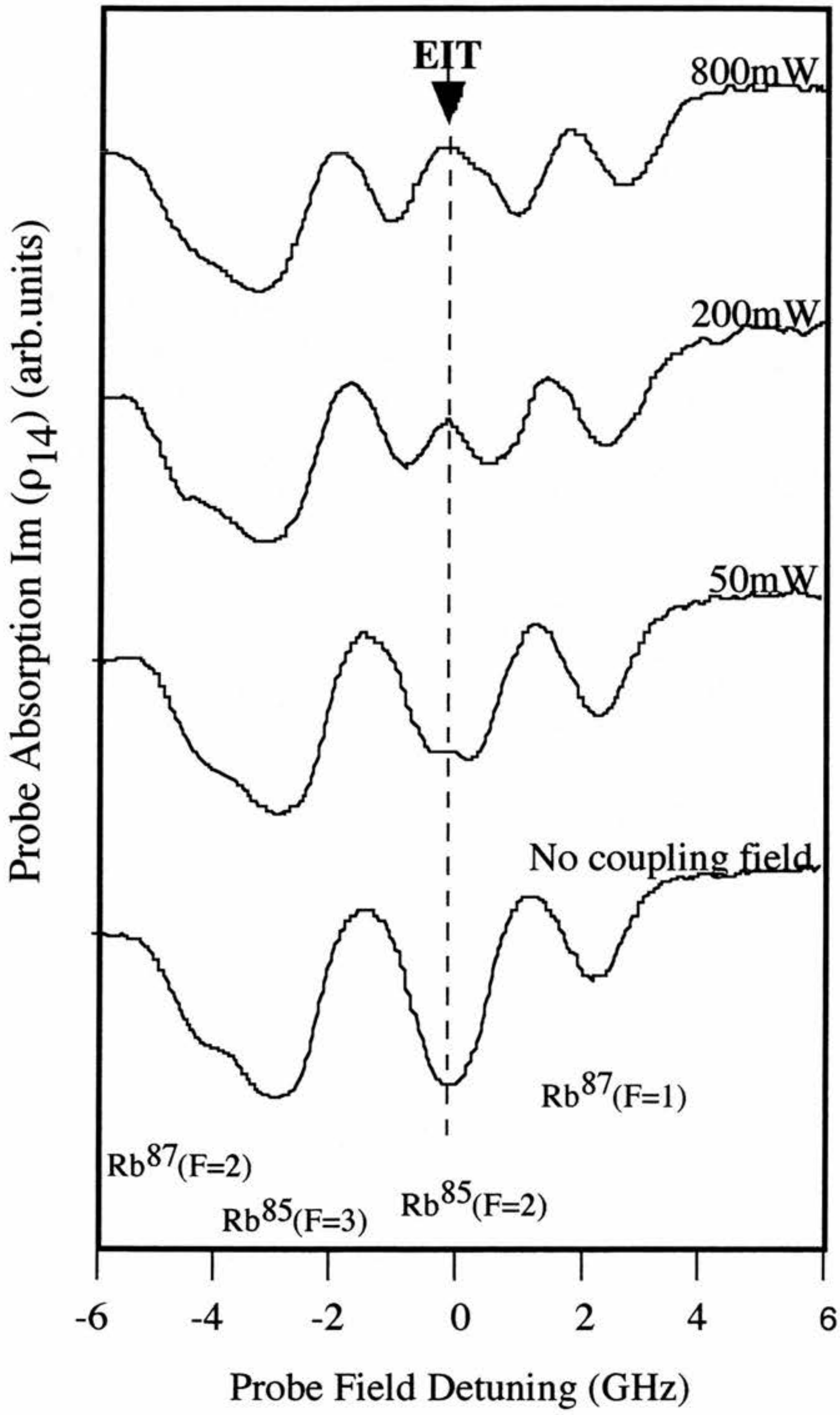

Figure 4.7.2: *Experimental traces of Im (ρ_{14}) (proportional to probe field absorption) vs detuning of the probe field at various coupling field powers 0 mW, 50 mW, 200 mW, and 800 mW.*

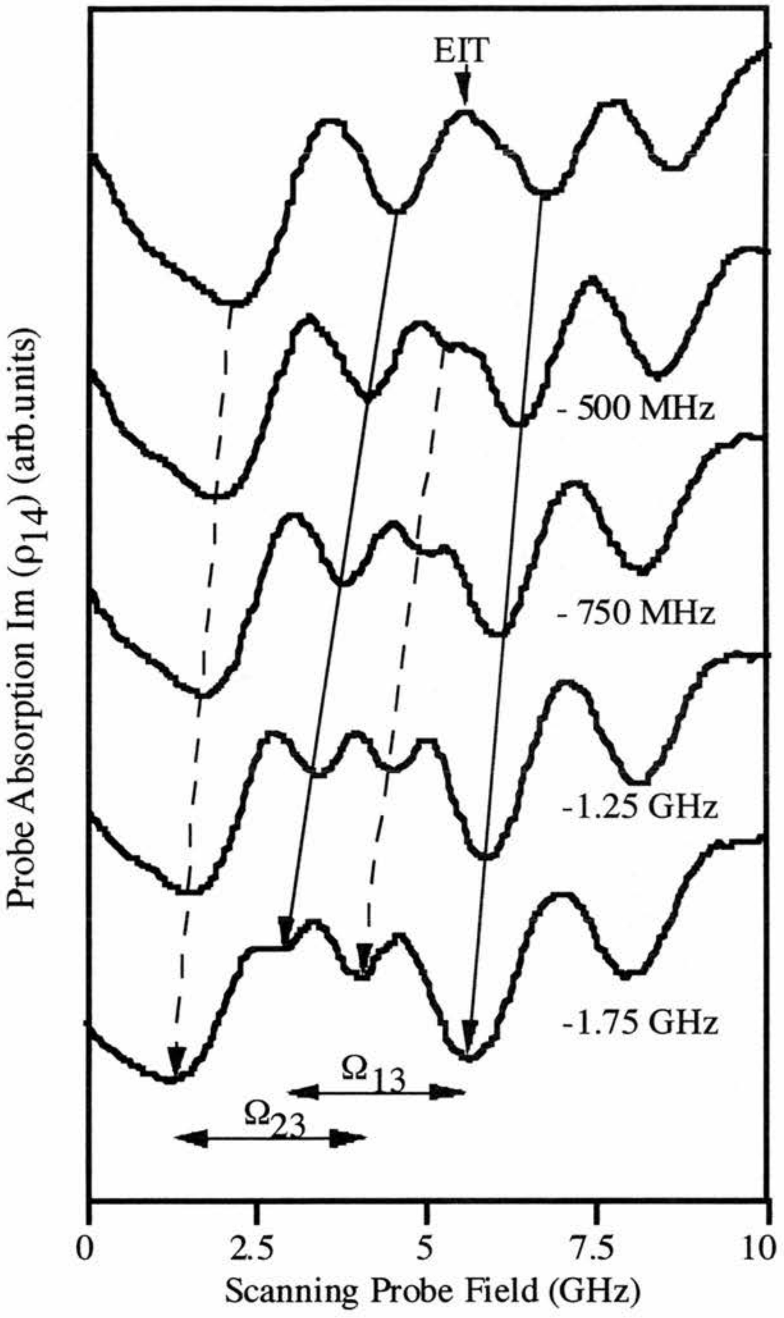

Figure 4.7.3: *Experimental traces of Im (ρ_{14}) (proportional to probe field absorption) vs detuning of the probe field for various coupling laser frequency detunings from resonance with peak 3 (^{85}Rb,F=2), in the range of -500 MHz to -1.75 GHz. The coupling field power equals 800 mW. The solid lines map the evolution of the Autler-Townes components associated with peak 3 (^{85}Rb,F=2), while the dashed lines map the evolution of the Autler-Townes components associated with peak 2 (^{85}Rb,F=3).*

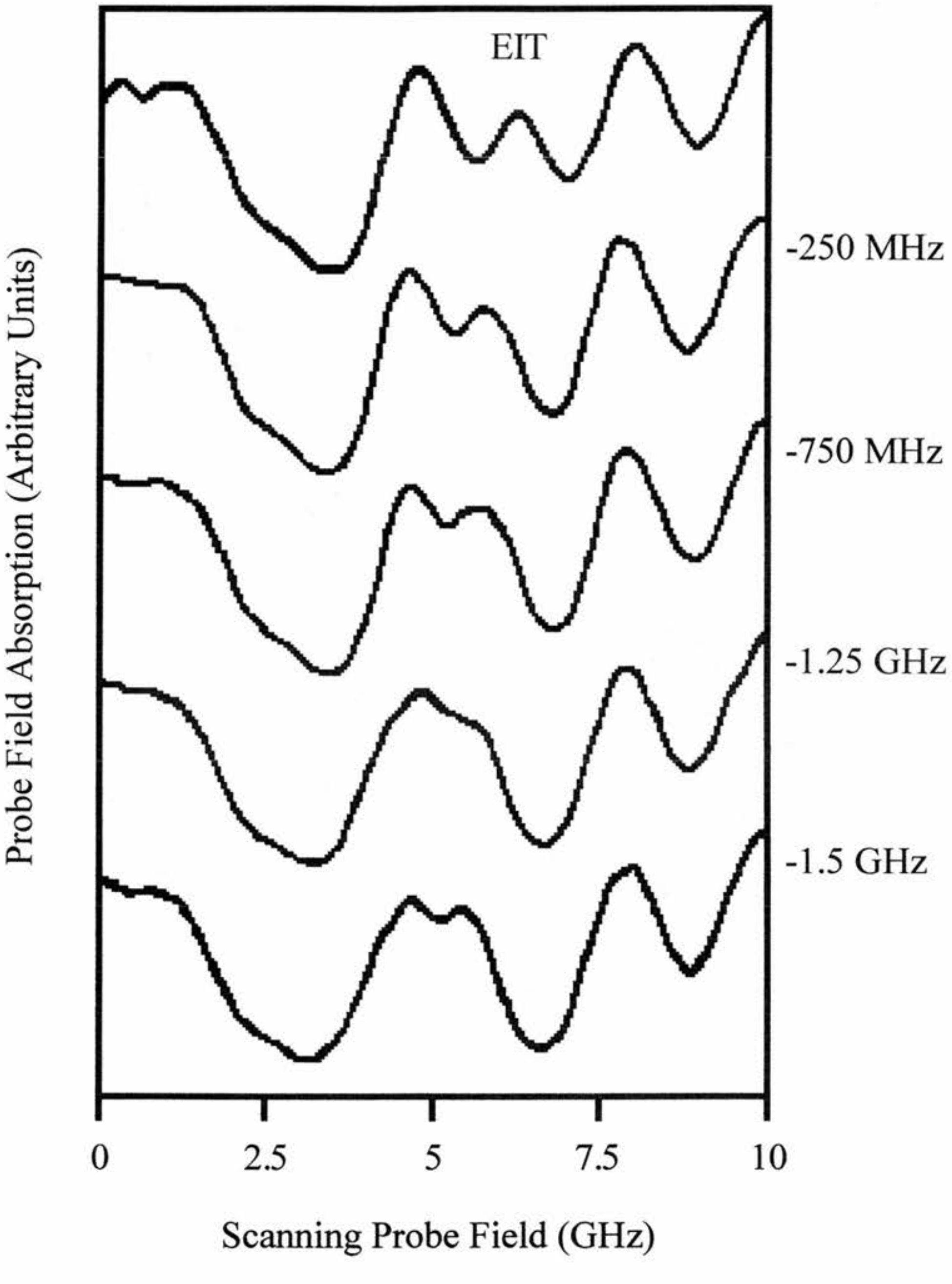

Figure 4.7.4: *Experimental traces of Im* (ρ_{14}) *(proportional to probe field absorption) vs detuning of the probe field for various coupling laser frequency detunings from resonance with peak 3* (^{85}*Rb,F=2), in the range of -250 MHz to -1.5 GHz. The coupling field power equals 200 mW.*

In addition to the splitting observed on peak 3 (^{85}Rb, F=2), coherently induced transparency is simultaneously observed on peak 2 (^{85}Rb, F=3). This occurs as a result of the high coupling field strength and dipole matrix element of the $5S_{1/2}$ - $5P_{3/2}$

transition. The Autler-Townes components associated with this additional transparency are shown by the dashed vertical lines in Fig 4.7.3. These lines converge because the detuning from level ^{85}Rb, F=3 decreases as the coupling laser frequency moves away from resonance with peak 3 and towards peak 2.

Figure 4.7.5 depicts the analysis of a specific detuning of -1.75 GHz from resonance with peak 3 (^{85}Rb, F=2) using

$$\bar{\Omega} = \sqrt{\Omega^2 + \Delta^2} \tag{4.7.1}$$

where $\bar{\Omega}$ is the observed Rabi splitting and Ω and Δ are the relevant, on resonance, the Rabi frequency and the detuning, respectively. This demonstrates agreement between theoretical analysis and the experimentally observed trace. This analysis can be readily extended to predict all of the splittings observed in figure 4.7.3 as a function of detunings.

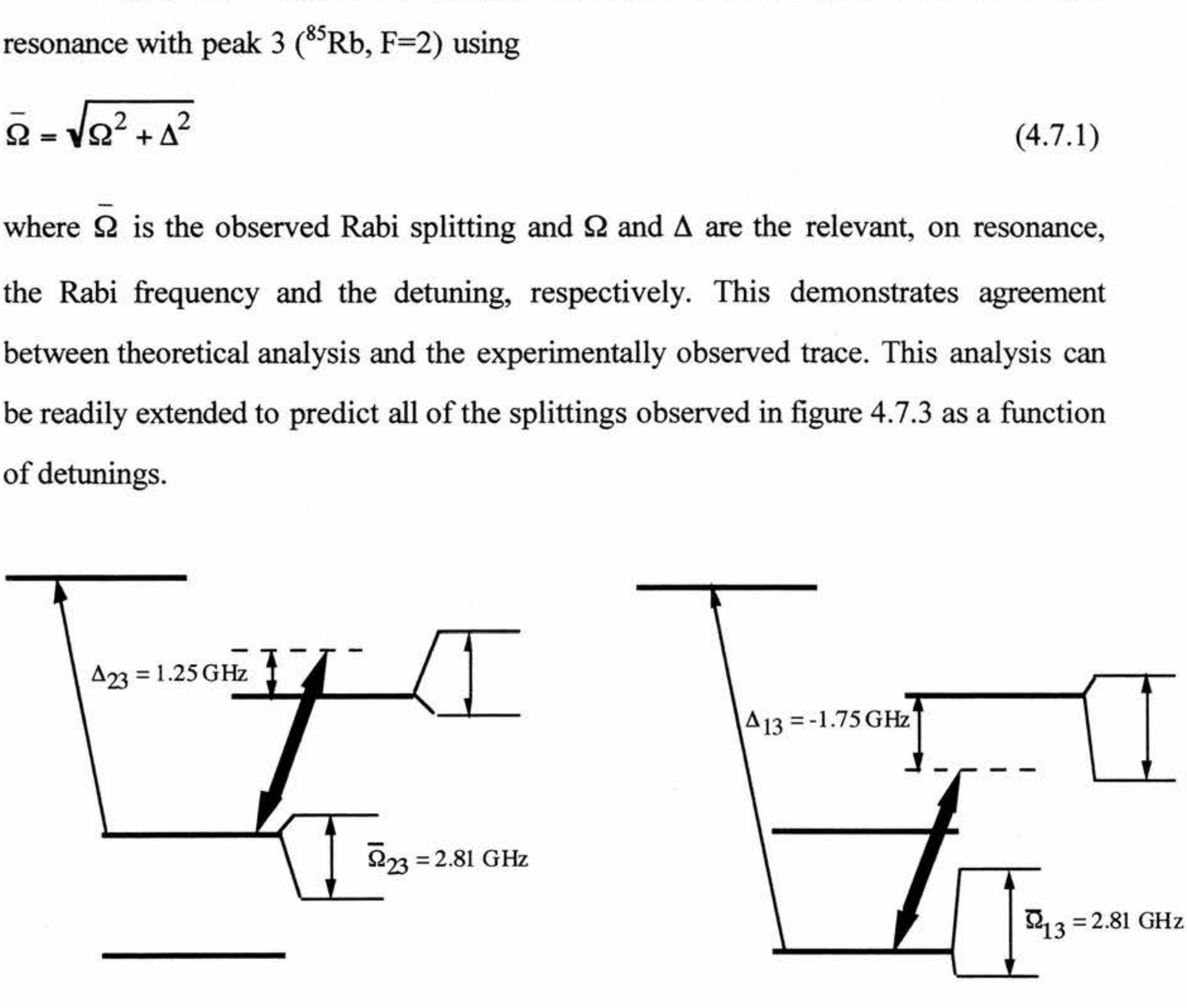

a) b)

Figure 4.7.5: *The last experimental curve of figure 4.7.3 may be explained, using the energy level picture of the coupling field at a power 800 mW, as follows: Detuning from peak 3 (^{85}Rb,F=2) by -1.75 GHz corresponds to a) An applied detuning of 1.25 GHz to peak 2, (^{85}Rb,F=3). b) An applied detuning of -1.75 GHz to peak 3 (^{85}Rb,F=2). The positions of the Autler-Townes components are shown split by the observed Rabi frequencies, $\bar{\Omega}_{13}$ and $\bar{\Omega}_{23}$, in which the detuning is taken into account in both a) and b) cases.*

4.8 Discussion-Comparison of theory and experiment.

The experimental traces have shown transparency on a blue probe in the presence of a strong infrared field. It is clear in the observations that transparency is induced at line centre of peak 3 and optical pumping is absent, at Rabi frequencies close or higher than the Doppler width of the probe transition. This is evidenced by the lack of an increase in absorption on the other hyperfine transition, peak 2. In order to give a brief explanation to the experimental results, we may now consider the four level energy scheme of section 4.1b.

Our theoretical model includes a collisional mixing rate between the two hyperfine levels of the ground state of ^{85}Rb. The hyperfine levels of the ground state are close enough for collisions to cause mixing of the population between the hyperfine sub-levels, because the kinetic energy of the atoms based on a cell temperature of around 130 °C, exceeds the energy separation of these states which is 3 GHz. Figure 4.8.1 depicts the relative populations in the ground states $|1>$ and $|2>$ for coupling field Rabi frequency Ω_c=2GHz (the highest observed) as a function of the ground state collisional mixing rate. The faint line represents the population in level $|1>$ and the bold line the population of level $|2>$, respectively. The dashed lines represent the thermal equilibrium of the populations (ρ_{11}:ρ_{22}=5:7). The graph shows that for a mixing rate of 200 MHz the ground state populations return to within 10% of their equilibrium values.

Therefore, if we make the assumption that the collisional mixing rate equals 200 MHz, we deduce the theoretical curves of figure 4.8.2. Figure 4.8.2(a) shows a trace of the probe field absorption as a function of detuning obtained by experiment with coupling field powers 800, 200, 50 and 0 mW. The theoretical results obtained by density matrix analysis of a four level model, using a mixing rate of 200 MHz are depicted in figure 4.8.2 (b). In this instance optical pumping is absent as predicted theoretically from the distribution of the ground state populations. These theoretical results agree more accurately with the experimental traces.

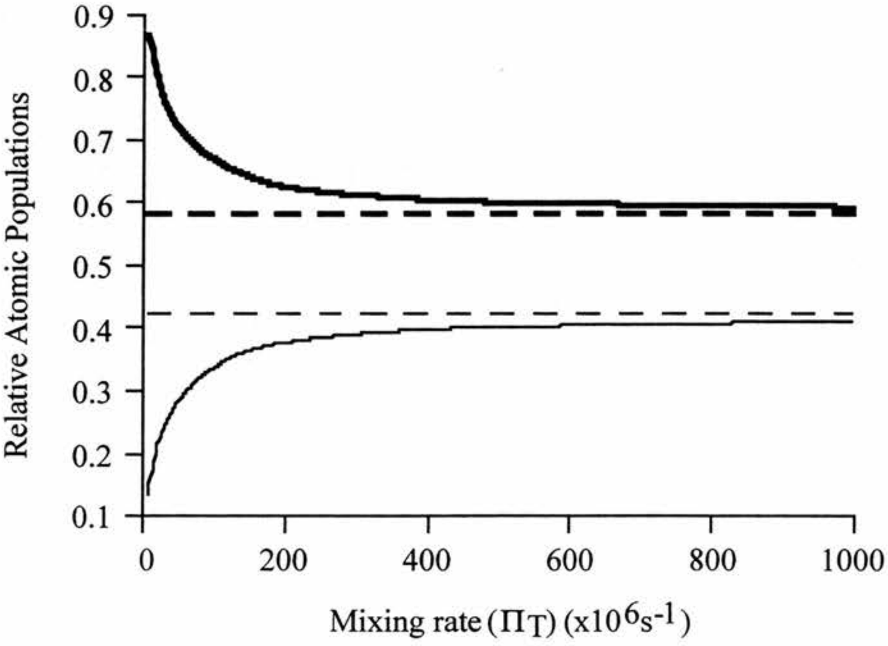

Figure 4.8.1: *The relative population in the hyperfine ground states, level |1> is represented by a faint line and level |2> by a bold line. The thermal equilibrium values are indicated by dashed lines.*

However, the calculated mixing rate for the experimental conditions has a value of 50 kHz (see section 4.4), which is less than that required to explain the experimental results. While it is true that the cross-section for the collisions may be greater, than that for collisions upon which the calculation of the collisional rate was based, the difference in the present parameters is not sufficient to explain a rate of 200 MHz. It is possible that mixing in the cell may be increased by cell impurities (existence of another gas), partial loss of vacuum pressure, temperature gradient in the cell, or additional collisions with the cell walls. There is no direct evidence to support this explanation of the experimental results.

As shown in the both the experimental and theoretical traces, the transparency for low coupling field Rabi frequencies (i.e. less than half of the Doppler width)

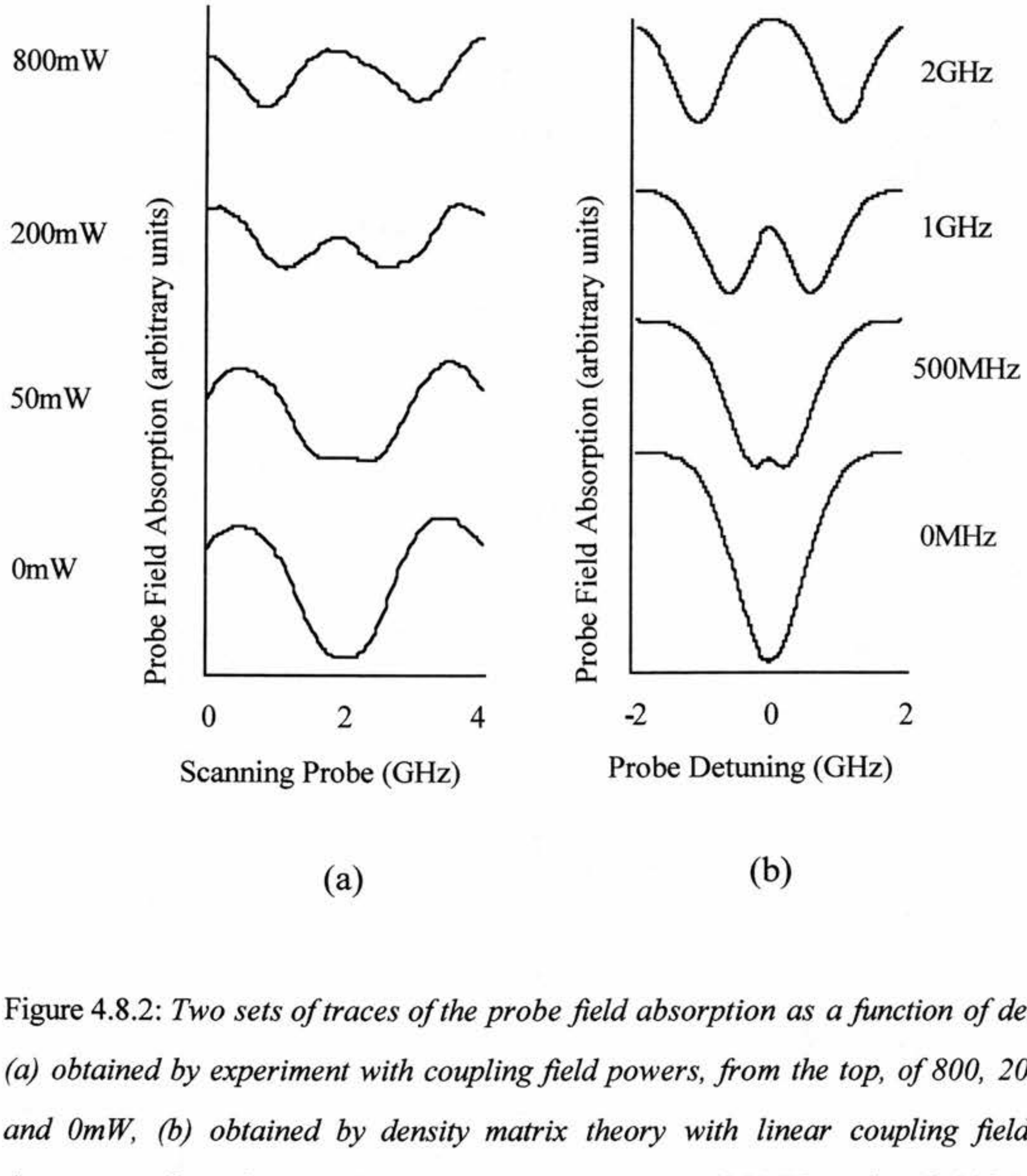

Figure 4.8.2: *Two sets of traces of the probe field absorption as a function of detuning (a) obtained by experiment with coupling field powers, from the top, of 800, 200, 50, and 0mW, (b) obtained by density matrix theory with linear coupling field Rabi frequencies, from the top, of 2GHz, 1GHz, 500MHz, and 0MHz and with 200 MHz of collisional mixing rate.*

expected in the case of the V-scheme is not observed. Hence, the advantage of a V-scheme as presented in Chapter 5 is not seen. Of course, the reason the theoretical curves do not show the onset of transparency at the lower Rabi frequencies, is the increased dephasing rate due to the high rate of collisional mixing. In a three-level V-

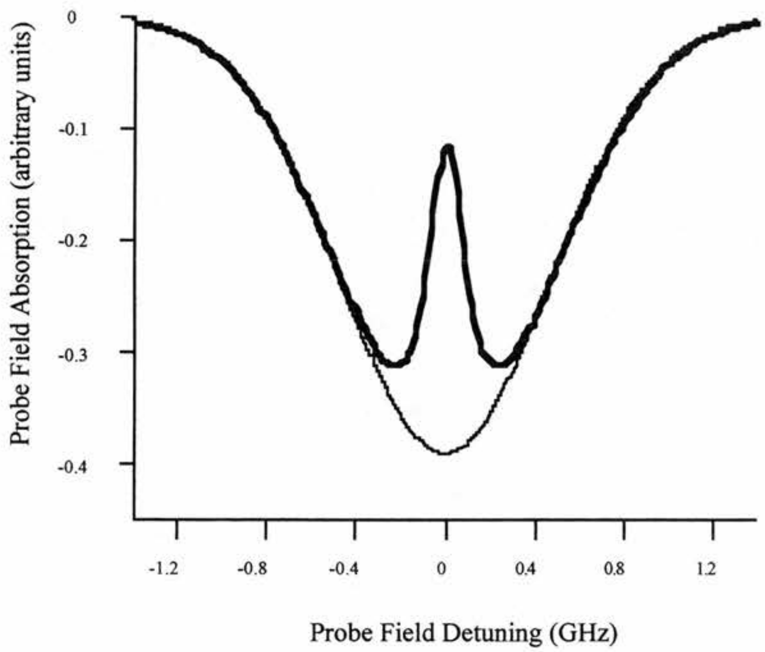

Figure 4.8.3: *The probe field absorption is plotted as a function of the probe field detuning in a three level V-scheme. The faint line shows the absorption in the absence of the coupling field and the bold line shows EIT for a coupling field Rabi frequency* $\Omega_c=100$ *MHz.*

type scheme in which optical pumping is precluded, EIT is present for Rabi frequencies much less than the Doppler width of the probe transition, as shown in figure 4.8.3. We can modify the four-level system in such a way that it approaches a three-level scheme. If we set $\Gamma_{32}=0$ in figure 4.1.1 and $\Gamma_{31}=40$ MHz, then there will be no population decay in level |2> of the ground state and hence, no optical pumping into this level. We can now introduce a collisional mixing rate of 50 kHz, which is very small in relation to dephasing the atomic coherences. (The collisional mixing rate is included in the dephasing rates.) With such a small value the dephasing rates are only determined by the radiative decay of the atomic levels. In this four-level model the hyperfine ground states are treated as a single level.

The probe field absorption is plotted as a function of the probe field detuning, for a coupling field Rabi frequency of 100 MHz, in the modified four-level model, see figure 4.8.4. The value of the Rabi frequency for transparency is obviously much smaller than the Doppler width of the probe transition, which is approximately 1.3 GHz. Transparency is present on line centre even in the case of Rabi frequencies much less than the Doppler width. This analysis demonstrates that even in the absence of optical pumping the theoretical model predicts a significant reduction in absorption due to EIT alone, for low coupling field Rabi frequencies.

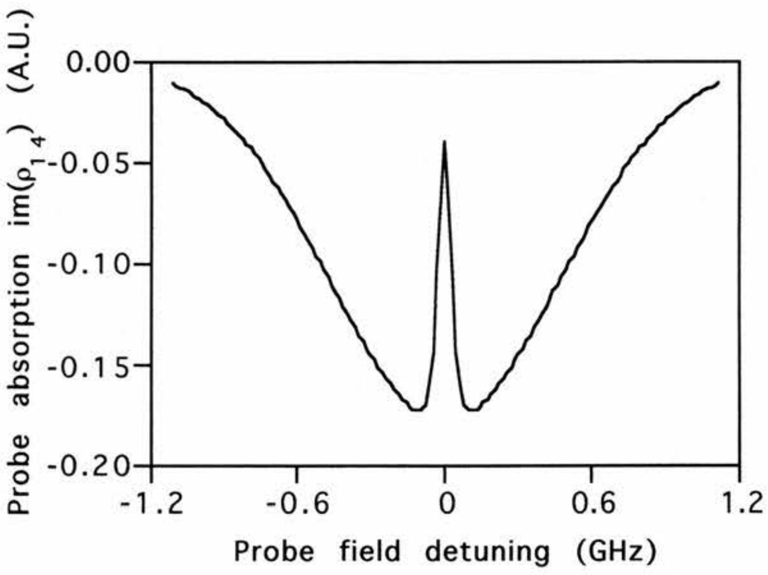

Figure 4.8.4: *The probe field absorption is plotted as a function of the probe field detuning, in a modified four level model. The Rabi frequency of the coupling field is* Ω_c*–100MHz. In this model the hyperfine splitting of the ground state is treated as a single level.*

There are two approaches to explaining the lack of observation of EIT at low coupling field powers. The first is that the collisional mixing rate is as high as 200

MHz. This not only explains the delay in the onset of transparency with increasing Rabi frequency, but also accounts for the lack of any observed optical pumping.

The second approach is that the collisional mixing rate is as calculated, but that coupling field absorption plays a role. In order to render the medium transparent, the coupling field must interact with its entire thickness. This is not the case for low coupling field powers.

To understand why the coupling field is absorbed, we must consider the relevant experimental conditions. The V-scheme of figure 4.1.1 contains a coupling field transition decay rate which is higher than that of the probe field transition. The blue transition decay rate is 8 MHz, whereas the infrared transition decay rate is 40 MHz. This occurs because the probe field transition has a comparatively weak dipole matrix element. In order to ensure a high signal to noise ratio for the probe absorption measurements, it is necessary to increase the particle density and hence, to raise the temperature in the cell. Since the coupling transition decay rate is high, the increase in particle density may lead to a corresponding absorption of the coupling field even in strong field powers.

Coupling field absorption results in the reduction of the Rabi frequency with distance into the cell. This has an impact on the probe absorption profile and on the level of the induced transparency. While significant transparency may be induced at the start of the vapour cell, this would be masked by the absorption of the probe field by atoms towards the end of the cell, where the coupling field would be reduced. Measurements of the coupling field absorption were made for a range of powers and temperatures. The results are depicted in figure 4.8.5.

The probe field absorption in the absence of the coupling field was measured, to verify the temperature that corresponded to that used in the experiment. A probe field absorption similar to that obtained in the experiment occurred for a cell temperature of 125 °C. As shown in figure 4.8.5 coupling field absorption is present at this temperature and it depends on the coupling laser power. For the low power results of 50 mW power, figure 4.8.5 shows that approximately 80% of the coupling

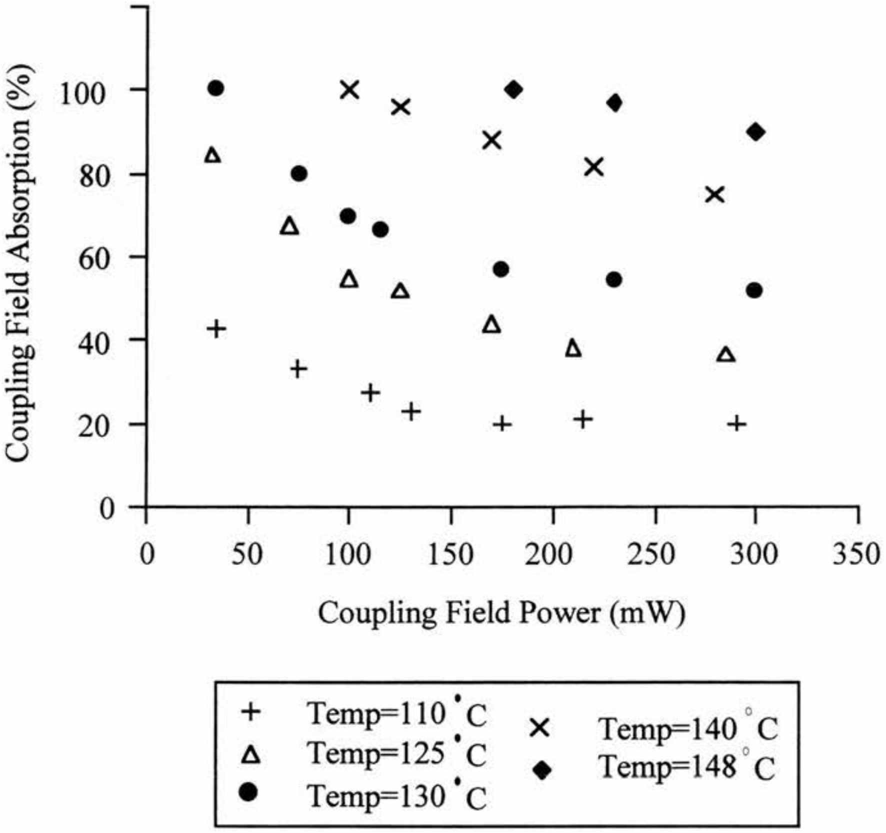

Figure 4.8.5: *Experimentally measured coupling field absorption as a function of the incident coupling field power at cell temperatures of 110, 125, 130, 140 and 148°C.*

field is absorbed in the 2 cm Rb cell. As a result, there is almost no coupling field to interfere with the probe field, and induce the desired transparency window.

The absorption of coupling field occurs in any mismatched system and is not linked to Doppler broadening effects. In our experiment the power at which EIT may be observed is limited by coupling field absorption rather than Doppler effects. Therefore, there is no advantage to be gained by moving to Doppler-free geometry. In order to observe transparency for coupling field Rabi frequencies lower than the Doppler width, we must choose a particle density in which coupling field absorption is negligible.

Of course, the latter approach does not explain the lack of observed optical pumping.

4.9 Conclusions.

In conclusion, we have reported the first experimental observation of coherently induced transparency in a Doppler-broadened V-type system employing mismatched wavelengths. The transparency was induced on a transition in the blue spectral region by an infrared coupling field. This has been achieved with cw laser sources. EIT was realised when $\lambda_c > \lambda_p$, for coupling field Rabi frequencies equal to or greater than the Doppler width of the probe transition. Although, we have not experimentally verified the transparency for low coupling field strengths, the theory showed that EIT would still be observed at coupling Rabi frequencies less than the Doppler width. The only limiting factor for achieving EIT in low Rabi frequencies is the coupling field absorption at high particle densities, rather than Doppler effects. Coupling field absorption can be compensated by reducing the operating cell temperature.

The significance of this work lies in the fact that it opens up a possible pathway to the realisation of EIT and subsequently to the realisation of inversionless gain. This work will lead us to a shorter wavelength for a lasing transition, using mismatched geometry.

Theoretical modelling has demonstrated the role of coherence in creating the transparency window. Importantly, the coherence is still the factor determining the level of transparency at high levels of Autler-Townes splitting. The lack of optical pumping is demonstrated experimentally, by the reduction of absorption on one hyperfine transition (the one on resonance), without the corresponding increase on the other transition.

All the expected characteristics of EIT, like the power and the detuning dependence have been demonstrated in the experimental results. As previous work has shown, *Zibrov et al* coherently induced transparency forms the first step for the production of inversionless gain. To achieve this it is necessary to move a small amount of population into $6P_{1/2}$, the upper level of the probe transition. An incoherent pump can be employed to fulfil this condition in the present system. It is necessary to utilise a pump source that is incoherent to ensure that the driving coherence on the $5P_{3/2}$ - $6P_{1/2}$ transition is not disturbed.

The results presented in this chapter represent the realisation of the first step in the process of creating an inversionless laser in the blue spectral region, by producing transparency at 422 nm in a V-type Doppler-broadened system. In addition to furthering the short wavelength aims of inversionless lasing, the results presented show the important role of the mechanism of EIT and the consequent quantum coherence effects.

References

Cohen-Tannoudgi M. and Kastler D., "Optical Pumping", Progress in optics, **V**, p.3-81

Fulton D.J, Quantum Interference Effects: EIT and focusing, Ph.D. thesis, University of St. Andrews, 1996.

Fulton D.J., Shepherd S., Moseley R.R, Sinclair B.D. and Dunn M.H., "Continuous-wave EIT: A comparison of V, Λ and cascade systems." Physical Review A, **52**, p.2302 (1995).

Moseley R.R., Sum-frequency mixing and quantum interference in 3-level atoms, Ph.D. thesis, University of St.Andrews, 1994.

Moseley R.R., Shepherd S., Fulton D.J., Sinclair B.D. and Dunn M.H , "Electomagnetically Induced Focusing", Physical Review A, **53**, p. 408 (1996)

Moseley R.R., Shepherd S., Fulton D.J., Sinclair B.D. and Dunn M.H , "Two-photon effects in CW electromagnetically induced transparency", Opt.Commun., **119**,p.61 (1995).

Shepherd S., Fulton D.J., and Dunn M.H, " Wavelength dependence of coherently induced transparency in a Doppler-broadened cascade medium", Physical Review A, **54**, p.5394 (1996).

Zibrov A.S., Lukin M.D., Nikonov D., Hollberg L., Scully M.O, Velichansky V.L. and Robinson H.G., "Experimental demonstration of laser oscillation without population inversion via quantum interference in Rb", Physical Review Letters, **75**, p.1499 (1995)

Chapter 5

Prediction of inversionless gain in a mismatched Doppler-broadened medium

---

5.1 Introduction.

The theoretical work presented in this chapter acts to show that inversionless gain is predicted in a Doppler broadened V-scheme in which the probe laser frequency is approximately twice that of the coupling laser. It has already been demonstrated that for inversionless systems to be useful, one must utilise matched wavelengths geometry (i.e. the coupling laser wavelength comparable to the probe lasing wavelength). The first inversionless laser oscillation in a Rb vapour was observed in a V-scheme, in which both the probe and coupling laser were infrared laser sources, *Zibrov et al.* A matched scheme was employed to avoid Doppler- broadening effects. In another experiment inversionless lasing was achieved using an atomic beam as an interaction medium, *Padmabandu et al.* This medium was used to provide operation in a Doppler- free regime.

Until recently inversionless gain has only been reported either in a Doppler - free medium or where the Doppler effect was reduced through a matched energy configuration. We have demonstrated experimentally that CW EIT is possible in a mismatched Doppler broadened system and furthermore we present a theoretical analysis of the production of inversionless gain in such a scheme. We propose a viable alternative to Doppler-free systems based on a V-scheme in which the Autler-Townes splitting and EIT are exploited to overcome the effects of Doppler broadening.

In this chapter a comparison is made of inversionless gain achieved via EIT in a Doppler broadened matched and mismatched wavelength systems. In this study all parameters, like decay rates, are made equal except the transition wavelength. It is shown that the gain produced for a given incoherent pumping rate is greater in the matched case than the mismatched wavelengths. The inversionless gain in the mismatched scheme is still significant, even in the presence of Doppler broadening.

The mismatched scheme uses a wavelength of the probe shorter than that of the coupling wavelength. This leads us to gain in the shorter wavelength regime.

In this comparison of matched and mismatched schemes, the mismatched scheme has an additional advantage over the matched scheme. It allows us to pump in two directions. With both schemes we predict inversionless gain using a R_{13} incoherent pump source, see figure 5.2.1, for the population transfer to the upper level of the probe transition. The mismatched scheme may use a R_{23} pump source as an alternative for pumping to level |3>. The matched scheme does not exhibit gain with such a pump to level |3>.

EIT is still present in mismatched configurations, for Rabi frequencies less than the Doppler width. Doppler broadening does not affect the coherence of the system and EIT is possible for low Autler-Townes splittings. When there is not additional collisional dephasing in the system, EIT and, hence inversionless lasing, are produced in mismatched schemes. The existence of Doppler broadening does not prevent the production of EIT and inversionless gain in mismatched V-type systems.

The real system to observe inversionless gain experimentally is a V-scheme in Rb vapour, using 422 nm as the lasing transition (probe beam) and 780 nm as the coupling laser field. Although there are sources to cover 422 nm it is important to demonstrate inversionless gain in this spectral region. Even in a mismatched geometry it is still possible to exploit quantum coherence phenomena for the realisation of such inversionless gain.

5.2 Theoretical analysis of a matched and mismatched scheme.

A theoretical comparison between a matched and a mismatched scheme has been made. In these schemes all parameters are made artificially equal, except for the transition wavelengths. The two scheme utilised for this comparison are depicted in figure 5.2.1. This figure shows the 3 energy level configuration for a matched and mismatched V-schemes, which were employed in the theoretical comparison presented in this chapter.

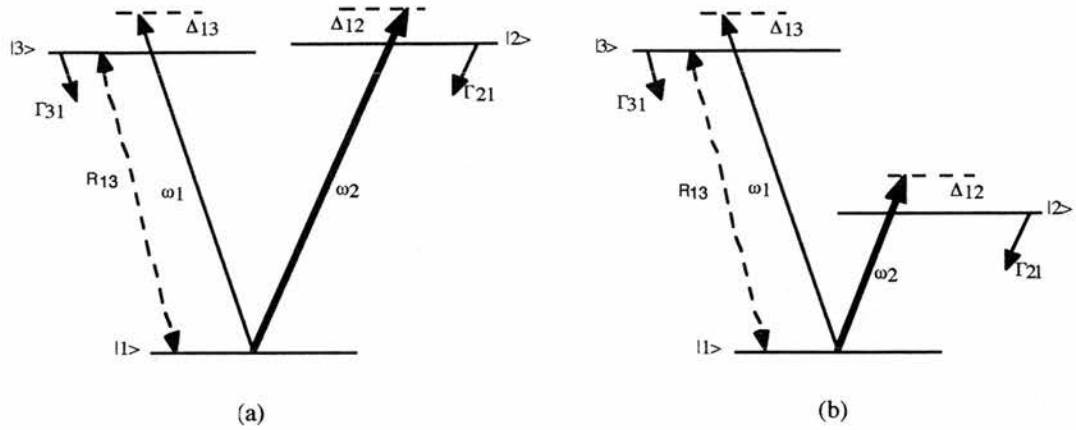

Figure 5.2.1: *Energy level configurations of the (a) matched and (b) mismatched 3-level V schemes employed in the theoretical comparison presented in this chapter.*

The mismatched scheme corresponds exactly to a real atomic scheme in rubidium where the probe transition is $5S_{1/2}$-$6P_{1/2}$ and the coupling transition is $5S_{1/2}$-$5P_{3/2}$. The hyperfine structure of Rubidium is ignored within the density matrix model and a simple 3-level V-scheme is considered. The wavelength of the probe beam is set to 421.6 nm and that of the coupling field to 780 nm for this mismatched scheme. In figure 5.2.1 for the mismatched case |1> is the ground state $5S_{1/2}$, |2> is the excited state $5P_{3/2}$ and |3> is the excited state $6P_{1/2}$. The probe field ω_1 is on resonance with the transition ω_{13} and the coupling field ω_2 is on resonance with the transition ω_{12}. The probe and the coupling fields can be detuned by Δ_{13} and Δ_{12} , from these transitions. The decay rates are set Γ_{21} and Γ_{31} from the two excited states.

The matched system is also based on rubidium, with the probe transition $5S_{1/2}$-$6P_{1/2}$ and the coupling transition $5S_{1/2}$-$6P_{3/2}$. The wavelength of the probe beam is set to 421.6 nm and that of the coupling field to 420.2 nm. In the scheme of figure 5.2.1 for the matched case |1> is the ground state $5S_{1/2}$, |2> is the excited state $6P_{3/2}$ and |3> is the excited state $6P_{1/2}$. The probe field is again ω_1 and is resonant with

ω_{13} transition slightly detuned by Δ_{13} and the coupling field ω_2 is on resonance with ω_{12} detuned by Δ_{12}. An incoherent pump is employed on the probe transition so as to transfer a small fractional population to the upper state, important for inversionless gain.

In both schemes the probe beam is the same transition. However, the decay rates of the coupling field transitions are different in each scheme. In order to set all parameters the same, the decay rate of the excited state $6P_{3/2}$ is set equal to that of the excited state $5P_{3/2}$. It has been artificially altered from its true value, for the purpose of the comparison. The temperature of the cell is taken to be 130° C. This temperature corresponds to an experimentally measured absorption of approximately 80% on the employed probe transition.

Theoretical modelling of these schemes was carried out using standard density matrix analysis for a 3 level V-scheme. The rates of change of the density matrix elements can be derived, yielding six simultaneous equations. Thus the equations for the closed V-scheme are as in Chapter 2:

$$\dot{\rho}_{11} = i\Omega_c(\tilde{\rho}_{21} - \tilde{\rho}_{12}) + i\Omega_p(\tilde{\rho}_{31} - \tilde{\rho}_{13}) + R_{13}(\rho_{33} - \rho_{11}) + \Gamma_{21}\rho_{22} + \Gamma_{31}\rho_{33} \tag{5.1a}$$

$$\dot{\rho}_{22} = i\Omega_c(\tilde{\rho}_{12} - \tilde{\rho}_{21}) - \Gamma_{21}\rho_{22} \tag{5.1b}$$

$$\dot{\rho}_{33} = i\Omega_p(\tilde{\rho}_{13} - \tilde{\rho}_{31}) - \Gamma_{31}\rho_{33} - R_{13}(\rho_{33} - \rho_{11}) \tag{5.1c}$$

$$\dot{\rho}_{12} = -i(\Delta_{12} - i\gamma_{12})\tilde{\rho}_{12} + i\Omega_c(\rho_{22} - \rho_{11}) - i\Omega_p\tilde{\rho}_{32} \tag{5.1d}$$

$$\dot{\rho}_{13} = -i(\Delta_{13} - i\gamma_{13})\tilde{\rho}_{13} + i\Omega_p(\rho_{33} - \rho_{11}) + i\Omega_c\tilde{\rho}_{23} \tag{5.1e}$$

$$\dot{\rho}_{23} = -i(\Delta_{12} - \Delta_{13} - i\gamma_{23})\tilde{\rho}_{23} + i\Omega_c\tilde{\rho}_{13} - i\tilde{\rho}_{21} \tag{5.1f}$$

where the subscripts refer to the three levels, numbered from the lowest to the highest energy state, as indicated in figure 5.2.1. The incoherent pumping rate R_{13} was included to allow for the excitation of atomic population into the upper level of the probe transition. It is taken as an incoherent source so that it does not affect the coherence of the system. The angular Rabi frequencies are defined in equation 5.2a for the probe field and equation 5.2b for the coupling field:

$$\Omega_p = \frac{\mu_{13}E_1}{\hbar} \tag{5.2a}$$

$$\Omega_c = \frac{\mu_{12}E_2}{\hbar} \tag{5.2b}$$

where E_1 and E_2 are the electric-field strengths, and μ_{13} and μ_{12} are the dipole matrix elements for the probe and coupling transitions respectively. The detunings are defined in both schemes as follows:

$$\Delta_{13} = \omega_1 - \omega_{13} - k_1 V_Z \tag{5.3a}$$

$$\Delta_{12} = \omega_2 - \omega_{12} - k_2 V_Z \tag{5.3b}$$

where ω_1 and ω_2 denote the angular frequencies of the applied probe and coupling fields respectively, V_z is the atomic velocity along the cell length, the wavevectors k_1 and k_2 of the probe and coupling fields, respectively, are defined as $k_i=2\pi n/\lambda_i$, and ω_{13} and ω_{12} are the angular transition frequencies, of the energy separations of the atom.

The decay rates are $\Gamma_{31}=8\times10^6 s^{-1}$ and $\Gamma_{21}=40\times10^6 s^{-1}$ in both systems. The decay rate Γ_{21} of the $6P_{3/2}$ (coupling transition) is artificially set equal to that of the $5P_{3/2}$ state in order to set all parameters the same, except the wavelengths. The decay rate of the $6P_{1/2}$ state (probe transition) is the same in reality and it is not artificially altered. The coherence decay rates in both schemes are defined as :

$$\gamma_{12} = \frac{1}{2}(\Gamma_{21} + R_{13}) \tag{5.4a}$$

$$\gamma_{13} = \frac{1}{2}(\Gamma_{31} + 2R_{13}) \tag{5.4b}$$

$$\gamma_{23} = \frac{1}{2}(\Gamma_{31} + \Gamma_{21} + R_{13}) \tag{5.4c}$$

Both the decay rates and the incoherent pumping rate contribute to the dephasing of the transition. It is worth mentioning that in this model there is not any additional collisional dephasing rate, due to the temperature, because the hyperfine structure is ignored. The ground state collisional mixing rate is not included in our analysis and in that respect the system is ideal.

The equations 5.1a-5.1f are solved using steady state conditions and setting all time derivatives to zero. Equations 5.1a-5.1f provide 9 simultaneous equations for the real and the imaginary part of the coherences. We can then use the density matrix system Ax=B and solve for x, using Mathematica software. Doppler broadening is included by integrating over the velocity distribution. The solutions are values for the real and the imaginary part of the coherence which correspond to the refractive index and to the absorption-gain of the system and the amount of the population in each energy level.

5.3 Calculation of the absorption.

The absorption or gain of the system may be calculated from the gain coefficient of equation 5.3.1, as it was derived in chapter 2.

$$\gamma(\omega) = \frac{3A_{41}N\lambda^2 \operatorname{Im}(\rho_{14})}{16\pi n\Omega_{14}} \tag{5.3.1}$$

where A_{41} the Einstein coefficient of the particular transition, N the atomic population density per cubic metre, λ the wavelength, n the refractive index and Ω_{14} the angular Rabi frequency as it was defined in equation 5.2a. The absorption coefficient is directly proportional to the imaginary part of ρ_{13} in our case, which is related to the absorption or gain of the scheme.

The intensity of the optical field varies exponentially with distance according to $\exp[\gamma z]$, that is to say $I=I_0 \exp[\gamma z]$. The percentage of the absorption can be derived from $\{1-\exp[\gamma z]\}\times 100$. The atomic population density was calculated from equation 5.3.2.

$$N=P/kT \tag{5.3.2}$$

where P the pressure of the vapour (Newtons m^{-2}), k the Boltzmann's constant (JK^{-1}) and T the temperature (K).

The pressure for pure rubidium is given by, *Thompson and Xu*

$$\log_{10}P=10.875-4420.4/T \quad (5.3.3)$$

Here the pressure is in mTorr and the temperature in degrees Kelvin. The Einstein coefficients were taken from *Weise and Martin.*

5.4 Theoretical results.

Figure 5.4.1 depicts the on-resonance absorption as a function of the linear coupling field Rabi frequency, when there is no incoherent pumping rate. As it is shown in the graph the transparency is deeper in the matched system than the mismatched system. The absorption is bigger for the mismatched system even for high Rabi frequencies. However, the graph also shows that approximately 75% of the absorption is removed in the mismatched system, for coupling field Rabi frequency of only 10 MHz .

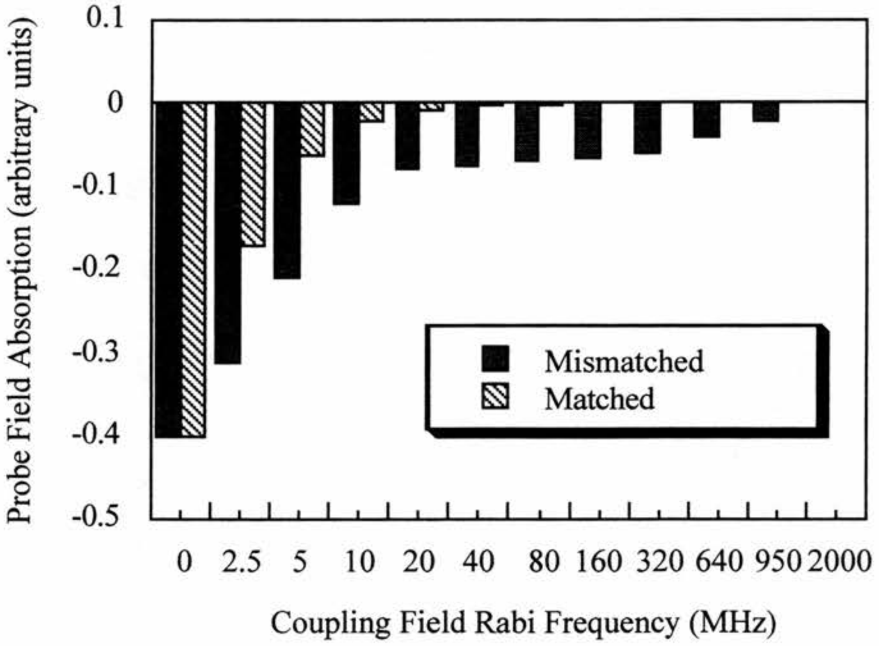

Figure 5.4.1: *Bar chart showing the 'on-resonance' absorption in the matched and mismatched systems for a range of coupling field Rabi frequencies. The vertical (absorption) scale is proportional to* $\rho^{i}{}_{13}$, *and hence the absorption coefficient.*

The Doppler width of the probe field is approximately 1.3 GHz and as is shown in the graph high transparencies are present in both schemes for coupling field Rabi frequencies much less than the Doppler width. Of course the matched system has the advantage over the mismatched system. Transparencies are reached more quickly in the matched than in the mismatched system.

Figure 5.4.2 shows how the absorption and the gain vary as a function of the probe field detuning, for a coupling field Rabi frequency of 160 MHz. The dashed line is the transparency in the absence of any incoherent pumping rate and the solid line is the inversionless gain that is achieved in both systems with an incoherent pumping rate of 10×10^6 s^{-1}. As is shown in the graph the gain on resonance for the mismatched scheme has only one peak on line centre, whereas the gain on resonance for the matched scheme is split into two components.

In tables I and II the results of a comparison between the matched and mismatched schemes are tabulated. Both tables contain values of the imaginary part of the coherence for the probe field ρ^i_{13}, both on resonance and the peak as well, along with the populations of the three levels ρ_{11}, ρ_{22} and ρ_{33}. The % absorption is calculated, along with the % gain and the gain bandwidth for a 2 cm cell at 130° C. The absorption is derived by setting the incoherent pumping rate to zero. Gain is then calculated by taking into account the incoherent pumping rate of 10×10^6 s^{-1} in both the matched and the mismatched systems. These values were derived for several Rabi frequenciesΩ_c=0 MHz, Ω_c=20 MHz, Ω_c=160 MHz, and Ω_c=950 MHz. All the Rabi frequencies are less than the Doppler width of the probe transition.

The imaginary part ρ^i_{13} of the density matrix is by convention negative for absorption and positive for gain. When there is no coupling field applied all the population remains in the ground state because the probe field is very weak.

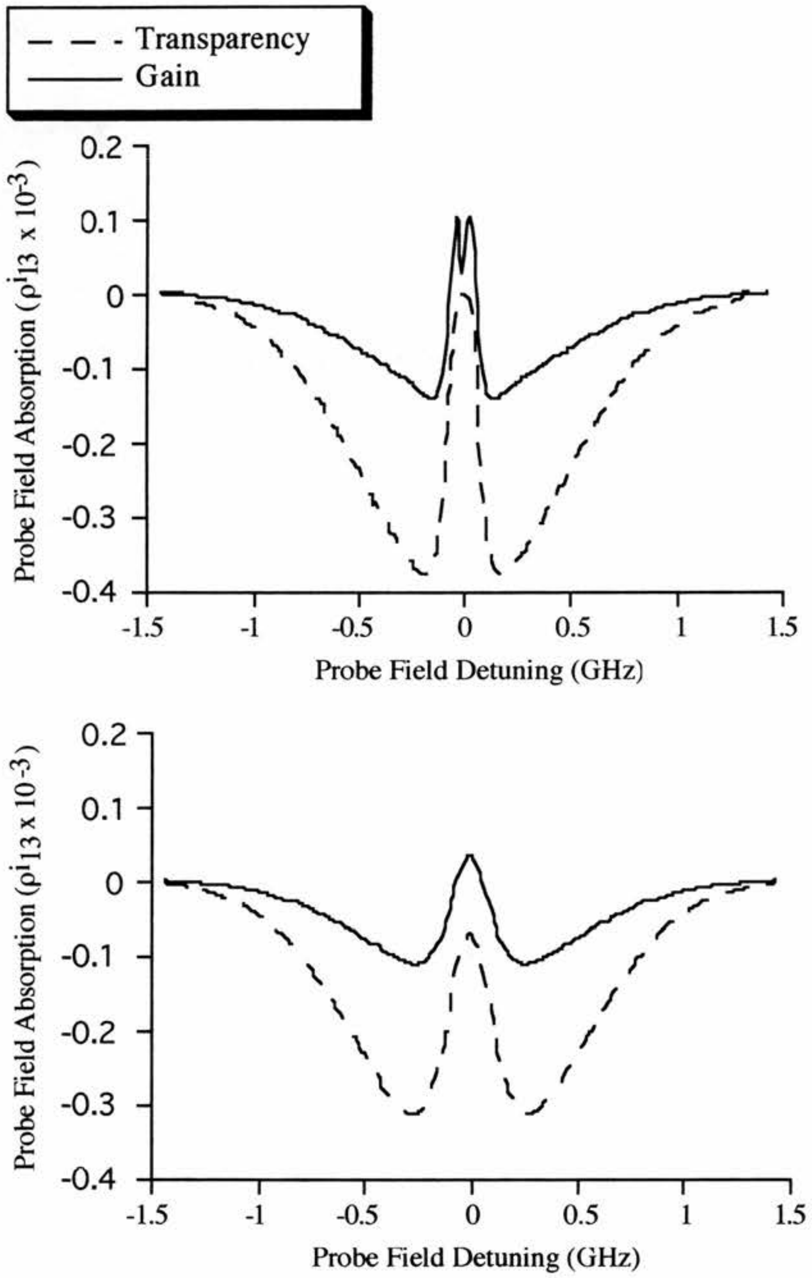

Figure 5.4.2: *The absorption as a function of probe field detuning in the absence and presence of incoherent excitation for (a) the matched and (b) the mismatched schemes. The dashed lines correspond to the transparency induced in the absence of incoherent excitation, and the solid lines represent the gain that may be achieved in each system with an incoherent pumping rate of* $10\times10^6 s^{-1}$.

That is why the population of the ground state has a value of 1. There is then straight forward absorption without any transparency window. This absorption is the same for both schemes because it refers to the same probe field transition.

As the coupling field is applied the absorption starts to reduce. As is presented in both tables the absorption is reduced more quickly in the matched scheme than in the mismatched. For a coupling field of 950 MHz the absorption in the matched scheme falls close to zero, whereas there is still 5% absorption in the mismatched configuration. However, the reduction of the absorption and hence the role of EIT are still significant in the case of the mismatched scheme. The population in level |1>is reduced as well and that of level |2> starts to increase, as the coupling field is turned on. The coupling field transfers more population in level |2> in the mismatched scheme than in the matched scheme. The population in level |3> is zero because we are working with a weak probe field and there is no incoherent pump to transfer population to this level.

Gain is predicted even for low Rabi frequencies such as 20 MHz. This Rabi frequency is much less than the Doppler width and still 5% gain exists for the mismatched scheme. The gain is significantly higher in the matched scheme than the mismatched scheme, but is still present for the mismatched configuration. This result is somewhat unexpected.

In the mismatched scheme the gain is increasing as the Rabi frequency increases. It reaches a point that the on-resonance gain starts to reduce. This happens because its bandwidth is increased and hence the gain is spread over a higher frequency range. At this point it is the integrated gain which is of interest. In this configuration there is not any difference between the peak gain and the gain on resonance. Gain is always produced exactly on line centre. In the matched scheme the gain is also increased as the coupling field increases. The magnitude of the gain reaches a maximum for a particular Rabi frequency. The gain is then split between the two components symmetrically spaced by the line centre, for higher coupling field strengths. Because of this splitting there is a reduction in the gain on resonance and only the peak gain which corresponds on either of the sidebands, is increased.

	Rabi frequency (MHz)	ρ^i_{13} resonance	ρ^i_{13} peak	ρ_{11}	ρ_{22}	ρ_{33}	Absorption %	Gain %	Gain bandwidth (MHz)
Absorption	Ω_c=0	-0.0004	-0.0004	1	0	0	64		
Transparency	Ω_c=20	-0.00002	-0.00002	0.9823	0.0177	0	5		
Transparency	Ω_c=160	-0.000001	-0.000001	0.875	0.125	0	0.3		
Transparency	Ω_c=950	0	0	0.62	0.38	0	0		
Gain	Ω_c=20	0.000082	0.000082	0.634	0.014	0.352		24	18
Gain	Ω_c=160	0.000025	0.000102	0.58	0.099	0.321		7 / 30	108
Gain	Ω_c=950	0.000001	0.000033	0.451	0.299	0.25		0.3 / 9	648

Table I: *Principal results of theoretical modelling for the matched system. Values are shown for the density matrix elements relating to absorption, gain and the relative atomic populations for various coupling field Rabi frequencies in the absence and presence of incoherent excitation. In the case of gain, the incoherent excitation, R_{13}, equals $10\times10^6 s^{-1}$. Absolute values of absorption and gain are also provided, in the later case the numbers before and after the oblique refer to the resonance and peak gain respectively. Conditions: T=130°C, cell length=2cm.*

	Rabi frequency (MHz)	ρ^i_{13} resonance	ρ^i_{13} peak	ρ_{11}	ρ_{22}	ρ_{33}	Absorption %	Gain %	Gain bandwidth (MHz)
Absorption	Ω_c=0	-0.0004	-0.0004	1	0	0	64		
Transparency	Ω_c=20	-0.000084	-0.000084	0.968	0.032	0	19		
Transparency	Ω_c=160	-0.000062	-0.000062	0.799	0.201	0	15		
Transparency	Ω_c=950	-0.00002	-0.00002	0.552	0.448	0	5		
Gain	Ω_c=20	0.000018	0.000018	0.627	0.025	0.348		5	27
Gain	Ω_c=160	0.0000315	0.0000315	0.541	0.159	0.3		8	108
Gain	Ω_c=950	0.000012	0.000012	0.418	0.351	0.231		3	324

Table II: *Principal results of theoretical modelling for the mismatched system. Values are shown for the density matrix elements relating to absorption, gain and the relative atomic populations for various coupling field Rabi frequencies in the absence and presence of incoherent excitation. In the case of gain, the incoherent excitation,* R_{13}, *equals* $10\times10^6 s^{-1}$. *Absolute values of absorption and gain are also provided. Conditions as in Table I.*

In the matched case the peak gain reaches its maximum value of 30% for a coupling field Rabi frequency of 160 MHz. It then reduces to 9% because it is spread over a wider region. The bandwidth of the gain then has its maximum value. This bandwidth is greater in the matched scheme than the mismatched scheme due to the existence of the splitting of the gain.

The populations provide the information that the gain is inversionless over the range of Rabi frequencies considered. The population in the ground state level |1> is always greater than the population of the upper probe transition level |3>. The population of the ground state is a bit higher in the matched scheme than this in the mismatched scheme. For a coupling field of 950 MHz the population has half of its initial value because the strong coupling field now populates level |2>, which is the upper level of the coupling field transition.

Figure 5.4.3 depicts an alternative scheme for the pumping of the system. The mismatched scheme has an advantage over the matched scheme. It may be pumped with an incoherent pump rate R_{23}. We predict gain without population inversion in such a configuration. Inversionless gain in a mismatched scheme is not affected

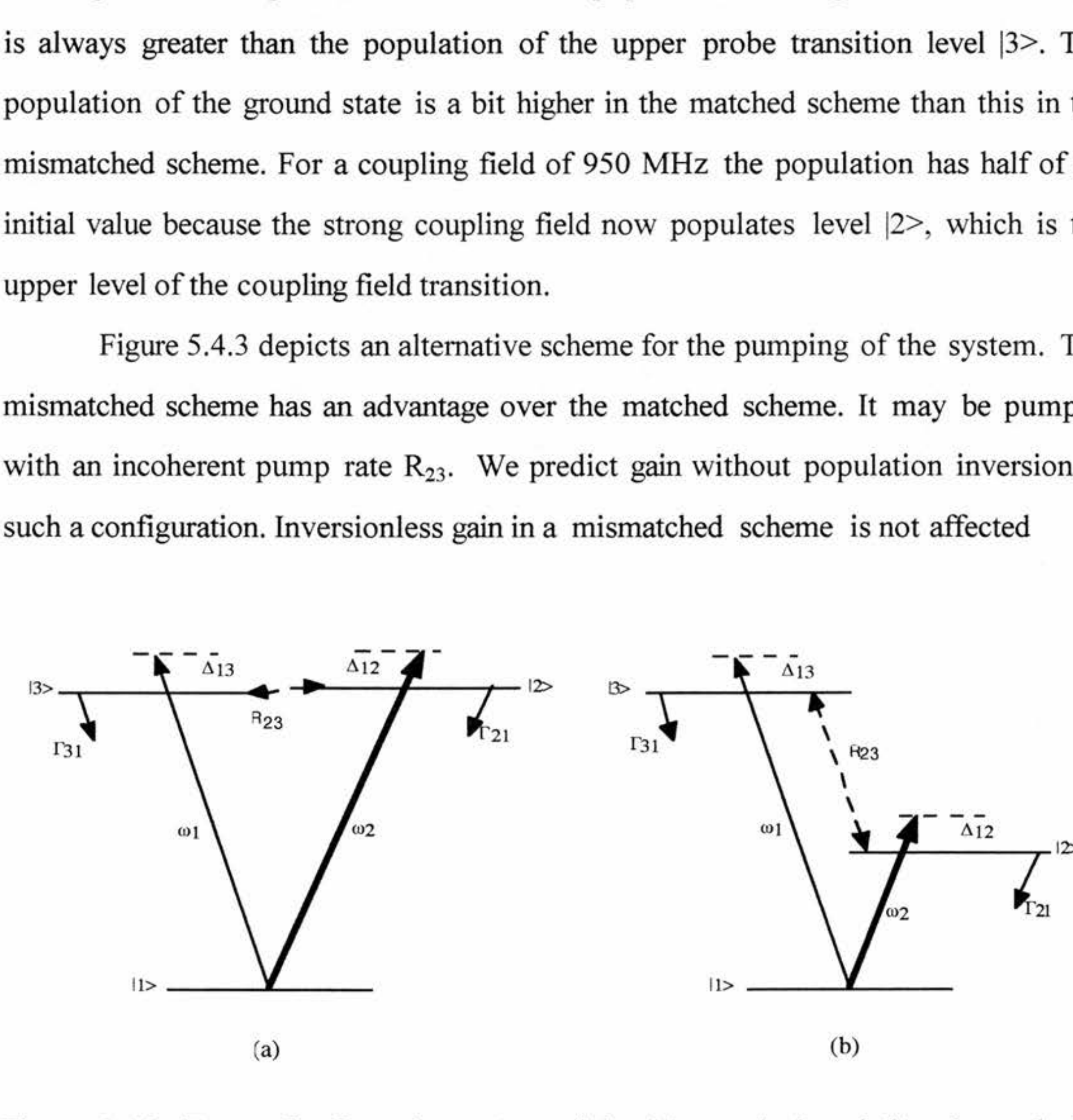

Figure 5.4.3: *Energy level configurations of the (a) matched and (b) mismatched V schemes employed in the theoretical comparison, with an incoherent pump rate employed at |2> to |3> transition R_{23}.*

by the way we pump the upper level of the probe transition, as shown in figure 5.4.4. In the case of the matched scheme we do not observe any gain with this pumping route. Moving population with an incoherent pumping rate R_{23} is advantageous over the pumping R_{13}, because the population is transferred from level |2> and not from the ground state. In this way the system is made more inversionless, the population in the ground state being higher than in the former case. The population in the ground state is now 0.743 and the populations in level |2> and |3> become 0.165 and 0.092 respectively.

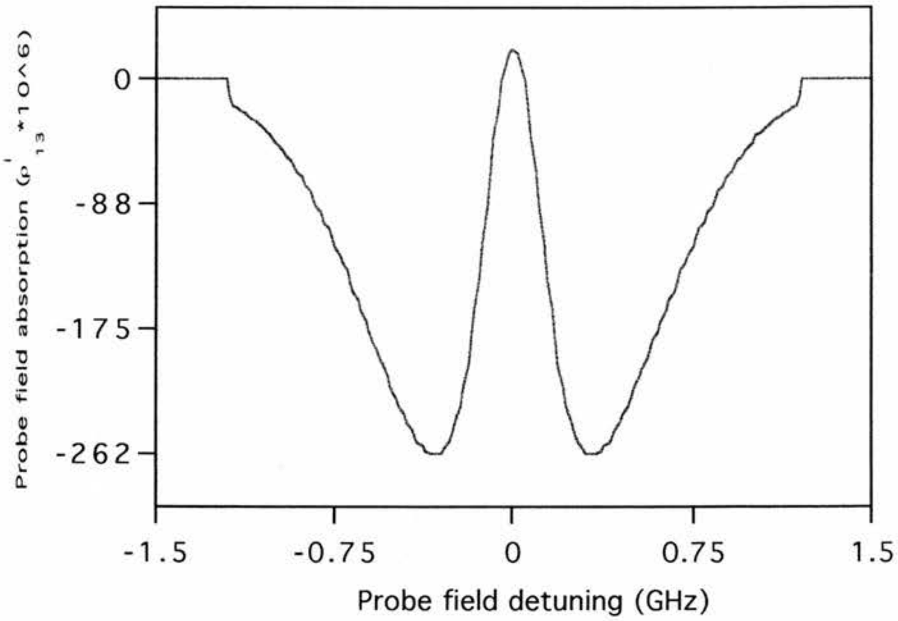

Figure 5.4.4 : *Inversionless gain is shown in a mismatched scheme with the addition of an incoherent pump* $R_{23}=10\times10^6\ s^{-1}$. *The probe field Rabi frequency is 1MHz and the coupling field Rabi frequency is set at 160 MHz. The scheme in which gain is predicted is depicted in 5.4.3 b.*

5.5 Discussion.

The results presented in this chapter show that EIT and inversionless gain is predicted for a probe field wavelength shorter than the wavelength of the coupling field, even in the presence of Doppler broadening. This may be achieved for Rabi frequencies much less than the Doppler width of the probe transition. This prediction can be explained by looking at the relative positions and magnitudes of Autler-Townes components, as well as the positions of the single and the two-photon process.

The frequency at which the probe experiences absorption due to the Autler-Townes split components of a level is affected by the velocity dependent detunings of both the coupling and the probe fields. The position of the Autler-Townes components in a V-scheme may be calculated in terms of the probe field detuning as follows:

For the coupling field the magnitude of the Autler -Townes splitting for each velocity group V_z, is the generalised Rabi frequency for that group Ω_R and is related to the velocity dependent detuning of the coupling laser $\Delta_{coupling}$, *Foulton thesis*

$$\Omega_R = \sqrt{\Omega_c^2 + \left(\Delta_{coupling} - k_2 V_z\right)^2} \tag{5.5.1}$$

where Ω_c the coupling field Rabi frequency, k_2 the wavevector of the coupling field and V_z the single velocity group.

As well as the atomic levels connected by the coupling field splitting as described, it is found that the central frequency position of the two peaks is shifted away from the unperturbed levels. In relation to the probe field these frequency shifts are given by $\frac{1}{2}\left(\Delta_{coupling} - k_2 V_z\right)$. The probe field is itself also frequency shifted within the system, by an amount $-k_1 V_z$, where k_1 the wavevector of the probe field. The overall effect of these three velocity dependent effects is that the probe is absorbed in a V-scheme at frequencies around the uncoupled resonant absorption position such that:

$$\Delta_{probe} = k_1 V_z + \frac{1}{2}\left(\Delta_{coupling} - k_2 V_z\right) \pm \frac{1}{2}\sqrt{\Omega_c^2 + \left(\Delta_{coupling} - k_2 V_z\right)^2} \qquad (5.5.2)$$

where $\Delta_{probe} = \omega_1 - \omega_{13}$ and $\Delta_{coupling} = \omega_2 - \omega_{12}$, which we refer to as the manual detuning from the transition. The single and two-photon resonance positions are given by equations (5.5.3) and (5.5.4) respectively:

$$\Delta_{probe} = k_1 V_z \qquad (5.5.3)$$

$$\Delta_{probe} = k_1 V_z - k_2 V_z + \Delta_{coupling} \qquad (5.5.4)$$

In the matched system EIT is clear since there is the two-photon cancellation for every atomic velocity group, because the two-photon resonance remains the same for every group. This is not the case for the mismatched scheme, since the two-photon resonance position will be different for each velocity group. However, EIT is still present for the mismatched scheme. Figure 5.5.1 shows the positions, in terms of the probe field detuning, of the Autler -Townes components and single and two-photon resonances for (a) matched and (b) the mismatched schemes. The solid lines correspond to the Autler-Townes components, the dotted lines to the single-photon resonances and the dashed lines to the two-photon resonances for both schemes. There is no manual detuning in our case, since $\Delta_{coupling}$ is set to zero. For the matched scheme as shown in the graph there is an EIT window on line centre and one can "see through the graph", so to speak, along a vertical line placed at zero probe field detuning. For the mismatched case there is not such a window and the secondary Autler-Townes components associated with the two-photon resonance, block it because they overlap with the transparency at line centre.

For both schemes and in the case of the zero velocity group the single-photon and the two-photon absorption resonances overlap at line centre. Quantum coherence of the system occurs where the single and the two-photon absorption routes are coincident on resonance and hence EIT is observed. The two absorptions are then equally split between the two Autler-Townes components that are evenly spaced about resonance for the zero velocity group.

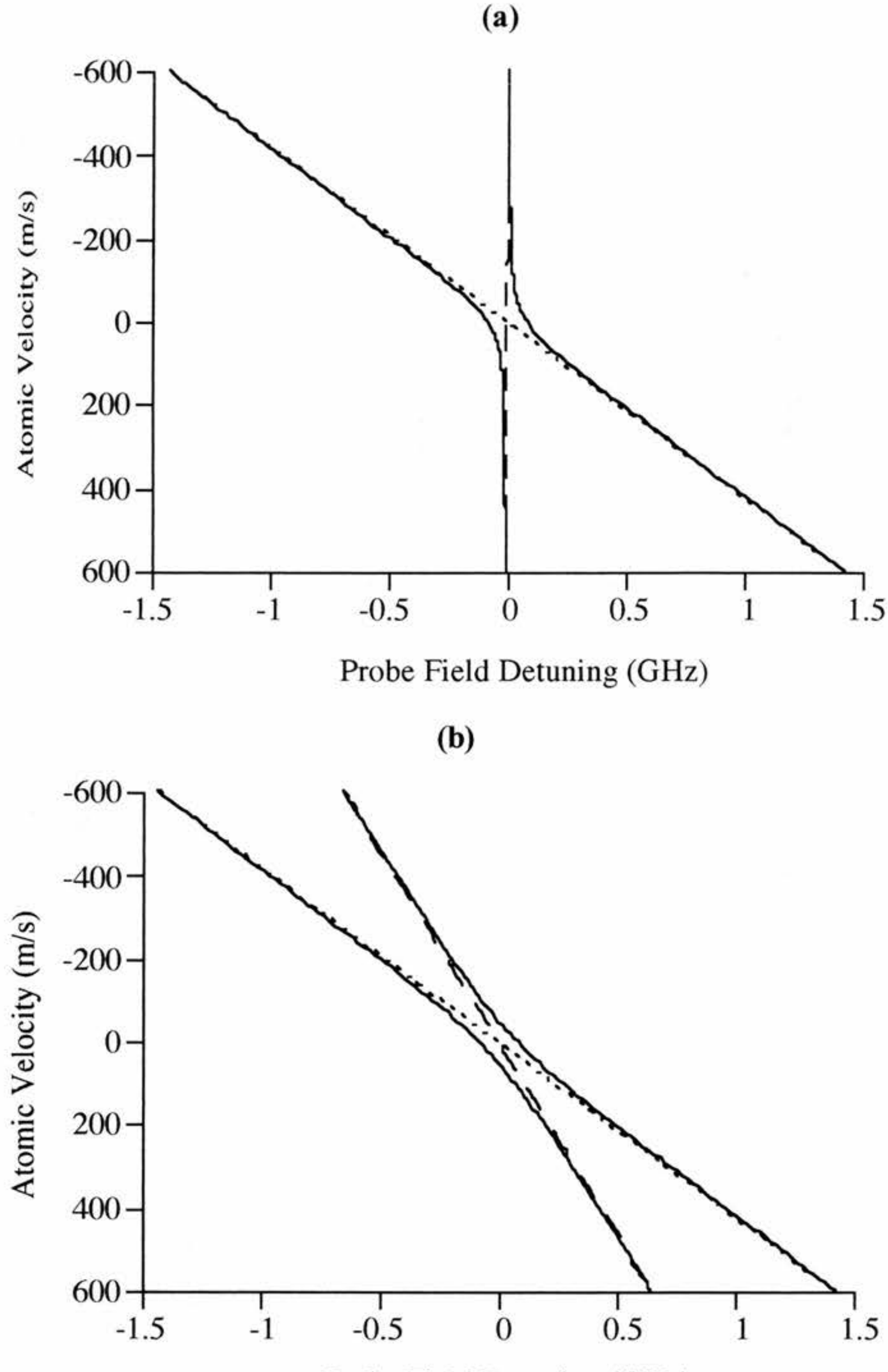

Figure 5.5.1: *The positions, in terms of probe field detuning, of the Autler-Townes components and single and two-photon resonances are shown for (a) the matched and (b) the mismatched schemes. The solid lines correspond to the Autler-Townes components, the dotted lines to the single-photon resonances, and the dashed lines to the two-photon resonances.*

In the case of the non zero velocity groups each Autler-Townes component is enhanced from either the single or the two-photon absorption process, according to which lies closest to it. As it is shown in the graph of figure 5.5.1, for the non zero velocity groups, the Autler-Townes components follow the single and the two-photon resonance positions. As a definition we regard the single-photon absorption as the primary component and that related with the two-photon absorption as the secondary Autler-Townes component.

As it is depicted in figure 5.5.1 the only difference between the matched and the mismatched V-scheme is that in the case of the mismatched scheme the secondary Autler-Townes components overlap with the EIT and eventually cover it. But inspite of this fact, EIT is still present in the case of the mismatched scheme. This happens because the magnitudes of these Autler-Townes components are not significant enough to diminish the transparency. The two-photon process in a V-scheme has the form of a |2>-|1>-|3> transition and it starts on the upper level of the coupling field transition. In the case of the non zero velocity group, the coupling field is detuned by the Doppler shift from the |1>-|2> resonance. Hence there is not any particularly significant transfer of the population to state |2>, to contribute to the masking of the transparency. Therefore, as we consider higher velocity groups the magnitude of the two-photon process is significantly reduced. Hence, the magnitude of the secondary Autler-Townes component is not enough to reduce the EIT window.

In figure 5.5.2a and 5.5.2 b there are depicted three-dimensional graphs of the absorption as a function of the atomic velocity and the probe field detuning for the matched and the mismatched schemes, respectively. The probe absorptions are calculated for a finite number of atomic velocities within the Doppler profile and only the velocity groups that contribute to the absorption near resonance are consider in these plots.

In the matched case for the zero velocity group of atoms, the two-photon resonance and the single-photon resonance coincide for zero probe field detuning. This results in a cancellation of the absorption, giving rise to the expected strong EIT effect (i.e. close to zero absorption at zero probe detuning, located between the two Atler-

Townes peaks). For the non-zero velocity groups, two-photon resonance is still maintained (being located at zero probe detuning), but because this is not the case for the single-photon process, associated with either the probe or coupling field, the magnitude or the two-photon absorption rapidly declines because of the decline in the population of level 2. As the secondary Autler-Townes component approaches the two-photon resonance condition with increasing detuning due to velocity, it is therefore rapidly reduced in magnitude, and does not hence obscure the EIT window.

Figure 5.5.2b shows that even for the case of the mismatched scheme transparency is observable due to the magnitude of the secondary Autler-Townes components. As is shown in the graph exactly on resonance the magnitude which corresponds to two-photon absorption is significantly small. This is the reason the EIT is still present in the mismatched scheme. In both, matched and mismatched, cases the secondary Autler-Townes components quickly disappear as the atomic velocity increases. Although in the mismatched case, the secondary Autler-Townes component crosses over the EIT window at zero probe field detuning, unlike the matched case, its attenuation by this point is such as to still allow significant overall transparency. This study of EIT has been motivated by its relevance to inversionless gain, with the addition of an incoherent pumping rate. Figure 5.5.2b shows that EIT is possible for a probe field wavelength almost half of the coupling field wavelength, even in a Doppler broadened system.

This theoretical prediction raises the question of how far we can mismatch the wavelengths in a Doppler broadened V-scheme. In figure 5.5.3 is shown a graph of the logarithm of the ratio of the absorption coefficient in the presence and absence of the coupling field as a function of the probe wavelength. The probe wavelength is varied while the coupling wavelength is held constant at 780 nm. The solid vertical line marks the matched scheme and the dashed vertical line marks the above mismatched scheme for this comparison. In the plot we consider the transparency for the conditions when, the incoherent pumping rate equals zero.

By plotting the logarithm of the absorption coefficient we can see that in the matched case a coupling field Rabi frequency of 950 MHz reduces the absorption by more than three orders of magnitude. However, in the mismatched case the same coupling field Rabi frequency still reduces the absorption by more than an order of magnitude. This is not the case for a coupling field Rabi frequency of 160 MHz . This coupling field strength is not sufficient to reduce the transparency, for the mismatched scheme, by an order of magnitude but by half of it. Nevertheless, this coupling field Rabi frequency for the matched case reduces the absorption by two orders of magnitude.

The matched scheme has an advantage over the mismatched scheme, but reduction of absorption is still significant for the mismatched configuration. As the

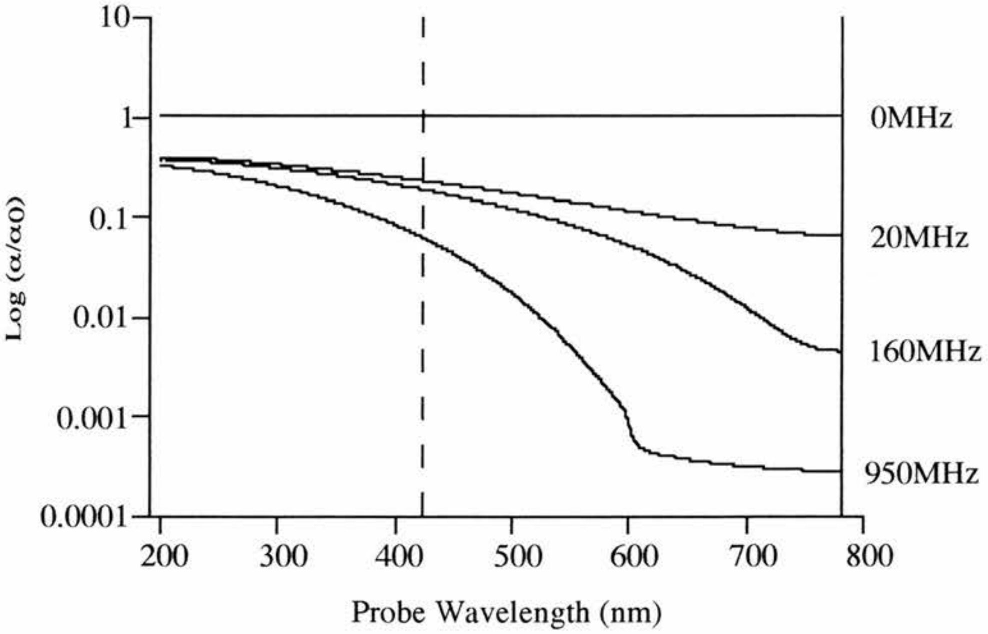

Figure 5.5.3: *The logarithm of the ratio of the absorption coefficient in the presence and absence of the coupling field is plotted as a function of the probe wavelength. The probe wavelength is varied while the coupling wavelength is held constant at 780nm. The solid vertical line marks the matched scheme and the dashed vertical line marks the mismatched system. The magnitude of the coupling field Rabi frequency is given on the right hand side of each trace.*

wavelength of the probe field decreases there is much less reduction in the absorption and hence the level of the transparency reduces. Moreover at the UV wavelength regime at 200 nm and for a coupling field Rabi frequency of 950 MHz , a transparency of approximately 60% is predicted.

5.6 Prediction for an experimental system.

This ideal theoretical system is used to predict inversionless gain in a mismatched V-type system. We based the theoretical mismatched scheme on an experimental system where mismatched EIT in a Doppler broadened medium has been demonstrated, *Boon et al.* We can calculate the gain from the exact experimental conditions. For a 2 cm cell length and a coupling Rabi frequency of 160 MHz we predict a gain of approximately 8% at 130° C, and at an incoherent pumping rate of $10\times10^{6}\ s^{-1}$. The Rabi frequency of 160 MHz can be easily achieved with CW lasers. The coupling field wavelength is twice that of the probe field. Gain is predicted for the 422 nm transition within the Rb cell. This mismatched system is a step towards the short wavelength regime, where inversionless gain is the goal of quantum coherence.

The level of transparency and hence the gain predicted by the density matrix analysis is always greater than that feasible in the experiment. There are uncertain conditions which may mask the magnitude of the gain. In reality it may be less than 8%. This may happen due to the variation of the Rabi frequency over the interaction cell length and cross-section. The Rabi frequency is dependent on the coupling field intensity, hence it will vary along the cell length as the beam is focused and across the cell cross-section with the intensity profile of the beam. Another parameter that we neglected completely is the hyperfine structure of rubidium and therefore the collisional mixing rate of the ground state. This rate acts to dephase the transitions and to reduce the magnitude of EIT observed in the experiment. Of course we are able to overcome these difficulties by setting the required particle density, by varying the cell temperature and the cell length. The gain varies exponentially with cell temperature so it is not unreasonable to assume that a sufficient level of gain will be achieved in the experiment. The gain also depends on the cell length and we can always increase the length to produce more gain.

5.7 Conclusions.

We have predicted that EIT is still possible in a mismatched configuration, even in the presence of Doppler broadening. (For the purposes of comparison with the matched scheme, we assumed all parameters are made equal except for the transition wavelength). In a V-scheme there is no need for matching the probe and the coupling field wavelengths in order to observe EIT. The magnitude of the secondary Autler-Townes components which overlap with the EIT window is not significant to erode the transparency in this case. Hence, a transparency window is demonstrated in a mismatched V-type system, where the probe frequency is approximately twice that of the coupling field. We find that a transparency window is produced , even for mismatched wavelengths , for coupling field Rabi frequencies greater than the homogeneous linewidth but substantially less than the Doppler width of the probe transition.

Subsequently, inversionless gain is analysed in such a system. We predict that gain without population inversion can be produced in a Doppler broadened mismatched scheme. Doppler broadening does not act as a limiting factor for the generation of inversionless gain. Following the experimental realisation of CW mismatched EIT in a Doppler broadened system, *Boon et al*, we presented a comprehensive theoretical analysis for the production of inversionless gain. A comparison is made of inversionless gain achieved via EIT in matched and mismatched wavelength systems.

The theory is related to an experimental system in atomic rubidium vapour. Appropriate experimental conditions have been used to calculate the values of the absolute gain. For a 2 cm cell length and a coupling field Rabi frequency of 160 MHz we predict an inversionless gain of approximately 8%. This calculation is based on the incoherent pumping rate of 10×10^6 s^{-1} and involves a coupling field Rabi frequency that can be easily covered by CW laser powers.

References

Boon J.R., Zekou E., Fulton D.J. and Dunn MH., " Experimental observation of a coherently induced transparency on a blue probe in a Doppler-broadened mismatched V-type system", Physical Review A, **57**, p1323, (1998)

Fulton D.J, Quantum Interference Effects: EIT and focusing, Ph.D. thesis, University of St. Andrews, 1996.

Padmabandu G.G, Welch G.R., Shubin I.N., Fry E.S., Nikonov D.E., Lukin M.D. and O. Scully M., "Laser oscillation without population inversion in a sodium atomic beam", Physical Review Letters, **76**, p2053 (1996).

Thompson D.C and Xu G.X., "Optical measurements of vapour pressures of Rb and Rb-K mixture", Canadian Journal of Physics, **60**, p1496 (1982).

Wiese W.L. and Martin G.A., "A physisist's Desk Reference (American Institute of Physics, 1989)

Zibrov A.S., Lukin M.D., Nikonov D., Hollberg L., Scully M.O, Velichansky V.L. and Robinson H.G., "Experimental demonstration of laser oscillation without population inversion via quantum interference in Rb", Physical Review Letters, **75**, p.1499 (1995) .

Chapter 6

Comparison of wavelength dependence in Cascade, Lambda and V-type schemes for electromagnetically induced transparency

---

6.1 Introduction.

In this chapter we present a theoretical comparison of mismatching wavelengths of the coupling and probe fields in a Doppler broadened medium for the three basic energy configurations used to produce electromagnetically induced transparency (EIT). The study of EIT has been motivated by its relevance to inversionless lasing. An inversionless CW laser was first demonstrated by *Zibrov et al.*, using a matched infrared energy level scheme (i.e. coupling laser wavelength comparable to the probe wavelength).

However, the real potential of inversionless lasing lies in the use of mismatched wavelengths (unequal probe and coupling field wavelengths), particularly where a high wavelength coupling field is used to produce gain on a low wavelength probe field. This way of mismatching may lead to gain without population inversion in the X-ray regime. Until recently, this was only thought possible at the power levels available from CW lasers, either in a Doppler-free medium or where the Doppler effect was set to zero through a matched scheme. This chapter considers the effects of mismatching the coupling and probe wavelengths on EIT in the Cascade, Lambda and V-type energy schemes of a Doppler broadened medium.

Three wavelength regimes are explored: mismatched wavelengths where the coupling field wavelength is greater than the probe wavelength, matched wavelengths where the coupling wavelength equals the probe wavelength and mismatched wavelengths where the coupling field wavelength is less than that of the probe field. The imaginary part of the probe coherence which is proportional to the absorption is calculated as a function of the atomic velocity and the probe detuning. We present how mismatching the wavelengths in the three regimes affects the position of the Autler-Townes components together with the single and two-photon absorption resonances. We also show how the Autler-Townes components vary with frequency. The transparency that is induced for these three regimes is compared for a Cascade, Lambda and V-scheme.

In the first wavelength regime, where $\lambda_c > \lambda_p$ EIT is possible only for a V-scheme in a Doppler broadened medium, where the coupling field Rabi frequency is less than the Doppler width. In the matched wavelength regime EIT is demonstrated for all three schemes, as expected. In the mismatched case, where $\lambda_c < \lambda_p$ the transparency is realised in all three schemes and it is much better than the matched case. The effect of EIT is more pronounced in a cascade scheme when $\lambda_c < \lambda_p$, *Shepherd et al*. However, EIT occurs for the other two schemes, as well. This chapter extends the study by including the three basic energy configurations for EIT and all the possible directions of mismatching and matching the wavelengths of the probe and coupling fields.

6.2 Theoretical comparison of the schemes.

A comparison of Cascade, Lambda and V-type schemes was made for the matched systems within Rb vapour, by *Fulton et al.* In the present work the comparison of the three schemes does not relate to real systems, such as Rb. Hence, a comparison is made only on the basis of the type of the system and the direction of the relative wavelength mismatch, while all other parameters are kept equal. This is of course not realisable, if we consider real atomic systems.

In this chapter we assume closed three-level systems as shown in figure 6.2.1 for the Cascade, the Lambda and the V-type schemes. All the decay rates shown in the figure are set to 40×10^6 s^{-1} and the dephasing on the unlinked transition is also set to 40×10^6 s^{-1} for each system. The dephasing has this value because it is defined as

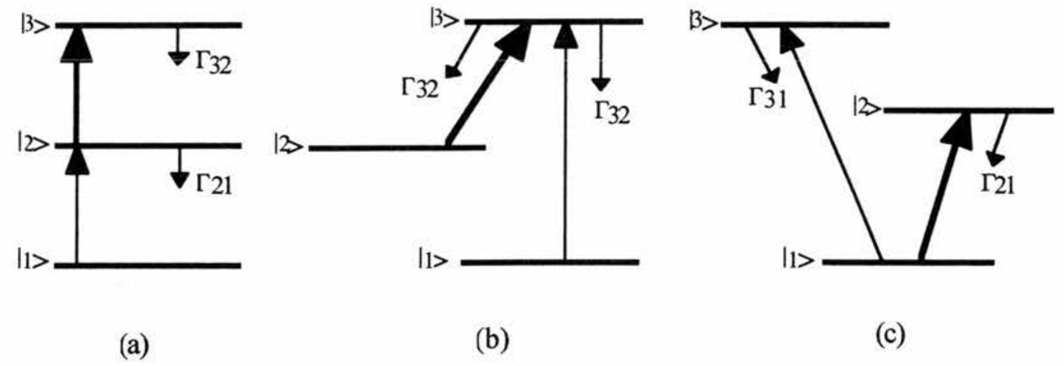

Figure 6.2.1: *Energy level configuration for (a) the Cascade, (b) the Lambda and the V-scheme employed in the theoretical comparison. Γ_{ij} are the decay rates from the energy level. The thin arrow is the probe field and the thick arrow is the coupling field.*

$\gamma_{ij} = \Gamma_{ij} / 2$, where Γ_{ij} the decay rate of the energy level. This value corresponds to the maximum dephasing that may occur due to the decay rates from the level. The systems do not include any collisional dephasing rate and in that respect they are assumed ideal.

The wavelength of the probe field has a constant value, while that of the coupling field has three different values. The probe wavelength is kept at 800 nm whereas the coupling field wavelength is taken as 400, 800 and 1600 nm. The probe field wavelength is kept constant so that we can compare all the absorption profiles. Changing the coupling wavelength by three values corresponds to nine simultaneous systems where the coupling field wavelength is less than that of the probe, equal to that of the probe and greater than that of the probe for the Cascade, Lambda and V-type configurations. The probe field Rabi frequency is taken 100 kHz and it is considered as a weak field case, in which the probe does not significantly populate the upper level of the probe transition. The coupling field Rabi frequency is set at approximately half the Doppler width which is 500 MHz and hence its value is 250 MHz.

Theoretical modelling of these schemes is carried out utilising standard density matrix analysis for the three schemes, see Chapter 2. The six equations for the slowly varying density matrix components are derived for all three closed systems, *Moseley et al, Imamoglu et al.* The equations are solved by invoking steady state conditions (appropriate because of the employment of CW lasers) and thus setting all time derivatives to zero, *Li et al.* These equations can then be split into nine real simultaneous equations, using properties of the density matrix, and solved using normal linear algebra routines. The solutions yield values for the real and the imaginary parts of the coherence on each transition, which can be related to the refractive index and the absorption, respectively and the proportion of the atomic population in each of the energy levels. Doppler-broadening is taken into account by integrating over the velocity distribution.

6.3 Theoretical results.

The absorption profiles are plotted against the probe field detuning for each system. In addition, the Autler-Townes absorption components along with the single and the two-photon absorption profiles are presented as a function of the atomic velocity for all schemes. In the plots of the Autler- Townes absorption components there are lines parallel to the x axis. These lines are drawn to indicate the magnitude of the Autler-Townes absorption components. The length of these lines is directly proportional to the imaginary part of the coherence on the probe transition and thus to the absorption coefficient. This length is calculated from three-dimensional graphs where the probe absorption is plotted as a function of the probe detuning and the atomic velocity. The three-dimensional plots were obtained from density matrix analysis of the systems. Hence , the two-dimensional plots with the lines considered provide a full description of the induced transparency in each of the absorption profiles.

The position of the Autler -Townes components are given for the Cascade and for the Lambda and V-schemes, in terms of the probe field detuning, by equations 6.3.1 and 6.3.2 respectively.

$$\Delta_{probe} = k_1 V_z - \frac{1}{2}\left(\Delta_{coupling} + k_2 V_z\right) \pm \frac{1}{2}\left(\sqrt{\Omega_c^2 + \left(\Delta_{coupling} + k_2 V_z\right)^2}\right) \quad (6.3.1)$$

$$\Delta_{probe} = k_1 V_z + \frac{1}{2}\left(\Delta_{coupling} - k_2 V_z\right) \pm \frac{1}{2}\left(\sqrt{\Omega_c^2 + \left(\Delta_{coupling} - k_2 V_z\right)^2}\right) \quad (6.3.2)$$

where Δ_{probe} and $\Delta_{coupling}$ are the manual detunings (i.e. the detunings of the probe and coupling field frequencies respectively, from line centre -i.e. zero velocity group- as measured in the lab frame), k_1 and k_2 are the wavevectors of the probe and the coupling field respectively, Ω_c is the Rabi frequency of the coupling field and V_z is the atomic velocity. In the above equations the beams in the Cascade scheme have counter-propagating geometry and in the Lambda and V-schemes the beams co-propagate. In the case where the manual detuning of the coupling field $\Delta_{coupling}$ is set to zero, equations 6.3.1 and 6.3.2 have the same form. That is to say that for a given wavelength, velocity group and coupling field Rabi frequency, the Autler-Townes components occur in the same position for all the schemes.

The two-photon resonance positions are given for a Cascade scheme and for a Lambda and V-schemes by equations 6.3.3 and 6.3.4 respectively.

$$\Delta_{probe} = k_1 V_z - k_2 V_z - \Delta_{coupling} \quad (6.3.3)$$

$$\Delta_{probe} = k_1 V_z - k_2 V_z + \Delta_{coupling} \quad (6.3.4)$$

If we assume that $\Delta_{coupling} = 0$, the two-photon resonance positions are given for all schemes by equation 6.3.5.

$$\Delta_{probe} = k_1 V_z - k_2 V_z \quad (6.3.5)$$

The positions of the absorption resonances for all three schemes are given for the single-photon absorption by :

$$\Delta_{probe} = k_1 V_z \quad (6.3.6)$$

When $\Delta_{coupling}$ equals zero the equations for the positions of the Autler-Townes components, together with the two-photon and single-photon resonance positions, are identical for all schemes. Figure 6.3.1 shows the positions of the Autler-Townes components and single and two-photon resonances, when $\Delta_{coupling} = 0$, for all the wavelength regimes. These figures apply to the cascade, the Lambda and the V-scheme. As we change the coupling field wavelength, the associated Autler-Townes components change along with the two-photon resonance position.

As we detune the probe frequency away from the zero velocity atoms, the Autler-Townes components split further apart. If we increase the velocity from negative to zero, one set of the Autler-Townes components follows the position of the single-photon resonance, while the other follows the position of the two-photon resonance and they change over at the zero velocity group and as we increase the velocity into the positive region. The Autler-Townes component related to the single-photon resonance is indicated in the plots as the primary component and the Autler-Townes component which follows the two-photon resonance is indicated as the secondary component. It is clearly shown in the graphs that the position of the primary components does not change for the different wavelengths, while the secondary Autler-Townes components change when the coupling field is altered.

Figure 6.3.2 shows the absorption profiles for all three schemes in the presence of the coupling field. EIT is presented in each case of the three wavelength regimes, $\lambda_c<\lambda_p$ (dotted line), $\lambda_c=\lambda_p$ (dashed line) and $\lambda_c>\lambda_p$ (solid line). In the Cascade scheme the best transparency window is shown for $\lambda_c<\lambda_p$ and it is obvious from the graph that there is no EIT when $\lambda_c>\lambda_p$. This fact happens also in the Lambda scheme. The difference lies in the V-configuration, where in the $\lambda_c>\lambda_p$ regime EIT is still seen to occur. The graphs of figure 6.3.2 are presented analytically for each energy case in a series of figures together with three-dimensional plots which depict the absorptions as a function of the atomic velocity and the probe field detuning for a discrete number of velocities.

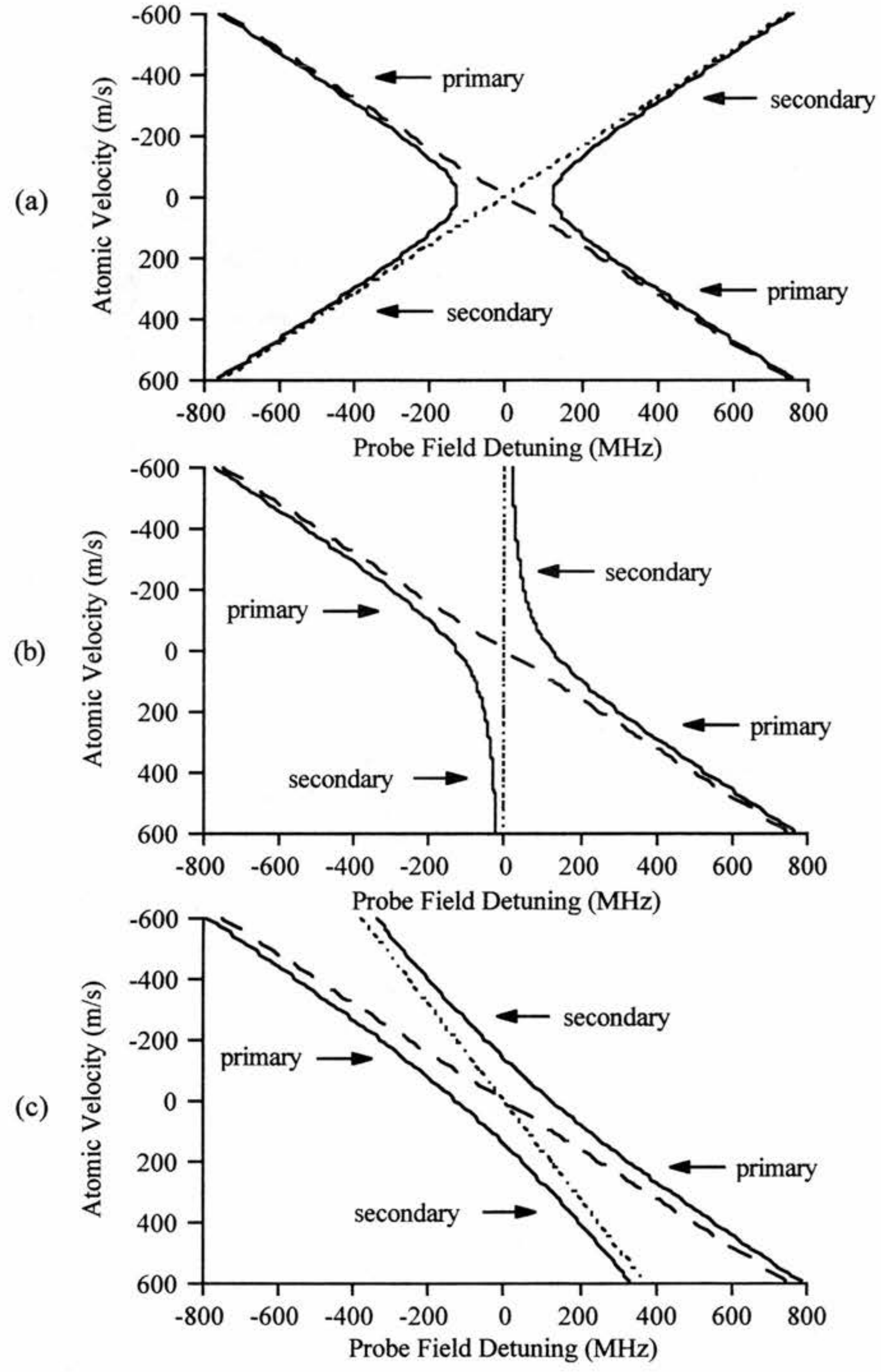

Figure 6.3.1: *The Autler-Townes and absorption resonance positions as a function of atomic velocity and probe field detuning for the three wavelength regimes:(a)*$\lambda_c<\lambda_p$, *(b)*$\lambda_c=\lambda_p$ *and (c)*$\lambda_c>\lambda_p$*. These figures apply for all three energy level schemes with* $\Delta_c=0$.

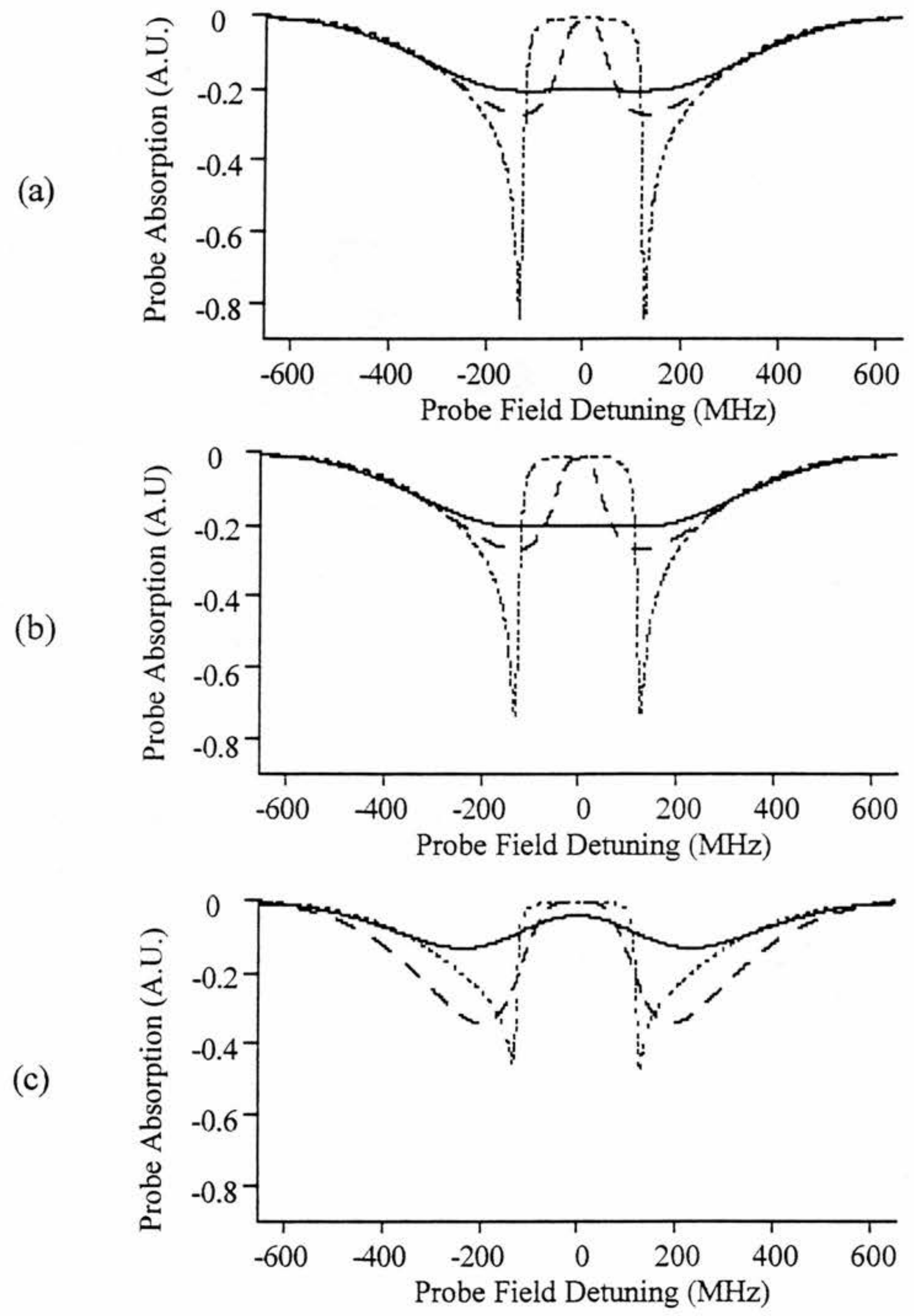

Figure 6.3.2 : *The probe field absorption is plotted as a function of the probe field detuning for (a) the Cascade, (b) the Lambda and (c) the V-schemes. In each case three wavelength regimes are considered:* $\lambda_c<\lambda_p$ *(dotted line),* $\lambda_c=\lambda_p$ *(dashed line) and* $\lambda_c>\lambda_p$ *(solid line).*

6.3.1 The cascade scheme.

- The regime where $\lambda_c<\lambda_p$.

In this wavelength regime the probe field wavelength is twice than that of the coupling field. Figure 6.3.3 depicts the probe field absorption as a function of the probe field detuning. Electromagnetically induced transparency is observed exactly on resonance. Figure 6.3.4 is a three-dimensional plot of the absorption as a function of the atomic velocity and the probe field detuning for a discrete number of velocities. The transparency is observed exactly on line centre in this three-dimensional plot.

- The regime where $\lambda_c=\lambda_p$.

In this wavelength regime the coupling field wavelength equals that of the probe field. Figure 6.3.5 shows the probe field absorption as a function of the probe field detuning. EIT is present exactly on resonance but in this case the transparency window is narrower than that observed on the mismatched $\lambda_c<\lambda_p$ case. Figure 6.3.6 depicts the three-dimensional plot of the absorption as a function of the atomic velocity and the probe field detuning.

- The regime where $\lambda_c>\lambda_p$.

In this wavelength regime the probe wavelength is half of that of the coupling field. Figure 6.3.7 shows the probe field absorption as a function of the probe field detuning. In this mismatched case there is no transparency window on resonance. Figure 6.3.8 shows the three-dimensional plot of the absorption as a function of the atomic velocity and the probe field detuning. As shown in the graph the Autler-Townes components overlap with the transparency window and this is the reason that the transparency is not observed in this mismatched case.

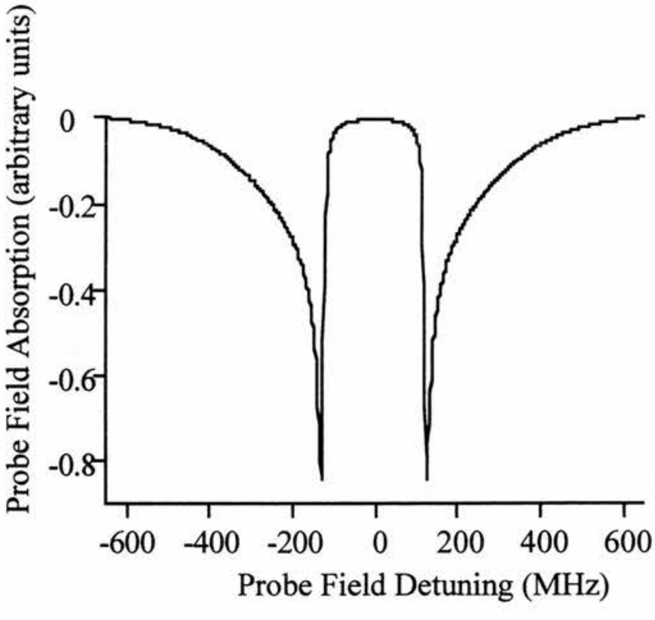

Figure 6.3.3: *Profile of probe field absorption (ρ^i_{12} in arbitrary units) as a function of probe field detuning produced by density matrix analysis of the Cascade scheme (λ_c = 400nm, and λ_p = 800nm).*

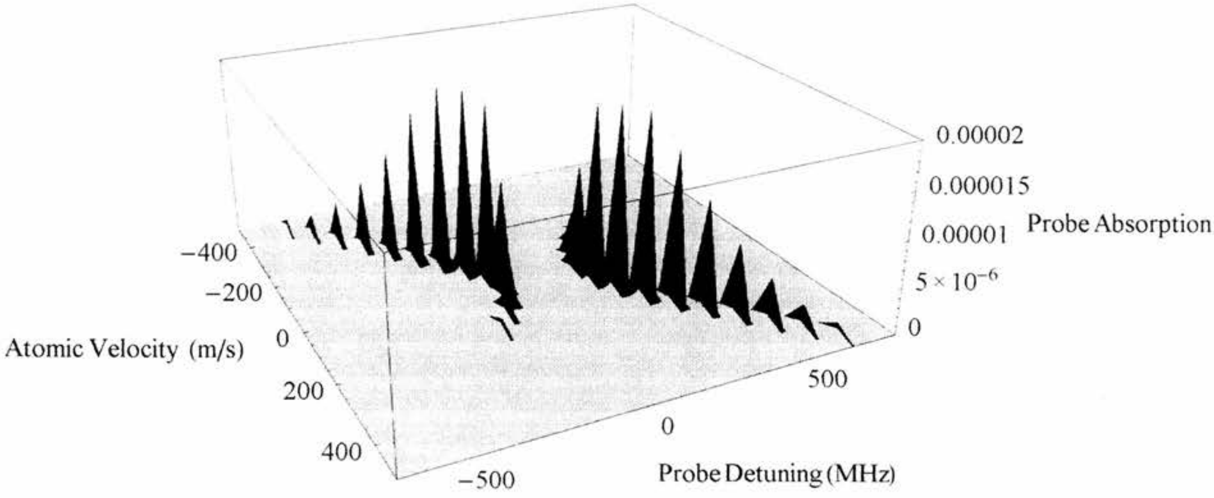

Figure 6.3.4: *Three-dimensional profile of probe field absorption (ρ^i_{12} in arbitrary units) as a function of probe field detuning and atomic velocity for several discrete velocities, produced by density matrix analysis of the Cascade scheme (λ_c = 400nm, and λ_p = 800nm).*

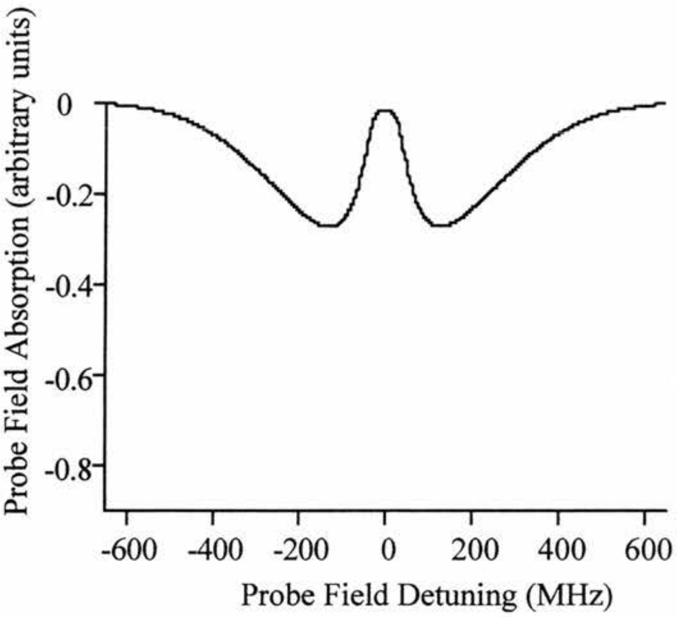

Figure 6.3.5: *Profile of probe field absorption ($\rho^i{}_{12}$ in arbitrary units) as a function of probe field detuning produced by density matrix analysis of the Cascade scheme (λ_c = 800nm, and λ_p = 800nm).*

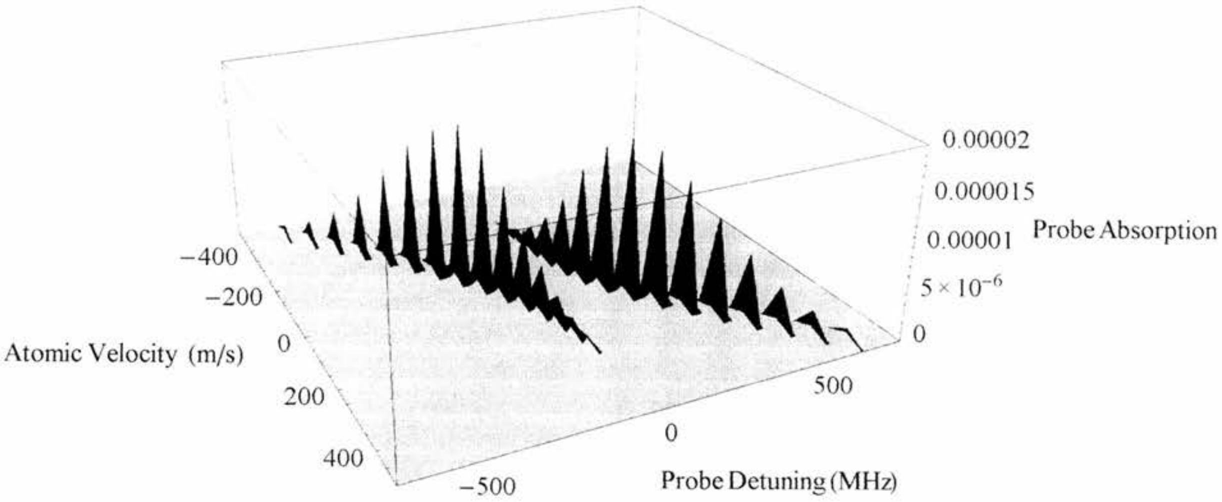

Figure 6.3.6: *Three-dimensional profile of probe field absorption ($\rho^i{}_{12}$ in arbitrary units) as a function of probe field detuning and atomic velocity for several discrete velocities, produced by density matrix analysis of the Cascade scheme (λ_c = 800nm, and λ_p = 800nm).*

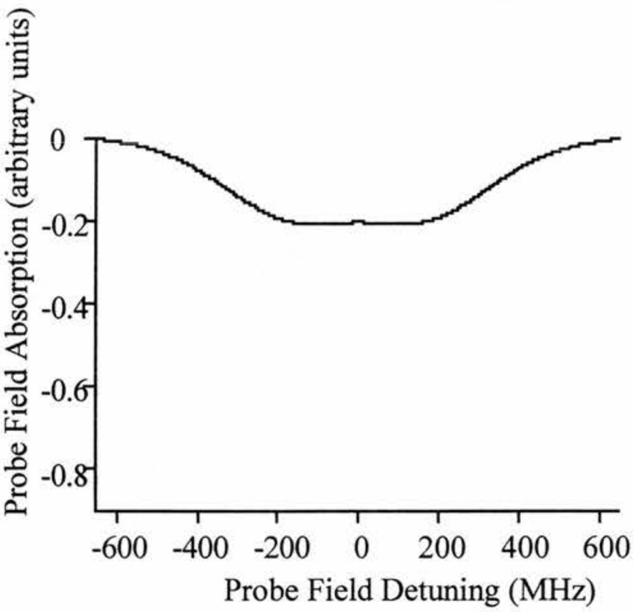

Figure 6.3.7: *Profile of probe field absorption (ρ^i_{12} in arbitrary units) as a function of probe field detuning produced by density matrix analysis of the Cascade scheme (λ_c = 1600nm, and λ_p = 800nm).*

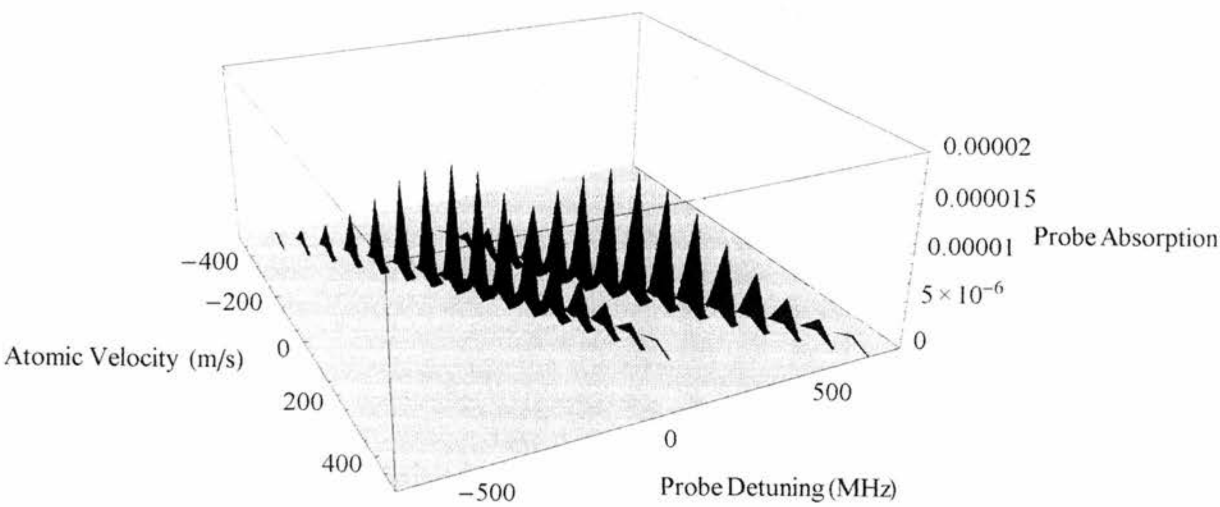

Figure 6.3.8: *Three-dimensional profile of probe field absorption (ρ^i_{12} in arbitrary units) as a function of probe field detuning and atomic velocity for several discrete velocities, produced by density matrix analysis of the Cascade scheme (λ_c = 1600nm, and λ_p = 800nm).*

6.3.2 The Lambda scheme.

- The regime where $\lambda_c<\lambda_p$.

In this wavelength regime the probe field wavelength is twice than that of the coupling field. Figure 6.3.9 shows the probe field absorption as a function of the probe field detuning. EIT is observed exactly on resonance. Figure 6.3.10 is a three-dimensional plot of the absorption as a function of the atomic velocity and the probe field detuning for a discrete number of velocities. A significant transparency window is observed on line centre in this three-dimensional plot.

- The regime where $\lambda_c=\lambda_p$.

In this wavelength regime the coupling field wavelength equals that of the probe field. Figure 6.3.11 shows the probe field absorption as a function of the probe field detuning. EIT is present exactly on resonance but in this case the transparency window is narrower than that observed in the mismatched $\lambda_c<\lambda_p$ case. Figure 6.3.12 depicts the three-dimensional graph of the absorption as a function of the atomic velocity and the probe field detuning.

- The regime where $\lambda_c>\lambda_p$.

In this wavelength regime the coupling field wavelength is twice than that of the probe field. Figure 6.3.13 shows the probe field absorption as function of the probe field detuning. In this mismatched scheme there is no transparency window on resonance. Figure 6.3.14 depicts a three-dimensional plot of the absorption as a function of the atomic velocity and the probe field detuning.

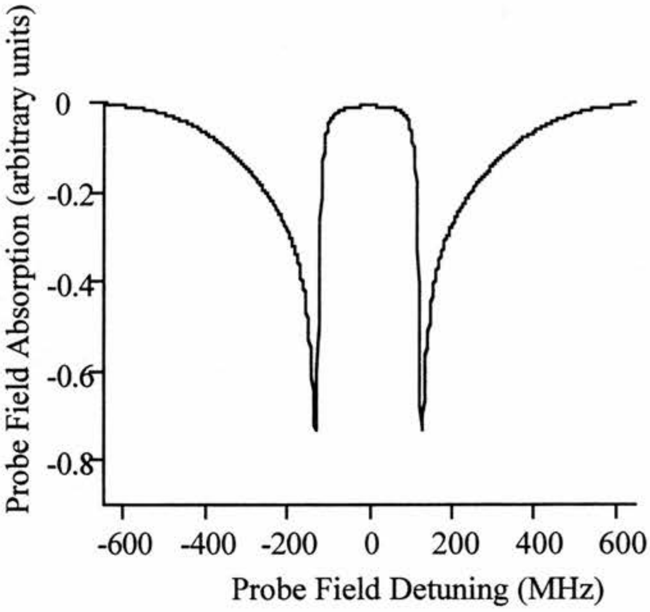

Figure 6.3.9: *Profile of probe field absorption (ρ^{i}_{13} in arbitrary units) as a function of probe field detuning produced by density matrix analysis of the Lambda scheme (λ_c = 400nm, and λ_p = 800nm).*

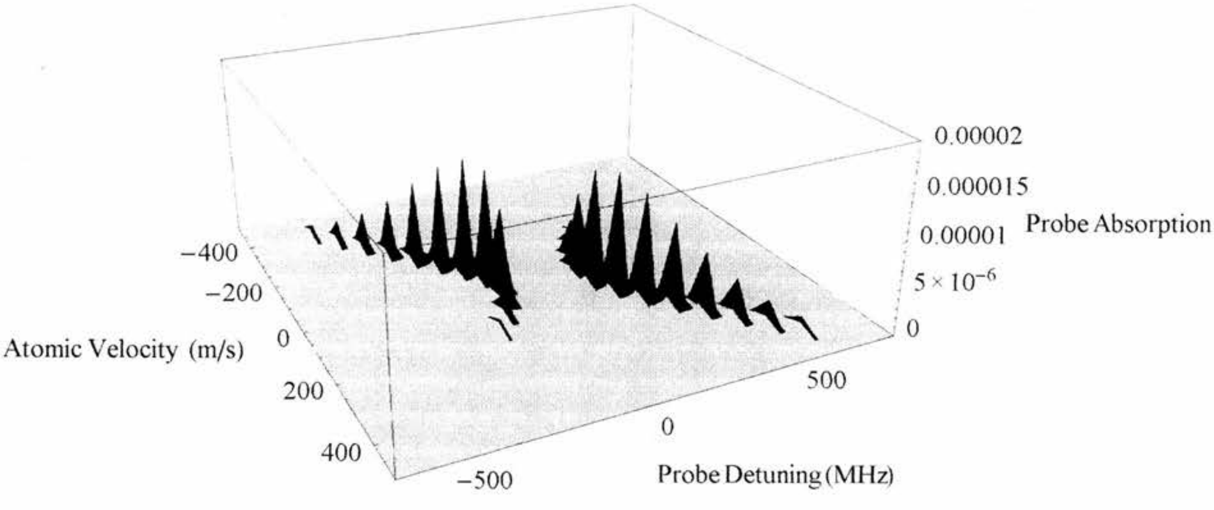

Figure 6.3.10: *Three-dimensional profile of probe field absorption (ρ^{i}_{13} in arbitrary units) as a function of probe field detuning and atomic velocity for several discrete velocities, produced by density matrix analysis of the Lambda scheme (λ_c = 400nm, and λ_p = 800nm).*

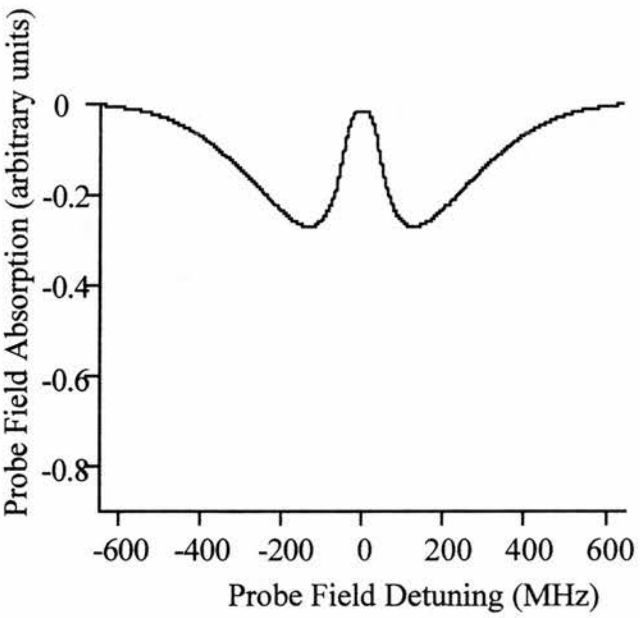

Figure 6.3.11: *Profile of probe field absorption (ρ^i_{13} in arbitrary units) as a function of probe field detuning produced by density matrix analysis of the Lambda scheme (λ_c = 800nm, and λ_p = 800nm).*

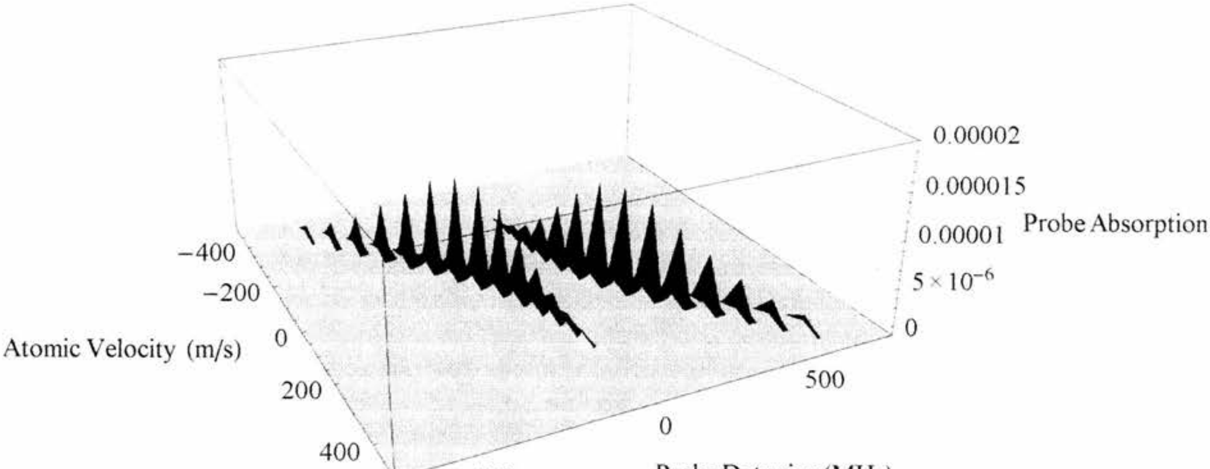

Figure 6.3.12: *Three-dimensional profile of probe field absorption (ρ^i_{13} in arbitrary units) as a function of probe field detuning and atomic velocity for several discrete velocities, produced by density matrix analysis of the Lambda scheme (λ_c = 800nm, and λ_p = 800nm).*

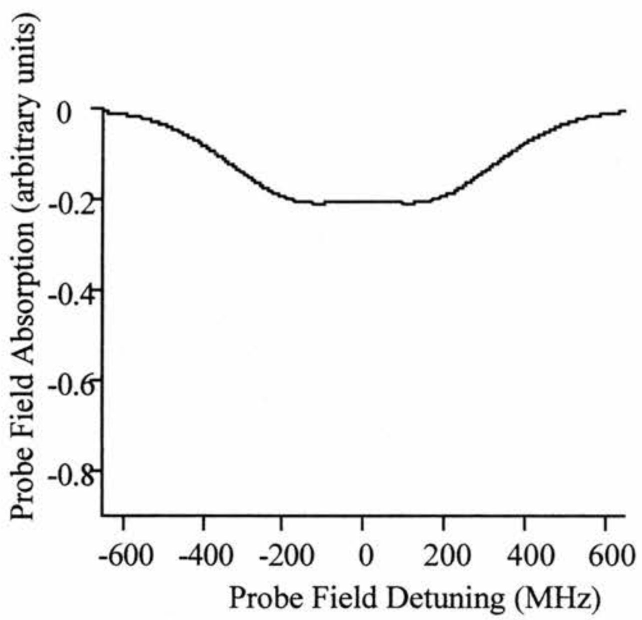

Figure 6.3.13: *Profile of probe field absorption ($\rho^i{}_{13}$ in arbitrary units) as a function of probe field detuning produced by density matrix analysis of the Lambda scheme (λ_c = 1600nm, and λ_p = 800nm).*

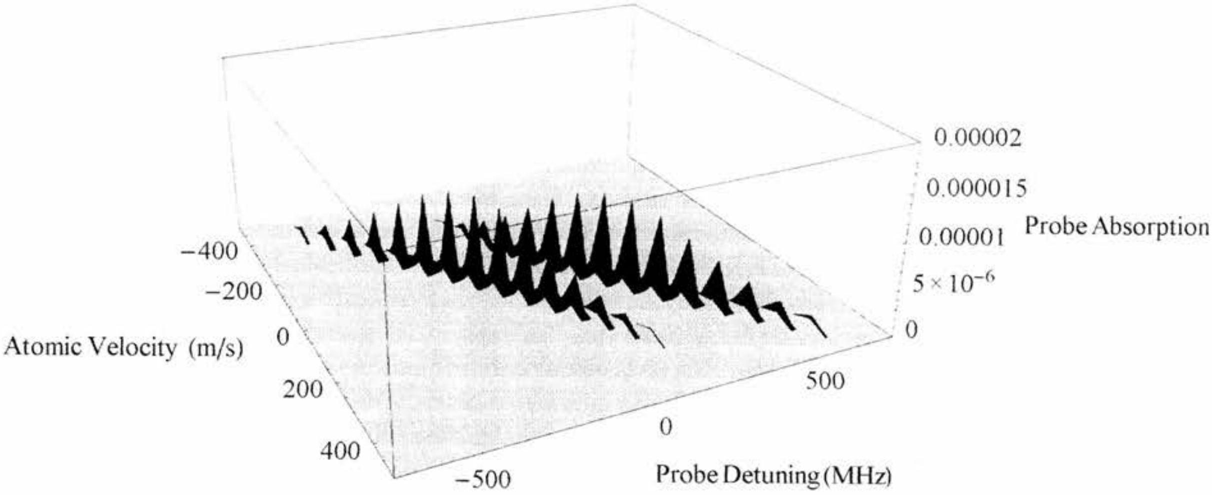

Figure 6.3.14: *Three-dimensional profile of probe field absorption ($\rho^i{}_{13}$ in arbitrary units) as a function of probe field detuning and atomic velocity for several discrete velocities, produced by density matrix analysis of the Lambda scheme (λ_c = 1600nm, and λ_p = 800nm).*

6.3.3 The V-scheme.

- The regime where $\lambda_c<\lambda_p$.

In this wavelength regime the probe field wavelength is twice than that of the coupling field. Figure 6.3.15 shows the probe field absorption as a function of the probe field detuning. EIT is observed exactly on resonance. Figure 6.3.16 is a three-dimensional plot of the absorption as a function of the atomic velocity and the probe field detuning for a discrete number of velocities. A significant transparency window is observed on line centre in this three-dimensional plot.

- The regime where $\lambda_c=\lambda_p$.

In this wavelength regime the coupling field wavelength equals that of the probe field. Figure 6.3.17 shows the probe field absorption as a function of the probe field detuning. EIT is present exactly on resonance. Figure 6.3.18 depicts the three-dimensional graph of the absorption as a function of the atomic velocity and the probe field detuning.

- The regime where $\lambda_c>\lambda_p$.

In this wavelength regime the coupling field wavelength is twice than that of the probe field. Figure 6.3.19 shows the probe field absorption as function of the probe field detuning. In this mismatched scheme there is a transparency window on resonance. This is the only scheme where the transparency window is maintained in this mismatched wavelength regime. Figure 6.3.20 depicts a three-dimensional plot of the absorption as a function of the atomic velocity and the probe field detuning.

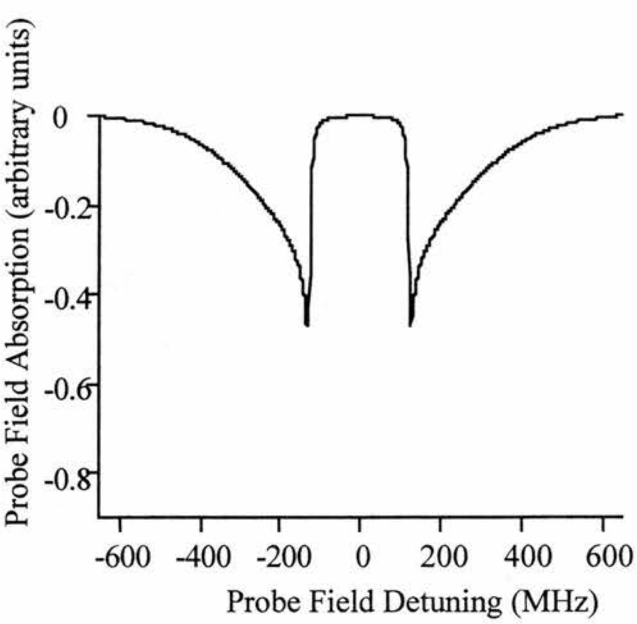

Figure 6.3.15: *Profile of probe field absorption (ρ^i_{13} in arbitrary units) as a function of probe field detuning produced by density matrix analysis of the V-type scheme (λ_c = 400nm, and λ_p = 800nm).*

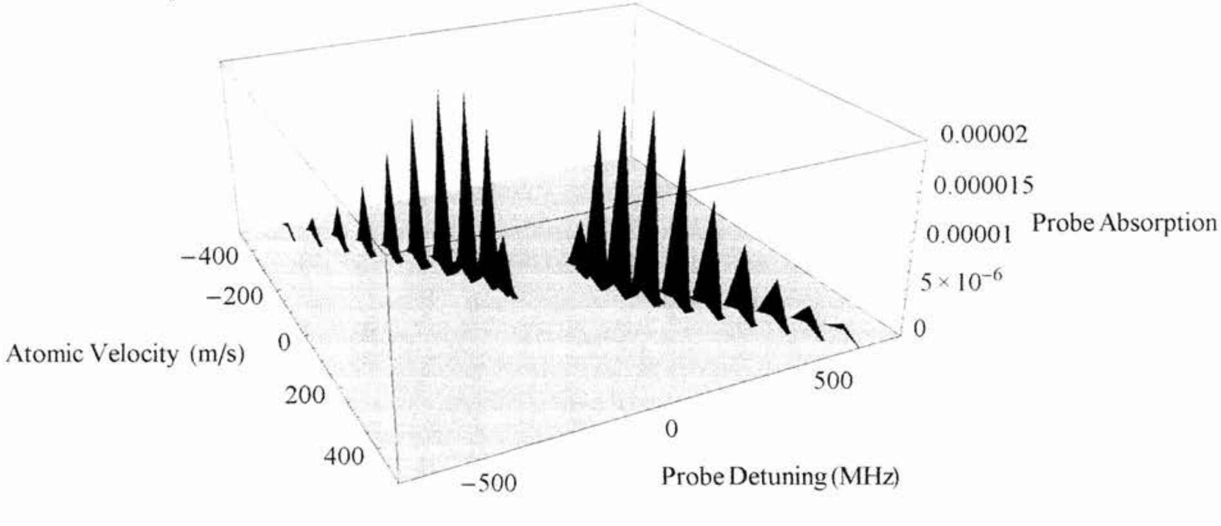

Figure 6.3.16: *Three-dimensional profile of probe field absorption (ρ^i_{13} in arbitrary units) as a function of probe field detuning and atomic velocity for several discrete velocities, produced by density matrix analysis of the V-type scheme (λ_c = 400nm, and λ_p = 800nm).*

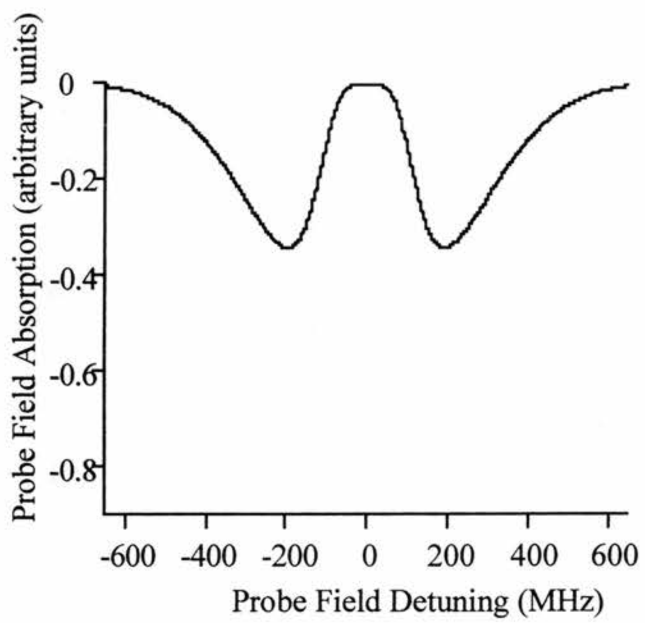

Figure 6.3.17: *Profile of probe field absorption (ρ^i_{13} in arbitrary units) as a function of probe field detuning produced by density matrix analysis of the V-type scheme (λ_c = 800nm, and λ_p = 800nm).*

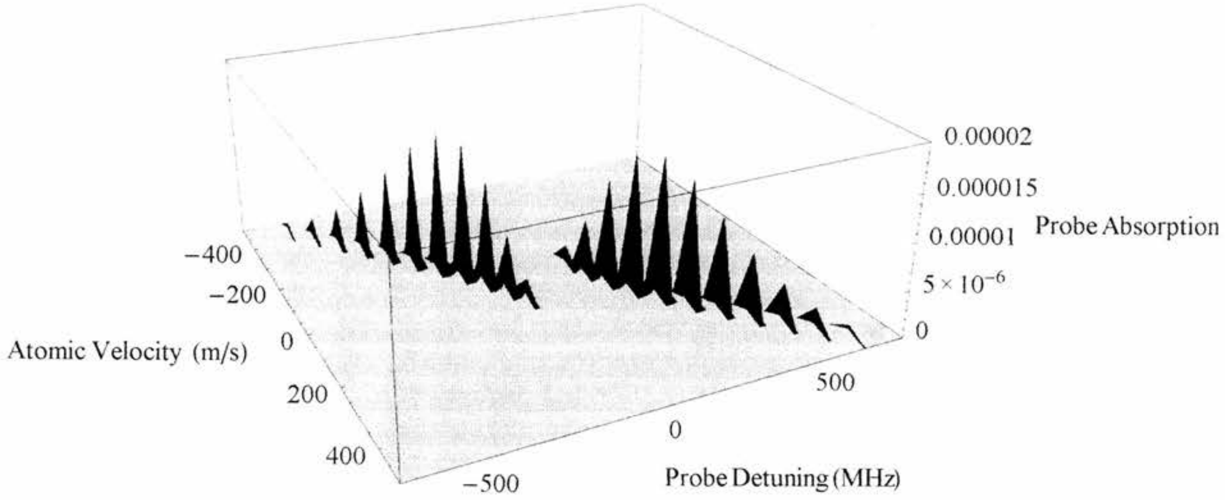

Figure 6.3.18: *Three-dimensional profile of probe field absorption (ρ^i_{13} in arbitrary units) as a function of probe field detuning and atomic velocity for several discrete velocities, produced by density matrix analysis of the V-type scheme (λ_c = 800nm, and λ_p = 800nm).*

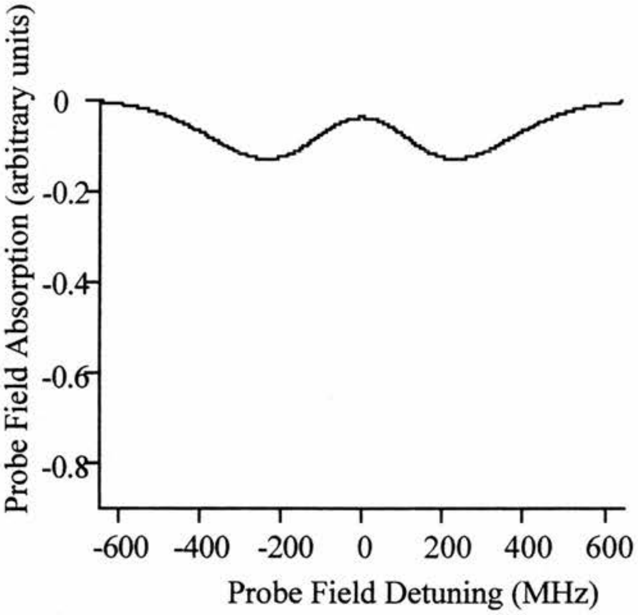

Figure 6.3.19: *Profile of probe field absorption ($\rho^i{}_{13}$ in arbitrary units) as a function of probe field detuning produced by density matrix analysis of the V-type scheme (λ_c = 1600nm, and λ_p = 800nm).*

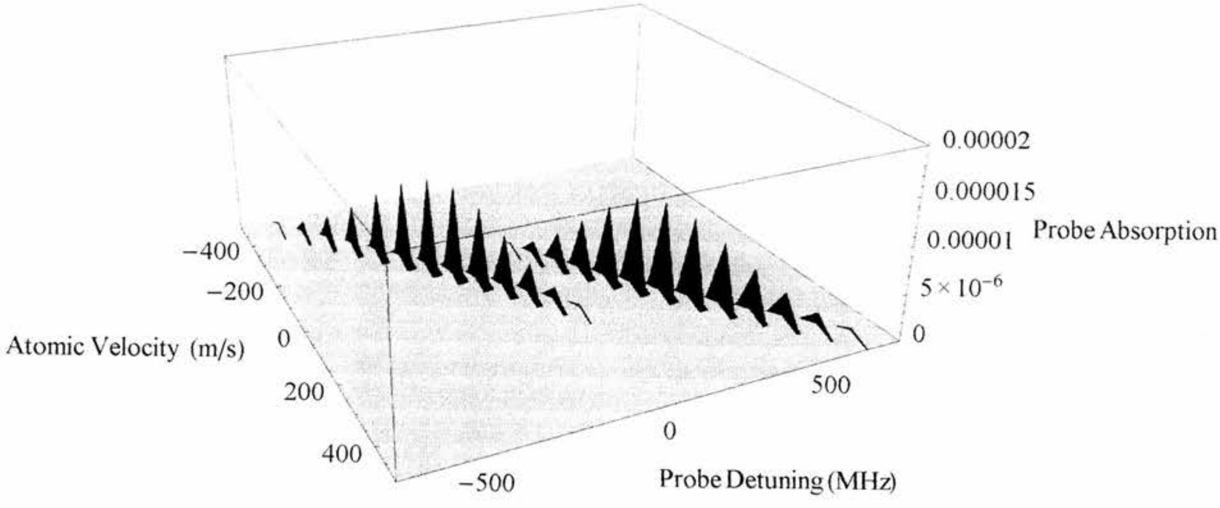

Figure 6.3.20: *Three-dimensional profile of probe field absorption ($\rho^i{}_{13}$ in arbitrary units) as a function of probe field detuning and atomic velocity for several discrete velocities, produced by density matrix analysis of the V-type scheme (λ_c = 1600nm, and λ_p = 800nm).*

In figure 6.3.21a there is a two-dimensional plot of the single Autler-Townes absorption component as a function of the atomic velocity, in the absence of a coupling field. When a two level atom is on resonance with one field we observe no Autler-Townes splitting and no two-photon resonance. Instead there is a single-photon absorption component which is directly related to the single-photon resonance position. In a Doppler broadened medium, and as we have seen in equation 6.3.6, the single-photon resonance position in terms of the detuning is proportional to the atomic velocity. This is the reason why in the graph the single-photon resonance has a linear dependence on the atomic velocity.

In figure 6.3.21b the probe field absorption is plotted as a function of the probe field detuning in the absence of a coupling field. This graph has the same form for all considered systems. The probe field absorption profile is the same for a Cascade, Lambda and V-scheme, when the coupling field is not employed.

Figures 6.3.22, 6.3.23 and 6.3.24 depict two-dimensional graphs of the Autler-Townes absorption components as a function of the atomic velocity, in the presence of the coupling field. The horizontal lines indicate the magnitudes of the Autler-Townes components, deduced using density matrix analysis. The actual graphs are plotted from the equations mentioned above. The position of the Autler-Townes components are shown by the solid lines, the single-photon resonance by a dashed line and the two-photon resonance by a dotted line. Three wavelength regimes are considered like before: $\lambda_c<\lambda_p$, $\lambda_c=\lambda_p$ and $\lambda_c>\lambda_p$. In figure 6.3.22 there are three graphs representing each wavelength regime, for the Cascade scheme, in figure 6.3.23 for the Lambda scheme and in figure 6.3.24 for the V-type scheme.

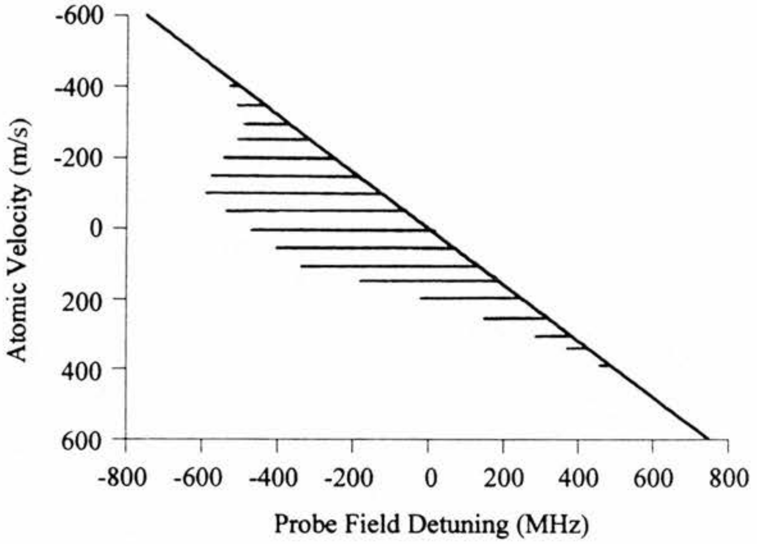

(a)

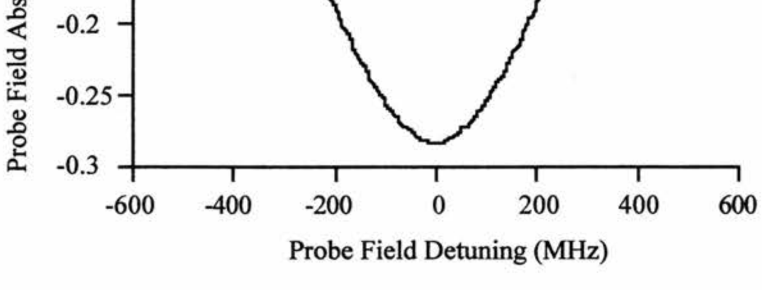

(b)

Figure 6.3.21: *(a) Two dimensional plot of the single Autler-Townes absorption component as a function of the atomic velocity, in the absence of a coupling field. (b) The probe field absorption is plotted against the probe field detuning in the absence of a coupling field.*

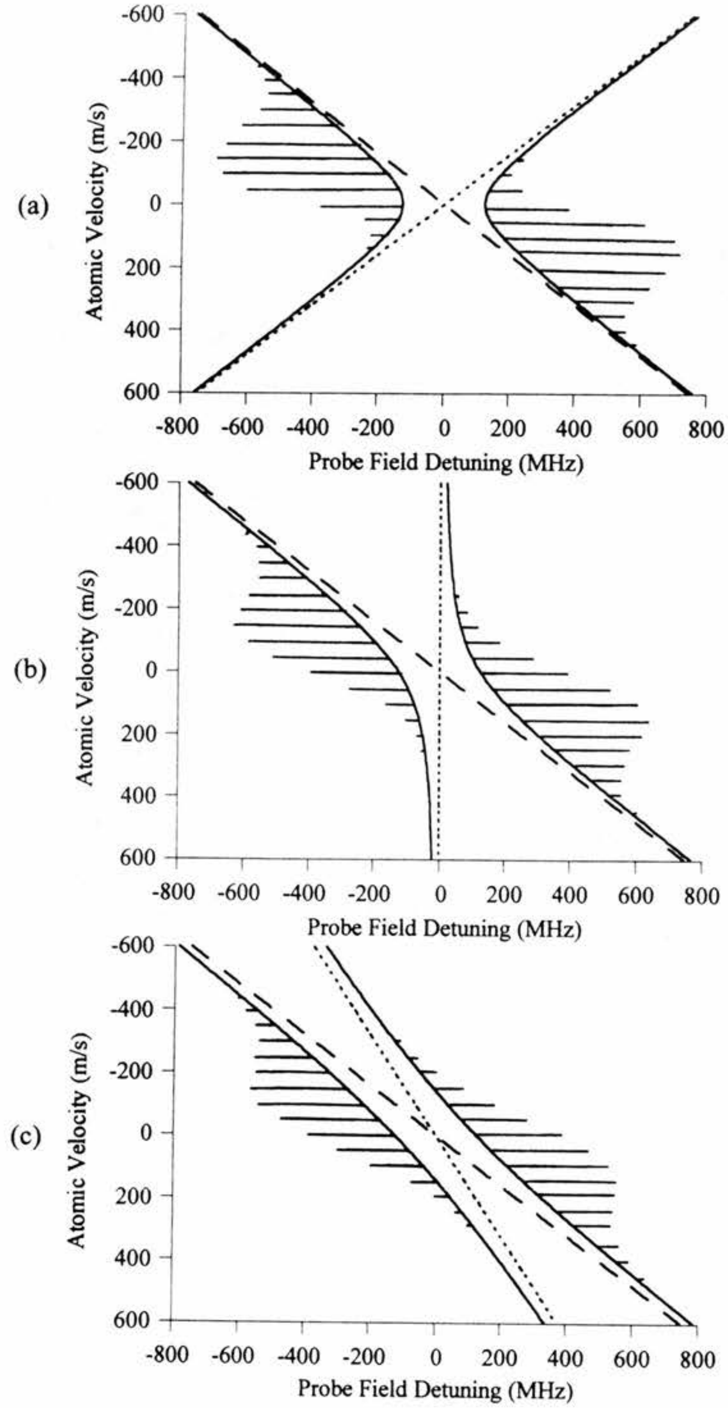

Figure 6.3.22: *Plots of the Autler-Townes components and single and two photon absorption positions as a function of the atomic velocity for the Cascade scheme. Three wavelength regimes are considered: (a)*$\lambda_c<\lambda_p$ *,(b)* $\lambda_c=\lambda_p$ *and (c)* $\lambda_c>\lambda_p$ *. The positions of the Autler-Townes components are shown by the solid lines, the single photon resonance by a dashed line and the two photon resonance by a dotted line.*

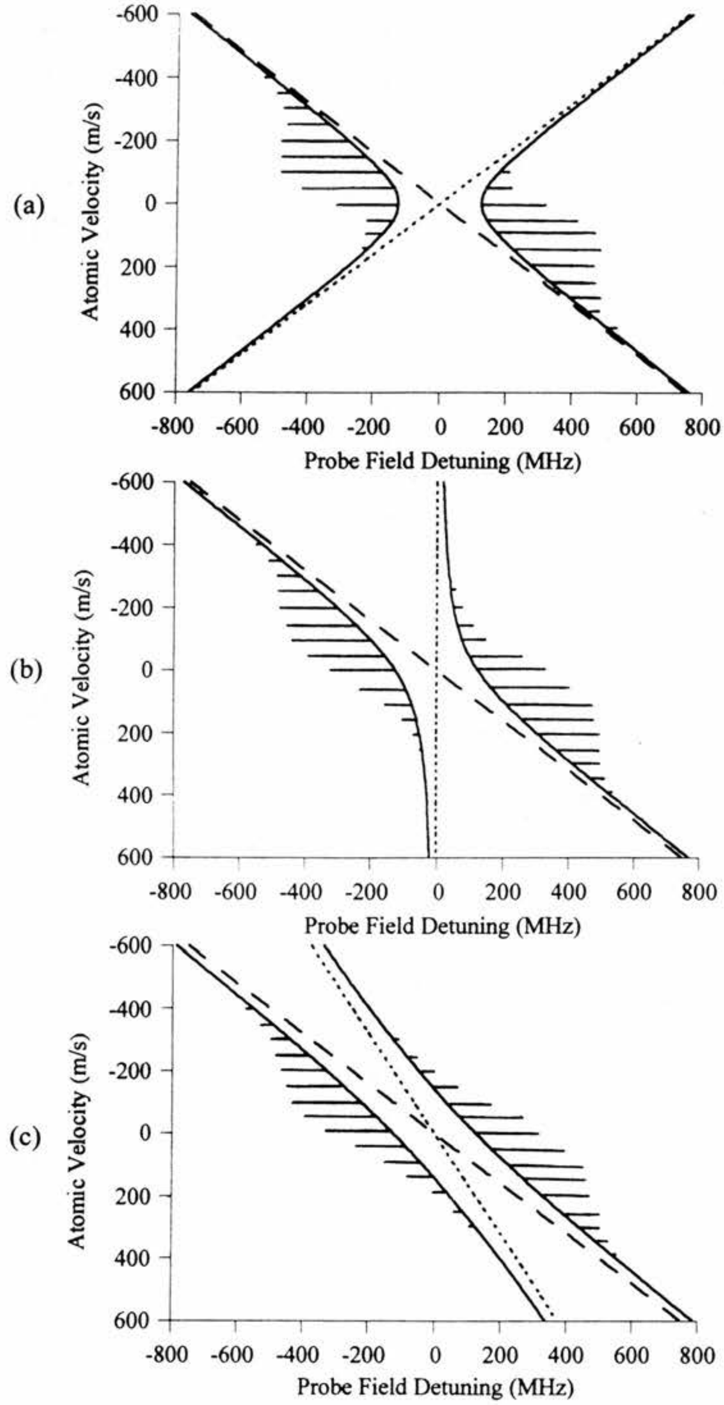

Figure 6.3.23: *Plots of the Autler-Townes components and single and two photon absorption positions as a function of the atomic velocity for the Lambda scheme. Three wavelength regimes are considered: (a)*$\lambda_c<\lambda_p$ *,(b)* $\lambda_c=\lambda_p$ *and (c)* $\lambda_c>\lambda_p$ *. The positions of the Autler-Townes components are shown by the solid lines, the single photon resonance by a dashed line and the two photon resonance by a dotted line.*

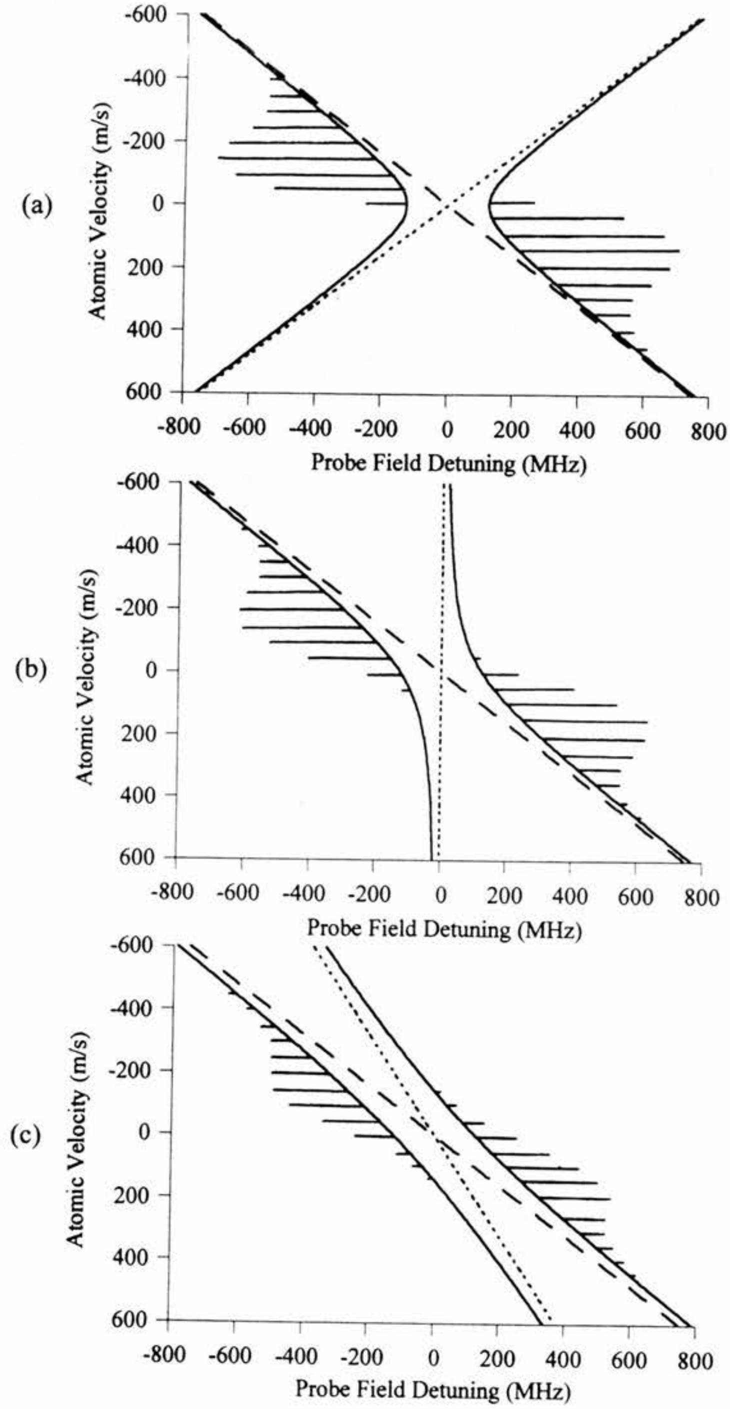

Figure 6.3.24: *Plots of the Autler-Townes components and single and two photon absorption positions as a function of the atomic velocity for the V-type scheme. Three wavelength regimes are considered: (a)$\lambda_c<\lambda_p$,(b) $\lambda_c=\lambda_p$ and (c) $\lambda_c>\lambda_p$. The positions of the Autler-Townes components are shown by the solid lines, the single photon resonance by a dashed line and the two photon resonance by a dotted line.*

6.4 Discussion.

Figure 6.3.2 depicts the absorption profiles for all three schemes. In these graphs the best transparency window occurs for the mismatched case where the coupling field wavelength is less than that of the probe ($\lambda_c<\lambda_p$). We can clearly see that the matched wavelength regime does not provide the best transparency in any of the energy level schemes. Instead the graphs show the advantage on having $\lambda_c<\lambda_p$ as the absorbing Autler-Townes components are shifted away from obscuring EIT, giving a better overall transparency window.

The best transparency happens in this mismatched region because of the Doppler shifted contribution to the coupling field detuning and subsequently to the Autler-Townes absorption positions. The Doppler shift of the coupling field is given as $-k_2V_z$ and for a non-zero velocity group it is inversely proportional to the coupling field wavelength. If we decrease the coupling field wavelength the Doppler shift increases. The Autler-Townes components are split and their splitting is dependent on the Doppler shift as shown in equations 6.3.1 and 6.3.2. Consequently, when the coupling field wavelength is less than that of the probe, the Autler-Townes components are shifted apart, providing a bigger EIT window on resonance. The EIT position for the zero velocity groups on resonance is unperturbed by the Autler-Townes components of the non-zero velocity atoms, for shorter coupling field wavelengths, because these components are Doppler shifted away from resonance and they do not overlap with the transparency window considered. It is therefore important to ensure that the absorbing Autler-Townes components for any one velocity group do not overlap with the maximum transparency points of the other velocity groups, as far as possible. Thus, by trading off the Autler-Townes absorption positions against the maximum transparency position across the velocity groups, it is possible to increase overall transparency by altering the coupling laser wavelength and in fact making it shorter than the probe field wavelength.

If we start increasing the coupling field wavelength the Doppler shift will tend to decrease. The Autler-Townes splitting which is dependent on the Doppler shift, will decrease in the same way as the Doppler shift. Hence, the Autler-Townes components move towards the line centre where the EIT position lies. The Autler-Townes splitting for the non-zero velocity groups will tend towards the zero velocity value and the Autler-Townes absorption components will start to overlap with the on resonance transparency.

The case where the coupling field wavelength equals that of the probe field is now considered. For a selected non-zero velocity group the Doppler shifts of the probe and the coupling fields are equal and they cancel. If the wavevector k_1 and k_2 are the same in magnitude, then the position of the two-photon resonance is the same for all velocity groups (see equation 6.3.5 for the two-photon resonance positions) and the medium can be considered as Doppler free. Consequently, the probe frequency for maximum EIT is the same for all velocity groups. In this matched wavelength regime EIT is demonstrated for all three schemes. The transparency at any point between the Autler-Townes absorption components depends on the dephasing. The magnitude of the dephasing determines where the maximum transparency lies. As we increase the dephasing, we also increase the linewidth of the Autler-Townes components near the resonance position and thus obscure the transparency on line centre. For ease of the comparison the dephasing is set at the same value for all three schemes.

If we increase the wavelength further, we come to the case where the coupling field wavelength is greater than that of the probe ($\lambda_c>\lambda_p$). In figure 6.3.2 (a) and (b) there is no EIT window for the Cascade and Lambda schemes, as expected. In this special regime the Autler-Townes components overlap with the on resonance transparency, as it is shown in the three-dimensional graphs 6.3.8 and 6.3.14 and in figures 6.3.22 and 6.3.23 (c), as well. However, this is not the case for the V-type configuration. In the V-scheme EIT is still observable.

In the case of the zero velocity group the single and two-photon resonances are coincident at line centre and the absorption is equally split between the Autler-Townes components that are evenly spaced about resonance. For the non-zero velocity groups each Autler-Townes component is preferentially enhanced by the absorption resonance that lies closest to it. We refer to the Autler-Townes component associated with the single-photon absorption as the primary component and that associated with two-photon absorption as the secondary Autler-Townes component. Transparency is predicted in this mismatched V-scheme because of the nature of the two-photon process. In a V-scheme the two-photon process (|2>-|1>-|3>) begins in the upper level of the coupling field transition. For non-zero velocity groups the coupling field is Doppler shifted away from the |1>-|2> transition and does not significantly populate level |2>. Therefore, as we consider atoms of a higher velocity the magnitude of the two-photon absorption process rapidly falls off, so that the secondary Autler-Townes components that mask the transparency window are very small in magnitude.

In figures 6.3.22, 6.3.23 and 6.3.24 it is shown that the positions of the single and two-photon absorption resonances are coincident for all schemes, only at the line centre i.e. for the zero velocity group. However, these absorption resonances do not occur for a single frequency, but over a homogeneously broadened function centred on the positions which are indicated by the horizontal lines in figures 6.3.22, 6.3.23 and 6.3.24. EIT is possible when these homogeneously broadened functions for the single and two-photon absorptions overlap. If the magnitudes of the absorption components are equal, then they cancel, providing a full EIT window. If the magnitudes of these absorption components is not equal then there is a partial cancellation. When the absorption resonances for a specific velocity group are shifted beyond one homogeneous linewidth, EIT does not occur and in order to maintain the transparency, these absorption components for any one velocity group should not overlap with the maximum transparency point of other velocity groups.

Figures 6.3.22, 6.3.23 and 6.3.24 show that while the positions of the Autler-Townes components happen at the same place, for a given set of wavelengths, the horizontal lines and hence their magnitudes are different. The magnitude of the secondary Autler-Townes components reduces more quickly in the case where the coupling field wavelength is less than that of the probe field. The above fact happens for all three schemes and it is depicted in figures 6.3.22, 6.3.23 and 6.3.24 (a). The reason is that the non-zero velocity atoms are split further apart and they do not overlap with the line centre transparency. As the detuning is increased due to the Doppler effect the two-photon resonance is shifted away from the line centre and is reduced in magnitude. Figures 6.3.22, 6.3.23 and 6.3.24 (c) depict that the secondary Autler-Townes components overlap on resonance with the transparency window. Their magnitude is significant for a cascade and Lambda schemes and therefore they destroy the transparency window. However, this is not the case for the V-type configuration, where their magnitude is reduced on line centre and EIT is still maintained.

Figures 6.4.1, 6.4.2 and 6.4.3 depict a series of absorption profiles having manual detuning of the coupling field for a Cascade, Lambda and V-schemes respectively. The topmost trace shows the single-photon and the two-photon resonance processes interfering to create EIT on resonance and the bottom trace shows the resolved absorption profiles of the single and two-photon absorption processes. Considering the detuning of the coupling field, we can see that its effect is to separate the two-photon process from the single-photon absorption. In this way we can observe the relative strength of each process for the different schemes. The single-photon absorption is significant for all schemes, but this is not the case for the two-photon absorption resonance. The two-photon process is clearly resolved in the Cascade and Lambda schemes for several detunings. In the V-scheme the two-photon process is present only for the zero velocity group because the coupling field is on resonance. When the coupling field is detuned the two-photon process falls off quickly. This is the reason why we can see a transparency window in the mismatched wavelength regime where $\lambda_c > \lambda_p$. The two-photon process is not strong when the coupling field is detuned from resonance and hence it does not destroy the EIT.

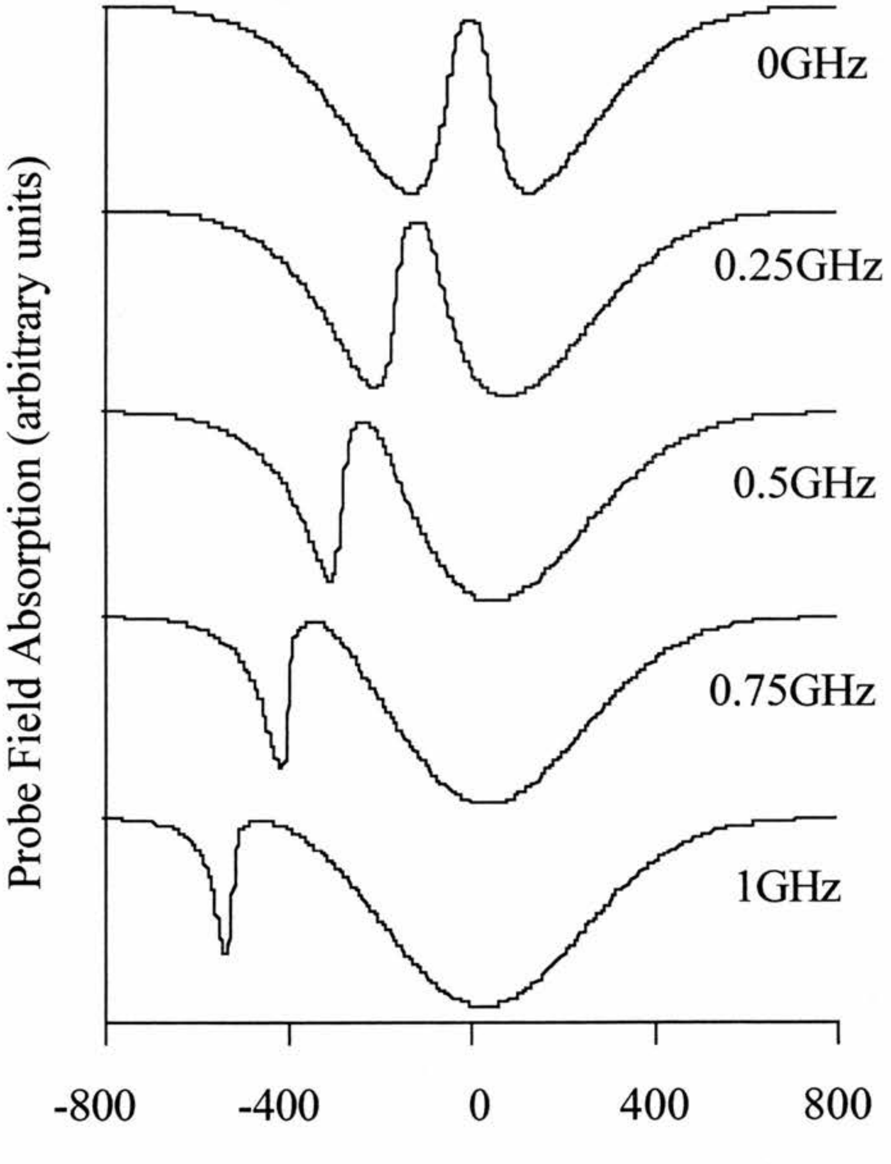

Figure 6.4.1: *A series of absorption profiles showing manual detuning of the coupling field for the Cascade system. The topmost trace shows the single and the two-photon absorption routes interfering to create EIT and the bottom trace shows the resolved absorption profiles of the single and the two-photon processes.*

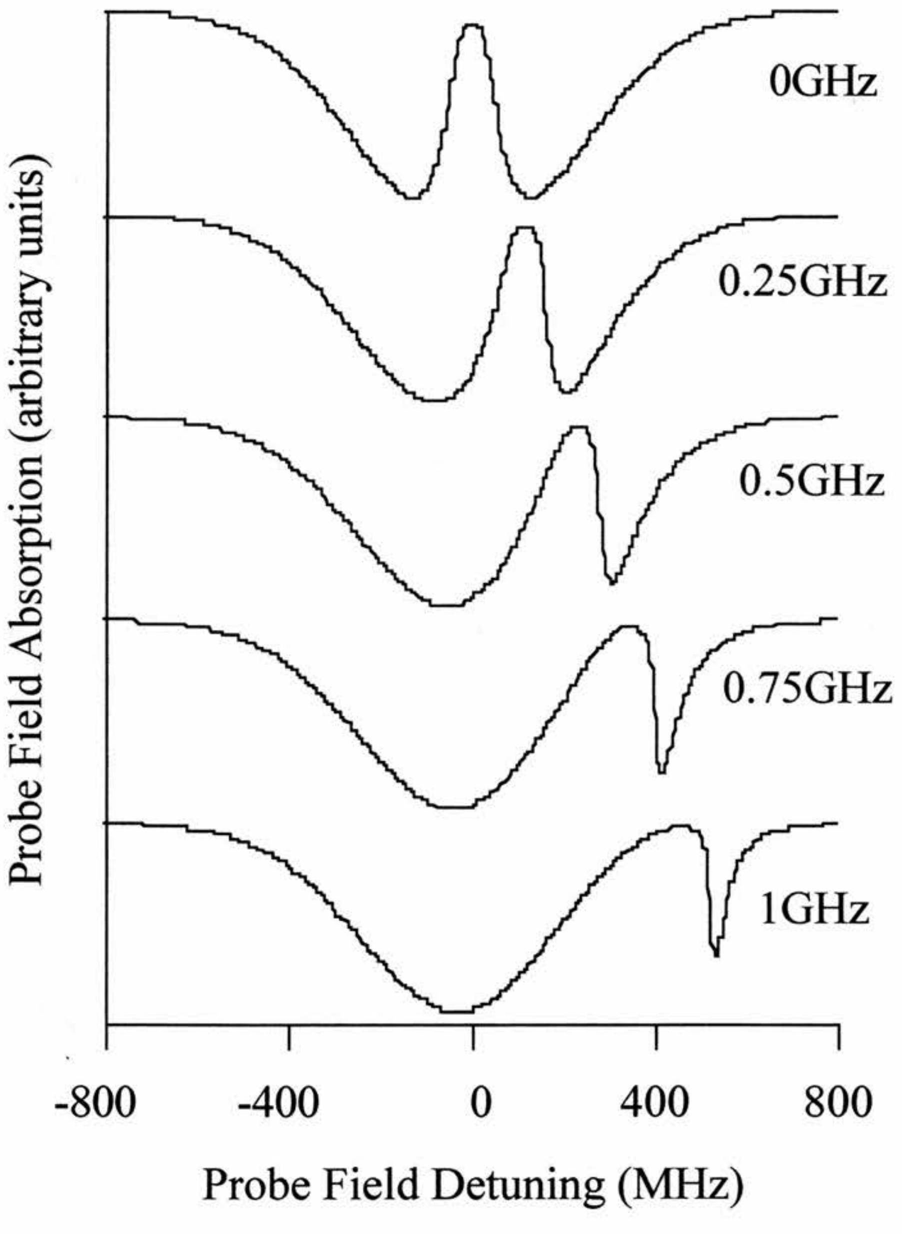

Figure 6.4.2: *A series of absorption profiles showing manual detuning of the coupling field for the Lambda system. The topmost trace shows the single and the two-photon absorption routes interfering to create EIT and the bottom trace shows the resolved absorption profiles of the single and the two-photon processes.*

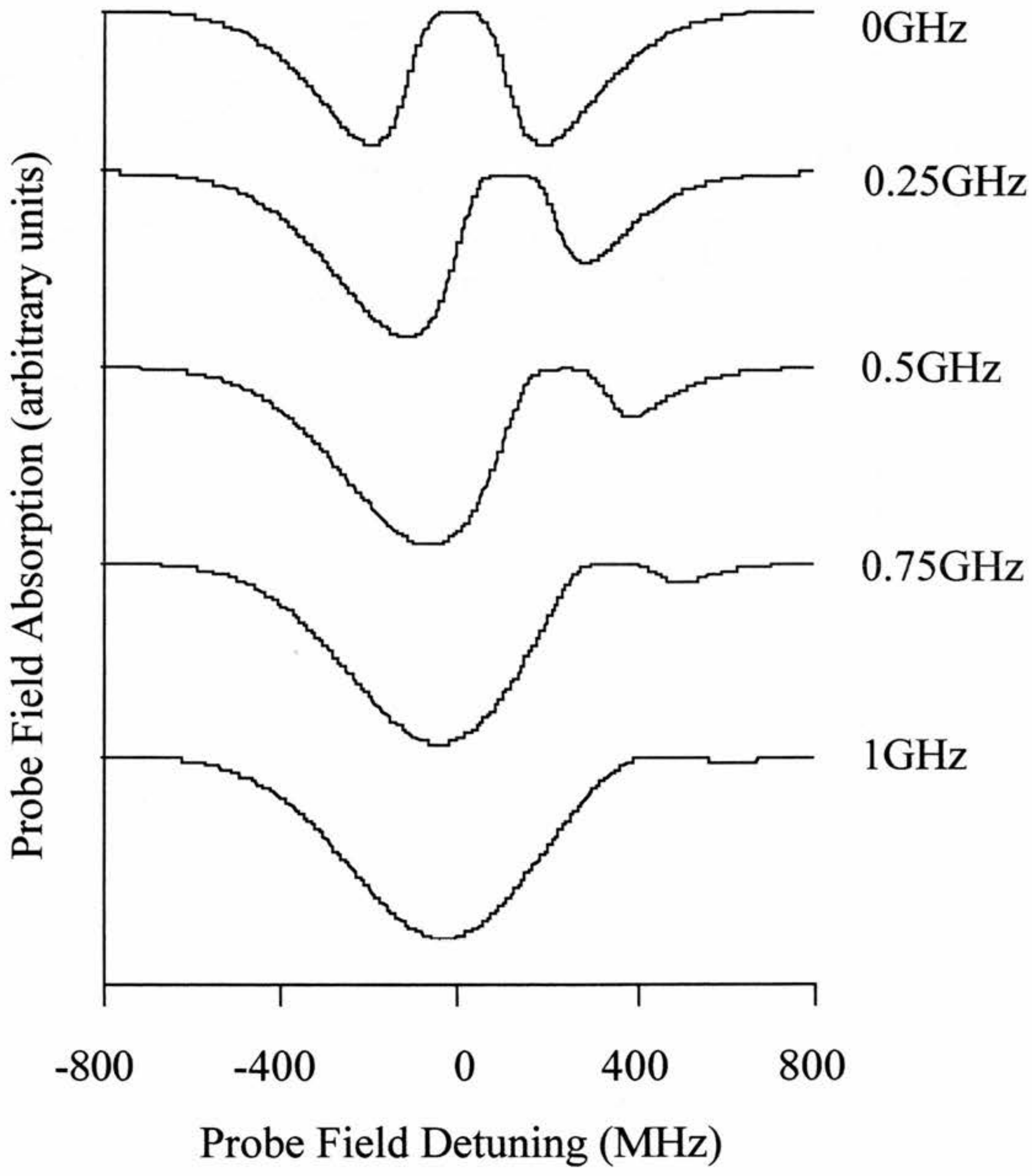

Figure 6.4.3: *A series of absorption profiles showing manual detuning of the coupling field for the V-type system. The topmost trace shows the single and the two-photon absorption routes interfering to create EIT and the bottom trace shows the resolved absorption profiles of the single and the two-photon processes.*

The transparency in a V-scheme is present for all three wavelength regimes due to the nature of the two-photon process. Specially in the $\lambda_c > \lambda_p$ regime there is no trace of the transparency for the Lambda and the Cascade schemes. Figure 6.4.4 shows the on resonance transparency as a function of the linear coupling field Rabi frequency for all three EIT schemes. The V-type configuration is depicted by a solid line and the Cascade and Lambda schemes are indicated by dotted and dashed lines respectively. It is obvious from the graph that the Lambda and the Cascade schemes vary in the same way as we increase the coupling field Rabi frequency. Only the V-type scheme differs. It is shown in the graph that transparency is still possible in the Lambda and the Cascade schemes, but only if we increase the coupling field Rabi frequency beyond the Doppler width.

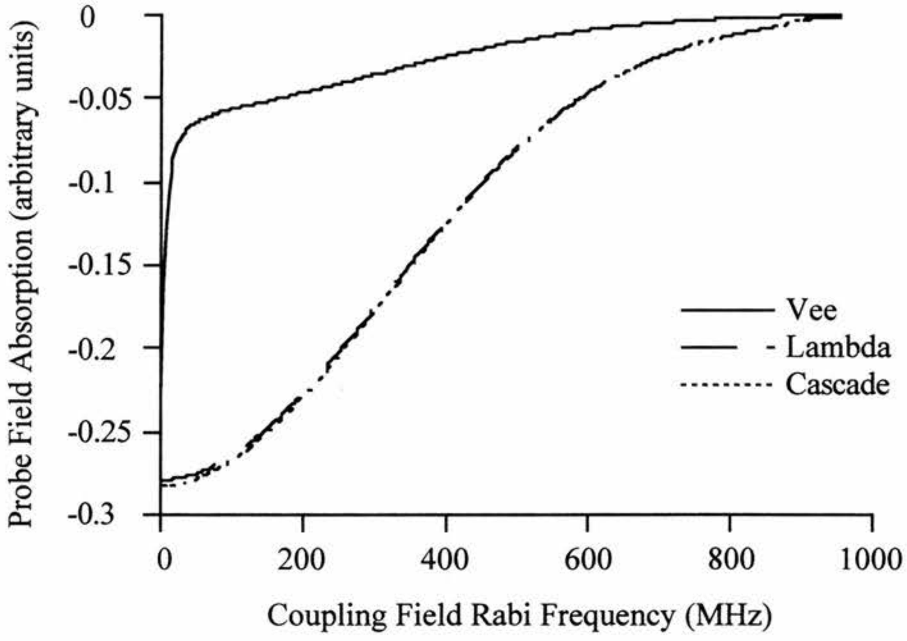

Figure 6.4.4: *The on-resonance absorption is plotted as a function of the coupling field Rabi frequency for all three schemes. The V-type scheme is depicted by a solid line and the Cascade and Lambda scheme are indicated by dotted and dashed lines respectively.*

In this way the Autler-Townes absorption components are split further apart from line centre. The V-type configuration exhibits a different nature. Transparency is predicted in a V-scheme for shorter coupling field Rabi frequencies.

6.5 Further theoretical considerations.

There is some more information in the theoretical results which will now be considered. In figures 6.3.22, 6.3.23 and 6.3.24 it is clear that as we increase the coupling field wavelength beyond the matched case, the range over which the absorption of the Autler-Townes components is observed, increases similarly. This increase occurs because of the existence of secondary Autler-Townes components for higher velocity atoms, due to the reduction in the magnitude of the Doppler shift for a given atomic velocity. As the increase in the bandwidth happens, we observe a corresponding reduction in the peak absorption. This occurs because the total number of absorbing atoms remains constant. For each scheme the total integrated absorption remains the same, regardless of the choice of the probe and the coupling field wavelengths.

In addition, if we observe the absorption profiles of the Lambda and Cascade scheme for the matched wavelength regime, they are almost similar, as shown in figure 6.3.2. This is not the case for the magnitude of the Autler-Townes components and in fact the Autler-Townes components, in figures 6.3.22 and 6.3.23, have a smaller magnitude in the Lambda scheme. The explanation of this lies in the linewidth effects. It is obvious from figure 6.2.1, that in the Lambda scheme the population decays as a result of both decay rates Γ_{31} and Γ_{32}. The total decay from the level, which determines the linewidth, has a value twice than that of a Cascade or a V-scheme. Hence, the absorption profile for each Autler-Townes component is reduced in magnitude. We have to note that if we integrate over all atomic velocities, the overall absorption stays the same in a Lambda and a Cascade scheme, for the matched wavelength regime.

Subsequently, it is worth noting the coupling field saturation for the V-type configuration. Coupling field saturation occurs in the V-scheme because the strong field is linked to the ground state and excites a substantial fraction of the population from the ground state into the upper level of the coupling field transition. This fraction of the population depends on the strength of the coupling field. There is a limit when the coupling field is so strong, that it equalises the population of the ground state and the excited state, and hence the coupling field transition is saturated.

In a Doppler broadened system this process is velocity selective. Coupling field saturation occurs for the velocity group of atoms that are on resonance with the field. The other groups for which the coupling field is detuned, will not experience the effect. In a V-scheme and for the mismatched $\lambda_c>\lambda_p$ regime, the transparency window is maintained because the secondary Autler-Townes components associated with the high velocity groups, that overlap on line centre, are very small in magnitude. When the coupling field is detuned from resonance and hence the coupling field saturation is negligible, the two-photon process is greatly reduced. Therefore the absence of any coupling field saturation effects, allow the transparency to occur for this mismatched configuration. On resonance there is the case that the absorption is halved by the coupling field saturation of the zero velocity groups, but EIT effects reduce the absorption well beyond this point.

The results discussed in this chapter can be broadly applied to any mismatched Doppler broadened system. For the V-type configuration when $\lambda_c>\lambda_p$, the transparency window is maintained, for the coupling field Rabi frequency which is half of the Doppler width of the probe field transition. In this system the ratio of the coupling and probe field wavelength is 2:1. If we assume that the coupling field wavelength is 200 nm, then this will induce the same level of transparency to 100 nm probe field wavelength, in the case where the Rabi frequency is adjusted to be half of the new Doppler width and the decay rates are unchanged.

We can then increase the ratio of the coupling and probe field wavelengths, and explore the effect which this has on the transparency window. We would expect the transparency to degrade. For this purpose the V-scheme is considered, with a coupling field wavelength in the visible of 500 nm which is kept constant, while the probe field wavelength is reduced. The transition decay rates have the same values, as before. The ratios are chosen to be 2:1, 4:1, 8:1 and 16:1 and the results are depicted in figure 6.5.1 and figure 6.5.2. This takes the probe field down to 30 nm. The Rabi frequency in each graph is altered in order to be kept half of the Doppler width for each case. It is clearly shown in the plots that when the ratio approaches 8:1, there is no transparency window observed.

The result of changing the ratio of the probe and the coupling field wavelengths is that EIT can be induced in cases where the Rabi frequency is half of the Doppler width, for coupling- probe field wavelength ratios of 4:1 or less. If we increase the ratio to a higher value, the transparency degrades. Hence, we need to apply Rabi frequencies comparable or greater than the Doppler width of the probe transition. This implication is very important when we want to apply these ideas of the V-scheme in a practical inversionless lasing experiment.

6.6 Conclusions.

A theoretical comparison of mismatching the coupling and the probe field wavelengths is presented in a Doppler broadened medium for the Cascade, the Lambda and the V-type schemes. Three wavelengths regimes are utilised $\lambda_c < \lambda_p$, $\lambda_c = \lambda_p$ and $\lambda_c > \lambda_p$. The imaginary part of the probe coherence which is proportional to the probe absorption is considered as a function of the atomic velocity and the probe detuning. The best EIT is shown for the mismatched case where $\lambda_c < \lambda_p$. This is a direct result of the increased Doppler shifted contribution to the coupling field detuning.

EIT is achieved for a V-scheme even in the mismatched regime of $\lambda_c > \lambda_p$. This happens due to the reduced magnitude of the secondary (two-photon) Autler-Townes components. Eventhough they overlap on line centre, their magnitude is not sufficient to destroy the transparency window. In this wavelength regime EIT is not observable for the Cascade and the Lambda schemes. The Autler-Townes components are considered, together with the single and the two-photon resonance processes. Their

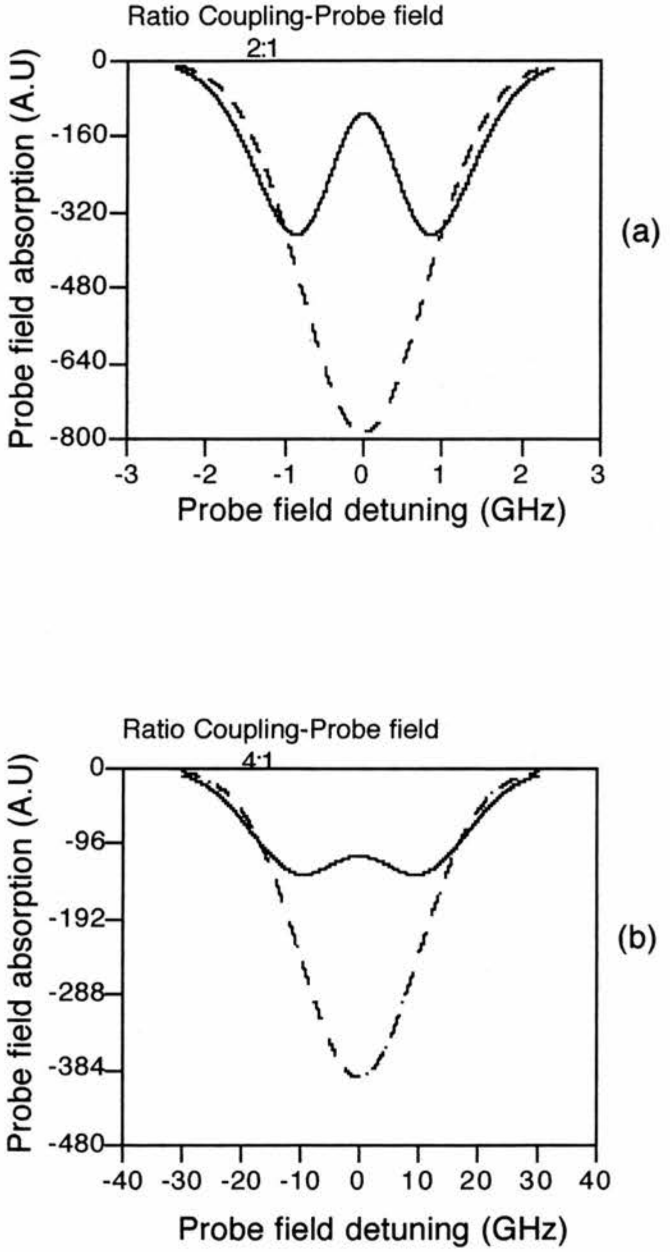

Figure 6.5.1: *Plots of the probe field absorption as a function of the probe field detuning in a mismatched V-scheme. In both cases the coupling field is 500 nm. In (a) the probe field is 250 nm and in (b) the probe field is 125 nm. The transparency window degrades as the ratio of the coupling to probe field wavelength is increased.*

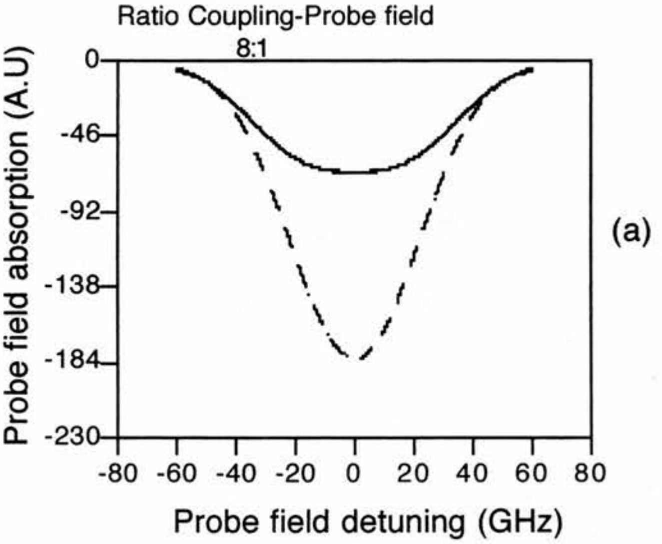

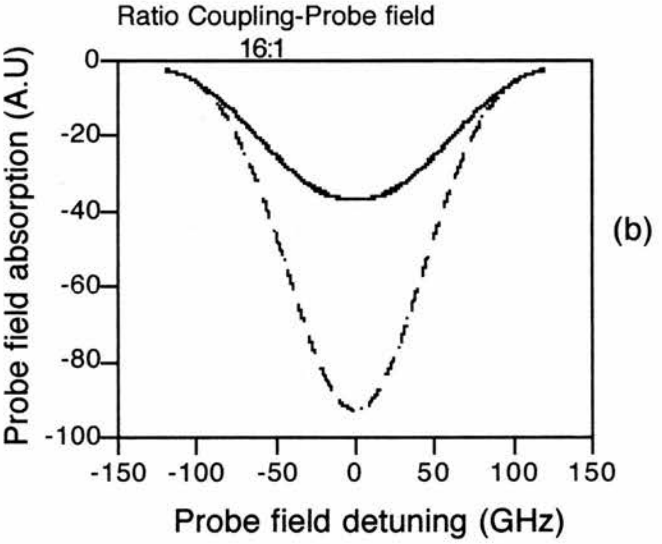

Figure 6.5.2: *Plots of the probe field absorption as a function of the probe field detuning in a mismatched V-scheme. In both cases the coupling field is 500 nm. In (a) the probe field is 60 nm and in (b) the probe field is 30 nm. The transparency window degrades as the ratio of the coupling to probe field wavelength is increased*

magnitude is also included in the discussion of the absorption in each scheme. Quantum coherence effects, such as EIT are not confined to the matched wavelength regime in a Doppler broadened medium. The V-scheme provides the best transparency in all wavelength regimes and especially in the regime where the coupling field wavelength is higher than that of the probe field, leading us to a shorter wavelength regime.

References

Fulton D.J., Shepherd S., Moseley R.R, Sinclair B.D. and Dunn M.H., "CW electromagnetically induced transparency: A comparison of V, Lambda and cascade systems", Physical Review A, **52**, p.2302 (1995)

Imamoglu A., Field J.E. and Harris S.E., "Lasers without inversion: A closed lifetime broadened system", Physical Review Letters, **66,** p1154 (1994)

Li Y. and Xiao M., Physical Review A, **51**, pR2703, (1995)

Moseley R.R., Shepherd S., Fulton D.J., Sinclair B.D. and Dunn M.H., " Interference between excitation routes in resonant sum-frequency mixing", Physical Review A, **50**, p4339 (1994)

Shepherd S., Fulton D.J., and Dunn M.H, " Wavelength dependence of coherently induced transparency in a Doppler-broadened cascade medium", Physical Review A, **54**, p.5394 (1996).

Zibrov A.S., Lukin M.D., Nikonov D., Hollberg L., Scully M.O, Velichansky V.L. and Robinson H.G., "Experimental demonstration of laser oscillation without population inversion via quantum interference in Rb", Physical Review Letters, **75**, p.1499 (1995) .

Chapter 7

The study of microwave induced transparency in Rubidium

7.1 Introduction.

In this chapter we present the study of electromagnetically induced transparency (EIT) in Rb atoms using an RF coupling field. Recent theoretical and experimental results indicate that quantum interference can lead to EIT and subsequently to lasing without population inversion for matched systems, *Zibrov et al*. Commonly used schemes for achieving EIT are three level systems with two electromagnetic fields on resonance, *Boller et al.* Usually the coupling field to induce transparency is an optical field i.e. a laser source. What will happen if we mismatch the wavelengths in such a way so that the coupling field wavelength lies in the microwave regime?

Ham et al reported an observation of radio frequency induced transparency in rare earth-doped solid, Pr^{3+}-doped Y_2SiO_5. This type of crystal was chosen because of its large oscillator strength. The system that they used was a ladder type inhomogeneously broadened scheme. The transition probe wavelength was 606 nm and the RF field was resonant on the 10.2 MHz splitting of the ground state. The medium was rendered transparent to the probe field, by the presence of the strong microwave pulse. The best transparency was obtained when the RF pulse area was 2π. The observed transparency was shown to be due to both the population change on the ground states and also from quantum interference (EIT). Therefore, this indicates that coherently induced transparency is possible, utilising a mismatched system with a coupling field frequency lying in the microwave regime. In the present chapter we consider an atomic system, instead of a solid and subsequently we propose an appropriate procedure to observe microwave induced transparency.

Rubidium consists of two isotopes ^{87}Rb and ^{85}Rb. One isotope ^{85}Rb has hyperfine structure in the ground state. Consequently, the ground state of ^{85}Rb splits in two other levels spaced by 3 GHz. We consider a V-scheme where the probe field is on resonance with an infrared transition and the coupling field is on resonance with the hyperfine splitting of the ground state in ^{85}Rb. In this chapter we show the viability of producing EIT in ^{85}Rb, utilising a coupling field of 3 GHz. This fact is demonstrated both in a Doppler broadened vapour and in an atomic beam. The Doppler broadened medium requires higher Rabi frequencies and hence more powerful microwave sources.

We also present the calculations for the construction of a TE_{011} cavity. This cavity either contains the Rb cell or the Rb atomic beam. The TE_{011} cavity resonates at 3 GHz. The cavity provides a high Q for the enhancement of the oscillating magnetic field at 3 GHz. The apparatus for the experiment is also described. The feasibility of such experiment depends on the microwave power required. The powers for the ^{85}Rb vapour are very high and the only way to proceed is the use of an atomic beam. However, the atomic beam experiment would itself require microwave sources at the 50-100 kW level. The oscillator presently available in the lab provides a maximum 10 W in the microwave regime of 1-10 GHz. Therefore, a new oscillator-amplifier configuration must be developed in order to achieve EIT in this microwave regime.

7.2 Theoretical modelling of the Doppler-broadened system.

The mismatched system used in the case of Doppler broadened ^{85}Rb scheme is depicted in figure 7.2.1.

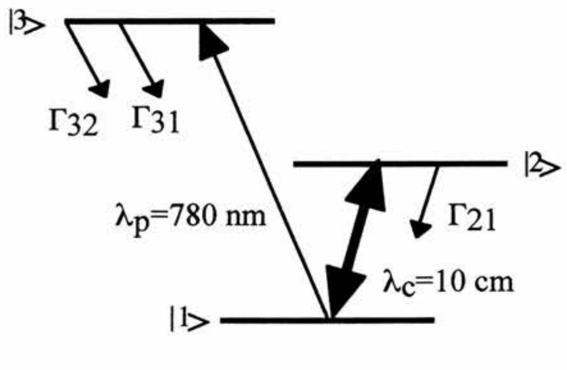

Figure 7.2.1: *The V-type energy configuration in ^{85}Rb. The probe field wavelength lies in the infrared regime whereas that of the coupling field lies in the microwave regime.*

The probe field wavelength lies in the infrared region of the spectrum and may easily be obtained by diode or Ti:Sapphire lasers. The probe field is on resonance with the $5S_{1/2}(F=2)$ to $5P_{3/2}$. The coupling field wavelength is in the microwave regime. The coupling field is on resonance with the two hyperfine levels of the ground state i.e. $5S_{1/2}(F=2)$ to $5S_{1/2}(F=3)$. The decay rates from the upper level are $\Gamma_{31}=20$ MHz and $\Gamma_{32}=20$ MHz respectively. The decay rate of the ground state is calculated as the transit time decay rate:

$$\Gamma_{21} = \gamma = \frac{\overline{v}}{d} = 5 \text{ Mrad/sec} \tag{7.2.1}$$

where $\overline{v}$ is the average velocity of the atoms and d is the probe field diameter. The average velocity of the atoms is given by:

$$\overline{v} = \sqrt{\frac{2kT}{m}} \tag{7.2.2}$$

where k is the Boltzman's constant, T the temperature of the atoms and m the atomic mass.

Theoretical modelling of the system is carried out using standard density matrix analysis; see chapter 2. The six equations for the slowly varying density matrix are derived for a closed system. The equations are solved by invoking steady state solutions. Considering the real and the imaginary part of the coherences these equations can then split into nine equations, using properties of the density matrix and they are solved using linear algebra routines with mathematica software. The solutions yield values for the real and the imaginary parts of the coherence in each transition, which can be related to the refractive index and the absorption respectively. The solutions provide also information about the proportion of the atomic population in each energy level. Eventually, Doppler broadening is taken into account by integrating over the velocity distribution from -500 m/s to 500 m/s.

The imaginary part of the probe coherence is plotted as a function of the probe field detuning, in figure 7.2.2. The coupling field Rabi frequency is taken Ω_c= 1 GHz and the probe field Rabi frequency is Ω_p = 1 MHz. As it is shown in the graph EIT is observable exactly on resonance for this scheme. Coherently induced transparency is present even in the case where the coupling field wavelength is in the microwave regime. Mismatching the wavelengths so far does not affect the transparency induced in such a scheme.

We may note at this point, that the Rabi frequency of the coupling field is in the range of GHz. The coupling field frequency is 3 GHz. Hence, higher Rabi frequencies become comparable to the actual frequency of the microwave coupling field. The model is less precise when we induce Rabi frequencies close to the frequency of the coupling field. We will not be able to apply the rotating wave approximation in our analysis, when we derive the rate equations for the density matrix components. Therefore, the coupling field Rabi frequency is limited in our theoretical modelling of this V-scheme, by the frequency of the microwave coupling field.

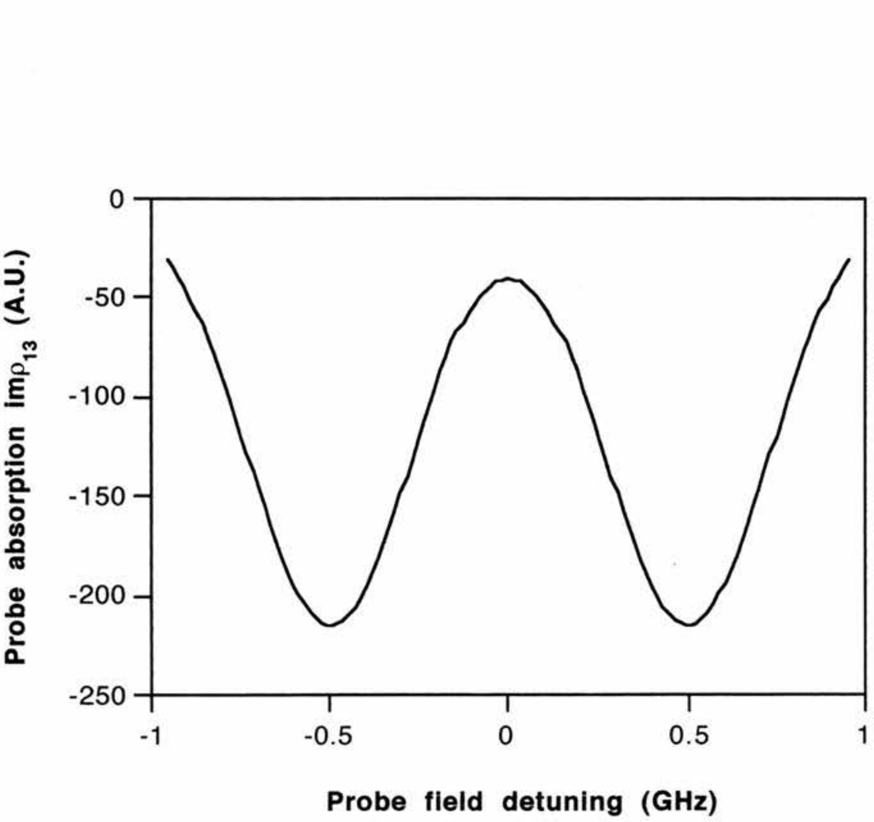

Figure 7.2.2: *The imaginary part of the probe coherence, which is proportional to the probe absorption is plotted as the function of the probe detuning. The coupling field Rabi frequency is taken $\Omega_c = 1$ GHz and the probe field Rabi frequency is $\Omega_p = 1$ MHz.*

7.3 Theoretical modelling of the atomic beam.

The theoretical system used in the calculation of EIT in an atomic beam is depicted in figure 7.3.1. The system is no longer closed and the transit time decay rate now determines the ground state decay rate and must be included in the population decays from all other energy levels, according to *Padmabandu G.G et. al.*

The atomic beam was selected because it provides a Doppler free medium. By observing the beam at right angles to its propagation direction we can see that the atoms have the close to zero resolved velocity. However, there will be a residual Doppler width. Its value is determined by the atomic beam parameters and in particular by the collimation ratio. The collimation ratio is given by:

$$C=D / S \tag{7.3.1}$$

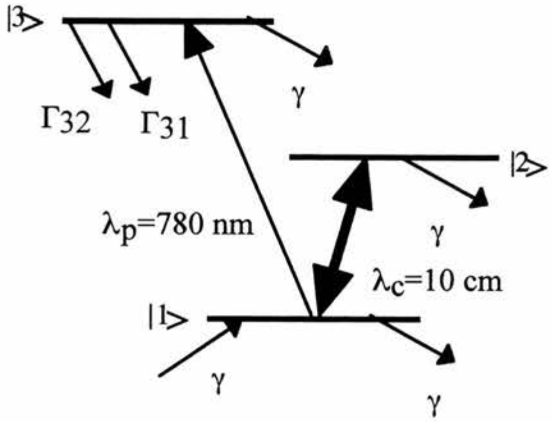

Figure 7.3.1: *The energy level configuration for a V-scheme, using an atomic beam as an interaction medium. The coupling field wavelength lies in the microwave regime whereas that of the probe beam lies in the infrared region of the spectrum.*

where D is the distance between the two collimating slits and S is the slit width in the direction of the observation. We want to calculate the collimation ratio in order to get a residual Doppler width in the order of 100's of kHz, i.e. consider the case of 250 kHz. A slit width of $S=0.1\times10^{-3}$ m and a slit to slit separation $D=95\times10^{-3}$ m provides a collimation ratio of C=950. The residual Doppler width may be calculated from the following expression :

$$\Delta\nu_B = 0.41\Delta\nu_D / C \tag{7.3.2}$$

where C is the collimation ratio and $\Delta\nu_D$ the Doppler width in the oven. If we want an atomic beam with a residual Doppler width of the order of $\Delta\nu_B$=250 kHz and work with a collimation ratio C=950, the Doppler width in the oven should have the value of $\Delta\nu_D=5.25\times10^8$ Hz.

We also require 15% absorption of the probe field at the wavelength of 780 nm. This amount of absorption is easily measurable. The percentage of the absorption is given by:

$$\%\mathrm{Abs}=1-\exp(al)=15\% \tag{7.3.3}$$

where a is the absorption coefficient and $l=1\times10^{-3}$ m the beam absorption width. The absorption coefficient required is then around -150 m^{-1}, and may be expressed as:

$$a = -\frac{2Nc^2\sqrt{\ln 2}}{8\pi(\nu_0)^2 tn^2\Delta\nu_B\sqrt{\pi}}\times\frac{5}{12}\times\frac{24}{5} = -150\ \mathrm{m}^{-1} \tag{7.3.4}$$

where N atoms/m^3 is the final beam density, $\nu_0=3.84\times10^{14}$ Hz the transition frequency, n=1 the refractive index, $t=26.7\times10^{-9}$ s the lifetime of the transition, 5/12 and 24/5 are factors due to degeneracy and $\Delta\nu_B$ =250 kHz is the residual Doppler width. From equation 7.3.4, we could now derive the final atomic beam density. Substituting all the above values gives $N=1.99\times10^{13}$ atoms/m^3. Knowing the final beam density, we can calculate the beam density required inside the oven and hence, the temperature of the oven, as shown in figure 7.3.2. The final beam density is given by the above equation:

$$N = \frac{N_i S L D_1^2}{S_1 L_1 D^2} \tag{7.3.5}$$

where $S=0.1\times10^{-3}$ m is the slit width, $L=5\times10^{-3}$ m is the slit length, $D=95\times10^{-3}$ m is the slit to slit separation, $S_1=1\times10^{-3}$ m the oven slit width, $L_1=1\times10^{-3}$ m is the oven slit length, $D_1 = 5\times10^{-3}$ m is the oven slit separation and N_i the beam density at the first slit.

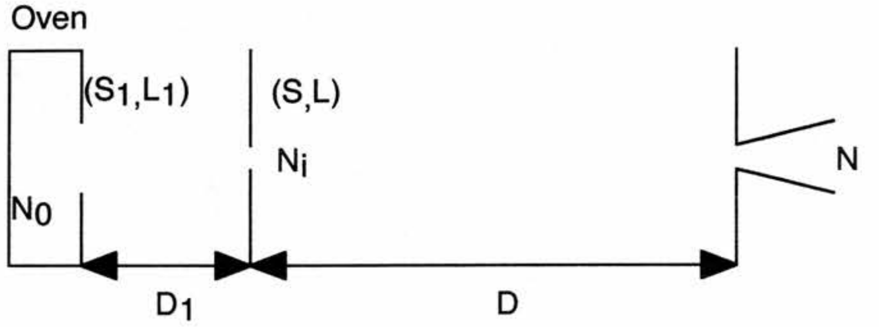

Figure 7.3.2: *The atomic beam configuration. After the oven there are two collimating slits. In the scheme N is the final beam density,* N_i *is the beam density after the first collimating slit and* N_o *the atomic density inside the oven.* $S=0.1\times10^{-3}$ *m is the slit width,* $L=5\times10^{-3}$ *m is the slit length,* $D=95\times10^{-3}$ *m is the slit to slit separation,* $S_1=1\times10^{-3}$ *m the oven slit width,* $L_1=1\times10^{-3}$ *m is the oven slit length,* $D_1= 5\times10^{-3}$ *m is the oven slit separation.*

The beam density at the first slit is given by:

$$N_i = \frac{N_0 S_1 L_1}{4\pi D_1^2} \tag{7.3.6}$$

Substituting equation 7.3.6 in 7.3.5, the final beam density is related to the atomic density inside the oven, as follows:

$$N = \frac{N_0 S L}{4\pi D^2} \tag{7.3.7}$$

where $S=0.1\times10^{-3}$ m is the slit width, $L=5\times10^{-3}$ m is the slit length, $D=95\times10^{-3}$ m is the slit to slit separation and $N=1.99\times10^{13}$ atoms/m^3.

The atomic beam of Rb consists of two isotopes ^{87}Rb and ^{85}Rb. We are particularly interested in ^{85}Rb isotope. The abundance of ^{85}Rb is 72% and the weighting factor due to degeneracy is 5/12. Hence, 5/12 of 72% of ^{85}Rb, i.e. 30% of the total atom density will interact. The oven density required of ^{85}Rb is $N_0=4.51\times10^{18}$ atoms/m^3 calculated from equation 7.3.7. The total atom density is given by:

$$N_T=\text{Pressure(Pascal)}/k_BT=1.5\times10^{19}\ \text{atoms/m}^3 \tag{7.3.8}$$

where Pressure(Pascal)= 133.32 Pressure(torr).

The pressure in torr is derived from an empirical formula using the Nesmeyov parameters for rubidium: q=15.88, r=4529.64, s=0.00059 and u=-2.99. The equation of the pressure has then the form:

$$\Pr\text{essure(torr)} = 10^{(q-r/T+sT+u\log_{10}T)} \tag{7.3.9}$$

Therefore, if we want 15% of the atomic density to be absorbed in an atomic beam with a collimation ratio of C=950 and a residual Doppler width of 250 kHz, we have to operate the oven at a temperature of T=120°C.

Then we can calculate the velocity width of the atoms from equation 7.3.10:

$$v = \Delta\nu_B\times\lambda \tag{7.3.10}$$

Thus for a wavelength of 780 nm the velocity width of the atoms is v=0.22 m/s. The velocity width of the atoms can have a smaller value if we change the value of the collimation ratio and in particular if we alter the slit width of the beam.

Density matrix analysis is followed for this configuration. The dephasings are given for each transition as follows:

$$\gamma_{12}= \gamma \tag{7.3.11}$$

$$\gamma_{13}= \gamma+\Gamma_{31}/2+\Gamma_{32}/2 \tag{7.3.12}$$

$$\gamma_{23}= \gamma+\Gamma_{31}/2+\Gamma_{32}/2 \tag{7.3.13}$$

The density matrix system is solved using linear algebra with Mathematica software. The residual Doppler width is taken into account by integrating over the velocity distribution for this width. The numerical results are shown in figure 7.3.3. The imaginary part of the probe coherence, which is proportional to the probe absorption is plotted against the probe field detuning for this scheme.

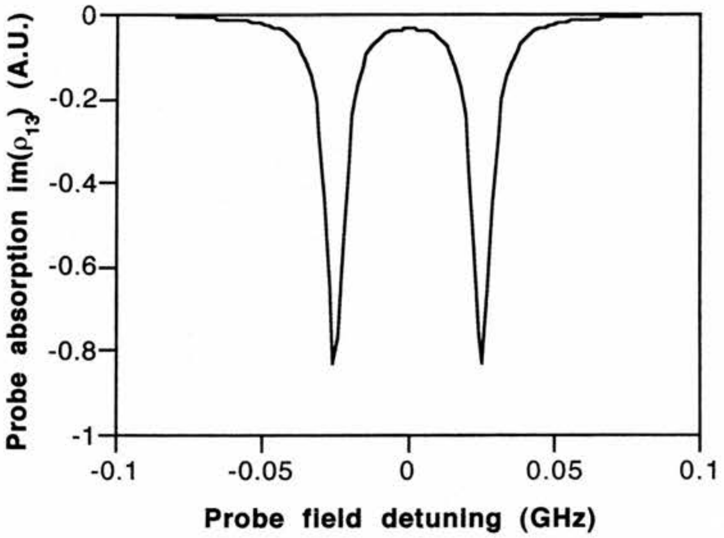

Figure 7.3.3: *The imaginary part of the probe coherence is plotted as a function of the probe field detuning. The coupling field Rabi frequency is set to 50 MHz and that of the probe is 1 MHz.*

In this trace EIT is present when the Rabi frequency of the coupling field is set at 50 MHz. This is an advantage of the atomic beam. The coupling field Rabi frequency required for EIT and hence the coupling field power is much smaller in a system utilising an atomic beam, rather than a cell. In the case of a vapour cell close to room temperature, the Doppler width of the probe transition is around 500 MHz, and Rabi frequencies of the order of 1 GHz on the RF coupling transition are then required, to attain EIT conditions (see 7.2). In the present case the residual Doppler width in the beam for the probe transition is around 250 kHz, so the process is dominated by homogeneous broadening.

This is also shown in figure 7.3.4 and figures 7.3.5 (a) and (b) from which it is deduced. In figure 7.3.4 the probe field absorption on resonance is plotted as function of the coupling field Rabi frequency. For coupling field strengths less than 5 MHz we observe coupling field saturation, as expected for a V-scheme, see figure 7.3.5(a). The reduction in the absorption and hence the transparency due to EIT itself, occurs for coupling field frequencies greater than 8 MHz, see figure 7.3.5 (a) and (b). The amount of the coupling field power required, is significantly reduced when the interaction medium is the atomic beam, and as may be seen from figure 7.3.5 (b), strong EIT effects occur for coupling field Rabi frequencies in excess of 10 MHz.

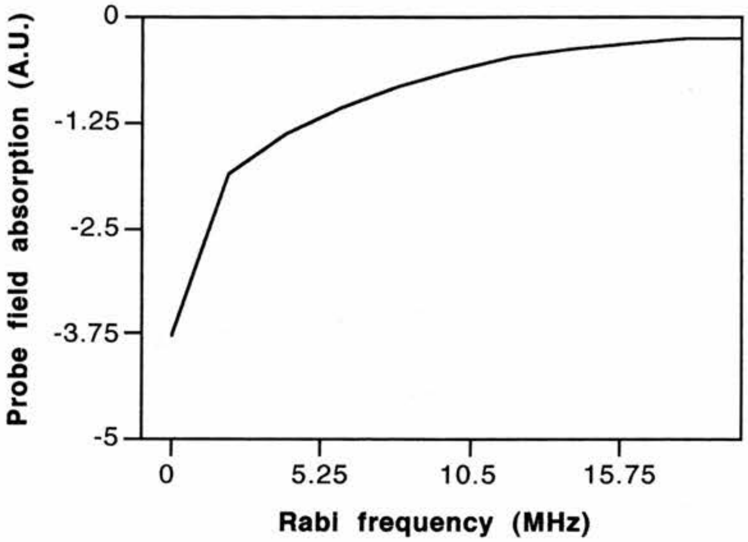

Figure 7.3.4: *The probe field absorption on resonance is plotted as a function of the Rabi frequency. The interaction medium is an atomic beam, which is a non-Doppler medium.*

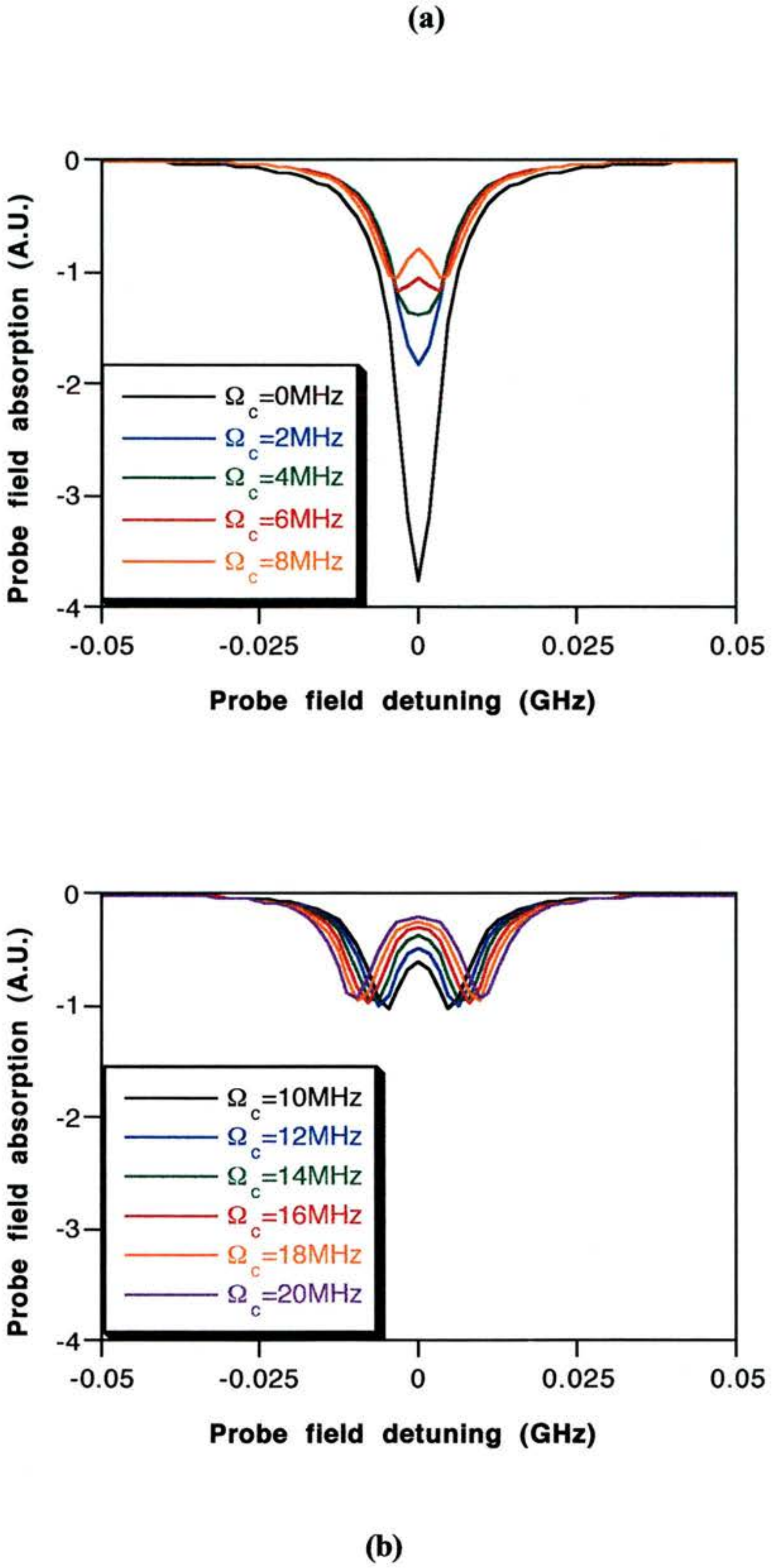

Figure 7.3.5: *The probe field absorption as a function of the probe field detuning for the atomic beam. The Rabi frequencies are (a) from 0-8 MHz and (b) from 10-20 MHz.*

7.4 Rabi frequency and power requirements.

For electric dipole transitions the Rabi frequency is given by:

$$\Omega_C = \frac{\mu_{ij} E}{\hbar} \tag{7.4.1}$$

where μ_{ij} is the electric dipole moment and E is the coupling field strength. The most experiments that demonstrate EIT use an optical field as a coupling field and hence the Rabi frequency is due to electric dipole transitions. However, if we want to use a microwave coupling field to couple hyperfine levels, we have to deal with magnetic dipole transitions. The strength of such magnetic dipole transitions is much weaker than that of the electric dipole ones. Therefore it is necessary to have stronger fields to induce the same Autler-Townes splitting.

The Rabi frequency for magnetic dipole moments may be derived as follows: A general Rabi frequency may be written in the form, *Pake:*

$$\Omega_c = g\, B_1 \tag{7.4.2}$$

where B_1 is the magnitude of the rotating field driving the magnetic dipole transition and g is the gyromagnetic ratio. The oscillating z component of the magnetic portion of the electromagnetic field B_z may be thought being composed of both a rotating and counterrotating component yielding, *Frueholz:*

$$|\, B_z| = 2\, B_1 \tag{7.4.3}$$

The gyromagnetic ratio relates the magnetic moment μ to the atomic angular momentum J as follows:

$$\mu = -g\hbar J \tag{7.4.4}$$

Neglecting the small nuclear contribution , the atomic magnetic moment may be written as:

$$\mu = -g_j \mu_0 J \tag{7.4.5}$$

with μ_0 the Bohr magneton and g_j the electronic g factor. For rubidium's ground state with L=0 and S=1/2, it is g_j=g_e=2 where g_e is the electron g factor. Comparing equations 7.4.4 and 7.4.5 it is apparent for the Rb hyperfine transition:

$$g = \frac{g_j \mu_0}{\hbar} \tag{7.4.6}$$

and combining this result with equations 7.4.2 and 7.4.3 yields :

$$\Omega_C = \frac{\mu_0 \mid B_z \mid}{\hbar} \tag{7.4.7}$$

The Rabi frequency for magnetic dipole transitions has the same form as the Rabi angular frequency for the electric dipole transitions. It is proportional to the Bohr magneton and the B field along the z-direction. The power is now related with the magnetic field as follows:

$$P=k\,B^2 \tag{7.4.8}$$

In order to proceed at this stage, empirical data due to *Frueholz and Camparo* is used, namely that the microwave power of 8 mW is used to generate 3.3×10^{-3} G (3.3×10^{7} T) magnetic field in a TE_{011} cavity containing the Rb cell. In this way we can calculate the constant k in equation 7.4.8. Substituting the above values in equation 7.4.8 yields to: $k=7.3\times 10^{10}$ W/T^2. Hence we can now have an expression of the power as a function of the Rabi frequency. Combining equations 7.4.7 and 7.4.8, the power may be written :

$$P = k(\frac{\hbar}{\mu_0})^2 \Omega_c^2 \tag{7.4.9}$$

From equation 7.4.9 we can obtain data for table 7.4.1. In table 7.4.1 there are several values of Rabi frequencies and the related values of the powers considered. As we can see from the table the power requirements are very demanding. The magnitude of the power for 50 MHz Rabi frequency used in the atomic beam modelling, lies in the kW regime. That is to say that we need high power sources to obtain the desirable Rabi frequencies. It is even worse considering the Rb vapour. The power for 1 GHz splitting is 9.45 MW. If we want to carry out an experiment using RF coupling we have to work with a non-Doppler broadened medium such as an atomic beam.

Rabi frequency	Power
1 MHz	9.45 W
5 MHz	236.18 W
10 MHz	944.70 W
50 MHz	23.62 kW
100 MHz	94.47 kW
500 MHz	2.36 MW
1 GHz	9.45 MW

Table 7.4.1: *A series of Rabi frequencies and their related powers are depicted for a system which is using microwave coupling.*

7.5 The use of an RF source in atomic coherent experiments.

An R.F generator may be used to obtain the microwave radiation at 3 GHz resonant frequency. The microwave field is tuned across the ground state hyperfine transition i.e. magnetic dipole transition. The experimental set up is depicted in figure 7.5.1.

The above experiment includes a microwave generator which is a travelling wave tube (TWT) (Thompson TOP1289) in the frequency range 2-4 GHz. Coaxial cable is connecting all the apparatus and it is indicated as a solid bold line in figure 7.5.1. A frequency counter (Systron-Donner model 6246A) (0.5-26 GHz) is positioned after the oscillator and before the TWT in order to measure the desired frequency. For this purpose a directional coupler (Wessex C3-10) provides 10dB attenuation in the range of 2-4 GHz.

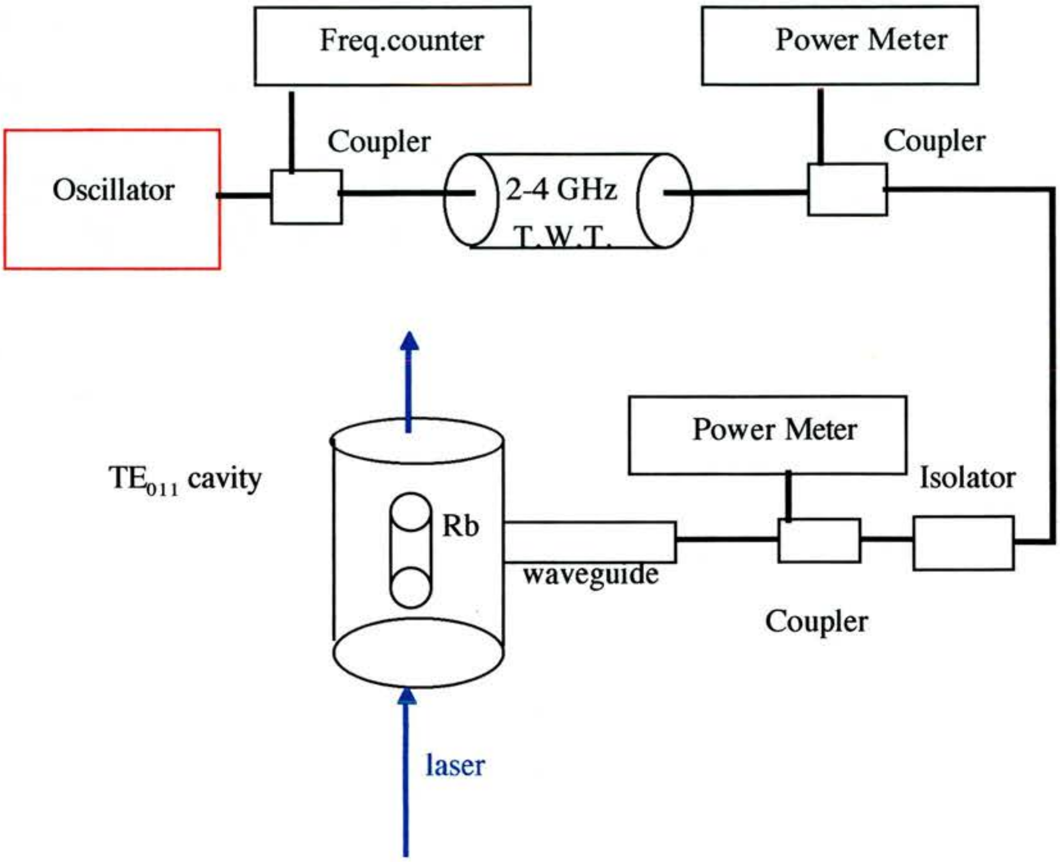

Figure 7.5.1: *The experimental set up for the generation of a microwave field of 3 GHz in order to induce magnetic dipole transitions.*

The power of the microwave field is measured at the power meter (Marconi) placed exactly after the TWT. An isolator protects the TWT from the reflected power propagating from the cavity. Another directional coupler is used to couple the reflected power from the cavity into the power meter, so as to indicate the instant of the exact resonance.

A microwave adapter from coaxial to waveguide (Flann) directs the field into the waveguide. The waveguide could be operated in the range 4.90-7.05 GHz and its dimensions are: width=4.04 cm, height=2.02 cm, length=35 cm and wall thickness=0.16 cm (brass) (*Baden Fuller*). The field is coupled into the cavity by a coupling hole. Its diameter is adjustable and is altered with an iris.

The resonant cavity is made from brass and it is designed to excite the TE_{011} mode. A circular stand inside the cavity holds the Rubidium cell exactly in the middle. The cell is heated by a one meter heating tape, (Electrothermal, for 72 Watts). A temperature controller (FGH series 900) may provide accuracy of ± 0.1° C. The cavity could be heated up to 90° C.

7.6 The mode structure of a cylindrical resonant cavity TE_{011}.

A microwave resonant cavity is a box fabricated from high conductivity metal with dimensions comparable to the wavelength. At resonance, the cavity is capable of sustaining microwave oscillations which form an interference pattern (standing wave configuration) from superposed microwaves multiply reflected from cavity walls. Each particular cavity size can sustain oscillations in a number of different standing wave configurations called modes (*Poole*).

Let the cylindrical cavity radius be a and let the length be d. The propagation constant is defined as:

$$k = (k_c^2 + k_z^2)^{1/2} = [\frac{(k_c a)_{mn}^2}{a^2} + (\frac{p\pi}{d})^2]^{1/2} \tag{7.6.1}$$

where $(k_c a)_{mn}$ is a Bessel function root since cylindrical waveguide modes have Besseloid radial variations, and $k_z = p\pi/d$.

The mode configuration for the general cylindrical TE_{mnp} mode, where the subscripts m,n and p refer to the number of half cycle variations in the angular (ϕ), radial (r) and longitudinal (z) directions, respectively, with n>0 and p>0 are:

$$H_r = \frac{k_z H_0}{(k_c^2 + k_z^2)^{1/2}} J_m'(k_c r) \cos m\varphi \cos k_z z \tag{7.6.2}$$

$$H_\varphi = \frac{m k_z H_0}{(k_c^2 + k_z^2)^{1/2}} \frac{J_m(k_c r)}{k_c r} \sin m\varphi \cos k_z z \tag{7.6.3}$$

$$H_z = \frac{k_c H_0}{(k_c^2 + k_z^2)^{1/2}} J_m(k_c r) \cos m\varphi \sin k_z z \tag{7.6.4}$$

$$E_r = -m(\mu / \varepsilon)^{1/2} H_0 \frac{J_m(k_c r)}{k_c r} \sin m\varphi \sin k_z z \tag{7.6.5}$$

$$E_{\varphi} = -(\mu / \varepsilon)^{1/2} H_0 J_m'(k_c r)\cos m\varphi \sin k_z z \tag{7.6.6}$$

$$E_z = 0 \tag{7.6.7}$$

where H_r is the magnetic field in the radial direction, H_φ the magnetic field in the angular direction, H_z the magnetic field in the longitudinal direction, and E_r, E_φ and E_z are the electric fields in the angular, radial and longitudinal directions, respectively. H_0 is the steady magnetic field strength. J_m is the m-th order Bessel function and J'_m is its first derivative.

The electromagnetic wave configuration for the TE_{011} mode is given by:

$$H_r = \frac{H_0}{2.6365} J_o'(k_c r)\cos(\frac{\pi z}{d}) \tag{7.6.8}$$

$$H_z = \frac{H_0}{1.0808} J_0(k_c r)\sin(\frac{\pi z}{d}) \tag{7.6.9}$$

$$E_{\varphi} = -(\mu / \varepsilon)^{1/2} H_0 J_o'(k_c r)\sin(\frac{\pi z}{d}) \tag{7.6.10}$$

$$H_\varphi = E_r = E_z = 0 \tag{7.6.11}$$

where J_o is the zero order Bessel function and J'_0 is its first derivative. At the centre of the resonant cavity r=0 and using two of the Bessel function properties:

$$J'_0(0) = -J_1(0) = 0 \text{ and } J_0(0) = 1 \tag{7.6.12}$$

the field has only one component, that of the magnetic field along z-axis:

$$H_z = \frac{H_0}{1.0808}\sin(\frac{\pi z}{d}) \tag{7.6.13}$$

One method of coupling to the TE_{011} mode in a cylindrical resonant cavity is diagrammatically sketched in figure 7.6.1 (*Poole*).

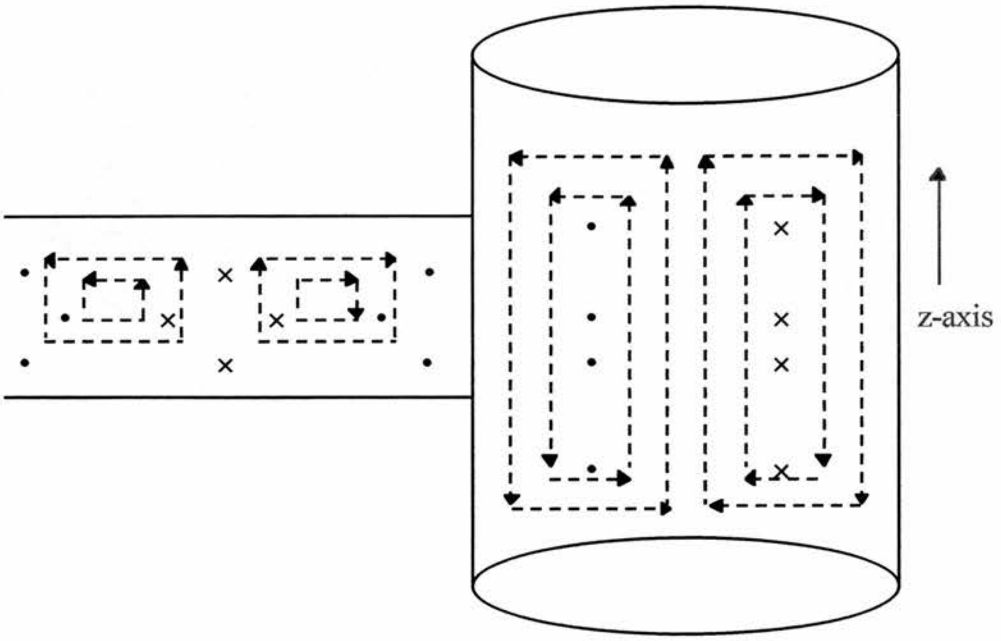

Figure 7.6.1: *A cylindrical cavity is rotated 90° about the waveguide axis to excite the* TE_{011} *mode. The magnetic field is indicated with the dotted lines and the electric field with the symbols • and ×.*

The dependence of the frequency ν on the radius a and the length d of a cylindrical cavity in a vacuum (or air) is easily presented graphically by equation:

$$(2a\nu)^2 = \left(\frac{c(k_c a)'_{mn}}{\pi}\right)^2 + \left(\frac{cp}{2}\right)^2\left(\frac{2a}{d}\right)^2 \tag{7.6.14}$$

where c is the velocity of light in vacuum and $(k_c a)'_{mn}$ is the first derivative of the nth root of $J_m(k_c a)$. The most useful Bessel roots can be found in tables (*Poole*). A graph of $(2a\nu)^2$ against $(2a/d)^2$ is plotted in figure 7.6.2. In designing a cavity it is best to select values of a and d so that there are no other modes near the design point.

The quality factor Q is defined as:

$$Q = \frac{2\pi(energy - stored)}{(energy - dissipated)/\, cycle} \tag{7.6.15}$$

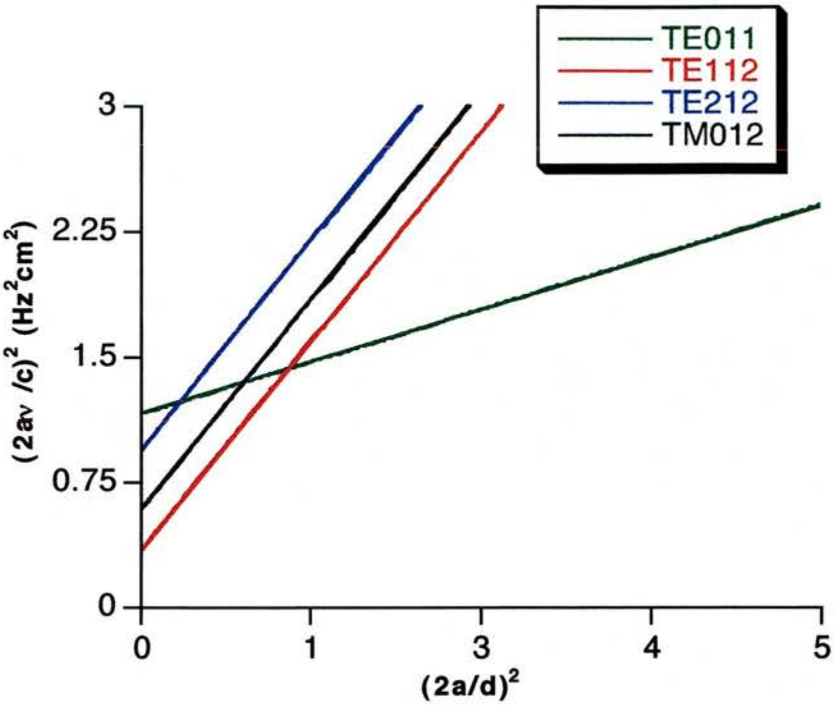

Figure 7.6.2: *Mode chart for right circular cylinder of radius a, length d and resonant frequency ν..*

The unloaded Q_u factor for the TE_{mnp} cylindrical mode may be calculated from the properties of the cavity and is:

$$Q_u \frac{\delta}{\lambda} = \frac{(1/2\pi)[1 - m/(k_c a)'^2_{mn}][(k_c a)'^2_{mn} + (p\pi a/d)^2]^{2/3}}{(k_c a)'^2_{mn} + (2a/d)(p\pi a/d)^2 + (1 - 2a/d)[mp\pi a/d(k_c a)'_{mn}]^2} \qquad (7.6.16)$$

where δ is the skin depth and it is defined as:

$$\delta = (2/\omega\mu\sigma)^{1/2} \qquad (7.6.17)$$

with ω being the angular frequency, $\mu = 4\pi\times10^{-7}$ H/m and σ being the conductivity of the metal. Equation (7.6.16) is used for the TE_{011} mode cavity. The substitution $(k_c a)'_{01p}=3.832$ is followed and the result is plotted in figure 7.6.3. One should note that the TE_{onp} mode has a maximum value of $Q_u\delta/\lambda$ when the cavity length equals the diameter 2a.

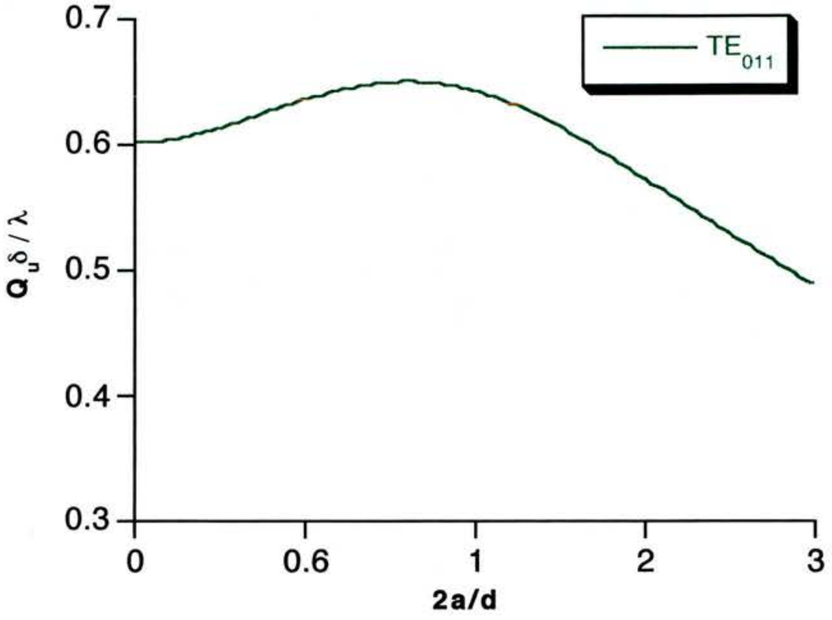

Figure 7.6.3: *$Q_u\delta / \lambda$ versus 2a/d for the TE$_{011}$ mode in a circular cavity.*

7.7 Designing a tuneable cylindrical cavity TE$_{011}$ resonant to a frequency of 3GHz.

The key information for the construction of a cylindrical resonant cavity is provided by equations 7.6.14 and 7.6.16 and subsequently, by the graphs of figure 7.6.2 and 7.6.3. Initially, the unloaded quality factor Q_u of cavities which excite the TE$_{01p}$ mode has its maximum value only when the length equals the diameter of the cylinder. Hence, the optimum cavity sizes are 2a = d.

From figure 7.6.3 it is $Q_u \lambda/\delta = 0.66$. The wavelength is $\lambda = 10$ cm and the skin depth is calculated from equation 7.6.17, by substituting for the conductivity of brass $\sigma = 1.57\times10^7$ mhos/m (*Montgomery, Dicke, Purcel*) and its value is $\delta = 2.319\times10^{-6}$ m. Therefore, the unloaded quality factor is $Q_u = 28{,}461$.

At resonance the Q of the resonant cavity may be expressed mathematically by adding the sample loss term Q_χ and Q_r due to the cavity coupling hole, as follows:

$$\frac{1}{Q} = \frac{1}{Q_u} + \frac{1}{Q_r} + \frac{1}{Q_\chi} \qquad (7.7.1)$$

For the case of critical coupling when the cavity is perfectly matched to the waveguide, (the coupling parameter is $\beta = 1$), $Q_u = Q_r$. Hence neglecting the losses of the sample in equation 7.7.1, the loaded Q of the cylindrical TE_{011} cavity has a value Q = 14,231.

The dimensions of the cavity are calculated from the graph of figure 7.6.2. When the cavity is resonant to the frequency $\nu = 3GHz$, from the plot $(d\,\nu)^2 = 15.625$ Hz^2cm^2. The length of the cavity is d = 13.176 cm and its diameter is 2a = 13.176 cm. The side view of a TE_{011} mode cylindrical cavity for the 3GHz region is shown in the model of figure 7.7.1.

The cylindrical TE_{011} cavity is especially useful since H_z is very strong along the cavity axis. Further, it has a fairly high Q factor, and there is no current flow in either the radial (r) or longitudinal (z) direction, but only in the angular (ϕ). This property enables one to use a pistonelike tuning plunger on the end plate, as shown in figure 7.7.1 for the rubidium cell, so that the frequency may be varied by screwing the end plate in and out. A three-dimensional schematic representation of the cavity and the atomic beam is depicted in figure 7.7.2. The same cavity is used to contain the atomic beam and an additional hole is made in the cavity for the propagation of the probe field.

The current flow property renders it unnecessary to achieve good electrical contact between the end plate and the cylinder. If a gap is deliberately opened between the piston edges and the walls (see figure 7.7.1), then other modes will be suppressed because they require RF current to flow across the gap. In particular, this will suppress the TM_{111} which is degenerate with the TE_{011} mode (*Poole*).

The coupling of the TE_{10} mode of the rectangular waveguide into the cylindrical cavity is achieved by rotation of the waveguide axis at 90° about the resonant cavity. The coupling parameters are of great importance and the size and the thickness of the circular hole is substantial to ensure critical matching. Therefore, an adjustable iris is positioned instead of a hole and its diameter could be altered from 2 cm (max aperture size) to 2mm (min aperture size).

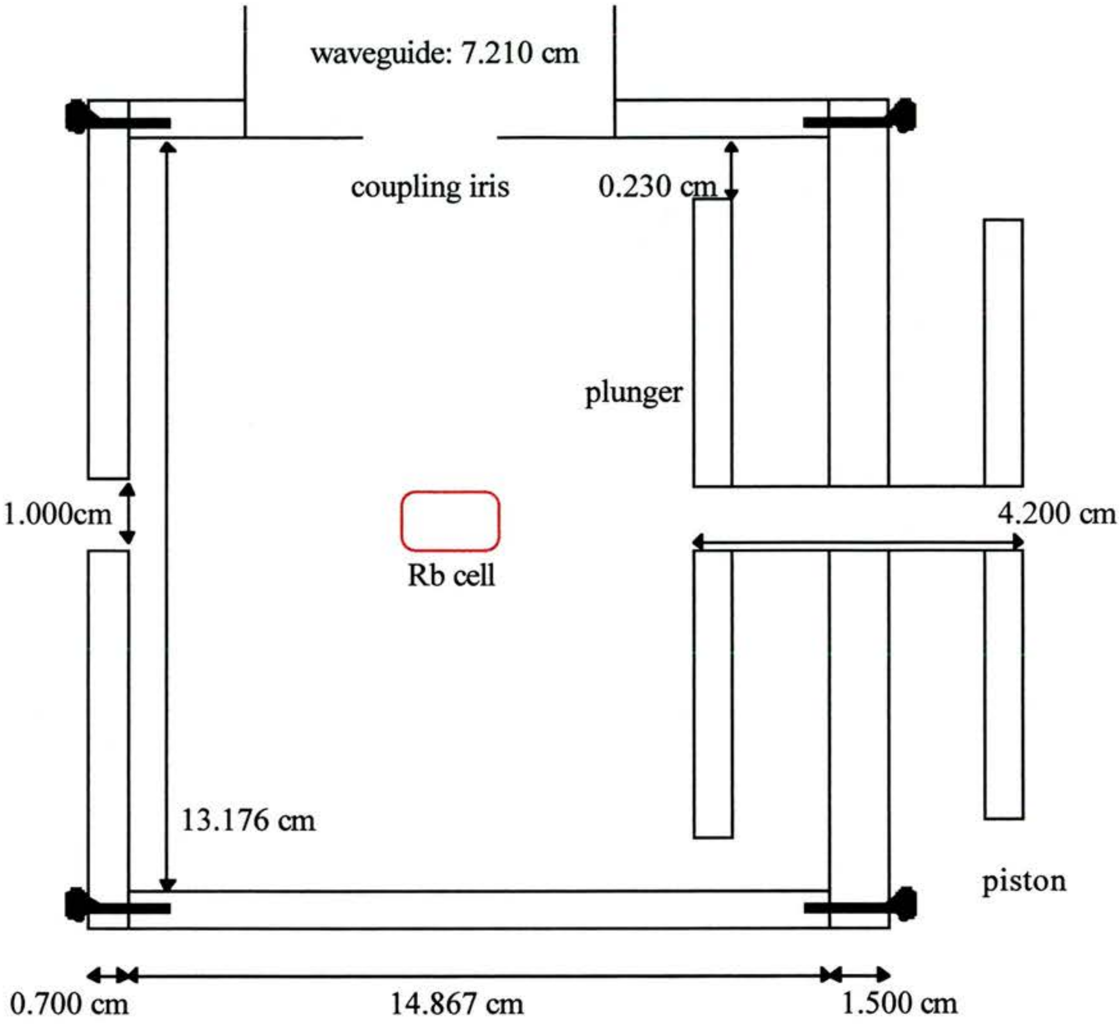

Figure 7.7.1: *The side view of a cylindrical* TE_{011} *cavity resonant at the frequency of 3 GHz.*

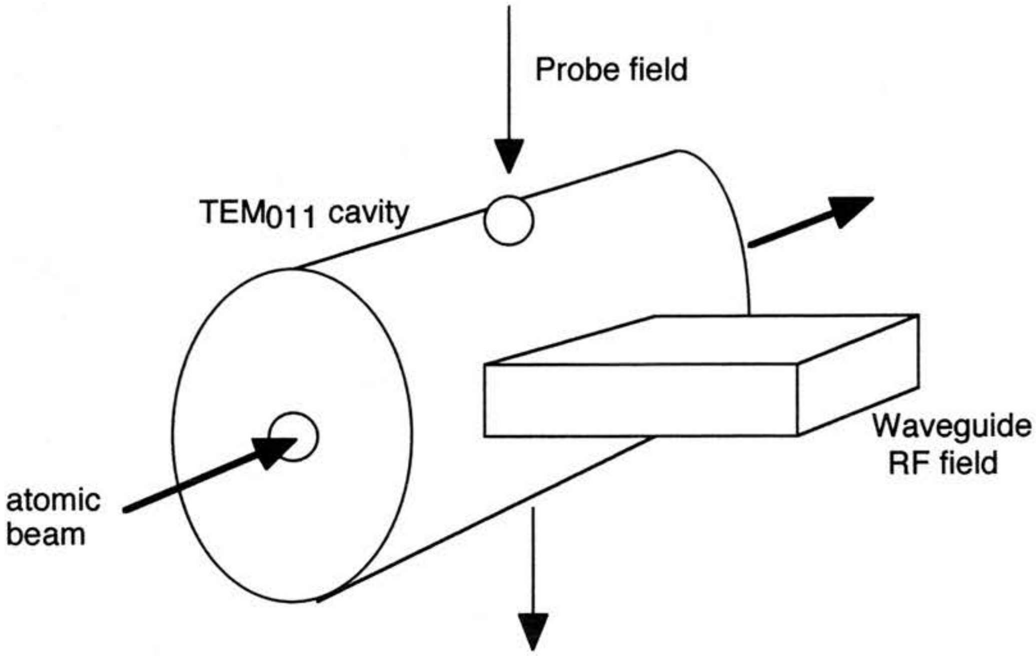

Figure 7.7.2: *A schematic representation of the resonant cavity for the experiment using the atomic beam as an interaction medium. An additional hole is positioned at right angles for the propagation of the probe field.*

7.8 Conclusions.

In this chapter we have demonstrated the possibility of achieving transparency by the use of a microwave field as the coupling field, in a V-type configuration. The active medium was chosen ^{85}Rb both as a Doppler broadened medium and as an atomic beam. The probe transition which was rendered transparent had a wavelength in the infrared regime. The Doppler broadened medium required high Rabi frequencies and therefore, more powerful microwave sources. The RF induces magnetic dipole transitions in the Rb ground state, that are very weak in strength. Even, by using the atomic beam the power demands were very high, 50-100 kW. Hence, there has been a necessity of a new microwave oscillator and amplifier, in order to reach such high powers.

Subsequently, we presented theoretical calculation for the construction of a TE_{011} cavity. This cavity was designed to resonate on 3 GHz which is the hyperfine splitting of ^{85}Rb ground state. The cylindrical TE_{011} cavity excites a magnetic field along the z-axis, which oscillates and induces magnetic dipole transitions. The corresponding apparatus for the experiment was also demonstrated. The feasibility of such experiment depends on the microwave power required.

References

Baden Fuller A.J., Microwaves, Pergamon Press 2nd edition, 1979.

Boller K.J., Imamoglou A. and Harris S.E., "Observation of Electromagnetically Induced Transparency", Physical Review Letters, **66**, p.2593 (1991).

Frueholz R.P. and Camparo J.C., " Microwave field strength measurement in a rubidium clock cavity via adiabatic rapid passage", J. Appl.Physics, **57**, p704 (1985)

Ham B.S., M.S. Shahriar and P.R. Hemmer, "Radio frequency induced optical gain in $Pr^{3+}:Y_2SiO_5$", Journal Opt. Soc. Am.B, **15**, p1541 (1998).

Montgomery, Dicke, Purcell, Principles of microwave circuits, McGraw Hill Series, 1948.

Padmabandu G.G, Welch G.R., Shubin I.N., Fry E.S., Nikonov D.E., Lukin M.D. and O. Scully M., "Laser oscillation without population inversion in a sodium atomic beam", Physical Review Letters, **76**, p2053 (1996).

Pake, Paramagnetic resonance, Benjamin, New York, 1962.

Poole C.P., Electron spin resonance, Interscience Publishers , 1967.

Zibrov A.S., Lukin M.D., Nikonov D., Hollberg L., O.Scully M., Velichansky V.L. and Robinson H.G., "Experimental demonstration of laser oscillation without population inversion via quantum interference in Rb", Physical Review Letters, **75**, p.1499 (1995)

Chapter 8

Conclusions and future work

8.1 Conclusions

In this thesis we initially described the basic concepts of electromagnetically induced transparency (EIT) and Autler-Townes splitting and we presented a detailed historical retrospective of EIT and lasing without inversion related experiments. This discussion was complemented by a review of work previously carried out, demonstrating quantum coherence effects, such as EIT, phaseonium (medium with high refractive index and no absorption) and lasing without population inversion.

In the second chapter a theoretical analysis was presented utilising density matrices. This theoretical modelling was the basis for analysing induced transparency in the three most important schemes, namely the Cascade, the V-type and the Lambda, in a Doppler broadened medium. Inversionless gain was numerically calculated for the V-type and the Lambda configurations. Four-level atomic models were also considered and the feasibility of transparency and gain was analysed in such schemes.

The interaction medium for the experiments and the theoretical modelling was Rb vapour. Most of the transitions explored in our analysis lay in the visible and the near-infrared regime. Therefore, the laser sources employed were Ti:sapphire lasers, either directly or with frequency doubling, in the CW mode of operation.

In chapter 4 we have reported the first experimental observation of coherently induced transparency in a Doppler broadened V-type system, employing mismatched wavelengths. The transparency was induced on a transition in the blue spectral region, by the presence of an infrared coupling field. This has been achieved in the absence of optical pumping. Transparency was observed for Rabi frequencies equal to or higher than the Doppler broadening of the probe field. As predicted from the theory EIT should be present for lower coupling field Rabi frequencies. In fact, transparency was not observed at low coupling field strengths, either due to the high dephasing dictated by the ground state collisional mixing rate or due to the coupling field absorption at high particle densities.

The coherence on the unlinked transition played an important role in creating the transparency window. The coherence is still the factor determining the level of transparency even at high levels of Autler-Townes splitting. The results shown, represent the realisation of the first step in the process of creating a blue inversionless laser, by producing transparency in the 422 nm in a Doppler broadened V-type system. Extension to the short wavelength regime is the potential application of lasing without population inversion and a goal of quantum coherence.

Following the experimental realisation of mismatched EIT in a Doppler broadened system, a theoretical comparison was made in chapter 5 for the matched and the mismatched wavelength cases, based on Rb. It was shown that in a V-scheme there is no need for matching the probe and the coupling field wavelengths in order to observe transparency on line centre, and that EIT is still possible even in the presence of Doppler broadening. This happens because the magnitude of the secondary Autler-Townes component, related to the two-photon process, which overlaps with the transparency window is not significant enough to erode the transparency. Hence, EIT is produced for coupling field Rabi frequencies less than the Doppler width of the probe transition.

Subsequently, gain without population inversion was predicted in a Doppler broadened mismatched scheme. A comparison was made of inversionless gain achieved via EIT, in matched and mismatched wavelength systems. While the predicted matched gain was higher in the matched system, gain was still significant in the mismatched case. The theory was related to an experimental system and for 2 cm cell length and a coupling field Rabi frequency of 160 MHz we predict an inversionless gain of approximately 8%. This calculation is based on a modest incoherent pumping rate and a Rabi frequency easily obtainable with CW laser powers.

The theoretical comparison of mismatching the probe and the coupling field wavelengths was extended to the cascade, the lambda and the V-schemes, in chapter 6.

Three wavelength regimes were explored in a Doppler broadened medium, $\lambda_c<\lambda_p$, $\lambda_c=\lambda_p$ and $\lambda_c>\lambda_p$. The model showed that matching the wavelengths enables EIT to be observed in all three systems. Importantly, the best transparency was shown for the mismatched case where $\lambda_c<\lambda_p$. This is a direct result of the increased Doppler shifted contribution to the coupling field detuning.

In the mismatched regime of $\lambda_c>\lambda_p$ transparency was predicted only for the V-scheme for Rabi frequencies less than the Doppler width. This fact may be explained by considering the roles of the different velocity groups within the Doppler distribution. The two-photon process is present in a V-scheme for the zero velocity atoms, enabling EIT to occur by destructive interference between the single and the two-photon routes to absorption. As the atomic velocity increases for higher velocity groups the two-photon process diminishes and the secondary Autler-Townes components, related to the two-photon absorptions of the non-zero velocity groups, which overlap with the transparency window, are not high enough to obscure EIT. This reduction of the two-photon absorptions occurs in the V-scheme because it starts in the upper level of the coupling field transition and is therefore reduced in magnitude when the coupling field is Doppler shifted from resonance. In this wavelength regime and for Rabi frequencies less than the Doppler width, EIT is not observable in the cascade and the lambda schemes.

How far can we mismatch the wavelength of the probe and the coupling fields? In the last chapter we have demonstrated the possibility of producing transparency on an infrared transition by the use of a microwave field as the coupling field. This was studied both in Rb vapour and in an atomic beam. The Rabi frequency of the coupling field required in the Doppler broadened medium was in the range of GHz , hence it dictates very powerful microwave sources (of the order of MW's). This is because the transitions involved are magnetic dipole transitions in the hyperfine levels of the ground state, and are very weak. Even using the atomic beam the power requirements are still high, since Rabi frequencies of the order of 50 MHz are still required, hence implying powers of the order of 50-100 kW. The experimental apparatus was assembled, including the design and construction of a TE_{011} cavity. The cylindrical cavity is on resonance to the 3 GHz hyperfine splitting of the ground state and produces a magnetic field along the z-axis of the cavity. The feasibility of such experiment depends on the microwave power required.

In conclusion, all the previous experiments demonstrating EIT and inversionless gain used matching wavelengths to avoid the consequences of Doppler broadening. We have shown that EIT is experimentally observed in a blue transition, utilising an infrared coupling field, even in a Doppler broadened V-type medium. Mismatching the wavelengths does not necessarily limit the transparency induced in a V-type configuration. Furthermore, by employing such a system, inversionless gain is predicted for Rabi frequencies less than the Doppler width. Choosing a probe field wavelength less than that of the coupling field, leads to a shorter wavelength for a lasing transition, which is a potential application of lasing without population inversion.

8.2 Future work.

In the last chapter we have already studied microwave induced transparency in atomic Rb. The complication with this system is that the magnetic dipole transitions are very weak, therefore the power requirements of the microwave field are high. In order to overcome this problem, we can use as interaction medium a molecular system and in particular ammonia (NH_3). Molecules can display strong electric dipole moments, associated with rotational-vibrational transitions. Ammonia is such a molecule, and because of the intensity and richness of its spectrum, has played a major role in the development of microwave spectroscopy. Ammonia was known for the maser oscillator at 23.87 GHz.

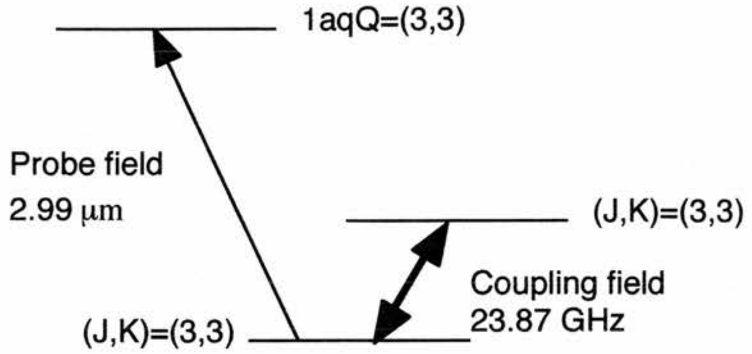

Figure 8.2.1: *The V-type system within ammonia molecule. The weak probe field has a wavelength in the mid-infrared, whereas the coupling field is a microwave field.*

The energy level scheme of the future experiment is depicted in figure 8.2.1. An experimental set-up is currently being designed. The proposed system is a V-type configuration. The probe field has a wavelength λ_p=2.99 μm, in the mid-infrared spectral region. A pump-enhanced geometry optical parametric oscillator (OPO) is being designed to act as the single frequency, scannable probe field. The OPO will be pumped by a single frequency, 30 GHz scan Microlase Ti:Sapphire laser. The probe field is on resonance with the transition of one doublet level (J,K)=(3,3) to the vibrational level 1aqQ(3,3). The strong coupling field is a microwave field of 23.87 GHz. This couples the doublet level (J,K)=(3,3) in ammonia. The microwave field will be introduced via a Gunn diode or a travelling wave tube into a resonant cavity.

The cylindrical cavity will be designed to excite an electric field along the z-axis, oscillating at 23.87 GHz. The cavity may provide a high Q in order to amplify the microwave field. The microwave field will be the strong coupling field, which induces transparency and Autler-Townes splitting to the mid-infrared transition. Ammonia will be contained in quartz tube running through the cavity and will be connected to a vacuum system. The ammonia tube and the microwave cavity will be situated in an optical cavity, which acts as a multipass resonator of the infrared radiation, to provide multiple optical paths through the ammonia, in order to enhance the detection of small changes in absorption. This is a novel system, because it includes molecules as an interaction medium and a mismatched geometry for observing quantum coherence phenomena, such as microwave induced transparency and perhaps in the future, inversionless gain.

Appendix A

Density matrix equations for 4-level atomic systems

$$\begin{bmatrix}
1.7\Lambda & \Lambda-\Gamma_{32} & \Lambda-\Gamma_{42} & 0 & 0 & 0 & 0 & 0 & 0 & 0 & 0 & 0 & -2\Omega_{23} & 0 & 0 \\
0 & \Gamma_{32}+\Gamma_{31} & 0 & 0 & 0 & 0 & 0 & 0 & 0 & 0 & 2\Omega_{13} & 0 & 2\Omega_{23} & 0 & 0 \\
0 & 0 & \Gamma_{42}+\Gamma_{41} & 0 & 0 & 0 & 0 & 0 & 0 & 0 & 0 & 2\Omega_{14} & 0 & 0 & 0 \\
0 & 0 & 0 & \gamma_{12} & 0 & 0 & 0 & 0 & 0 & \Delta_{23}-\Delta_{13} & -\Omega_{23} & 0 & -\Omega_{13} & -\Omega_{14} & 0 \\
0 & 0 & 0 & 0 & \gamma_{13} & 0 & 0 & 0 & 0 & -\Omega_{23} & -\Delta_{13} & 0 & 0 & 0 & -\Omega_{14} \\
0 & 0 & 0 & 0 & 0 & \gamma_{14} & 0 & 0 & 0 & 0 & 0 & -\Delta_{14} & 0 & 0 & -\Omega_{13} \\
0 & 0 & 0 & 0 & 0 & 0 & \gamma_{23} & 0 & 0 & \Omega_{13} & 0 & 0 & -\Delta_{23} & 0 & 0 \\
0 & 0 & 0 & 0 & 0 & 0 & 0 & \gamma_{24} & 0 & \Omega_{14} & 0 & 0 & 0 & \Delta_{13}-\Delta_{14}-\Delta_{23} & \Omega_{23} \\
0 & 0 & 0 & 0 & 0 & 0 & 0 & 0 & \gamma_{34} & 0 & \Omega_{14} & \Omega_{13} & 0 & \Omega_{23} & \Delta_{13}-\Delta_{14} \\
0 & 0 & 0 & \Delta_{13}-\Delta_{23} & \Omega_{23} & 0 & -\Omega_{13} & -\Omega_{14} & 0 & \gamma_{12} & 0 & 0 & 0 & 0 & 0 \\
-\Omega_{13} & -2\Omega_{13} & -\Omega_{13} & \Omega_{23} & \Delta_{13} & 0 & 0 & 0 & -\Omega_{14} & 0 & \gamma_{13} & 0 & 0 & 0 & 0 \\
-\Omega_{14} & -\Omega_{14} & -2\Omega_{14} & 0 & 0 & \Delta_{14} & 0 & 0 & -\Omega_{13} & 0 & 0 & \gamma_{14} & 0 & 0 & 0 \\
\Omega_{23} & -\Omega_{23} & 0 & \Omega_{13} & 0 & 0 & \Delta_{23} & 0 & 0 & 0 & 0 & 0 & \gamma_{23} & 0 & 0 \\
0 & 0 & 0 & \Omega_{14} & 0 & 0 & 0 & \Delta_{14}-\Delta_{13}+\Delta_{23} & -\Omega_{23} & 0 & 0 & 0 & 0 & \gamma_{24} & 0 \\
0 & 0 & 0 & 0 & \Omega_{14} & -\Omega_{13} & 0 & -\Omega_{23} & \Delta_{14}-\Delta_{13} & 0 & 0 & 0 & 0 & 0 & \gamma_{34}
\end{bmatrix}
\begin{bmatrix}
\rho_{22} \\ \rho_{33} \\ \rho_{44} \\ re(\rho_{12}) \\ re(\rho_{13}) \\ re(\rho_{14}) \\ re(\rho_{23}) \\ re(\rho_{24}) \\ re(\rho_{34}) \\ im(\rho_{12}) \\ im(\rho_{13}) \\ im(\rho_{14}) \\ im(\rho_{23}) \\ im(\rho_{24}) \\ im(\rho_{34})
\end{bmatrix}
=
\begin{bmatrix}
\Lambda \\ 0 \\ 0 \\ 0 \\ 0 \\ 0 \\ 0 \\ 0 \\ 0 \\ 0 \\ -\Omega_{13} \\ -\Omega_{14} \\ 0 \\ 0 \\ 0
\end{bmatrix}$$

Matrix 2.1 : The matrix system of a four-level V-energy scheme in rubidium.

$$\begin{bmatrix}
1.7\Lambda + R_{23} & \Lambda - \Gamma_{32} - R_{23} & \Lambda - \Gamma_{42} & 0 & 0 & 0 & 0 & 0 & 0 & 0 & 0 & 0 & 0 & 0 & 0 \\
-R_{23} & \Gamma_{32} + \Gamma_{31} + R_{23} & 0 & 0 & 0 & 0 & 0 & 0 & 0 & 0 & 2\Omega_{13} & 0 & 0 & 0 & 0 \\
0 & 0 & \Gamma_{42} + \Gamma_{41} & 0 & 0 & 0 & 0 & 0 & 0 & 0 & 0 & 2\Omega_{14} & 0 & 0 & 0 \\
0 & 0 & 0 & \gamma_{12} & 0 & 0 & 0 & 0 & 0 & -\Delta_{12} & 0 & 0 & -\Omega_{13} & -\Omega_{14} & 0 \\
0 & 0 & 0 & 0 & \gamma_{13} & 0 & 0 & 0 & 0 & 0 & -\Delta_{13} & 0 & 0 & 0 & -\Omega_{14} \\
0 & 0 & 0 & 0 & 0 & \gamma_{14} & 0 & 0 & 0 & 0 & 0 & -\Delta_{14} & 0 & 0 & -\Omega_{13} \\
0 & 0 & 0 & 0 & 0 & 0 & \gamma_{23} & 0 & 0 & \Omega_{13} & 0 & 0 & \Delta_{12} - \Delta_{13} & 0 & 0 \\
0 & 0 & 0 & 0 & 0 & 0 & 0 & \gamma_{24} & 0 & \Omega_{14} & 0 & 0 & 0 & \Delta_{12} - \Delta_{14} & 0 \\
0 & 0 & 0 & 0 & 0 & 0 & 0 & 0 & \gamma_{34} & 0 & \Omega_{14} & \Omega_{13} & 0 & 0 & \Delta_{13} - \Delta_{14} \\
0 & 0 & 0 & \Delta_{12} & 0 & 0 & -\Omega_{13} & -\Omega_{14} & 0 & \gamma_{12} & 0 & 0 & 0 & 0 & 0 \\
-\Omega_{13} & -2\Omega_{13} & -\Omega_{13} & 0 & \Delta_{13} & 0 & 0 & 0 & -\Omega_{14} & 0 & \gamma_{13} & 0 & 0 & 0 & 0 \\
-\Omega_{14} & -\Omega_{14} & -2\Omega_{14} & 0 & 0 & \Delta_{14} & 0 & 0 & -\Omega_{13} & 0 & 0 & \gamma_{14} & 0 & 0 & 0 \\
0 & 0 & 0 & \Omega_{13} & 0 & 0 & \Delta_{13} - \Delta_{12} & 0 & 0 & 0 & 0 & 0 & \gamma_{23} & 0 & 0 \\
0 & 0 & 0 & \Omega_{14} & 0 & 0 & 0 & \Delta_{14} - \Delta_{12} & 0 & 0 & 0 & 0 & 0 & \gamma_{24} & 0 \\
0 & 0 & 0 & 0 & \Omega_{14} & -\Omega_{13} & 0 & 0 & \Delta_{14} - \Delta_{13} & 0 & 0 & 0 & 0 & 0 & \gamma_{34}
\end{bmatrix}
\begin{bmatrix}
\rho_{22} \\ \rho_{33} \\ \rho_{44} \\ re(\rho_{12}) \\ re(\rho_{13}) \\ re(\rho_{14}) \\ re(\rho_{23}) \\ re(\rho_{24}) \\ re(\rho_{34}) \\ im(\rho_{12}) \\ im(\rho_{13}) \\ im(\rho_{14}) \\ im(\rho_{23}) \\ im(\rho_{24}) \\ im(\rho_{34})
\end{bmatrix}
=
\begin{bmatrix}
\Lambda \\ 0 \\ 0 \\ 0 \\ 0 \\ 0 \\ 0 \\ 0 \\ 0 \\ 0 \\ -\Omega_{13} \\ -\Omega_{14} \\ 0 \\ 0 \\ 0
\end{bmatrix}$$

Matrix 2.2: The matrix system of a four-level V-energy scheme with an incoherent pump R_{23}.

Appendix B

Publications and Conference proceedings

Publications

Experimental observation of a coherently induced transparency on a blue probe in a Doppler-broadened mismatched V-type system
James R. Boon, Evangelini Zekou, David J. Fulton, and Malcolm H. Dunn
Physical Review A **57**, p. 1323-1328, (1998).

Prediction of inversionless gain in a mismatched Doppler-broadened medium
James R. Boon, Evangelini Zekou, David McGloin, and Malcolm H. Dunn
Physical Review A **58**, p.2560, (1998).

Comparison of wavelength dependence in Cascade, Lambda and Vee-type schemes for electromagnetically induced transparency
James R. Boon, Evangelini Zekou, David McGloin, and Malcolm H. Dunn
Physical Review A, submitted 11/6/98 and accepted January 1999.

Conference proceedings

Inversionless lasing in the visible spectrum
Evangelini Zekou and James R. Boon
Poster 14 at the Inaugural Meeting of the Scottish Lasers and Electro-Optics Society (LEOS) Chapter, Glasgow, 1996.

Coherently induced transparency and inversionless gain on a blue probe field in a Doppler-broadened V-type medium
David J. Fulton, Sara Shepherd, Evangelini Zekou, James R. Boon, and Malcolm H. Dunn
Quantum Electronics and Laser Science Conference 1997 (QELS 97), Technical Digest Series, Vol. 12, paper QTuE8 (Optical Society of America, Washington DC, 1997).

Coherently induced transparency and inversionless gain on a blue probe in a Doppler-broadened medium
David J. Fulton, James R. Boon, Evangelini Zekou, Sara Shepherd, and Malcolm H. Dunn
Thirteenth UK National Quantum Electronics Conference (QE-13), Cardiff, 1997.

A study of inversionless gain in mismatched Doppler-broadened systems
James R. Boon, Evangelini Zekou, David McGloin, and Malcolm H. Dunn
International Quantum Electronics Conference (IQEC) 1998, Technical Digest Series, Vol. 7, paper QWK6 (Optical Society of America, Washington DC, 1998).

Progress in EIT and Inversionless gain in Doppler broadened mismatched systems.
David McGloin, James R. Boon, Evangelini Zekou and Malcolm H. Dunn
SUSSP-52, Scottish summer school, Advances in lasers and applications, St.Andrews, 1998.

Progress in EIT and Inversionless gain in Doppler broadened mismatched systems.
David McGloin, James R. Boon, Evangelini Zekou and Malcolm H. Dunn
Poster at the Meeting of the Scottish Lasers and Electro-Optics Society (LEOS) Chapter, St.Andrews, November 1998.